

Aus der
Walther-Straub-Institut für Pharmakologie und Toxikologie
Institut der Ludwig-Maximilians-Universität München



**Identification of pharmacological compounds selectively acting on
the kinases-coupled channels TRPM6 and TRPM7**

Dissertation
zum Erwerb des Doktorgrades der Medizin
an der Medizinischen Fakultät
der Ludwig-Maximilians-Universität München

vorgelegt von
Anna Rössig

aus
Köln

Jahr
2025

Mit Genehmigung der Medizinischen Fakultät der
Ludwig-Maximilians-Universität München

Erstes Gutachten:	Prof. Dr. Thomas Gudermann
Zweites Gutachten:	Prof. Dr. Hans-Joachim Anders
Drittes Gutachten:	Prof. Dr. Christian Wahl-Schott
weitere Gutachten:	Priv. Doz. Dr. Kerstin Hill

Dekan:	Prof. Dr. med. Thomas Gudermann
--------	---------------------------------

Tag der mündlichen Prüfung: 28.03.2025

Affidavit



Promotionsbüro
Medizinische Fakultät



Affidavit

Rössig, Anna

Surname, first name

I hereby declare, that the submitted thesis entitled:

Identification of pharmacological compounds selectively acting on the kinases-coupled channels TRPM6 and TRPM7

is my own work. I have only used the sources indicated and have not made unauthorised use of services of a third party. Where the work of others has been quoted or reproduced, the source is always given.

I further declare that the submitted thesis or parts thereof have not been presented as part of an examination degree to any other university.

Köln, 01.05.2025

place, date

Anna Rössig

Signature doctoral candidate

Table of content

Affidavit	3
Table of content	4
List of abbreviations	5
List of publications	6
1. Contribution to the publications	7
1.1 Contribution to publication I [1]	7
1.2 Contribution to publication II [10]	9
1.3 Contribution to publication III [12]	11
2. Introduction	12
2.1 Domain topology and tetrameric assembly of TRPM6 and TRPM7 channel-kinase complexes	12
2.2 Functional characteristics of the TRPM6 and TRPM7 channels	14
2.3 Pathophysiological roles of TRPM6 and TRPM7	16
2.4 Pharmacological modulators of TRPM6 and TRPM7	18
3. Research goals	20
4. Summary (in English)	21
5. Zusammenfassung (deutsch)	22
6. Publication I	23
7. Publication II	49
Appendix A: Publication III	70
References	99
Acknowledgements	106
Curriculum vitae	108

List of abbreviations

ARL15 protein	ADP-ribosylation factor-like protein 15
CNNM	Cyclin and CBS domain divalent metal cation transport mediator
CryoEM	Cryogenic electron microscopy
DVF solution	Divalent cation-free solution
EC ₅₀	Half-maximal effective concentration
HEK293 cells	Human embryonic kidney 293 cells
HEK293T cells	Human embryonic kidney 293T cells
IC ₅₀	Half-maximal inhibitory concentration
ILO	lloperidone
IFE	Ifenprodil tartrate
I–V relationship	Current–voltage relationship
MD	Molecular dynamic
NS8593	NS
PIP ₂	Phosphatidylinositol 4,5-bisphosphate
PLC	Phospholipase C
TRP channel	Transient receptor potential channel
TRPM6	Transient receptor potential melastatin-subfamily member 6
TRPM7	Transient receptor potential melastatin-subfamily member 7
TS cells	Trophoblast stem cells
VER	VER155008
WT	Wild-type

List of publications

1. **Rössig A**, Hill K, Nörenberg W, Weidenbach S, Zierler S, Schaefer M, Gudermann T, Chubarov V, Pharmacological agents selectively acting on the channel moieties of TRPM6 and TRPM7. Cell Calcium. 2022; 10.1016/j.ceca.2022.102640.
2. Schmidt E, Narangoda C, Nörenberg W, Egawa M, **Rössig A**, Leonhardt M, Schaefer M, Zierler S, Kurnikova M, Gudermann T, Chubarov V, Structural mechanism of TRPM7 channel regulation by intracellular magnesium. Cellular and Molecular Life Science. 2022; 10.1007/s00018-022-04192-7
3. Kollwe A, Chubarov V, Tseung FT, Correia L, Schmidt E, **Rössig A**, Zierler S, Haupt A, Müller CS, Bildl W, Schulte U, Nicke A, Fakler B, Gudermann T, The molecular appearance of native TRPM7 channel complexes identified by high-resolution proteomics. Elife. 2021; 10.7554/eLife.68544.

1. Contribution to the publications

1.1 Contribution to publication I [1]

In Publication I [1], I searched for new pharmacological agents acting as specific inhibitors of the channel moieties of TRPM6 and TRPM7 using the Spectrum Collection library of drug-like molecules (2000 compounds; Microsource Discovery Systems) and the Selleckchem Compound Library II (4718 compounds; Selleck Chemicals) and Ca^{2+} imaging approach. Next, I used the patch-clamp technique to study further the effects of the candidate compounds that affected the channel activity of TRPM6 and TRPM7. The previously published inhibitor of the TRPM6 and TRPM7 channels, NS8593 (NS) [2], was used as a positive control. I found that two compounds, iloperidone (ILO) and ifenprodil (IFE), suppressed the TRPM6 channel and showed no effects on TRPM7. Besides, I observed that another agent, VER155008 (VER), inhibited the TRPM7 channel and did not affect TRPM6. The results of these experiments are described in Figures 1–6 and Suppl. Figures S2–6 and S10 of Publication I [1].

Figure 1: To examine the effects of NS and ILO on TRPM6, I transiently expressed mouse TRPM6 in HEK293T cells and performed whole-cell patch-clamp experiments. Both compounds efficiently suppressed TRPM6 currents. Additionally, I evaluated the concentration-dependent inhibition of TRPM6 currents by ILO and determined an IC_{50} value of 0.73 μM .

Figure 2: Using the similar patch-clamp settings as in Figure 1, I investigated the impact of IFE on TRPM6 currents. I determined the concentration-dependent suppression of the TRPM6 channel with an IC_{50} value of 3.33 μM .

Figure 3: To analyse the effects of NS and VER on TRPM7, I transiently expressed mouse TRPM7 in HEK293T cells and conducted patch-clamp experiments. VER caused suppression of TRPM7 currents with an IC_{50} value of 0.11 μM .

Figure 4A: To study whether VER can suppress endogenous TRPM7 currents, I examined untransfected HEK293T cells. Untreated HEK293T cells displayed characteristic TRPM7 currents, which were blocked upon exposure of the cells to 10 μM VER.

Figure 5: To further evaluate the effects of ILO and VER on endogenous membrane currents, I examined two cell lines expressing both TRPM6 and TRPM7. First, I studied wild-type (WT) and *Trpm6*^{-/-} mouse embryonic trophoblast stem (TS) cells [3]. I found that 10 μ M VER or 10 μ M ILO inhibited TRPM6/M7-like currents in WT TS cells, indicating that TRPM6/M7 heteromers primarily mediated these currents. Administration of ILO to *Trpm6*^{-/-} cells (i.e., expressing only TRPM7) did not affect the endogenous TRPM7 currents, in line with our conclusion that ILO is a specific inhibitor of TRPM6. This finding also aligns with our concept that TRPM6 functions as a regulatory subunit of TRPM7 [4]. Second, I examined neuroblastoma SHEP-21N cells [5]. 10 μ M ILO caused a substantial reduction of TRPM6/M7-like currents, whereas 10 μ M VER completely abolished such currents. Hence, similar to TS cells, SHEP-21N cells primarily express TRPM6/M7 heteromers and, therefore, respond to the application of inhibitors of each channel, TRPM6 and TRPM7.

Figure 6: To further assess the effects of ILO on cells expressing both, TRPM6 and TRPM7, I analysed HEK293T cells transiently transfected with *Trpm6* and *Trpm7* cDNA ratios of 3:1, 1:1 and 1:3. 10 μ M of ILO blocked currents in cells co-transfected with the 3:1 *Trpm6/Trpm7* ratio and only partially suppressed currents when cells were transfected with the 1:1 *Trpm6/Trpm7* ratio. In line with the data obtained with *Trpm6*^{-/-} TS cells, ILO did not significantly inhibit HEK293T cells co-transfected with the 1:3 *Trpm6/Trpm7* ratio.

Suppl. Figure S2: I used the Ca²⁺ imaging approach to verify the effects of 10 μ M ILO and IFE on TRPM6- and TRPM7-mediated Ca²⁺ influx in HEK293T cells overexpressing TRPM6 or TRPM7. These experiments recapitulated our findings obtained with the patch-clamp technique shown in Figures 1–2 and Suppl. Figure S4.

Suppl. Figure S3: Using the same experimental settings as in Figure S2, I investigated the effect of VER on mouse TRPM6, mouse TRPM7 and human TRPM7. I observed that VER inhibited the human and mouse TRPM7 channels but did not impact the mouse TRPM6 channel, supporting our electrophysiological analysis in Figure 3 and Suppl. Figure S4.

Suppl. Figure S4: I used the patch-clamp technique for testing ILO and IFE in the 5–30 μ M range and found that ILO and IFE did not affect TRPM7 currents. In

addition, I reported that 5–30 μM VER did not inhibit TRPM6 currents. These results supported our conclusions from the findings shown in Figures S2 and S3.

Suppl. Figure S5: To test whether the inhibitory effects of ILO and IFE on the TRPM6 channel and VER on the TRPM7 channel are reversible, I transiently exposed the transfected HEK283T cells to the pharmacological agents when TRPM6 and TRPM7 currents were fully developed. The inhibitory action of 10 μM ILO and 20 μM IFE on TRPM6 currents was fully reversible after the wash-out of the compound. In contrast, the effect of 10 μM of VER on TRPM7 currents was irreversible.

Suppl. Figure S6: Because VER is an adenosine-derived compound [6], I examined whether the kinase domain of TRPM7 is involved in the inhibitory effect of this agent. To this end, I transiently transfected HEK293T cells with *Trpm7* cDNA containing a kinase-dead point mutation (K1646R) [7, 8]. Patch-clamp measurements revealed that 10 μM VER fully inhibited the K1646R-TRPM7 channel.

Suppl. Figure S10: The SHEP-21N cell line was engineered to express N-MYC under negative regulation through a tetracycline-dependent repressor [5, 9]. It was shown that in the absence of tetracycline, SHEP-21N cells upregulated N-MYC levels, leading to increased TRPM6 and unchanged TRPM7 expression levels [5]. I conducted experiments to verify this finding in our laboratory and found that the application of tetracycline to cell culture medium suppressed endogenous TRPM6/M7-like currents in SHEP-21N cells. Consequently, I used SHEP-21N cells to test the effects of VER, ILO and IFE (Figure 5).

Taken together, I concluded that ILO, IFE, and VER enable selective suppression of the TRPM6 and TRPM7 channels, thereby offering new tools for the specific regulation of TRPM6 and TRPM7 currents *in vitro* and in animal disease models.

1.2 Contribution to publication II [10]

Intracellular Mg^{2+} is a well-defined negative regulator of the TRPM7 channel [8, 11]. In Paper II [10], our laboratory aimed to identify the regulatory site mediating the inhibitory action of Mg^{2+} on TRPM7. Using electrophysiological analysis, site-directed mutagenesis and molecular dynamic (MD) simulation, our group demonstrated that intracellular Mg^{2+} interacts with side chains of N1097 located

in the lower gate region of the TRPM7 channel. According to MD simulation, four N1097 residues form a common Mg^{2+} binding site that regulates the channel opening. In line with this concept, the N1097Q mutation in TRPM7 reduced the potency of intracellular Mg^{2+} but did not affect the channel's response to other regulators (naltriben, NS and PIP_2). In addition, our study proposed that the closely located N1098 residues form the net of hydrogen bonds of N1097, stabilizing the channel gate in the closed state. The mutation N1098Q impairs these interactions, resulting in a constitutively active TRPM7 channel that is insensitive to intracellular Mg^{2+} and other ligands of TRPM7. In the presenting study, I performed experiments in Figure 3G and Suppl. Figures S3 and S5.

Figure 3G: I Investigated the effect of 9 mM $[Mg \cdot ATP]_i$ on TRPM7 currents. The WT TRPM7 channel was suppressed, whereas N1097Q and N1098Q TRPM7 channel variants remained active under these experimental conditions.

Suppl. Figure S3: Ba^{2+} is frequently used in electrophysiological experiments to test the regulatory role of divalent cations on ion channels. In the present study, I examined the response of the TRPM7 channel to 0.55 and 1 mM $[Ba^{2+}]_i$. I transiently transfected HEK293T cells with the WT, N1097Q and N1098Q TRPM7 channel variants and performed whole-cell patch-clamp measurements. These experiments demonstrated that the WT TRPM7 channel was suppressed by 0.55 and 1 mM $[Ba^{2+}]_i$, whereas the N1097Q channel variant was sensitive to only 1 mM $[Ba^{2+}]_i$. The N1098Q TRPM7 channel remained unaffected in both experimental conditions. We concluded that N1097Q and N1098Q similarly affected the sensitivity of the TRPM7 channel to Mg^{2+} and Ba^{2+} .

Suppl. Figure S5: To further test the effects of 9 mM $[Mg \cdot ATP]_i$ in the presence of the physiological range of $[Mg^{2+}]_i$ concentrations, I used a second internal solution containing 1 mM free $[Mg^{2+}]_i$. In line with the results in Figure 3G, the WT TRPM7 channel remained inactive in the adjusted experimental settings. In Figure 3G, N1097Q TRPM7 was active in the presence of 550 μM free $[Mg^{2+}]_i$ but was silent after the administration of 1 mM free $[Mg^{2+}]_i$, supporting the idea that N1097Q affected the regulatory effect of Mg^{2+} , but not $Mg \cdot ATP$. N1098Q TRPM7 was unaffected in both conditions, indicating that the N1098Q mutation resulted in a constitutively active TRPM7 channel.

1.3 Contribution to publication III [12]

In Publication III [12], our laboratory demonstrated that in rodent brains, TRPM7 forms multi-protein complexes containing four metal transporter proteins CNNM1–4 and a small G-protein, ADP-ribosylation factor-like protein named 15 (ARL15). We used a combination of multi-epitope affinity purification of TRPM7 complexes, quantitative mass spectrometry and electrophysiological analysis of TRPM7 in heterologous expression in HEK293 and *Xenopus laevis* oocytes. We found that ARL15 potently inhibits TRPM7 currents, whereas CNNM3 elicited no effect on the TRPM7 channel activity. In spite of that, CNNM3 suppressed the kinase activity of TRPM7. In the presenting work, I performed experiments illustrated in Figure 3-Figure Supplement 4. I conducted patch-clamp experiments in untransfected HEK293 cells and in HEK293 cells transfected with mouse *Arl15* expression vector to test the effects of ARL15 on endogenous TRPM7 currents. Transient expression of ARL15 caused a profound suppression of the TRPM7 channel, supporting the concept that ARL15 functions as the regulatory subunit of native TRPM7 channel complexes.

2. Introduction

2.1 Domain topology and tetrameric assembly of TRPM6 and TRPM7 channel-kinase complexes

The transient receptor potential cation channel, subfamily M (melastatin), members 6 and 7 (TRPM6 and TRPM7) are homologous membrane proteins containing cation channel units fused to cytosolic serine/threonine protein kinase domains [13-15]. Both channels belong to the large gene superfamily of transient receptor potential (TRP) ion channels [16]. TRPM6 and TRPM7 show ~50% amino acid sequence identity [17]. Endogenous TRPM7 forms TRPM7 homotetramers and TRPM6/M7 heterotetramers [18, 19]. In TRPM6/M7 heterotetramers, TRPM6 functions as a regulatory subunit. Genetic deletion of TRPM7 leads to the complete silence of TRPM6/M7 channel complexes, whereas disruption of TRPM6 causes alterations in the biophysical characteristics of TRPM7 currents [4].

The N-terminal portion of TRPM6 and TRPM7 contains four conserved domains called melastatin-homology domains (MHD) (Figure 1). The transmembrane segments of TRPM6 and TRPM7 comprise six transmembrane helices (S1–6) and the channel pore-forming region between S5 and S6 [20-22]. S6 is linked to a highly conserved TRP box. C-terminal segments of TRPM6 and TRPM7 contain a coiled-coiled (CC) domain followed by a kinase substrate (SD) domain and an α -type serine/threonine protein kinase (KD) (Figure 1).

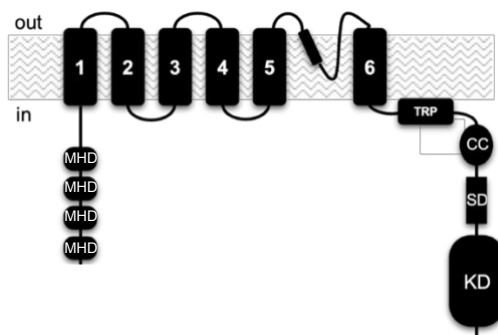


Figure 1. Domain topology of TRPM6 and TRPM7.

The N-terminus of TRPM6 and TRPM7 contains four conserved domains called melastatin-homology domains (MHD), followed by six transmembrane helices (1–6) forming the channel segment of TRPM6 and TRPM7. The pore-forming loop is located between the helices 5 and 6. The C-terminus consists of a transient receptor potential (TRP) domain, a coiled-coil (CC) domain, a kinase substrate domain (SD) and a kinase domain (KD). Figure was taken and modified from [20].

Several TRPM7 kinase substrates have been identified, including annexin I [23], myosin II [24], phospholipase C gamma 2 (PLC γ 2) [25], eEF-2 kinase [26] and TRPM6 [27]. The kinase domain of TRPM7 is known to autophosphorylate its residues, most of which are located in the SD (Figure 1) [14]. Some studies suggested that the TRPM7 kinase domain plays a role in the channel's sensitivity to internal Mg²⁺ and Mg·ATP [28]. Of note, the complete removal of the kinase domain did not inactivate TRPM7 currents, indicating that this domain is not essential for the channel activity of TRPM7 [29].

Cryo-electron microscopy (cryo-EM) structures of TRPM7 have recently been published (Figure 2) [30, 31]. These studies provided atomic-level insights into the three-dimensional folding and tetrameric assembly of the channel in the closed and open states [30, 31]. Besides, cryo-EM analysis uncovered the specific rearrangements in the TRPM7 structure caused by the binding of two TRPM7 inhibitors (NS and VER) and an activator, naltriben [31].

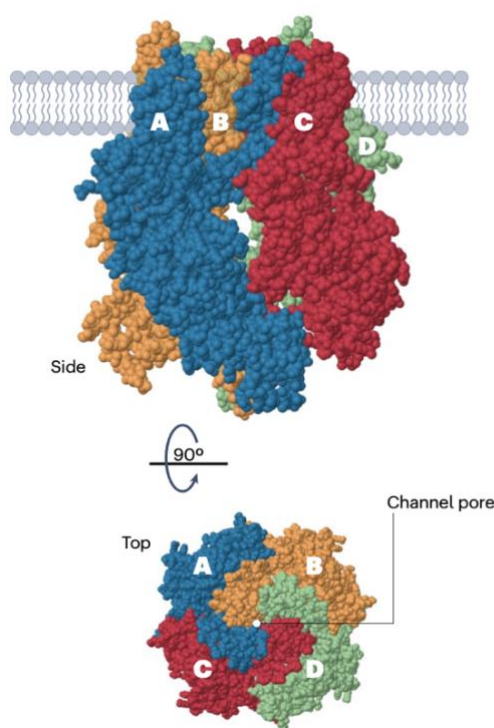


Figure 2. The tetrameric assembly of TRPM6 and TRPM7 based on cryo-EM analysis [31].

The top panel illustrates the TRPM7 tetramer shown from the side view with four differently coloured subunits (A–D). The lower panel shows the tetramer from the top view. Figure was taken and modified from [15].

2.2 Functional characteristics of the TRPM6 and TRPM7 channels

TRPM7 forms a constitutively active channel selective for divalent cations with the following permeability sequence: $\text{Zn}^{2+} \approx \text{Ni}^{2+} \gg \text{Ba}^{2+} > \text{Co}^{2+} > \text{Mg}^{2+} \geq \text{Mn}^{2+} \geq \text{Sr}^{2+} \geq \text{Cd}^{2+} \geq \text{Ca}^{2+}$ [11, 32, 33]. Induction of TRPM7 currents in patch-clamp experiments is commonly achieved by applying patch pipette solutions containing high concentrations of EDTA/EGTA, thereby removing intracellular Mg^{2+} (free Mg^{2+}) and Mg^{2+} bound to nucleotides, i.e. $\text{Mg} \cdot \text{ATP}$ [11, 34]. The current–voltage (I–V) relationship of the TRPM7 channel has a characteristic outward rectification (Figure 3). This outward rectification of TRPM7 currents is caused by a permeation block of the channel by extracellular divalent cations [35]. Accordingly, in divalent cation-free (DVF) conditions, this block is absent, and TRPM7 currents show a semi-linear I–V relationship (Figure 3) [20].

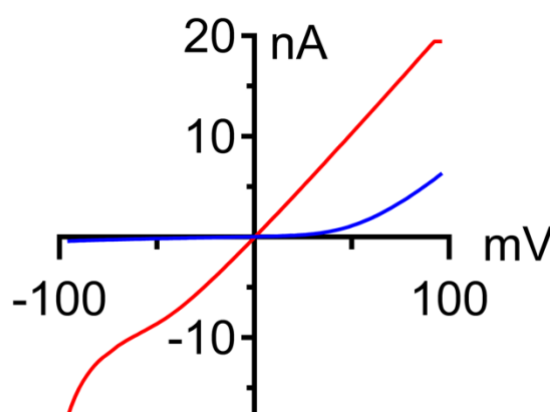


Figure 3. Representative current–voltage (I–V) relationships of TRPM7 overexpressed in HEK293T cells. Whole-cell currents were measured in the presence of standard external saline containing 1 mM Ca^{2+} and 2 mM Mg^{2+} (blue) or after the exposure of the cells to the divalent cations-free (DVF) solution (red).

The functional characteristics of TRPM6 remain less understood and discussed differently. Several laboratories showed that TRPM6 co-assembles with TRPM7 and that without TRPM7, TRPM6 cannot form functional homotetrameric channel complexes on the cell surface [4, 36, 37]. TRPM6/M7 heteromultimers exhibited differing biophysical properties compared to homomultimeric TRPM7 channels [4, 20, 36, 37]. On the contrary, two other groups could detect functional homomultimers of TRPM6 expressed from the bicistronic pCINeo-IRES-GFP

vector [17, 38-40]. In these settings, homomeric TRPM6 showed biophysical characteristics similar to TRPM7 [17, 37, 41].

Intracellular Mg^{2+} was defined as the critical regulator of the TRPM6 and TRPM7 channels [8, 14, 17, 20]. Removal of internal Mg^{2+} leads to slow induction of TRPM6 and TRPM7 currents [35, 42, 43]. The IC_{50} values for TRPM7 inhibition by Mg^{2+} were 0.72 [28], 1.29 [20] and 0.57 mM [40], matching the range of physiological concentrations of free Mg^{2+} in mammalian cells (0.5–1 mM) [44, 45]. Experiments with recombinant TRPM6 resulted in controversial results. Two groups examined human TRPM6 and reported IC_{50} values of 510 and 29 μ M for free Mg^{2+} [17, 40]. Ferioli *et al.* studied mouse TRPM6 and found that TRPM6 is highly sensitive to cytosolic Mg^{2+} and can be entirely suppressed by traces of free Mg^{2+} [20].

Besides free Mg^{2+} , cells contain a larger pool of intracellular Mg^{2+} bound to metabolites, primarily ATP ($Mg\cdot ATP$ complex) [44]. Intracellular concentrations of $Mg\cdot ATP$ were reported in the range of 3 to 9 mM [44, 45]. $Mg\cdot ATP$ represents another negative regulator of the TRPM7 channel. The calculated IC_{50} value for $Mg\cdot ATP$ was determined to be ~2 mM [11, 28]. Free Mg^{2+} and $Mg\cdot ATP$ appear to act on TRPM7 through different sites [10, 11, 28]. The inhibitory effects of $Mg\cdot ATP$ on TRPM6 were discussed differently. One group reported that $Mg\cdot ATP$ did not block the human TRPM6 channel [40], whereas another laboratory found that $Mg\cdot ATP$ inhibits human TRPM6 with the IC_{50} of 1.3 mM [39]. Yet, a third study suggested that recombinant mouse TRPM6 is fully inhibited by unphysiologically low 210 μ M $Mg\cdot ATP$ [20]. Mechanistically, the regulatory roles of free Mg^{2+} and $Mg\cdot ATP$ on TRPM6 and TRPM7 remain poorly understood.

Additionally, TRPM6 and TRPM7 are known to be positively regulated by phosphatidylinositol 4,5-bisphosphate (PIP_2) [15]. It has been reported that GPCR-mediated activation of phospholipase C (PLC) depletes plasma membrane PIP_2 levels, consequently inhibiting TRPM6 and TRPM7 currents [33, 41]. The underlying mechanisms of the PIP_2 effects on TRPM6 and TRPM7 remain to be established.

Recently, our laboratory conducted a proteome-wide interactome analysis of rodent brains and revealed an association of native TRPM7 with metal transporters CNNM1–4 and ADP-ribosylation factor-like protein 15 (ARL15) [46, 47]. Additionally, an interaction between TRPM6 and CNNM proteins was

reported by another group [48]. CNNM1–4 are highly conserved membrane proteins ubiquitously expressed throughout the human body [49–51]. CNNMs appear to mediate the efflux of Mg^{2+} from the cell [49, 50]. However, another study proposed that CNNM proteins regulate the influx of Mg^{2+} into the cell [52]. Bai *et al.* suggested that CNNM1–4 can indirectly control both the efflux and influx of Mg^{2+} , likely due to the regulation of the TRPM7 channel [48]. In contrast to this view, our group suggested that CNNM3 acts as a negative regulator of the TRPM7 kinase activity [12].

ARL15 is a small G-protein and part of the large ARF gene family. ARF proteins are involved in phospholipid metabolism, membrane trafficking, and cytoskeleton remodelling [53]. Single-nucleotide polymorphism (SNP) association analysis suggested that ARL15 may be linked to Mg^{2+} homeostasis and energy metabolism in humans [54]. In our study, the co-expression of TRPM7 and ARL15 caused inhibition of the TRPM7 channel in various experimental conditions [12]. Recently, this finding was replicated by other laboratories [48, 55]. Further studies are necessary to elucidate the physiological relevance of TRPM7/ARL15/CNNM1–4 interactions.

2.3 Pathophysiological roles of TRPM6 and TRPM7

TRPM6 is predominantly expressed in epithelial cells of the intestine and kidneys [17, 56, 57] but was also found in other tissues such as the placenta, lung and testis [58]. TRPM6 plays a crucial role in the systemic homeostasis of Mg^{2+} . Loss-of-function mutations in the human *TRPM6* gene were identified in patients with an autosomal recessive disease known as Hypomagnesemia with secondary hypocalcaemia (HSH) [56, 58]. The characteristic symptom of HSH is low serum Mg^{2+} levels, leading to hypocalcaemia and other secondary symptoms, including seizures and tetany. Intravenous or dietary Mg^{2+} administration can restore blood Mg^{2+} levels and relieve all symptoms of the affected individuals [59]. Untreated hypomagnesemia can lead to neurological damage and can even be lethal [4, 56].

Recently, *Trpm6*^{−/−} mice were studied to elucidate pathomechanisms of HSH. Unexpectedly, two groups found that mice homozygous for null mutations in *Trpm6* lead to embryonic death [60, 61]. Our laboratory investigated a mouse strain with a conditional floxed mutation in *Trpm6* [3]. This genetic model allowed

us to overcome the prenatal mortality of animals with a constitutive null mutation in *Trpm6* [60]. Adult mice lacking TRPM6 in the whole body developed severe hypomagnesemia due to insufficient intestinal Mg^{2+} uptake [3]. This defect was associated with growth failure and 100% postnatal mortality of the mutant mice [3]. Similar to HSH patients, dietary Mg^{2+} supplementation fully rescued the phenotypes of *Trpm6* gene-deficient animals [3]. Thus, studies with mouse genetic models revealed the primary role of intestinal Mg^{2+} uptake through TRPM6 for systemic Mg^{2+} homeostasis [3].

TRPM7 transcripts were detected in all tissues and cell lines, indicating that it is a ubiquitously expressed gene. In line with this notion, native TRPM7 currents were detected in an extensive collection of primary cells and stable cell lines [2, 62-66]. Experiments with cultured cells demonstrated that TRPM7 regulates many cellular processes, including Mg^{2+} homeostasis [8, 67], Ca^{2+} signalling [68, 69], exocytosis [70], cell motility [24, 71], proliferation [11, 68, 72-74] and differentiation [75-77]. TRPM7 is involved in anoxic neuronal death [62, 78, 79] and may play a role in multiple sclerosis, Alzheimer's disease and stroke [80]. TRPM7 was associated with various cardiovascular diseases, including hypertension [63, 81-83] and tissue fibrosis [84-86]. Experiments with cancer cells revealed that TRPM7 regulates cell proliferation, differentiation, and migration [87-90].

Clinical studies have linked TRPM7 to several human diseases [15]. Stritt and colleagues identified two patients who were heterozygous for point mutations in *TRPM7* and exhibited macrothrombocytopenia associated with reduced Mg^{2+} platelet contents and abnormal thrombopoiesis [91]. Another study found one patient with trigeminal neuralgia who was heterozygous for a point mutation in *TRPM7* [92]. They hypothesised that the aberrant TRPM7 channel mediates atypical Na^+ currents, which trigger pain by depolarizing the trigeminal neurons [92].

Mouse genetic models were used to study the *in vivo* role of TRPM7. Generated *Trpm7*^{-/-} mice displayed early embryonic mortality [67, 75]. Experiments with conditional tissue-restricted mutagenesis of *Trpm7* uncovered that an epiblast-restricted knockout of *Trpm7* leads to embryonic death, indicating that *Trpm7* is required for the embryo proper [75]. Our group explored a mouse strain with intestine-specific deletion of *Trpm7* to show that TRPM7 controls intestinal uptake

of Zn^{2+} , Mg^{2+} and Ca^{2+} and that this mechanism is vital for the postnatal development of mice [93]. Consequently, Mg^{2+} , Ca^{2+} and Zn^{2+} supplementation of mothers during pregnancy and breastfeeding ameliorated the survival rate of the *Trpm7*-gene deficient pups [93].

2.4 Pharmacological modulators of TRPM6 and TRPM7

Several pharmacological compounds have been identified to modulate TRPM6 and TRPM7 channels (Table 1). The first potent TRPM7 inhibitors to be identified were waixenicin A and NS8593 (NS). Waixenicin A suppressed TRPM7 irreversibly with an IC_{50} of 7 μM and showed no effect on TRPM6 [94]. Our laboratory identified several pharmacological agents suppressing the TRPM7 channel [2, 95]. Among other compounds, NS was the most potent regulator of TRPM7, displaying an IC_{50} of 1.6 μM [2]. NS also suppressed TRPM6 currents [3, 96].

Sphingosine and its synthetic homologue FTY720 were found to be inhibitors of the TRPM6 and TRPM7 channels [97]. Sphingosine displayed an IC_{50} of 0.5 and 0.6 μM on TRPM6 and TRPM7, respectively, and FTY720 inhibits TRPM7 with an IC_{50} of 0.7 μM [97]. Recently, Guan and colleagues found that CCT128930 inhibits the TRPM7 channel with an IC_{50} of 0.9 μM [98]. CCT128930 showed no effects on the TRPM6 channel [98]. The TRPM7 inhibitors were found to be instrumental in the assessment of the cellular roles of endogenous TRPM7 in healthy and disease conditions [15].

In the present study, several new modulators of TRPM6 and TRPM7 were identified [1]. VER suppressed TRPM7 irreversibly with an IC_{50} of 0.1 μM and did not affect TRPM6 [1]. Additionally, I found that ILO and IFE inhibited TRPM6 with an IC_{50} of 0.7 and 3.3 μM , respectively [1]. In contrast, ILO and IFE did not cause changes in TRPM7 currents [1].

Furthermore, several activators of the TRPM7 channel were identified (Table 1). Naltriben represents the most potent activator of TRPM7 with an EC_{50} value of 21 μM [99]. This compound activates TRPM7 currents in the presence of intracellular Mg^{2+} and after depletion of PIP_2 . Naltriben does not affect TRPM6 currents [20, 99].

Table 1. Pharmacological modulators of TRPM6 and TRPM7.

Compound	Effect on TRPM6	Effect on TRPM7
Waixenicin A [94]	No effect	Inhibitor, IC ₅₀ 7 μ M
Sphingosine [97]	Inhibitor, IC ₅₀ 0.5 μ M	Inhibitor, IC ₅₀ 0.6 μ M
FTY720 [97]	Inhibitor, IC ₅₀ n.d.	Inhibitor, IC ₅₀ 0.7 μ M
NS8593 [2]	Inhibitor, IC ₅₀ n.d.	Inhibitor, IC ₅₀ 1.6 μ M
CCT128930 [98]	No effect	Inhibitor, IC ₅₀ 0.9 μ M
VER155008 [1]	No effect	Inhibitor, IC ₅₀ 0.1 μ M
lloperidone [1]	Inhibitor, IC ₅₀ 0.7 μ M	No effect
Ifenprodil [1]	Inhibitor, IC ₅₀ 3.3 μ M	No effect
Naltriben [99]	No effect	Activator, EC ₅₀ 21 μ M
Mibefradil [100]	No effect	Activator, EC ₅₀ 53 μ M

Note: n.d. = not detected

In the recent cryo-EM analysis of TRPM7, our laboratory identified the channel's NS- and VER-binding pockets [31]. This site is formed by the N-terminal part of S3, the C-terminal part of S4, the S4–S5 linker and the TRP helix [31]. In addition, our group found a naltriben binding site in TRPM7 located in the MHR4/Pre-S1 region of TRPM7 [31].

There is only one known inhibitor of the TRPM6 and TRPM7 kinases, TG100-115. Song *et al.* reported that this compound suppresses TRPM7 kinase activity with an IC₅₀ of 2 μ M [101]. Our group found that TG100-115 also blocks the TRPM6 kinase [20].

Taken together, several pharmacological modulators of TRPM6 and TRPM7 have been identified. These molecules were applied to study the pathophysiological roles of TRPM6 and TRPM7. In addition, pharmacological modulators of TRPM7 were found useful to investigate structural mechanisms of activation and inhibition of the TRPM7 channel.

3. Research goals

The kinase-coupled TRPM6 and TRPM7 form homo- and heteromeric channel complexes, which play an essential role in the membrane transport of Ca^{2+} , Mg^{2+} and Zn^{2+} . TRPM6 and TRPM7 were proposed as new drug targets for treating cardiovascular, neurological, and immune disorders. In the present study, we aimed to identify small molecules allowing the selective regulation of the TRPM6 and TRPM7 channels. Specifically, we intended to address the following research goals:

1. To identify new pharmacological agents acting as specific inhibitors of the TRPM6 channel (Publication I).
2. To find new compounds selectively inhibiting the TRPM7 channel (Publication I).
3. To apply the identified pharmacological agents in aims 1 and 2 for comparative analysis of TRPM6 and TRPM7 in human and mouse cells expressing both proteins (Publication I).
4. To apply the approaches developed in aims 1–3 to assess the role of intracellular Mg^{2+} and the small G-protein ARL15 in the modulation of the TRPM7 channel (Publication II–III).

4. Summary (in English)

The transient receptor potential cation channel, subfamily M, members 6 and 7 (TRPM6 and TRPM7) are homologous membrane proteins comprising cation channel domains fused to protein kinase domains. Experiments with animal disease models and clinical investigations revealed that pharmacological inhibition of TRPM6 and TRPM7 can be applied to treat immune, cardiovascular, neurological and other disorders. Nonetheless, the suitable pharmacological tools remain underdeveloped. The present study uncovers new compounds that specifically target the channel moieties of TRPM6 and TRPM7. Using the patch-clamp technique in combination with Ca^{2+} imaging, we demonstrated that two pharmacological agents, iloperidone and ifenprodil, inhibited the channel activity of TRPM6 with IC_{50} values of 0.73 and 3.33 μM , respectively. Remarkably, iloperidone and ifenprodil showed no impact on the TRPM7 channel. In addition, we found that another compound, VER155008, suppressed the TRPM7 channel with an IC_{50} value of 0.11 μM . VER155008 did not block TRPM6. In many regards, the inhibitory action of VER155008 resembled the effects of intracellular Mg^{2+} , $\text{Mg}\cdot\text{ATP}$ and small G-protein ARL15, the known endogenous negative regulators of TRPM7. Finally, iloperidone and VER155008 were suitable for inactivating endogenous TRPM6 and TRPM7 currents in several cell lines, including HEK293T, A549 and mouse trophoblast stem cells. Altogether, our study identified a collection of pharmacological agents allowing the selective regulation of TRPM6 and TRPM7. The identified compounds represent new tools to investigate the function of TRPM6 and TRPM7 in native cellular environments and to study the role of these proteins in preclinical models of human diseases.

5. Zusammenfassung (deutsch)

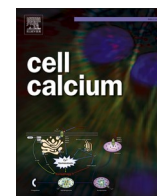
Die *transient receptor potential cation channel*, Unterfamilie M (Melastatin), Mitglieder 6 und 7 (TRPM6 und TRPM7) sind homologe Membranproteine, die aus einer mit einer Proteinkinase-Domäne gekoppelten Kationenkanal-Domäne bestehen. Klinische Studien und Experimente mit Tiermodellen legen nahe, dass die pharmakologische Hemmung von TRPM6 und TRPM7 zur Behandlung von Immun-, Herz-Kreislauf- und neurologischen Erkrankungen sowie anderen Pathologien eingesetzt werden kann. Das geeignete pharmakologische Instrumentarium ist jedoch weiterhin unterentwickelt. In der vorliegenden Studie wurden neue Substanzen identifiziert, die spezifisch auf die Kanäle TRPM6 und TRPM7 wirken. Mit Hilfe der Patch-Clamp-Technik in Kombination mit Ca^{2+} -Imaging konnten wir zeigen, dass zwei pharmakologische Wirkstoffe, Iloperidon und Ifenprodil, die Kanalaktivität von TRPM6 mit IC_{50} -Werten von 0,73 bzw. 3,33 μM unterdrücken können. Bemerkenswerterweise zeigten Iloperidon und Ifenprodil keine Auswirkungen auf den TRPM7-Kanal. Darüber hinaus fanden wir heraus, dass eine andere Substanz, VER155008, den TRPM7-Kanal mit einem IC_{50} -Wert von 0,11 μM hemmte. Im Gegensatz dazu blockierte VER155008 TRPM6 nicht. In vielerlei Hinsicht ähnelte die hemmende Wirkung von VER155008 den regulatorischen Effekten von intrazellulärem Mg^{2+} , $\text{Mg}\cdot\text{ATP}$ und dem kleinen G-Protein ARL15, den bekannten endogenen Regulatoren von TRPM7. Schließlich konnten wir zeigen, dass Iloperidon und VER155008 geeignet sind, endogene TRPM6- und TRPM7-Ströme in mehreren Zelllinien zu inaktivieren, darunter HEK293T, A549 und Maus-Trophoblast-Stammzellen. Zusammenfassend wurden in unserer Studie eine Reihe von pharmakologischen Wirkstoffen identifiziert, die eine selektive Regulierung von TRPM6 und TRPM7 ermöglichen. Die identifizierten Wirkstoffe stellen neue Instrumente dar, um die Funktion von TRPM6 und TRPM7 in nativen Zellen zu untersuchen und die Rolle dieser Proteine in präklinischen Modellen menschlicher Krankheiten zu erforschen.

6. Publication I

Title: Pharmacological agents selectively acting on the channel moieties of TRPM6 and TRPM7

<https://www.sciencedirect.com/science/article/pii/S0143416022001130>

<https://doi.org/10.1016/j.ceca.2022.102640>



Pharmacological agents selectively acting on the channel moieties of TRPM6 and TRPM7

Anna Rössig^a, Kerstin Hill^b, Wolfgang Nörenberg^b, Sebastian Weidenbach^a, Susanna Zierler^{a,c}, Michael Schaefer^b, Thomas Gudermann^{a,d,*}, Vladimir Chubnov^{a,*}

^a Walther-Straub Institute of Pharmacology and Toxicology, LMU Munich, Munich, Germany

^b Rudolf-Boehm Institute of Pharmacology and Toxicology, Leipzig University, Leipzig, Germany

^c Institute of Pharmacology, Johannes Kepler University Linz, Linz, Austria

^d Comprehensive Pneumology Center, a member of the German Center for Lung Research (DZL), Munich, Germany

ARTICLE INFO

Keywords:

TRP channels
TRPM6
TRPM7
NS8593
iloperidone
ifenprodil
VER155008

ABSTRACT

The transient receptor potential cation channel, subfamily M, members 6 and 7 (TRPM6 and TRPM7) are homologous membrane proteins encompassing cation channel units fused to cytosolic serine/threonine-protein kinase domains. Clinical studies and experiments with animal disease models suggested that selective inhibition of TRPM6 and TRPM7 currents might be beneficial for subjects with immune and cardiovascular disorders, tumours and other pathologies, but the suitable pharmacological toolkit remains underdeveloped. The present study identified small synthetic molecules acting specifically on the channel moieties of TRPM6 and TRPM7. Using electrophysiological analysis in conjunction with Ca^{2+} imaging, we show that iloperidone and ifenprodil inhibit the channel activity of recombinant TRPM6 with IC_{50} values of 0.73 and 3.33 μM , respectively, without an impact on the TRPM7 channel. We also found that VER155008 suppresses the TRPM7 channel with an IC_{50} value of 0.11 μM but does not affect TRPM6. Finally, the effects of iloperidone and VER155008 were found to be suitable for blocking native endogenous TRPM6 and TRPM7 in a collection of mouse and human cell models. Hence, the identification of iloperidone, ifenprodil, and VER155008 allows for the first time to selectively manipulate TRPM6 and TRPM7 currents.

1. Introduction

The channel-kinase TRPM6 and its close homolog TRPM7 have been invoked as molecular correlates of ubiquitous membrane cation currents controlling the cellular uptake of divalent cations, including Ca^{2+} , Mg^{2+} and Zn^{2+} [1–7]. These currents were initially discovered in patch-clamp experiments after removing cytosolic Mg^{2+} and $\text{Mg}\cdot\text{ATP}$ and were thought to be conducted by the calcium release-activated Ca^{2+} (CRAC) channel [8]. However, follow-up electrophysiological studies and functional profiling using poly-specific channel modulators, such as spermine, ruthenium red and 2-APB, ruled out the role of the CRAC channel [9–11], whereas recombinant expression technology allowed to establish that TRPM7 is the molecular correlate of such Mg^{2+} - and $\text{Mg}\cdot\text{ATP}$ -inhibited cation currents [7,12–16]. At present, the prevailing view is that TRPM7 forms ubiquitously expressed channel complexes responsible for the cellular uptake of divalent cations and that cytosolic Mg^{2+} and $\text{Mg}\cdot\text{ATP}$ control the TRPM7 channel to synchronise the

uptake of essential divalent cations and the cell's metabolic state [6,7,12,17–21]. Extensive analyses of animal genetic models and clinical studies revealed that impaired function of TRPM7 prevents normal prenatal development and healthy adulthood [4,22–29].

In contrast to the ubiquitously expressed TRPM7, TRPM6 is primarily present in transporting epithelial cells of the placenta, intestine and kidneys and likely in cardiomyocytes and tumour-derived cells [1,3,30–32]. Conditional tissue-specific inactivation of the *Trpm6* gene in mice showed that TRPM6 is vital for the placental Mg^{2+} supply of the embryo [5]. In adult mice, the deletion of *Trpm6* results in systemic Mg^{2+} deficiency due to impaired intestinal uptake of Mg^{2+} [5], recapitulating the etiology of hypomagnesemia in humans with loss-of-function mutations in the *TRPM6* gene [1,33–35]. Collectively, these studies demonstrated that TRPM6 is functionally nonredundant, but the exact role of TRPM6 remains incompletely understood. Electrophysiological analysis of trophoblast stem (TS) cells derived from wild-type (WT), *Trpm6*^{−/−} and *Trpm7*^{−/−} mouse blastocysts [5] and the

* Corresponding authors.

E-mail addresses: thomas.gudermann@lrz.uni-muenchen.de (T. Gudermann), vladimir.chubnov@lrz.uni-muenchen.de (V. Chubnov).

<https://doi.org/10.1016/j.ceca.2022.102640>

Received 19 April 2022; Received in revised form 10 August 2022; Accepted 14 August 2022

Available online 17 August 2022

0143-4160/© 2022 The Author(s). Published by Elsevier Ltd. This is an open access article under the CC BY-NC-ND license (<http://creativecommons.org/licenses/by-nc-nd/4.0/>).

human neuroblastoma cell line SHEP-21N subjected to silencing of either *TRPM6* or *TRPM7* transcripts [32] supported the concept that native TRPM6 primarily functions as a subunit of heteromeric TRPM6/7 channels, which are less susceptible to Mg^{2+} ATP inhibition than TRPM7 homomers [19,33]. Thus, the assembly of TRPM6 and TRPM7 uncouples Mg^{2+} influx from the metabolic demand of the cell and, consequently, maintains the constitutive transcellular transport of Mg^{2+} [5,19,33,36]. However, the question as to whether such functional interplay of TRPM6 with TRPM7 epitomises a general physiological mechanism remains unanswered.

Several drug-like molecules were identified as inhibitors of the TRPM7 channel [37–39]. Among others, waixenicin A, FTY720 and NS8593 represent the most extensively characterised modulators of TRPM7 acting at low μM concentrations [40–42]. More recently, activators of the TRPM7 channel, such as naltriben, were identified [43,44]. Consequently, waixenicin A, FTY720, NS8593 and naltriben were broadly used to assess TRPM7 currents in the growing number of isolated primary cells and stable cell lines [37–39]. Moreover, these compounds were instrumental in exploring the therapeutic potential of TRPM7 for the treatment of human diseases, such as tumour progression, immune and cardiovascular disorders [37–39]. Despite the physiological and clinical importance of TRPM6, pharmacological compounds selectively acting on the channel and kinase domains of TRPM6 are not yet available.

In the present paper, we report new small synthetic molecules acting in the nM to low μM range as selective inhibitors of the channel units of TRPM6 and TRPM7. The identified compounds represent new tools to decipher the role of TRPM6 and TRPM7 in native cellular environments and to test the impact of these bifunctional proteins in preclinical models of human diseases.

2. Methods

2.1. Pharmacological agents, plasmid DNAs

NS8593 was acquired from Tocris. VER155008, ifenprodil tartrate and iloperidone were purchased from Sigma–Aldrich. Mouse *Trpm7* and mouse *Trpm6* in the *pIRES2-EGFP* expression vector were reported previously [19,33]. Human *TRPM7* in pcDNA4/TO was described earlier [12].

2.2. Cell culture

HEK293T cells were kept at 37°C and 5% CO₂ in Eagle's minimal essential medium supplemented with 10% fetal calf serum, 100 $\mu g/ml$ streptomycin and 100 U/ml penicillin (all from Thermo Fisher Scientific). Cells were transiently transfected using Lipofectamine 2000 reagent (Thermo Fisher Scientific) according to the manufacturer's instructions. A549 cells were kept at 37°C and 5% CO₂ in Ham's F-12K medium supplemented with 10% fetal calf serum, 100 $\mu g/ml$ streptomycin and 100 U/ml penicillin (Thermo Fisher Scientific). The wild-type and *Trpm6*^{-/-} trophoblast stem (TS) cells were described previously [5]. TS cells were kept at 37°C and 5% CO₂ in RPMI 1640 medium (Thermo Fisher Scientific) supplemented with 20% fetal bovine serum (ES type, Thermo Fisher Scientific), 1 mM sodium pyruvate (Cell culture type, Sigma–Aldrich), 100 μM β -mercaptoethanol (Sigma–Aldrich), 50 $\mu g/ml$ streptomycin and 50 U/ml penicillin (Thermo Fisher Scientific), 1.0 $\mu g/ml$ heparin (Cell culture type, Sigma–Aldrich), 25 ng/ml human recombinant FGF4 (R&D systems), 5 ng/ml human recombinant TGF- β 1 (R&D systems), and 10 ng/ml recombinant activin A (R&D Systems). For the culture of *Trpm6*^{-/-} TS cells, 10 mM MgCl₂ was added to the medium. Human neuroblastoma SHEP-21N cells were cultured as reported in [32,45]. N-Myc expression in SHEP-21N cells was suppressed by the addition of 100 ng/ml tetracycline (Thermo Fisher Scientific) to the cell culture medium.

2.3. Aequorin-based measurements of intracellular Ca²⁺ levels ([Ca²⁺]_i)

Measurements of [Ca²⁺]_i were performed as reported previously with several modifications [40,44,46]. HEK293T cells cultured in 6-well plates were transfected with 2 $\mu g/dish$ *Trpm6* or *Trpm7* plasmid DNA and 0.1 $\mu g/dish$ *pGSA* plasmid DNA encoding EGFP fused to *Aequorea victoria* aequorin. 24 h after transfection, the cells were washed with PBS and mechanically resuspended in PBS. Cell suspensions were centrifuged twice at 600 rpm for 3 min and resuspended in Mg^{2+} -free HEPES-buffered saline (Mg^{2+} -free HBS: 140 mM NaCl, 6 mM KCl, 0.5 mM CaCl₂, 10 mM HEPES, 5 mM glucose and 0.1% BSA, pH 7.4). For reconstitution of aequorin, cell suspensions were incubated with 5 μM coelenterazine (Biaffin GmbH) in Mg^{2+} -free HBS for 30 min at room temperature. Cells were washed twice by centrifugation at 600 rpm for 3 min, resuspended in Mg^{2+} -free HBS and placed in 96-well plates (1 \times 10⁵ cells per well). Luminescence was detected using a FLUOstar OPTIMA microplate reader at 37°C (BMG LABTECH GmbH). To monitor Ca²⁺ influx, extracellular Ca²⁺ was increased by injecting Mg^{2+} -free HBS containing 10 mM CaCl₂ (final concentration). Experiments were terminated by lysing cells with 0.1% (v/v) Triton X-100 in Mg^{2+} -free HBS to record total bioluminescence. Bioluminescence rates (counts/sec) were analysed at 1-s intervals and calibrated as [Ca²⁺]_i values using the following equation:

$$p[Ca^{2+}]_i = 0.332588 (-\log(k)) + 5.5593$$

k represents the rate of aequorin consumption, i.e., counts/s divided by the total number of counts.

2.4. Electrophysiological techniques

Patch-clamp experiments were performed as reported previously with a few modifications [5,19]. HEK293T cells grown in 35-mm dishes to ~70% confluence were transiently transfected with *Trpm6* and *Trpm7* cDNAs in the *pIRES2-EGFP* vector (2 $\mu g/dish$). Patch-clamp experiments were conducted 20–24 h after transfection with cells displaying EGFP fluorescence. Whole-cell currents were measured using an EPC10 patch-clamp amplifier and PatchMaster software (Harvard Bioscience). Voltages were corrected for a liquid junction potential of 10 mV. Currents were elicited by a ramp protocol from -100 mV to +100 mV over 50 ms acquired at 0.5 Hz and a holding potential of 0 mV. Inward and outward current amplitudes were extracted at -80 mV and +80 mV and were normalised to the cell size as pA/pF. Capacitance was measured using the automated capacitance cancellation function of EPC10. Unless stated otherwise, a standard extracellular solution contained (in mM): 140 NaCl, 2.8 KCl, 1 CaCl₂, 2 MgCl₂, 10 HEPES-NaOH, and 11 glucose (all from Sigma–Aldrich). Solutions were adjusted to pH 7.2 using an FE20 pH meter (Mettler Toledo) and 290 mOsm using a Vapro 5520 osmometer (Wescor Inc). Endogenous currents in HEK293T, A549 and TS cells were measured using the standard extracellular solution containing 3 mM CaCl₂ and no MgCl₂. Patch pipettes were made of borosilicate glass (Science Products) and had a resistance of 2–3.7 M Ω when filled with the standard Mg^{2+} -free intracellular ([Mg²⁺]_i) pipette solution containing (in mM) 120 Cs-glutamate, 8 NaCl, 10 Cs-EGTA, 5 Cs-EDTA, and 10 HEPES-CsOH. The intracellular solution was also adjusted to pH 7.2 and 290 mOsm.

To determine the IC₅₀ values for the inhibitory effects of the compounds examined, the data were fitted with the following equation:

$$E(c) = E_{\min} + (E_{\max} - E_{\min}) \times \left(1 / \left(1 + (IC_{50}/c)^h \right) \right)$$

where E is the effect/current at a given concentration c of inhibitor, E_{min} is the minimal effect/current, E_{max} is the maximally achievable effect, IC₅₀ is the half-maximal concentration and h is the Hill factor. Fitting of dose–response curves was performed using GraphPad Prism 6.0.

2.5. Statistical analysis

Data are presented as the means \pm standard errors of the means (SEM). Data showed a normal distribution. Unless indicated otherwise, data were compared by a two-tailed t test. For multiple comparisons, ANOVA (GraphPad Prism 6.0 software) was used. Significance was accepted at $P \leq 0.05$.

3. Results

3.1. Identification of new modulators of TRPM6 and TRPM7 channels

We systematically evaluated libraries of drug-like small molecules, including the Spectrum Collection (2000 compounds; Microsource Discovery Systems) and the Selleckchem Compound library II (4718 compounds; Selleck Chemicals), and found that only three compounds, iloperidone, ifenprodil and VER155008, affected the channel activity of TRPM6 and TRPM7 differentially (Suppl. Fig. S1). In these experiments, we took advantage of our previously developed microfluorometric $[Ca^{2+}]_i$ measurements [47] and highly sensitive aequorin-based $[Ca^{2+}]_i$

assay, which allows monitoring of Ca^{2+} influx in HEK293T cells transiently transfected with mouse *Trpm6* and *Trpm7* cDNAs in the *pIR-ES2-EGFP* expression vector (detailed reasoning for the use of these expression plasmids was reported previously [19]). As shown in Suppl. Fig. S2, a one-step elevation of the external Ca^{2+} level from 0.5 to 10 mM elicited fast and sustained increases in intracellular Ca^{2+} in HEK293T cells expressing either TRPM6 (Suppl. Fig. S2A) or TRPM7 (Suppl. Fig. S2B). Previously, we demonstrated that NS8593 is a potent inhibitor of TRPM6 and TRPM7 channels [40]. In line with this notion, Ca^{2+} levels were only modestly increased in the presence of 10 μ M NS8593, likely due to background Ca^{2+} influx through other channels (Suppl. Fig. S2A, B). Additionally, we found that 10 μ M iloperidone and ifenprodil elicited inhibitory effects on TRPM6 (Suppl. Fig. S2A, C). In contrast, a similar assessment of HEK293T cells transfected with *Trpm7* revealed that 10 μ M iloperidone and ifenprodil had no significant effects on TRPM7-mediated Ca^{2+} influx (Suppl. Fig. S2B, D). In addition, we observed that 10 μ M VER155008 suppressed the channel activity of mouse and human TRPM7 (Suppl. Fig. S3A, B) but did not display a detectable impact on mouse TRPM6 (Suppl. Fig. S3C). Thus, iloperidone, ifenprodil and VER155008 represent a group of structurally

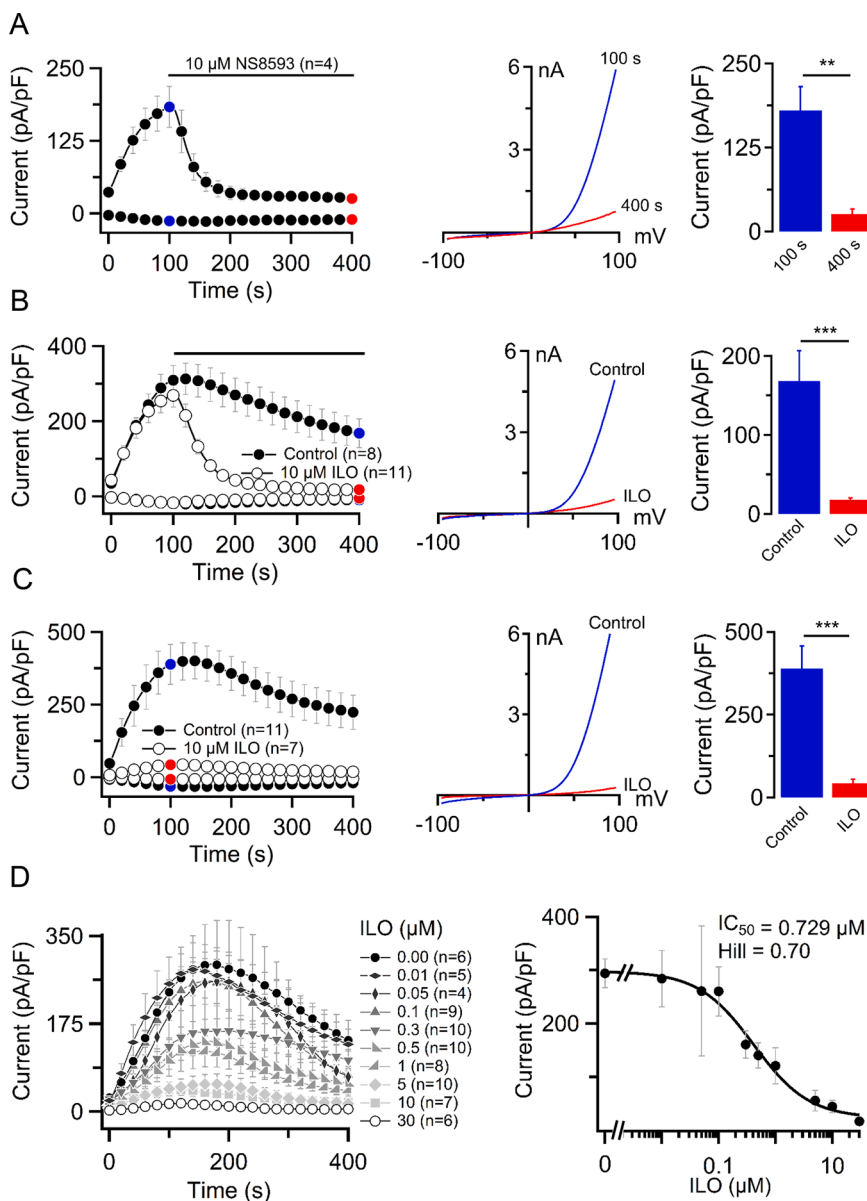


Fig. 1. Inhibition of TRPM6 currents by NS8593 and iloperidone.

Whole-cell currents were measured in *Trpm6*-transfected HEK293T cells exposed to NS8593 (A) and iloperidone (B-D). (A) *Left panel:* Current amplitudes (mean \pm SEM) were measured at -80 and +80 mV and plotted over time. When currents were developed, cells were exposed to 10 μ M NS8593 as indicated by the horizontal bar. *Middle panel:* Representative current-voltage relationships obtained from individual ramps before (blue) and after (red) application of NS8593 as indicated in the *Left panel*. *Right panel:* Bar graphs of outward currents (+80 mV, mean \pm SEM) obtained from untreated (blue) and NS8593-treated cells (red) as indicated in the *Left panel*. (B) Experiments were performed and analysed similarly to (A). The cells were exposed to an external solution without (Control) or with 10 μ M iloperidone (ILO), as indicated by the horizontal bar in the *Left panel*. (C) Experiments were performed similarly to (A), except that the cells were exposed to an external solution without (Control) or with 10 μ M iloperidone (ILO) before the recording of whole-cell currents. (D) Concentration-dependent inhibition of TRPM6 currents by iloperidone. Experiments were performed as outlined in (C) with the cells exposed to the indicated concentrations of iloperidone (ILO). *Left panel:* Current amplitudes (mean \pm SEM) acquired at +80 mV and plotted over time. *Right panel:* Dose-dependent suppression of outward currents (+80 mV, maximal currents) shown in the *Left panel*. n, number of cells measured; ** $P < 0.01$, *** $P < 0.001$ (two-tailed t test).

unrelated modulators of the channel-kinases with different selectivity towards TRPM6 versus TRPM7.

3.2. Impacts of iloperidone, ifenprodil and VER155008 on TRPM6 and TRPM7 currents

To investigate whether iloperidone and ifenprodil suppress TRPM6 and TRPM7 currents, we employed the patch-clamp technique. Fig. 1A illustrates whole-cell currents measured in HEK293T cells transfected with *Trpm6*. Removal of intracellular Mg^{2+} induced large currents with a characteristic shape of the current-voltage (I-V) relationship: steep outward rectification, a reversal potential of approximately 0 mV and very tiny inward currents (Fig. 1A). After the channel had activated to saturation, we perfused cells with either 10 μM NS8593 (Fig. 1A) or 10 μM iloperidone (Fig. 1B). In accordance with the Ca^{2+} imaging experiments (Suppl. Fig. S2A), we found that both compounds efficiently inhibited TRPM6 currents with similar kinetics (Fig. 1A, B). In line with our previous study [19], we observed that TRPM6 currents peaked at ~ 100 s of recordings, followed by a gradual decline presumably due to an intrinsic inactivation mechanism (Fig. 1B). We noted that such a run-down of TRPM6 currents overlapped with the inhibitory effect of iloperidone, interfering with accurate quantification of the iloperidone action (Fig. 1B). Therefore, we studied whether exposure of *Trpm6*-transfected HEK293T cells to iloperidone would prevent the development of TRPM6 currents and found that this was indeed the case (Fig. 1C). Consequently, we used this approach to determine the concentration dependence of the effect of iloperidone on TRPM6 (Fig. 1D). The fitting of the obtained data with the Hill equation resulted in an IC_{50} value of 0.73 μM (Fig. 1D). Additionally, we noted that exposure of

Trpm7-transfected cells to iloperidone in the relevant range of concentrations (5–30 μM) only caused a delay in TRPM7 current development, whereas the current amplitudes of fully induced TRPM7 currents were not significantly affected (Suppl. Fig. S4A).

Next, we used the same patch-clamp settings to analyse the effects of ifenprodil on TRPM6 currents (Fig. 2A). We observed that the external application of 10 μM ifenprodil resulted in the inactivation of TRPM6 currents (Fig. 2A), but this effect developed slower than that of NS8593 or iloperidone (Fig. 1A, B). Nevertheless, preexposure of *Trpm6*-transfected HEK293T cells to 10 μM ifenprodil strongly interfered with the induction of TRPM6 currents (Fig. 2B). Next, we determined the concentration-dependent inhibition of TRPM6 currents (Fig. 2C). The calculated IC_{50} value of ifenprodil was 3.33 μM (Fig. 2C). In contrast, the application of 10–30 μM ifenprodil did not suppress TRPM7 currents (Suppl. Fig. S4B).

We studied whether the inhibitory effects of iloperidone and ifenprodil on TRPM6 currents could be reversed after wash-out of the compounds (Suppl. Fig. S5A, B). After currents had activated to saturation, we transiently perfused cells with either 10 μM iloperidone or 20 μM ifenprodil. We found that the inhibitory effects of both compounds were fully reversible. We also noted that the I-V relationships of TRPM6 currents in the presence of iloperidone and ifenprodil were indistinguishable from I-V characteristics in untreated cells (Suppl. Fig. S5A, B), suggesting that under the experimental conditions chosen, the inhibitory effect of iloperidone and ifenprodil does not appear to be voltage dependent.

Since VER155008 efficiently inhibited TRPM7-mediated Ca^{2+} uptake (Suppl. Fig. S3A), we compared the capability of 10 μM NS8593 and VER155008 to inactivate the TRPM7 channel in patch-clamp

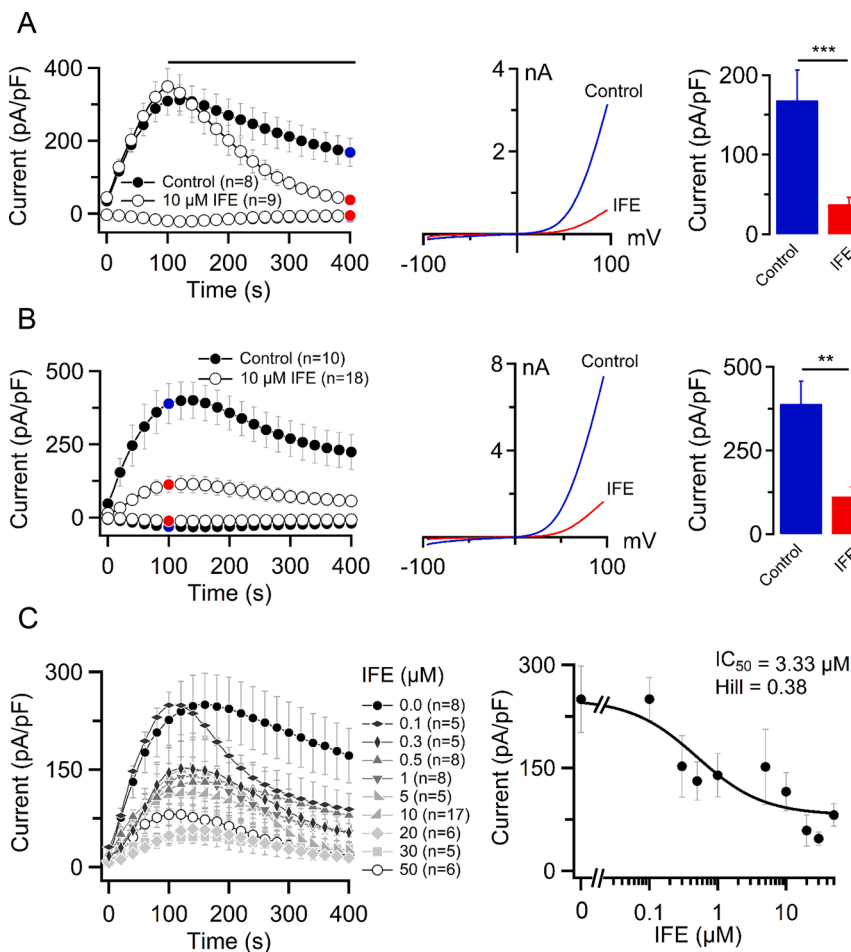


Fig. 2. Inhibition of TRPM6 currents by ifenprodil.

Whole-cell currents were measured in *Trpm6*-transfected HEK293T cells exposed to ifenprodil. (A) Left panel: Current amplitudes (mean \pm SEM) were measured at -80 and +80 mV and plotted over time. When currents were developed, cells were exposed to 10 μM ifenprodil (IFE), as indicated by the horizontal bar. Middle panel: Representative current-voltage relationships obtained from individual ramps before (blue) and during (red) the application of ifenprodil as indicated in the Left panel. Right panel: Bar graphs of outward currents (+80 mV, mean \pm SEM) obtained from untreated (blue) and ifenprodil-treated cells (red), as indicated in the Left and Middle panels. (B) Experiments were performed similarly to (A), except that the cells were exposed to an external solution without (Control) or with 10 μM ifenprodil (IFE) before the recording of whole-cell currents. (C) Concentration-dependent inhibition of TRPM6 currents by ifenprodil (IFE). Experiments were performed as outlined in (C) with the cells exposed to the indicated concentrations of iloperidone. Left panel: Current amplitudes (mean \pm SEM) acquired at +80 mV and plotted over time. Right panel: Dose-dependent suppression of outward currents (+80 mV, maximal currents) shown in the Left panel. n, number of cells measured; ** $P < 0.01$, *** $P < 0.001$ (two-tailed t test).

experiments (Fig. 3). We found that both compounds caused suppression of fully developed TRPM7 currents, but VER155008 acted more slowly than NS8593 (Fig. 3A, B). The I-V relationships of TRPM7 currents in the absence and presence of VER155008 were indistinguishable, suggesting the voltage-independent action of VER155008 on TRPM7. We also observed that exposure of HEK293T cells to 10 μ M VER155008 prevented the induction of TRPM7 currents (Fig. 3C). Using the latter settings, we obtained concentration-response datasets and obtained an IC_{50} value of 0.11 μ M (Fig. 3D). Notably, 10–30 μ M VER155008 showed no effect on TRPM6 currents (Suppl. Fig. S4C). To investigate whether the inhibitory effects of VER155008 on TRPM7 currents could be reversed after the compound's removal, we transiently perfused TRPM7-transfected HEK293T cells with 10 μ M VER155008. We observed that the inhibitory action of VER155008 could not be reversed after wash-out of the compound (Suppl. Fig. S5C), resembling the inhibitory effect of another TRPM7 inhibitor, waixenicin A [41].

Because VER155008 is an adenosine-derived compound [48], we asked whether the kinase moiety of TRPM7 plays a role in the inhibitory effect on TRPM7 currents. To this end, we examined HEK293T cells expressing TRPM7 containing a kinase-dead point mutation (K1646R)

[12,18,22]. The K1646R TRPM7 channel variant was fully inhibited by 10 μ M VER155008 (Suppl. Fig. S6).

These findings collectively indicate that the functional effects of iloperidone, ifenprodil and VER155008 are robust and can be reliably monitored irrespective of whether Ca^{2+} imaging or patch-clamp techniques are applied and that these compounds allow selective suppression of the channel activity of TRPM6 and TRPM7 with IC_{50} values in the nM to low μ M range.

3.3. Effects of iloperidone, ifenprodil and VER155008 on the TRPM2, TRPM3 and TRPM8 channels

Because the biophysical characteristics of TRPM6 and TRPM7 currents are well distinguishable from those of other known channels, we do not foresee intractable pitfalls in the use of iloperidone, ifenprodil and VER155008 in patch-clamp measurements. However, potential off-target effects of these compounds will be more difficult to rule out in Ca^{2+} imaging experiments. Therefore, we investigated whether iloperidone, ifenprodil and VER155008 would impact the channel activity of genetically related TRPM proteins [46] such as TRPM2, TRPM3 and

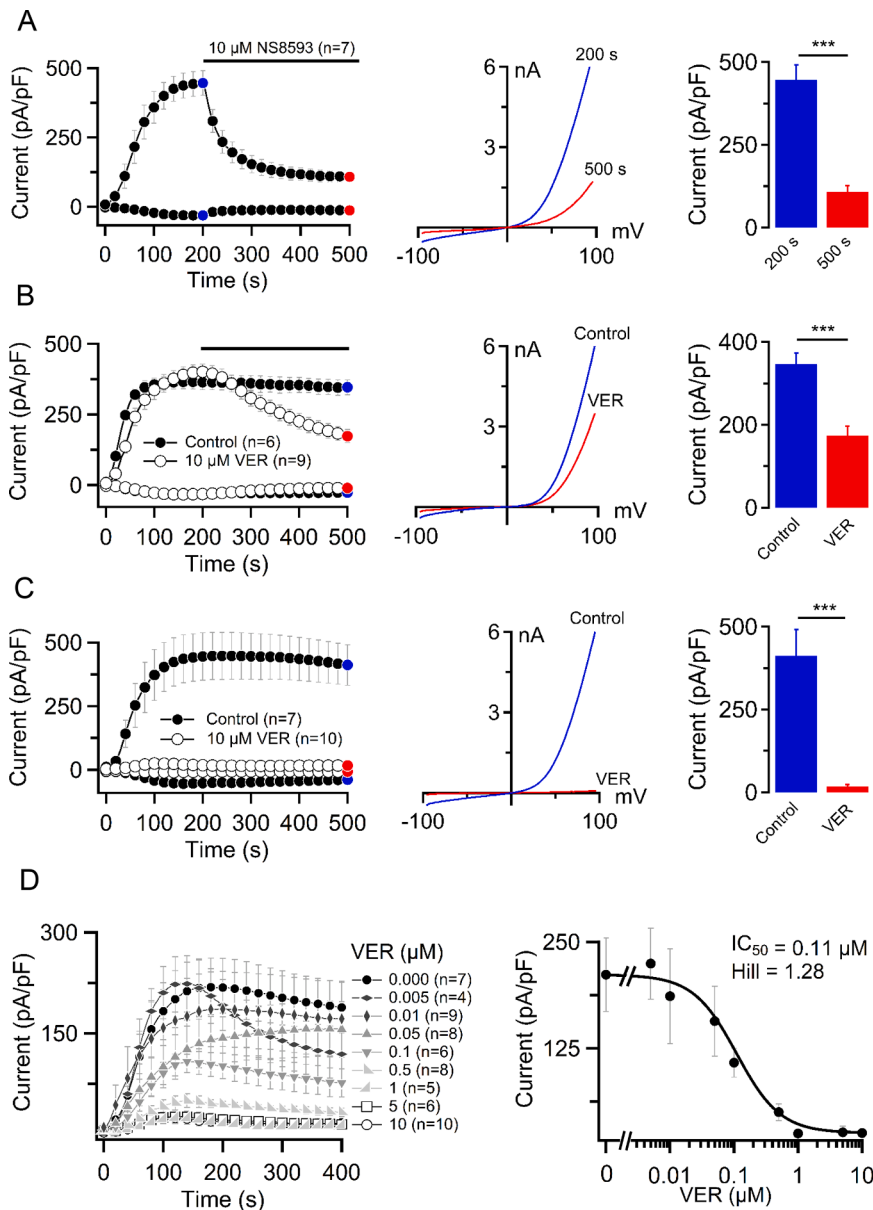


Fig. 3. The inhibitory effects of NS8593 and VER155008 on the TRPM7 channel.

Whole-cell currents were measured in *Trpm7*-transfected HEK293T cells exposed to NS8593 (A) and VER155008 (B–D). (A) *Left panel:* Current amplitudes (mean \pm SEM) were measured at -80 and +80 mV and plotted over time. When currents were developed, cells were exposed to 10 μ M NS8593, as indicated by the horizontal bar. *Middle panel:* Representative current-voltage relationships obtained from individual ramps before (blue) and after (red) application of NS8593 as indicated in the *Left panel*. *Right panel:* Bar graphs of outward currents (+80 mV, mean \pm SEM) obtained from untreated (blue) and NS8593-treated cells (red) as indicated in the *Left and Middle panels*. (B) Experiments were performed similarly to (A). The cells were exposed to an external solution containing 10 μ M VER155008 (VER), as indicated by the black bar in the *Left panel*. (C) Experiments were performed and analysed similarly to (A), except that the cells were exposed to an external solution without (Control) or with 10 μ M VER155008 (VER) before the recording of whole-cell currents. (D) Concentration-dependent inhibition of TRPM7 currents by VER155008. Experiments were performed as outlined in (C) with the cells exposed to the indicated concentrations of VER155008 (VER). *Left panel:* Current amplitudes (mean \pm SEM) acquired at +80 mV and plotted over time. *Right panel:* Dose-dependent suppression of outward currents (+80 mV, maximal currents) shown in the *Left panel*. n, number of cells measured; *** P < 0.001 (two-tailed t test).

TRPM8 stably expressed in HEK293T cells [49,50]. To this end, we used fura-2-assisted Ca^{2+} imaging to monitor H_2O_2 -stimulated TRPM2 channel activity in the absence of compounds or the presence of 10 μM iloperidone, 10 μM ifenprodil or 10 μM VER155008 and found that none of the three agents changed the responses of the TRPM2 channel (Suppl. Fig. S7).

To investigate the TRPM3 channel, we measured pregnenolone sulfate-induced Ca^{2+} increases in TRPM3-expressing cells (Suppl. Fig. S8). We found that coapplication of 10 μM ifenprodil or 10 μM VER155008 caused no detectable alterations in TRPM3-mediated Ca^{2+} influx (Suppl. Fig. S8B, D), whereas 10 μM iloperidone moderately suppressed the response of TRPM3, but this effect was not statistically significant (Suppl. Fig. S8C, E).

To assess the impact of iloperidone, ifenprodil and VER155008 on TRPM8, we measured Ca^{2+} levels in TRPM8-expressing cells exposed to menthol (Suppl. Fig. S8). These experiments revealed that all three compounds applied at ≥ 10 μM elicited inhibitory effects on TRPM8 responses to menthol (Suppl. Fig. S9A-D). Therefore, we evaluated the concentration-dependent inactivation of TRPM8 and found that iloperidone and ifenprodil inactivated the channel with IC_{50} values of 6.1 and 8.2 μM , respectively (Suppl. Fig. S9F-G). High concentrations of VER155008 incompletely suppressed the TRPM8 channel, thus precluding a reliable estimation of the IC_{50} (Suppl. Fig. S9H).

Hence, our results indicate that 10 μM iloperidone, 10 μM ifenprodil and 10 μM VER155008 did not affect the channel activity of TRPM2 and TRPM3. However, these compounds elicited an inhibitory effect on the TRPM8 channel and should be used cautiously in Ca^{2+} imaging experiments with cells expressing TRPM8.

3.4. Targeting of endogenous TRPM7 currents by VER155008

We asked whether VER155008 can suppress endogenous TRPM7 currents. TRPM7 is a ubiquitously expressed protein, and patch-clamp experiments revealed that native TRPM7-like currents were present in all examined cells. For instance, independent studies reported that human HEK293T cells express endogenous TRPM7-like currents, which were not detectable in HEK293T cells with an introduced null mutation in the *TRPM7* gene or in cells exposed to NS8593 [7,18,40,51]. To this end, we analysed HEK293T cells to assess the impact of VER155008 on endogenous cation currents. Fig. 4A illustrates native cation currents in HEK293T cells induced by removing cytosolic Mg^{2+} . The I-V relationships of these currents displayed the biophysical characteristics of the

TRPM7 channel in cells expressing the recombinant TRPM7 protein (Fig. 3A). We found that exposure to 10 μM VER155008 effectively suppressed TRPM7-like currents to background levels (Fig. 4A).

We next studied the effect of 10 μM VER155008 on endogenous TRPM7-like currents in human respiratory A549 cells (Fig. 4B). We found that TRPM7-like currents were persistently detectable in untreated A549 cells but not in cells exposed to 10 μM NS8593 or 10 μM VER155008 (Fig. 4B). Hence, we concluded that VER155008 was equally efficient in targeting native human TRPM7 channels.

3.5. Impact of iloperidone on endogenous cation currents in cells coexpressing TRPM6 and TRPM7

Because TRPM6 is inevitably coexpressed with the ubiquitously present TRPM7 [1,3,30–32], the functional assessment of TRPM6 in native environments remains a challenging task in the field. Therefore, we asked whether the newly identified TRPM6 inhibitor iloperidone would allow us to conduct such experiments. Previously, we performed a comparative analysis of native currents in trophoblast stem (TS) cells derived from *Trpm6*^{−/−} and *Trpm7*^{−/−} mouse blastocysts [5]. We found that wild-type (WT) TS cells express both *Trpm6* and *Trpm7* transcripts and exhibit characteristic TRPM6/M7-like currents [5]. Genetic inactivation of *Trpm6* reduced current amplitudes, whereas deletion of *Trpm7* resulted in the complete disappearance of such currents [5], presumably because TRPM6 was primarily present in TRPM6/M7 heteromers [33]. Along these lines, we used WT and *Trpm6* gene-deficient (*Trpm6*^{−/−}) TS cells to verify the effects of iloperidone and VER155008 (Fig. 5). In accordance with the genetic approach [5], we found that administration of 10 μM VER155008 abrogated the induction of TRPM6/M7-like currents in WT and *Trpm6*^{−/−} TS cells (Fig. 5A, B). However, the impact of iloperidone was different in WT and *Trpm6*^{−/−} TS cells. In WT TS cells exposed to iloperidone, cation currents started to develop during the first 100 s of measurement, but there was a complete run-down of currents afterwards (Fig. 5A). In contrast, 10 μM iloperidone did not significantly alter cation currents measured in *Trpm6*^{−/−} cells (Fig. 5B). Collectively, these results support the notion that iloperidone inhibits channel complexes containing TRPM6 without an impact on TRPM7 homomers. Our data also suggest that WT TS cells primarily contain TRPM6/M7 heteromers suppressible by both compounds, iloperidone and VER155008.

To test the ability of iloperidone to suppress the activity of endogenous human TRPM6, we investigated the neuroblastoma SHEP-21N cells

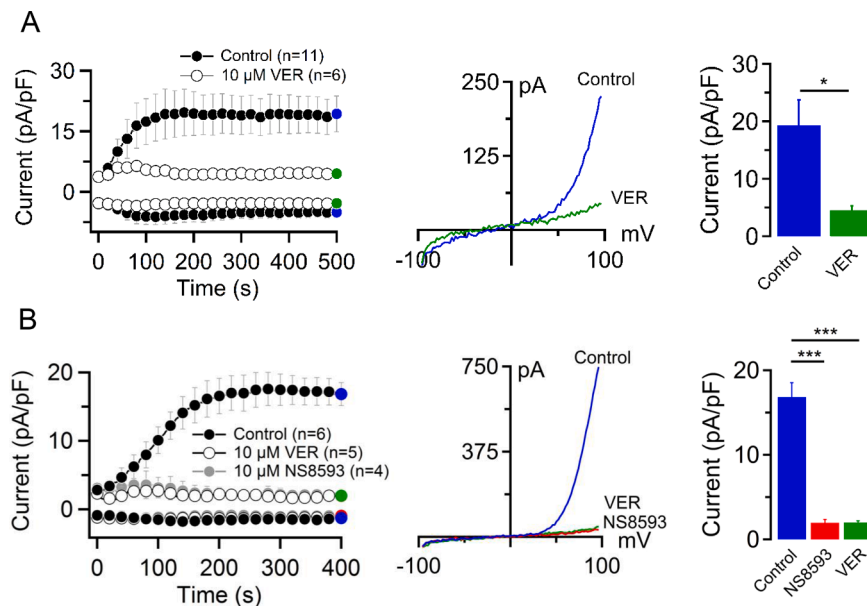


Fig. 4. Effects of VER155008 on endogenous currents in HEK293T and A549 cells.

Whole-cell currents were measured in HEK293T (A) and A549 (B) cells. (A) *Left panel:* Current amplitudes (mean \pm SEM) were measured at -80 and +80 mV and plotted over time. HEK293T cells were exposed to an external solution without (Control) or with 10 μM VER155008 (VER) before the recording of whole-cell currents. *Middle panel:* Representative current-voltage relationships obtained from individual ramps at 500 s as indicated in the *Left panel*. *Right panel:* Bar graphs of outward currents (+80 mV, mean \pm SEM) obtained at 500 s as indicated in the *Left and Middle panels*. n, number of cells measured; * $P < 0.05$ (two-tailed t test). (B) Experiments were performed with A549 cells similarly to (A), except that the effects of 10 μM VER155008 and 10 μM NS8593 were examined at 400 s. n, number of cells measured; *** $P < 0.001$ (ANOVA).

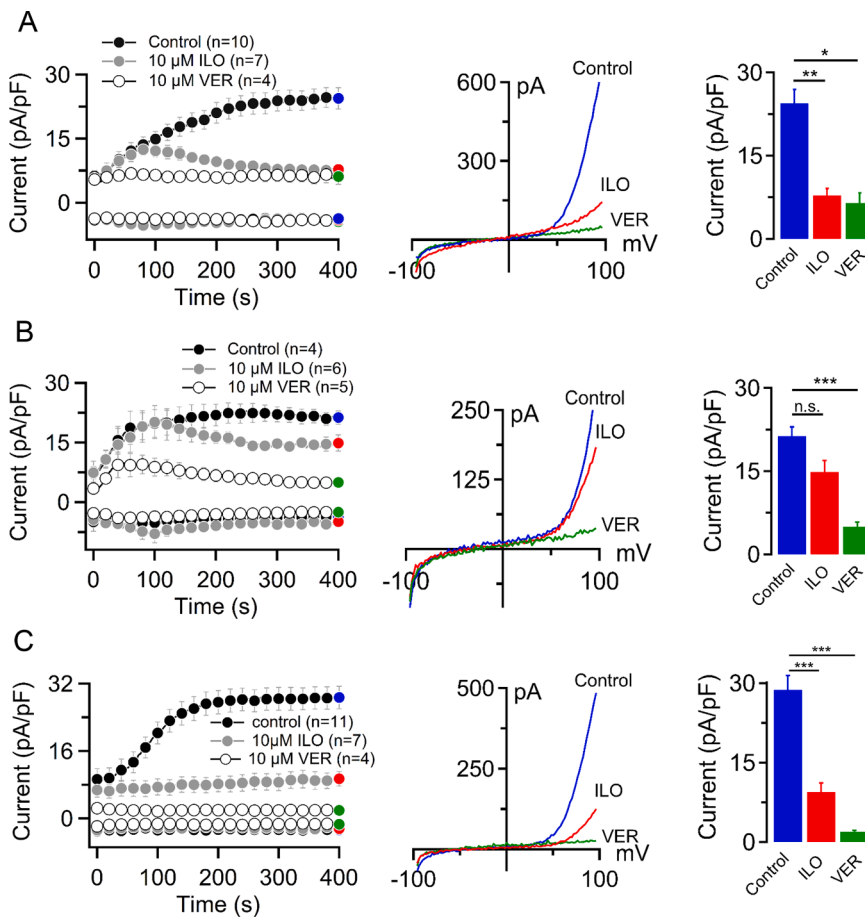


Fig. 5. Effects of iloperidone and VER155008 on endogenous cation currents in mouse embryonic trophoblast stem (TS) cells and human neuroblastoma SHEP-21N cells.

(A, B) Whole-cell currents were measured in wild-type (WT) (A) and *Trpm6*^{-/-} (B) TS cells. *Left panel*: Current amplitudes (mean ± SEM) were acquired in cells at -80 and +80 mV and plotted over time. The cells were exposed to the external solution without (Control), with 10 μM iloperidone (ILO) or 10 μM VER155008 (VER). *Middle panel*: Representative current-voltage relationships obtained from individual ramps at 400 s as indicated by coloured data points in the *Left panel*. *Right panel*: Bar graphs of outward currents (+80 mV, 400 s, mean ± SEM) obtained from control (blue), iloperidone-treated (red) and VER155008-treated cells (green) as indicated in the *Left panel*. (C) Experiments were performed similarly to (A), except that human SHEP-21N cells were examined. n, number of cells measured; * P < 0.05, ** P < 0.01, *** P < 0.001; n.s., not significant (ANOVA).

expressing TRPM6 and TRPM7 [32]. The SHEP-21N cell line was engineered to express N-Myc under the control of a tetracycline-dependent repressor [32,45]. It was demonstrated that high levels of N-Myc upregulate the expression of *TRPM6* but not *TRPM7*, leading to an increase of endogenous TRPM6/M7 currents and that this effect can be reversed by the exposure of SHEP-21N cells to tetracycline to downregulate N-Myc levels or by using small interfering RNA (siRNA) against *TRPM6* [32]. In accord with this study, we observed that adding tetracycline to the cell culture medium could significantly suppress TRPM6/M7-like currents in SHEP-21N cells (Suppl. Fig. 10). Consequently, we examined the effects of iloperidone and VER155008 using untreated SHEP-21N cells and found that 10 μM iloperidone caused a substantial reduction of TRPM6/M7-like currents, while exposure of the cells to 10 μM VER155008 resulted in complete inactivation of such currents (Fig. 5C). We interpreted these findings to mean that, analogously to the situation with WT mouse TS cells (Fig. 5B), TRPM6/M7 heteromers mainly contributed to the endogenous divalent cation currents in SHEP-21N cells.

Finally, we asked whether iloperidone can be used to estimate the abundance of TRPM6-containing channel complexes in cells expressing different ratios of recombinant TRPM6 and TRPM7. To this end, we analysed the effects of 10 μM iloperidone on whole-cell currents in HEK293T cells transiently transfected with *Trpm6* and *Trpm7* cDNA ratios of 3:1, assuming that under such conditions, the majority of TRPM7 will be present in TRPM6/M7 complexes (Fig. 6A). We found that untreated HEK293T cells developed characteristic TRPM6/M7-like currents (Fig. 6A). In the cells exposed to iloperidone (Fig. 6A), such cation currents developed during 120 s of recordings but were significantly inactivated afterwards (30.8% of the control values at 400 s), thus mirroring our findings in WT TS cells (Fig. 5A) and SHEP-21N cells (Fig. 5C). Of note, the impact of 10 μM iloperidone was moderate after

cotransfection of *Trpm6* and *Trpm7* plasmid cDNAs at a ratio of 1:1 (52.7% of the control currents, Fig. 6B) and was not statistically significant at a ratio of 1:3 (68.17% of the control currents, Fig. 6C), likely because iloperidone-insensitive TRPM7 homomers were abundantly present in the latter setting. In line with this idea, co-application of two compounds, iloperidone and VER155008, to HEK293T cells transfected with *Trpm6* and *Trpm7* cDNA ratios of 1:3 caused complete ablation of TRPM6/M7 currents (0.7% of control currents, Fig. 6C).

Taken together, we conclude that iloperidone represents the first pharmacological agent allowing us to map the functional role of TRPM6 in the presence of TRPM7.

4. Discussion

Ca²⁺, Zn²⁺ and Mg²⁺ are essential divalent cations required for countless cellular processes. An emerging paradigm is that the kinase-coupled TRPM6 and TRPM7 channels control the organismal balance of these cations. However, several crucial functional aspects of TRPM6 and TRPM7 remain elusive. Against this backdrop, there is a pressing need for pharmacological agents acting as potent and selective modulators of the channel and kinase moieties of TRPM6 and TRPM7. Such compounds are also necessary to verify whether TRPM6 and TRPM7 are viable therapeutic targets. In the present paper, we report three drug-like small molecules allowing the selective suppression of the channel moieties of TRPM6 and TRPM7.

Currently, the available pharmacological toolkit suitable for the modulation of kinase domains in TRPM6 and TRPM7 is limited to only one compound, TG100-115. TG100-115 was initially introduced as a potent inhibitor of phosphoinositide 3-kinases [52]. Later, TG100-115 was found to reversibly block the kinase moieties of TRPM6 and TRPM7 [18,19,53]. A collection of small organic molecules was

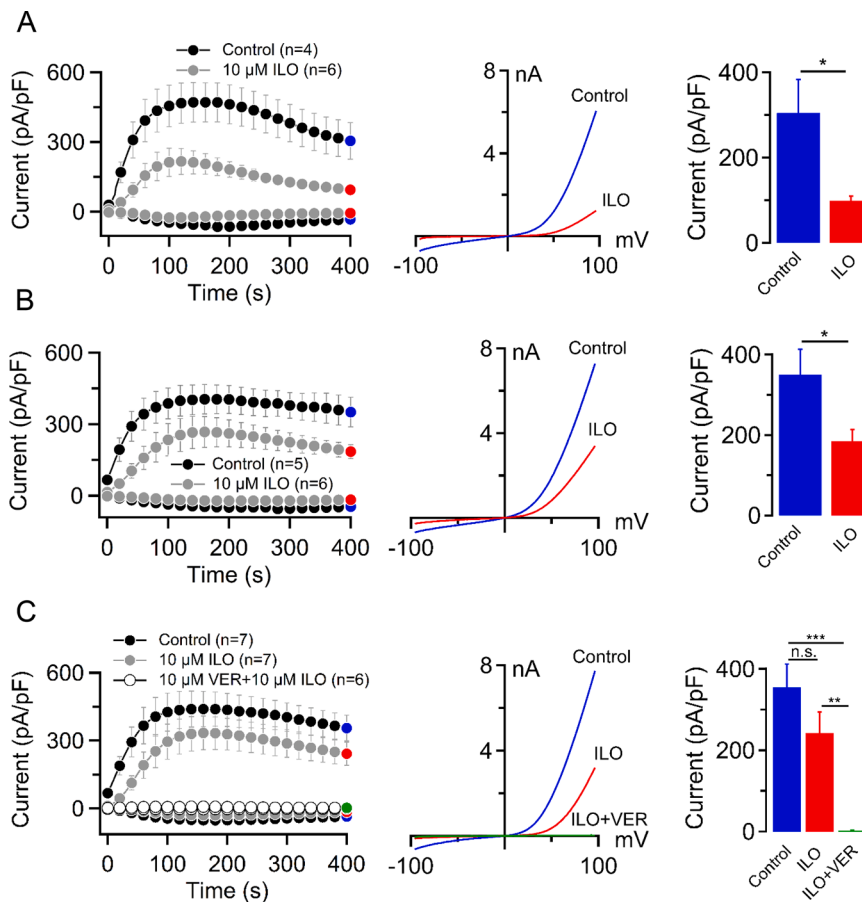


Fig. 6. Effects of iloperidone on cation currents in HEK293T cells transfected with different ratios of *Trpm6* and *Trpm7*.

Whole-cell currents were measured in HEK293T cells cotransfected with *Trpm6* and *Trpm7* cDNA plasmids. (A) HEK293T cells were cotransfected with a mixture of the *Trpm6* and *Trpm7* expression constructs (3:1 ratio), and whole-cell currents were measured as outlined in Fig. 1. Left panel: Current amplitudes (mean \pm SEM) were acquired at -80 and +80 mV and plotted over time. The cells were exposed to an external solution without (Control) or with 10 μ M iloperidone (ILO). Middle panel: Representative current-voltage relationships obtained from individual ramps at 400 s as indicated by coloured data points in the Left panel. Right panel: Bar graphs of outward currents (+80 mV, mean \pm SEM) obtained from untreated (blue) and iloperidone-treated cells (red) as indicated in the Left panel. (B, C) Experiments were performed similarly to (A), except that HEK293T cells were cotransfected with the *Trpm6* and *Trpm7* plasmid DNAs mixed at the 1:1 (B) and 1:3 (C) ratios. In (C), the cells were exposed to an external solution without (Control), 10 μ M iloperidone (ILO) or 10 μ M iloperidone (ILO) with 10 μ M VER155008 (VER). n, number of cells measured; * $P < 0.05$, ** $P < 0.01$, *** $P < 0.001$; n.s., not significant (ANOVA).

reported as inhibitors of the TRPM7 channel, effective in the μ M to mM range [37–39]. NS8593, FTY720 and waixenicin A represent the most potent modulators of the TRPM7 channel [40–42], which subsequently were used in dozens of publications aiming to interrogate the cellular role of TRPM7 [37–39]. Waixenicin A is a complex natural terpenoid extracted from the Hawaiian soft coral *Sarcothelia edmondsoni*. Waixenicin A irreversibly inactivates TRPM7 currents in a Mg^{2+} -dependent manner with an IC_{50} of 7 μ M (in the absence of intracellular Mg^{2+}) and showed no effect on TRPM6 [41]. However, the use of waixenicin A in preclinical disease models is limited because its chemical synthesis is unestablished. NS8593 and FTY720 are small synthetic molecules able to suppress TRPM7 currents with IC_{50} values of 1.6 and 0.7 μ M, respectively [40,42]. However, NS8593 and likely FTY720 also block TRPM6 [19,42] and, therefore, are unsuitable for manipulating TRPM6 versus TRPM7 selectively. Finally, a collection of small molecules acting as agonists of the TRPM7 channel were identified, including naltriben [44], whereas activators of TRPM6 remain to be established.

The present study reports new drug-like compounds acting on TRPM6 and TRPM7 channels. We found that iloperidone and ifenprodil blocked TRPM6 currents with IC_{50} values of 0.73 and 3.33 μ M, respectively, while these compounds did not elicit inhibitory effects on the TRPM7 channel. Although the inhibitory effect of ifenprodil was significantly slower than that of iloperidone, both compounds suppressed TRPM6 currents on a minute timescale, reversibly and without an apparent impact on the I-V characteristics suggesting that iloperidone and ifenprodil acted as negative gating regulators rather than channel pore blockers. The difference in inhibition kinetics of iloperidone and ifenprodil can be explained by distinct physicochemical profiles of the compounds (i.e. size, polarity, hydrophobicity, Suppl. Fig. S1) or alternative interaction mechanisms with TRPM6. The closely related channels TRPM2 and TRPM3 were not sensitive to iloperidone and

ifenprodil. However, these compounds could inhibit TRPM8.

VER155008 inhibited TRPM7 currents with an IC_{50} value of 0.11 μ M, thus showing the highest potency among known pharmacological inhibitors of the TRPM7 channel assessed in the absence of intracellular Mg^{2+} . Notably, VER155008 did not induce a significant effect on TRPM6 and was suitable for suppressing endogenous TRPM7 currents in human HEK293T and A549 cells. TRPM2 and TRPM3 did not respond to relevant concentrations of VER155008. However, high concentrations of VER155008 partially suppressed TRPM8. Interestingly, the inhibitory effect of VER155008 on TRPM7 was irreversible, resembling the behavior of another highly potent TRPM7 inhibitor, waixenicin A [41]. One possible explanation for this characteristic is that potent inhibitors can bind TRPM7 very tightly, and consequently, the dissociation rate was effectively zero at the relevant timescale. However, a covalent interaction of VER155008 with TRPM7 cannot be completely ruled out. The difference in inhibition kinetics of VER155008 and NS8593 may be due to a structural dissimilarity of these compounds (Suppl. Fig. S1) or distinct mechanisms of action.

Despite extensive electrophysiological and genetic studies, an open question still is how TRPM6 cooperates with TRPM7 in regulating the cellular uptake of Ca^{2+} , Zn^{2+} and Mg^{2+} and why such functional interactions are vital for prenatal development and healthy adulthood [4, 5]. As a proof-of-concept, we used iloperidone and VER155008 to show that these compounds allow us to differentiate between the contribution of TRPM6 and TRPM7 to endogenous divalent cation currents in mouse embryonic TS cells and human neuroblastoma SHEP-21N cells. In particular, we found that exposure of WT TS cells to iloperidone and VER155008 suppressed divalent cation currents, whereas *Trpm6*^{-/-} cells responded only to VER155008 application. These results accord with our previous analysis of TS cells after genetic inactivation of *Trpm6* and *Trpm7* and support the idea that native TRPM6 functions primarily

in heteromeric TRPM6/M7 channel complexes [5,33]. Moreover, our electrophysiological assessment of SHEP-21N cells using iloperidone and VER155008 recapitulated the main findings obtained after siRNA silencing of *TRPM6* and *TRPM7* [32], reinforcing the idea that TRPM6/M7 heteromers primarily maintained native currents in these cells. Finally, the primary outcome of our experiments with TS and SHEP-21N cells could be replicated in HEK293T cells cotransfected with *Trpm6* and *Trpm7* cDNA plasmids, followed by exposure to iloperidone and VER155008. Thus, such a pharmacological approach may serve as a blueprint for the electrophysiological assessment of TRPM6 and TRPM7 in other cells.

Iloperidone was established as a nonspecific antagonist of serotonin, dopamine, noradrenaline and histamine receptors [54,55]. The FDA approved iloperidone for the treatment of schizophrenia [56]. Ifenprodil was defined as an antagonist of *N*-methyl-D-aspartate receptors 1 and 2B (NMDAR1, 2B) and the sigma-1 receptor [57,58]. Interestingly, ifenprodil is currently in phase III clinical trial to treat patients infected with COVID-19 [58] (ClinicalTrials.gov identifier: NCT04382924). Given the ability of iloperidone and ifenprodil to inhibit TRPM6, it will be crucial to elucidate whether the intake of these drugs induces organismal depletion of Mg^{2+} in patients. In addition, iloperidone and ifenprodil can be repurposed to treat hypermagnesemia or pathologies associated with upregulation of *TRPM6*, such as colorectal cancer [31,59] and neuroblastoma [32,36].

VER155008 has been developed as an adenosine-derived inhibitor of heat shock protein 70 (Hsp70) [48]. VER155008 was found to be a potent inhibitor of cell proliferation in several tumours and, consequently, was suggested as a new type of anticancer agent [60–66]. However, because pharmacological suppression of TRPM7 also leads to growth arrest of tumour cells [37–39], it cannot be ruled out that the antiproliferative effects of VER155008 were induced due to its action on ubiquitously expressed TRPM7.

5. Conclusions

Our results indicate that iloperidone, ifenprodil and VER155008 allow for selective pharmacological inhibition of TRPM6 and TRPM7 channels, thus blazing the trail for selective targeting of TRPM6 and TRPM7 in animal disease models and human cells derived from blood or tissue biopsies.

Funding

Susanna Zierler, Vladimir Chubanov, Thomas Gudermann, Kerstin Hill and Michael Schaefer were supported by the Deutsche Forschungsgemeinschaft (DFG), TRR 152 (P14, P15 and P18). Thomas Gudermann was supported by Research Training Group 2338 (DFG).

CRedit authorship contribution statement

Anna Rössig: Investigation, Formal analysis, Visualization, Writing – original draft. **Kerstin Hill:** Investigation, Formal analysis, Visualization, Writing – review & editing. **Wolfgang Nörenberg:** Investigation, Formal analysis, Visualization. **Sebastian Weidenbach:** Investigation, Formal analysis, Visualization. **Susanna Zierler:** Methodology, Formal analysis, Writing – review & editing. **Michael Schaefer:** Methodology, Resources, Writing – review & editing. **Thomas Gudermann:** Resources, Writing – original draft, Writing – review & editing, Supervision, Project administration, Funding acquisition. **Vladimir Chubanov:** Conceptualization, Formal analysis, Supervision, Funding acquisition, Writing – original draft, Writing – review & editing.

Declaration of competing interests

The authors declare that they have no competing interests.

Data Availability

Data will be made available on request.

Acknowledgements

We thank Joanna Zaisserer and Anna Erbacher for their excellent technical assistance. We thank Andrea Fleig for sharing SHEP-21N cells and Carsten Schmitz for providing human *TRPM7* cDNA.

Supplementary materials

Supplementary material associated with this article can be found, in the online version, at doi:[10.1016/j.ceca.2022.102640](https://doi.org/10.1016/j.ceca.2022.102640).

References

- [1] V Chubanov, L Mittermeier, T Gudermann, Role of kinase-coupled TRP channels in mineral homeostasis, *Pharmacol Ther* 184 (2018) 159–176.
- [2] A Fleig, V Chubanov, *Trpm7*, *Handb Exp Pharmacol* 222 (2014) 521–546.
- [3] V Chubanov, T Gudermann, *Trpm6*, *Handb Exp Pharmacol* 222 (2014) 503–520.
- [4] L Mittermeier, et al., TRPM7 is the central gatekeeper of intestinal mineral absorption essential for postnatal survival, *Proc Natl Acad Sci U S A* 116 (10) (2019) 4706–4715.
- [5] V Chubanov, et al., Epithelial magnesium transport by TRPM6 is essential for prenatal development and adult survival, *Elife* 5 (2016).
- [6] MK Montell-Zoller, et al., TRPM7 provides an ion channel mechanism for cellular entry of trace metal ions, *J Gen Physiol* 121 (1) (2003) 49–60.
- [7] MJ Nadler, et al., LTRPC7 is a Mg-ATP-regulated divalent cation channel required for cell viability, *Nature* 411 (6837) (2001) 590–595.
- [8] HH Kerschbaum, MD Cahalan, Single-channel recording of a store-operated Ca^{2+} channel in Jurkat T lymphocytes, *Science* 283 (5403) (1999) 836–839.
- [9] M Prakriya, RS Lewis, Separation and characterization of currents through store-operated CRAC channels and Mg^{2+} -inhibited cation (MIC) channels, *J Gen Physiol* 119 (5) (2002) 487–507.
- [10] JA Kozak, HH Kerschbaum, MD Cahalan, Distinct properties of CRAC and MIC channels in RBL cells, *J Gen Physiol* 120 (2) (2002) 221–235.
- [11] MC Hermosura, MK Montell-Zoller, AM Scharenberg, R Penner, A Fleig, Dissociation of the store-operated calcium current I(CRAC) and the Mg-nucleotide-regulated metal ion current MagNum, *J Physiol* 539 (Pt 2) (2002) 445–458.
- [12] C Schmitz, et al., Regulation of vertebrate cellular Mg^{2+} homeostasis by TRPM7, *Cell* 114 (2) (2003) 191–200.
- [13] LW Runnels, L Yue, DE Clapham, TRP-PLIK, a bifunctional protein with kinase and ion channel activities, *Science* 291 (5506) (2001) 1043–1047.
- [14] LW Runnels, L Yue, DE Clapham, The TRPM7 channel is inactivated by PIP(2) hydrolysis, *Nat Cell Biol* 4 (5) (2002) 329–336.
- [15] LV Ryazanova, MV Dorovkov, A Ansari, AG Ryazanov, Characterization of the protein kinase activity of TRPM7/ChaK1, a protein kinase fused to the transient receptor potential ion channel, *J Biol Chem* 279 (5) (2004) 3708–3716.
- [16] E Schmidt, et al., Structural mechanism of TRPM7 channel regulation by intracellular magnesium, *Cell Mol Life Sci* 79 (5) (2022) 225.
- [17] R Penner, A Fleig, The Mg^{2+} and $Mg(2+)$ -nucleotide-regulated channel-kinase TRPM7, *Handb Exp Pharmacol* (179) (2007) 313–328.
- [18] A Kollwe, et al., The molecular appearance of native TRPM7 channel complexes identified by high-resolution proteomics, *Elife* 10 (2021).
- [19] S Ferioli, et al., TRPM6 and TRPM7 differentially contribute to the relief of heteromeric TRPM6/7 channels from inhibition by cytosolic $Mg(2+)$ and Mg-ATP, *Sci Rep* 7 (1) (2017) 8806.
- [20] Z Bai, et al., CNM proteins selectively bind to the TRPM7 channel to stimulate divalent cation entry into cells, *PLoS Biol* 19 (12) (2021), e3001496.
- [21] J Duan, et al., Structure of the mammalian TRPM7, a magnesium channel required during embryonic development, *Proc Natl Acad Sci U S A* 115 (35) (2018) E8201–E8210.
- [22] A Romagnani, et al., TRPM7 kinase activity is essential for T cell colonization and alloreactivity in the gut, *Nat Commun* 8 (1) (2017) 1917.
- [23] S Stritt, et al., Defects in TRPM7 channel function deregulate thrombopoiesis through altered cellular $Mg(2+)$ homeostasis and cytoskeletal architecture, *Nat Commun* 7 (2016) 11097.
- [24] J Jin, et al., Deletion of *Trpm7* disrupts embryonic development and thymopoiesis without altering Mg^{2+} homeostasis, *Science* 322 (5902) (2008) 756–760.
- [25] J Jin, et al., The channel kinase, TRPM7, is required for early embryonic development, *Proc Natl Acad Sci U S A* 109 (5) (2012) E225–E233.
- [26] R Sah, et al., Timing of myocardial *trpm7* deletion during cardiogenesis variably disrupts adult ventricular function, conduction, and repolarization, *Circulation* 128 (2) (2013) 101–114.
- [27] R Sah, et al., Ion channel-kinase TRPM7 is required for maintaining cardiac automaticity, *Proc Natl Acad Sci U S A* 110 (32) (2013) E3037–E3046.
- [28] LV Ryazanova, et al., TRPM7 is essential for $Mg(2+)$ homeostasis in mammals, *Nat Commun* 1 (2010) 109.

- [29] MC Hermosura, et al., A TRPM7 variant shows altered sensitivity to magnesium that may contribute to the pathogenesis of two Guamanian neurodegenerative disorders, *Proc Natl Acad Sci U S A* 102 (32) (2005) 11510–11515.
- [30] I Andriule, et al., Evidence for the expression of TRPM6 and TRPM7 in cardiomyocytes from all four chamber walls of the human heart, *Sci Rep* 11 (1) (2021) 15445.
- [31] F Luongo, et al., TRPM6 is Essential for Magnesium Uptake and Epithelial Cell Function in the Colon, *Nutrients* 10 (6) (2018).
- [32] Z Zhang, et al., N-Myc-induced up-regulation of TRPM6/TRPM7 channels promotes neuroblastoma cell proliferation, *Oncotarget* 5 (17) (2014) 7625–7634.
- [33] V Chubanov, et al., Disruption of TRPM6/TRPM7 complex formation by a mutation in the TRPM6 gene causes hypomagnesemia with secondary hypocalcemia, *Proc Natl Acad Sci U S A* 101 (9) (2004) 2894–2899.
- [34] RY Walder, et al., Mutation of TRPM6 causes familial hypomagnesemia with secondary hypocalcemia, *Nat Genet* 31 (2) (2002) 171–174.
- [35] KP Schlingmann, et al., Hypomagnesemia with secondary hypocalcemia is caused by mutations in TRPM6, a new member of the TRPM gene family, *Nat Genet* 31 (2) (2002) 166–170.
- [36] Z Zhang, et al., The TRPM6 kinase domain determines the Mg.ATP sensitivity of TRPM7/M6 heteromeric ion channels, *J Biol Chem* 289 (8) (2014) 5217–5227.
- [37] V Chubanov, T Gudermann, Mapping TRPM7 Function by NS8593, *Int J Mol Sci* 21 (19) (2020).
- [38] HS Sun, et al., Waixenicin A, a marine-derived TRPM7 inhibitor: a promising CNS drug lead, *Acta Pharmacol Sin* 41 (12) (2020) 1519–1524.
- [39] V Chubanov, S Ferioli, T Gudermann, Assessment of TRPM7 functions by drug-like small molecules, *Cell Calcium* 67 (2017) 166–173.
- [40] V Chubanov, et al., Natural and synthetic modulators of SK (K(ca)2) potassium channels inhibit magnesium-dependent activity of the kinase-coupled cation channel TRPM7, *Br J Pharmacol* 166 (4) (2012) 1357–1376.
- [41] S Zierler, et al., Waixenicin A inhibits cell proliferation through magnesium-dependent block of transient receptor potential melastatin 7 (TRPM7) channels, *J Biol Chem* 286 (45) (2011) 39328–39335.
- [42] X Qin, et al., Sphingosine and FTY720 are potent inhibitors of the transient receptor potential melastatin 7 (TRPM7) channels, *Br J Pharmacol* 168 (6) (2013) 1294–1312.
- [43] S Schafer, et al., Mibefradil represents a new class of benzimidazole TRPM7 channel agonists, *Pflugers Arch* 468 (4) (2016) 623–634.
- [44] T Hofmann, et al., Activation of TRPM7 channels by small molecules under physiological conditions, *Pflugers Arch* 466 (12) (2014) 2177–2189.
- [45] W Lutz, et al., Conditional expression of N-myc in human neuroblastoma cells increases expression of alpha-prothymosin and ornithine decarboxylase and accelerates progression into S-phase early after mitogenic stimulation of quiescent cells, *Oncogene* 13 (4) (1996) 803–812.
- [46] M Mederos y Schnitzler, J Waring, T Gudermann, V Chubanov, Evolutionary determinants of divergent calcium selectivity of TRPM channels, *FASEB J* 22 (5) (2008) 1540–1551.
- [47] W Norenberg, et al., Positive allosteric modulation by ivermectin of human but not murine P2X7 receptors, *Br J Pharmacol* 167 (1) (2012) 48–66.
- [48] AJ Massey, et al., A novel, small molecule inhibitor of Hsc70/Hsp70 potentiates Hsp90 inhibitor induced apoptosis in HCT116 colon carcinoma cells, *Cancer Chemother Pharmacol* 66 (3) (2010) 535–545.
- [49] I Straub, et al., Flavanones that selectively inhibit TRPM3 attenuate thermal nociception in vivo, *Mol Pharmacol* 84 (5) (2013) 736–750.
- [50] JC Lenz, HP Reusch, N Albrecht, G Schultz, M Schaefer, Ca²⁺-controlled competitive diacylglycerol binding of protein kinase C isoenzymes in living cells, *J Cell Biol* 159 (2) (2002) 291–302.
- [51] SA Abiria, et al., TRPM7 senses oxidative stress to release Zn(2+) from unique intracellular vesicles, *Proc Natl Acad Sci U S A* 114 (30) (2017) E6079–E6088.
- [52] J Doukas, et al., Phosphoinositide 3-kinase gamma/delta inhibition limits infarct size after myocardial ischemia/reperfusion injury, *Proc Natl Acad Sci U S A* 103 (52) (2006) 19866–19871.
- [53] TY Kim, SK Shin, MY Song, JE Lee, KS Park, Identification of the phosphorylation sites on intact TRPM7 channels from mammalian cells, *Biochem Biophys Res Commun* 417 (3) (2012) 1030–1034.
- [54] MR Szezewczak, et al., The pharmacological profile of iloperidone, a novel atypical antipsychotic agent, *J Pharmacol Exp Ther* 274 (3) (1995) 1404–1413.
- [55] JT Strupczewski, et al., 3-[[[Aryloxy]alkyl]piperidinyl]-1,2-benzisoxazoles as D2/5-HT₂ antagonists with potential atypical antipsychotic activity: antipsychotic profile of iloperidone (HP 873), *J Med Chem* 38 (7) (1995) 1119–1131.
- [56] A Nair, A Salem, AL Asamoah, R Gosal, GT Grossberg, An update on the efficacy and safety of iloperidone as a schizophrenia therapy, *Expert Opin Pharmacother* 21 (15) (2020) 1793–1798.
- [57] H Mizusawa, H Fujiwara, [Pharmacological effects of 2-(4-benzyl-piperidino)-1-(4-hydroxyphenyl)-1-propanol (ifenprodil), with special reference to its effects on isolated arteries], *Nihon Yakurigaku Zasshi* 70 (6) (1974) 785–799.
- [58] K Hashimoto, Repurposing of CNS drugs to treat COVID-19 infection: targeting the sigma-1 receptor, *Eur Arch Psychiatry Clin Neurosci* 271 (2) (2021) 249–258.
- [59] G Pietropaolo, et al., Magnesium Absorption in Intestinal Cells: Evidence of Cross-Talk between EGF and TRPM6 and Novel Implications for Cetuximab Therapy, *Nutrients* 12 (11) (2020).
- [60] R Schlecht, et al., Functional analysis of Hsp70 inhibitors, *PLoS One* 8 (11) (2013) e78443.
- [61] W Wen, W Liu, Y Shao, L Chen, VER-155008, a small molecule inhibitor of HSP70 with potent anti-cancer activity on lung cancer cell lines, *Exp Biol Med* (Maywood) 239 (5) (2014) 638–645.
- [62] X Tang, et al., Gold nanorods together with HSP inhibitor-VER-155008 micelles for colon cancer mild-temperature photothermal therapy, *Acta Pharm Sin B* 8 (4) (2018) 587–601.
- [63] K Sakai, et al., Functional inhibition of heat shock protein 70 by VER-155008 suppresses pleural mesothelioma cell proliferation via an autophagy mechanism, *Thorac Cancer* 12 (4) (2021) 491–503.
- [64] L Huang, et al., Blockade of HSP70 by VER-155008 synergistically enhances bortezomib-induced cytotoxicity in multiple myeloma, *Cell Stress Chaperones* 25 (2) (2020) 357–367.
- [65] F Xu, et al., HSP70 inhibitor VER155008 suppresses pheochromocytoma cell and xenograft growth by inhibition of PI3K/AKT/mTOR and MEK/ERK pathways, *Int J Clin Exp Pathol* 12 (7) (2019) 2585–2594.
- [66] D Brunnert, et al., The heat shock protein 70 inhibitor VER155008 suppresses the expression of HSP27, HOP and HSP90beta and the androgen receptor, induces apoptosis, and attenuates prostate cancer cell growth, *J Cell Biochem* 121 (1) (2020) 407–417.

Supplementary information publication I

Supplementary Methods

Microfluorometric single-cell $[Ca^{2+}]_i$ assays

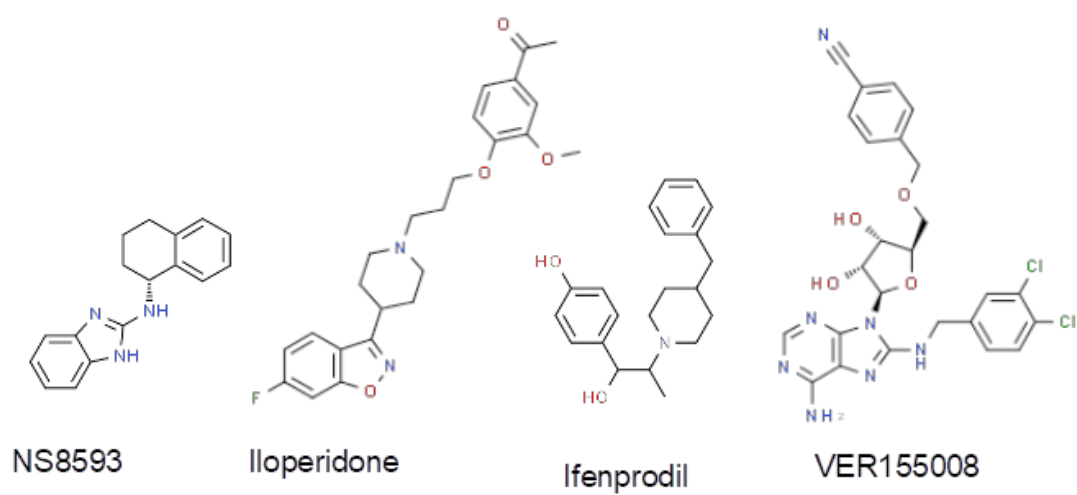
Human embryonic kidney (HEK 293) cells stably expressing myc-tagged mouse TRPM3 $_{\alpha 2}$ (HEK_{TRPM3}) or human TRPM2 (HEK_{TRPM2}) were obtained as described earlier (49). Cells were grown in DMEM (Invitrogen, Darmstadt, Germany) supplemented with 10% FCS, 2 mM L-glutamine, 100 units/ml penicillin and 0.1 mg/ml streptomycin at 37°C in a humidified atmosphere containing 5% CO₂. YFP-tagged human TRPM8 was transiently transfected in HEK293 cells using Lipofectamine 2000 (Invitrogen) according to the manufacturer's protocol.

All fluorometric $[Ca^{2+}]_i$ assays were performed in HEPES-buffered saline (HBS), containing 10 mM HEPES, 134 mM NaCl, 6 mM KCl, 1 mM MgCl₂, and 1 mM CaCl₂, (adjusted to pH 7.4 with NaOH). For microfluorometric single-cell analysis of $[Ca^{2+}]_i$, cells were seeded on poly-L-lysine-coated 25-mm glass coverslips 24 h prior to measurements. Cells were incubated with 2 μ M fura-2/AM in HBS buffer at 37°C for 30 min, rinsed, and mounted in a bath chamber for monochromator-assisted (TILL-Photonics, Graefelfing, Germany) digital epifluorescence videomicroscopy, built around an inverted microscope (Zeiss Axiovert 100, Jena, Germany). The fluorescence of fura-2 was sequentially excited at 340, 358, and 380 nm through the imaging objective (Fluar 10x/0.5; Carl Zeiss, Jena, Germany). Emitted light was filtered through a 512-nm long-pass filter and recorded with a 12-bit cooled CCD camera (IMAGO, TILL-Photonics, Graefelfing, Germany). The $[Ca^{2+}]_i$ concentration was calculated as described before (50).

For the generation of concentration-response curves, a custom-made fluorescence plate imager built into a robotic liquid handling station was used, as described previously (47). In brief, HEK 293 cells were transiently transfected with human YFP-tagged TRPM8 and were loaded with 4 μ M fluo-4/AM (Invitrogen) in the cell culture medium for 30 min, washed in HBS and seeded into black pigmented clear-bottom 384-well plates (10.000 cells/well; Corning, USA). Plates were mounted on the imager, and fluorescence was recorded through a 515 nm long pass filter after excitation with a 470 nm LED array. Compounds were added by a liquid handling device (47). ImageJ software was used for image analysis.

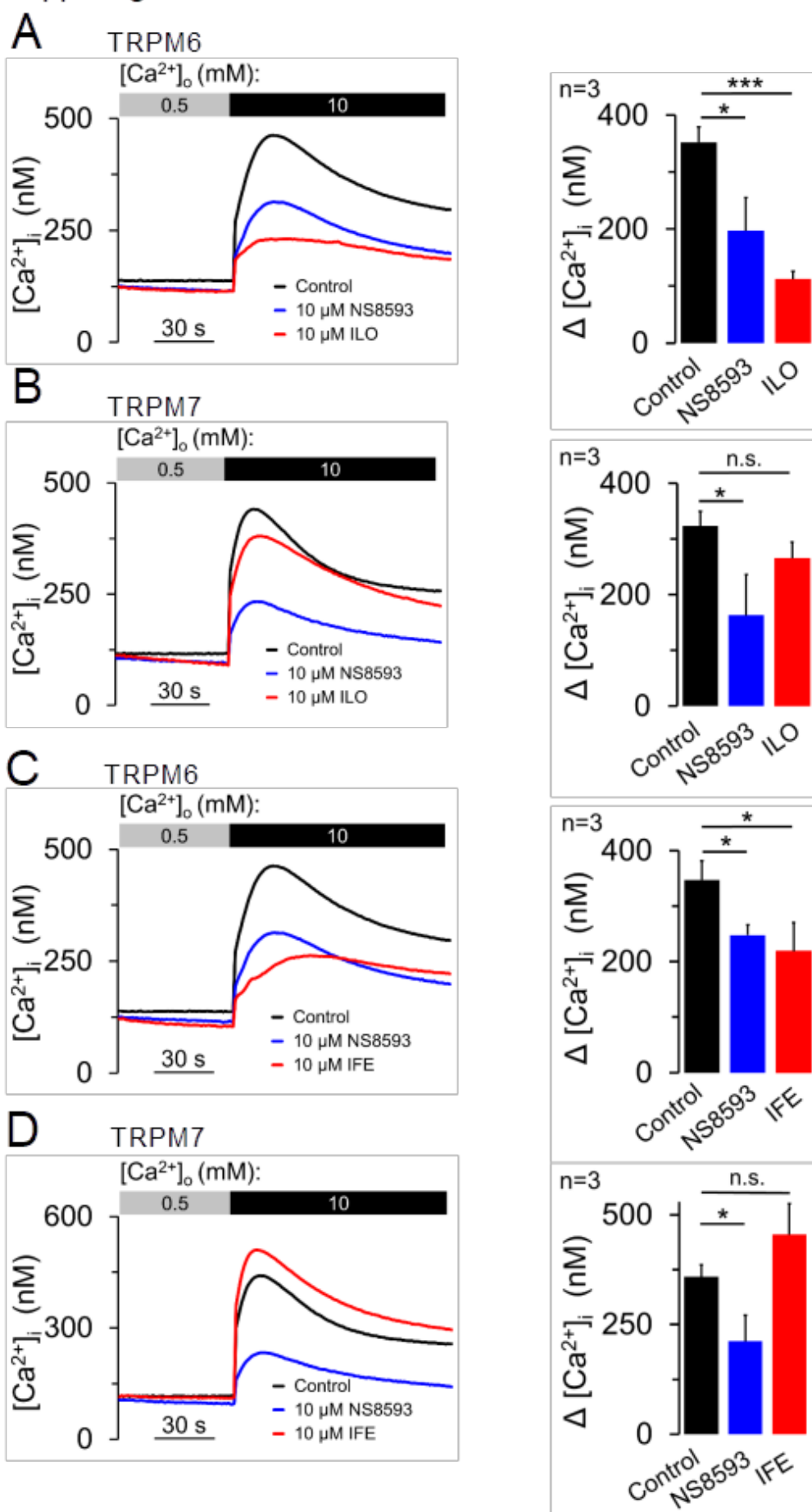
Supplementary Figure legends

Suppl. Figure S1



Supplementary Figure S1. Chemical structures of NS8593, iloperidone, ifenprodil and VER155008.

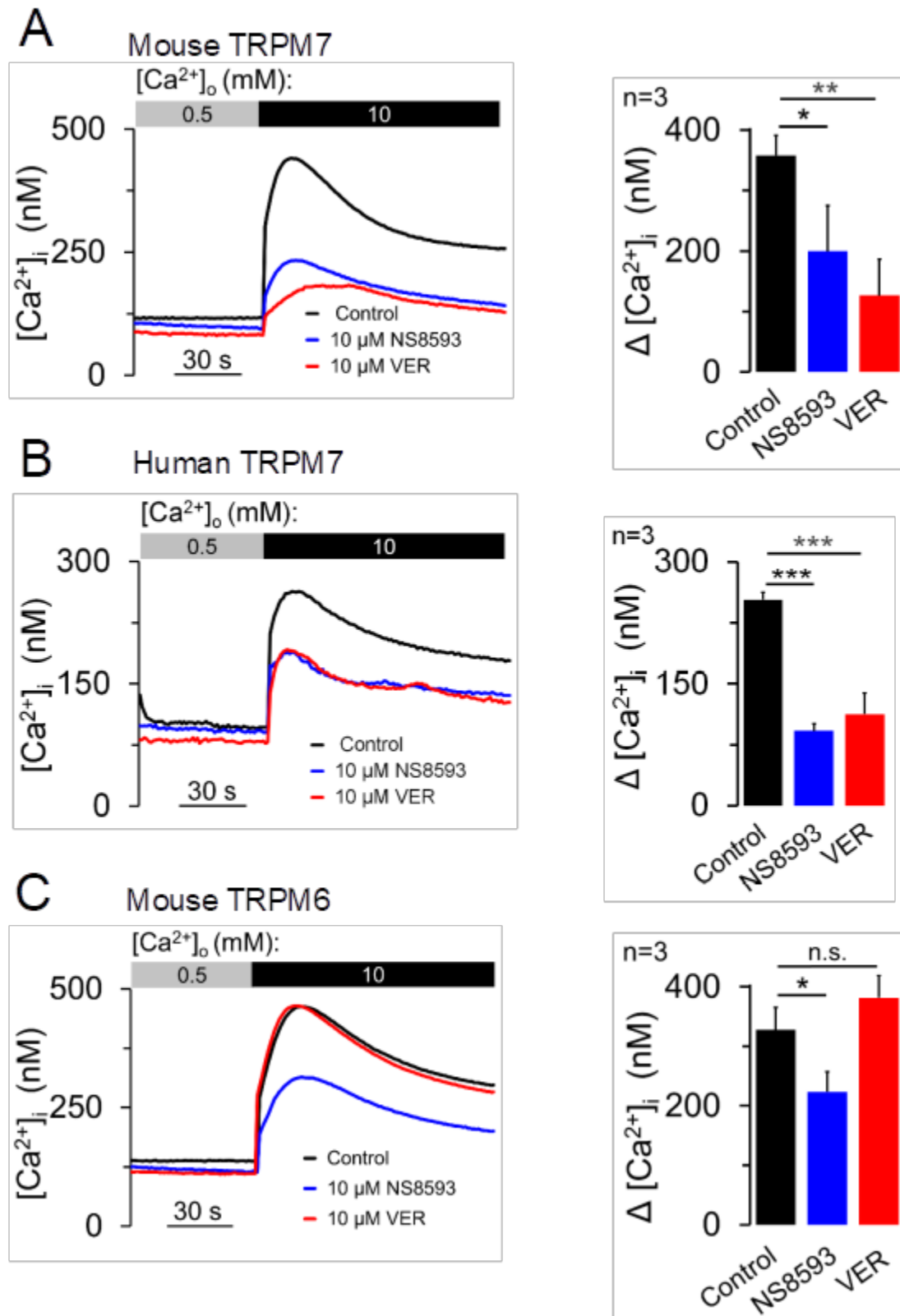
Suppl. Figure S2



Supplementary Figure S2. Assessment of NS8593, iloperidone (ILO) and ifenprodil (IFE) using a bioluminescence-based assay.

Intracellular Ca^{2+} levels ($[\text{Ca}^{2+}]_i$) were measured in HEK293T cells transfected with *Trpm6* (**A, C**) or *Trpm7* (**B, D**) plasmid DNA in the absence of modulators (Control) or in the presence of 10 μM NS8593, 10 μM iloperidone (ILO) and 10 μM ifenprodil (IFE), as indicated. *Left panels:* $[\text{Ca}^{2+}]_i$ was measured in the presence of 0.5 or 10 mM external Ca^{2+} ($[\text{Ca}^{2+}]_o$) as indicated by the horizontal bars. Representative traces are shown from 3 independent experiments with similar results. *Right panels:* Ca^{2+} rises ($\Delta[\text{Ca}^{2+}]_i$, mean \pm SEM, $n=3$) were calculated from measurements shown in the *Left panels* by subtraction of the resting $[\text{Ca}^{2+}]_i$ from the maximal $[\text{Ca}^{2+}]_i$ after application of 10 mM $[\text{Ca}^{2+}]_o$. n , number of independent measurements. * $P < 0.05$; *** $P < 0.001$ (two-tailed t test); n.s., not significant.

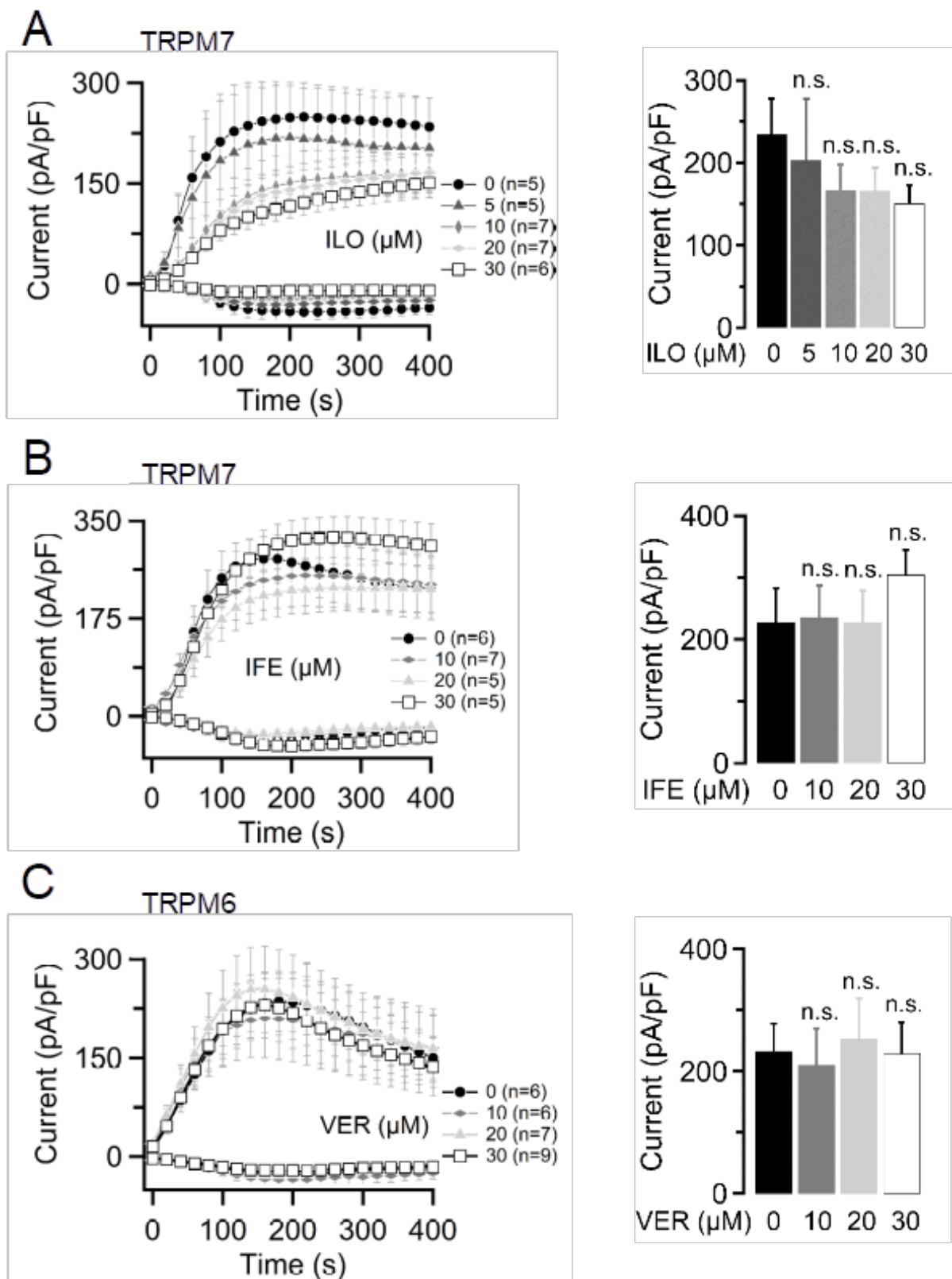
Suppl. Figure S3



Supplementary Figure S3. Assessment of NS8593 and VER155008 using a bioluminescence-based assay.

[Ca²⁺]_i was measured in HEK293T cells transfected with mouse *Trpm7* (**A**) human *TRPM7* (**B**) or mouse *Trpm6* (**C**) cDNA plasmids in the absence of modulators (Control) or in the presence of 10 μM NS8593 or 10 μM VER155008 (VER). *Left panels*: [Ca²⁺]_i was measured in the presence of 0.5 or 10 mM external Ca²⁺ ([Ca²⁺]_o) as indicated by the horizontal bars. Representative traces are shown from 3 independent experiments with similar results. *Right panels*: Ca²⁺ rises (Δ[Ca²⁺]_i, mean ± SEM, n=3) were calculated from measurements shown in the *Left panels* by subtraction of the resting [Ca²⁺]_i from the maximal [Ca²⁺]_i after application of 10 mM [Ca²⁺]_o. n, number of independent measurements; * P < 0.05; ** P < 0.01; *** P < 0.001 (two-tailed t test); n.s., not significant.

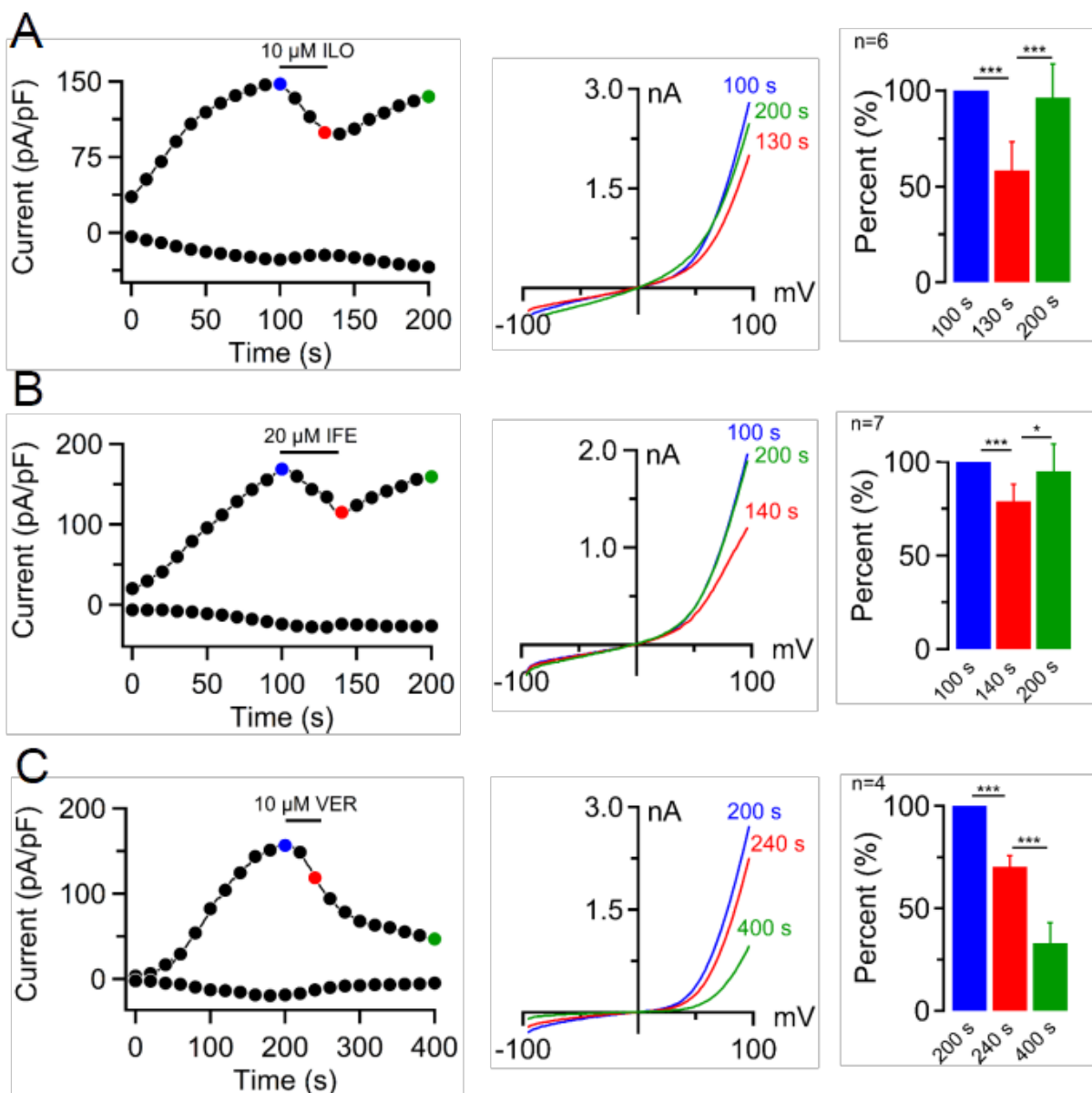
Suppl. Figure S4



Supplementary Figure S4. The effects of iloperidone, ifenprodil and VER155008 on TRPM6 and TRPM7 currents.

Whole-cell currents were measured in *Trpm7*-transfected HEK293T cells exposed to 10 μ M iloperidone (**A**) or 10 μ M ifenprodil (**B**) and in *Trpm6*-transfected HEK293T cells treated with 10 μ M VER155008 (**C**). *Left panels*: Current amplitudes (mean \pm SEM) were measured at -80 and +80 mV and plotted over time. The cells were exposed to the external solutions containing the indicated concentrations of compounds before the recording of whole-cell currents. *Right panels*: Bar graphs of outward currents (+80 mV, mean \pm SEM) obtained at 200 s in the corresponding *Left panels*. n, number of independent measurements; n.s., not significant (ANOVA).

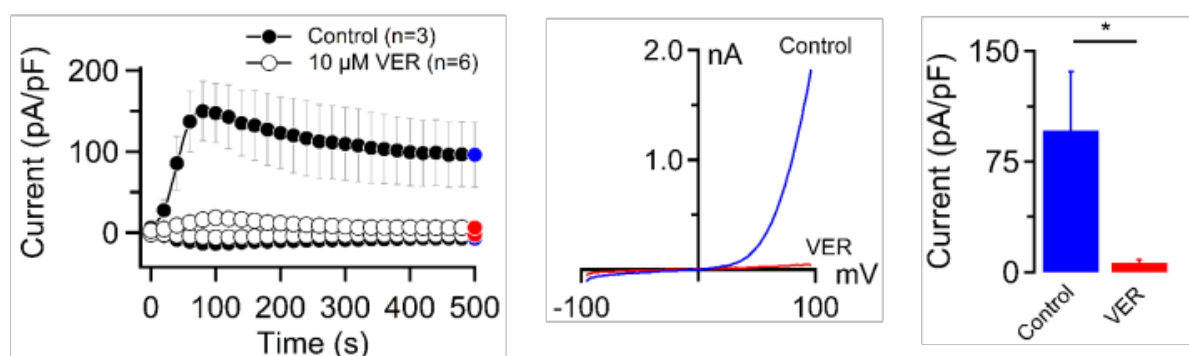
Suppl. Figure S5



Supplementary Figure S5. The ability of TRPM6 and TRPM7 currents to recover after transient application of iloperidone, ifenprodil and VER155008.

(A, B) Whole-cell currents were measured in *Trpm6*-transfected HEK293T cells exposed to iloperidone **(A)** and ifenprodil **(B)**. *Left panel:* Representative current amplitudes were measured in HEK293T cells at -80 and +80 mV and plotted over time. When currents were developed, cells were transiently exposed to 10 μ M iloperidone (ILO) or 20 μ M ifenprodil (IFE), as indicated by the horizontal bar. *Middle panel:* Representative current-voltage relationships obtained from individual ramps before (blue), during (red) and after (green) application of the compounds as indicated in the *Left panel*. *Right panel:* Bar graphs of outward currents (+80 mV, mean \pm SEM) obtained from before (blue), during (red) and after (green) exposure of the cells as indicated in the *Left panel*. **(C)** Experiments were performed and analysed similarly to (A), except that *Trpm7*-transfected HEK293T cells were treated with 10 μ M VER155008 (VER). n, number of cells measured; * $P < 0.05$, ** $P < 0.01$; *** $P < 0.001$; n.s., not significant (two-tailed t test).

Suppl. Figure S6

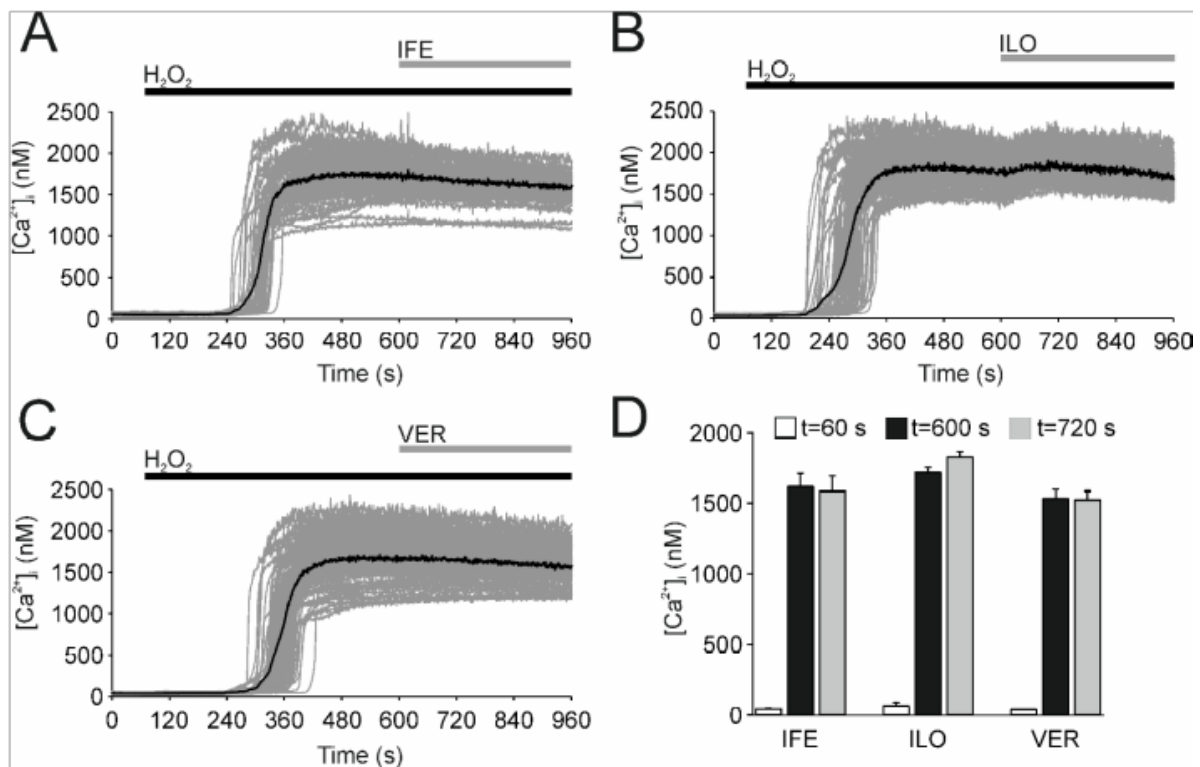


Supplementary Figure S6. The inhibitory effects of VER155008 on the kinase-dead K1646R mutant variant of TRPM7.

Whole-cell currents were measured in HEK293T cells transfected with the K1646R mutant variant of TRPM7. *Left panel:* Current amplitudes (mean \pm SEM) were

acquired at -80 and +80 mV and plotted over time. The cells were exposed to an external solution without (Control) or with 10 μ M VER155008 (VER). *Middle panel:* Representative current-voltage relationships obtained from individual ramps at 500 s as indicated by coloured data points in the *Left panel*. *Right panel:* Bar graphs of outward currents (+80 mV, mean \pm SEM) obtained from untreated (blue) and VER155008-treated cells (red) as indicated in the *Left panel*. n, number of cells measured; * $P < 0.05$ (two-tailed t test).

Suppl. Figure S7

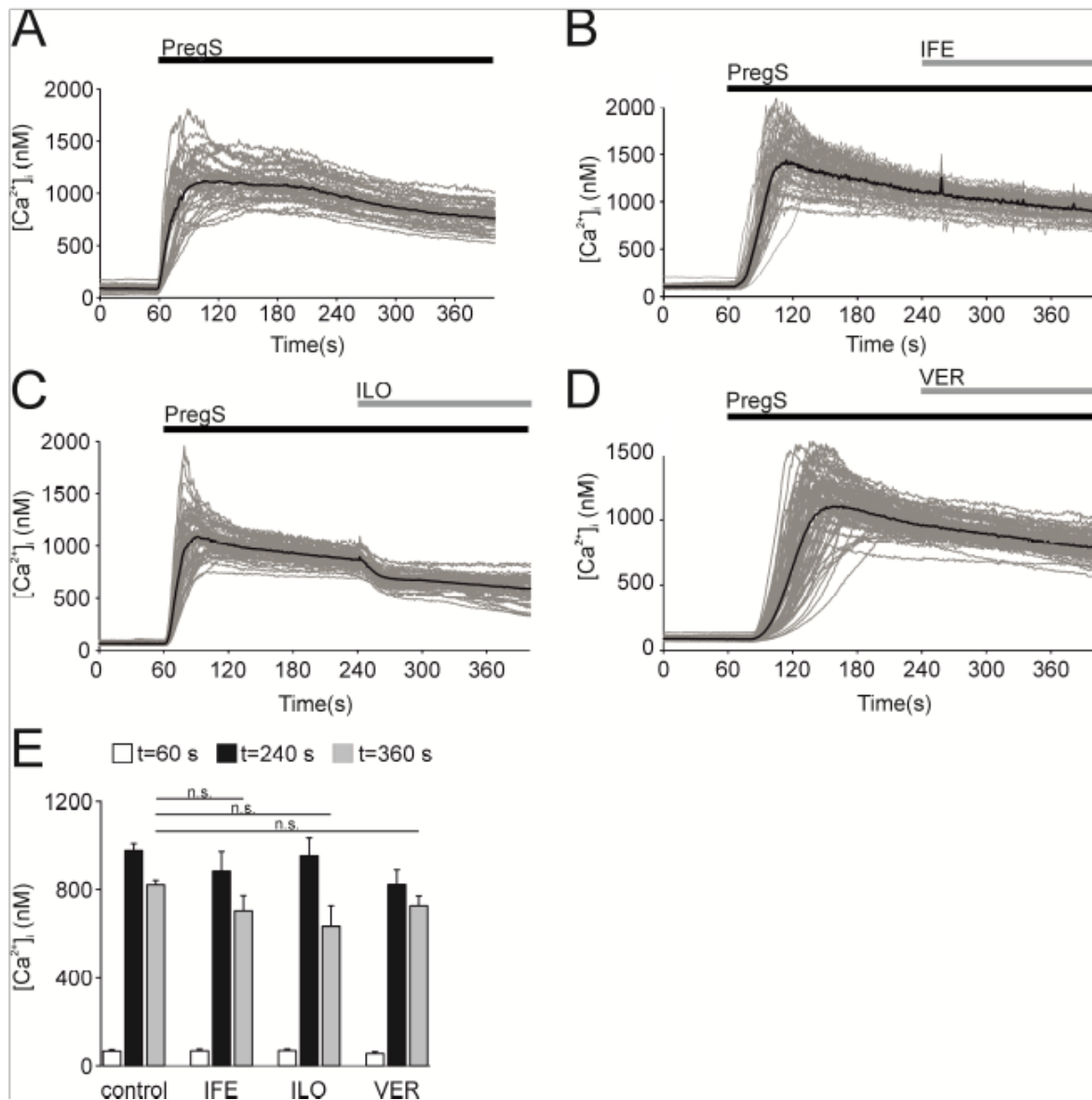


Supplementary Figure S7. Effects of ifenprodil, iloperidone and VER155008 on the TRPM2 channel.

(A-C) Time course of exemplary microfluorometric single-cell $[Ca^{2+}]_i$ assays using fura-2-loaded HEK293_{TRPM2} cells stimulated with 1 mM H_2O_2 and subsequent addition of 10 μ M ifenprodil (IFE) **(A)**, 10 μ M iloperidone (ILO) **(B)** or 10 μ M VER155008 (VER) **(C)** as indicated by the horizontal bars. **(D)** Statistical analysis of 4-6 independent experiments, as in (A-C). $[Ca^{2+}]_i$ (mean + SEM) was determined at

60 s (open bar), 600 s (black bar), and 720 s (gray bar). Gray lines depict Ca^{2+} responses of individual cells; black lines depict mean Ca^{2+} responses.

Suppl. Figure S8

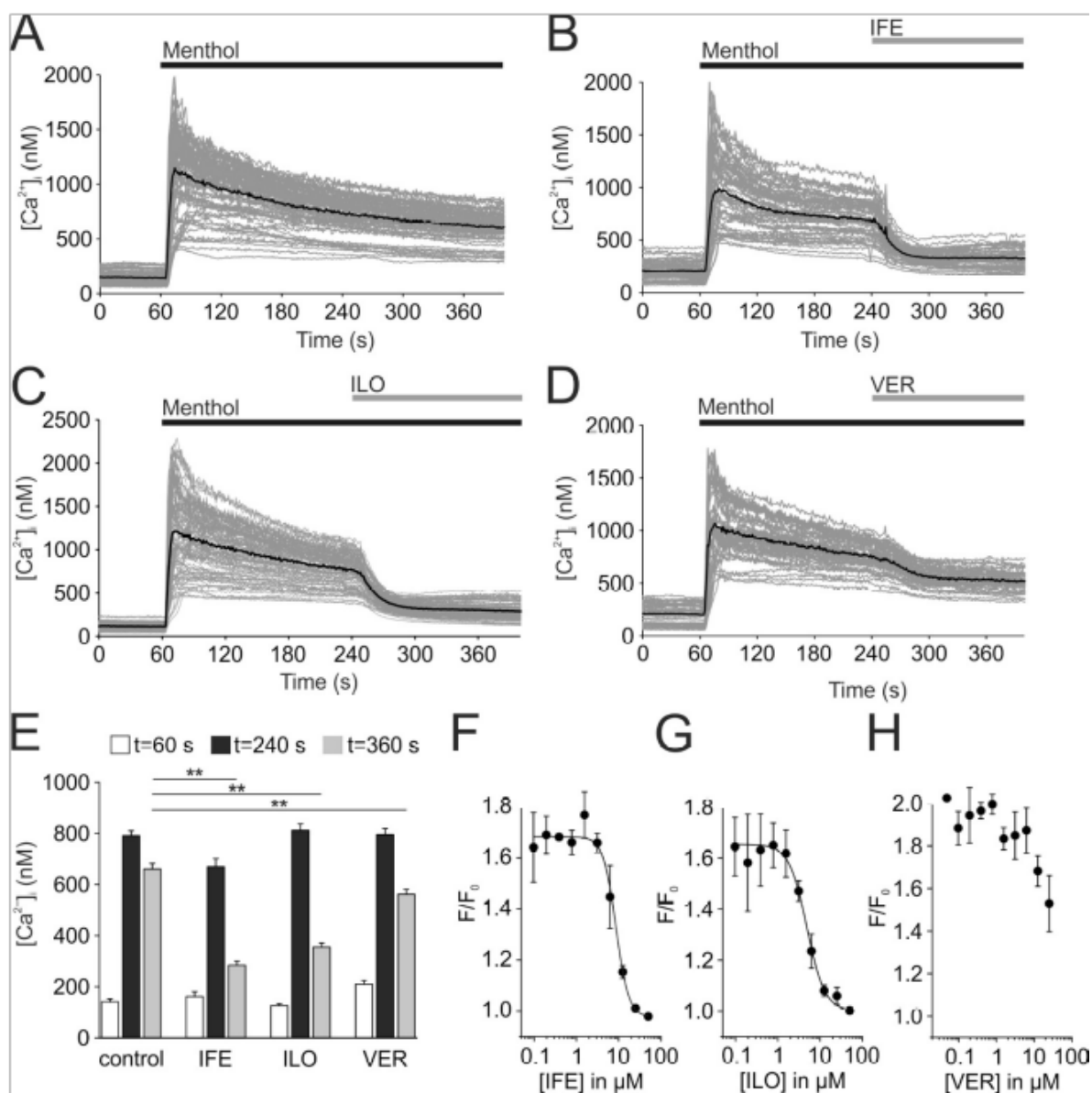


Supplementary Figure S8. Effects of ifenprodil, iloperidone and VER155008 on the TRPM3 channel.

Time course of exemplary microfluorometric single-cell $[\text{Ca}^{2+}]_i$ assays using fura-2-loaded HEK293_{TRPM3} cells stimulated with 35 μM pregnenolone sulfate (PregS) alone (Control) (A) or the subsequent addition of 35 μM pregnenolone with 10 μM ifenprodil (IFE) (B), 10 μM iloperidone (ILO) (C) and 10 μM VER155008 (VER) (D), as

indicated by the horizontal bars. **(E)** Statistical analysis of 4-6 independent experiments, as in (A-D). $[Ca^{2+}]_i$ (mean + SEM) was determined at 60 s (open bar), 240 s (black bar), and 360 s (gray bar). n.s., not significant (Mann–Whitney-Test).

Suppl. Figure S9

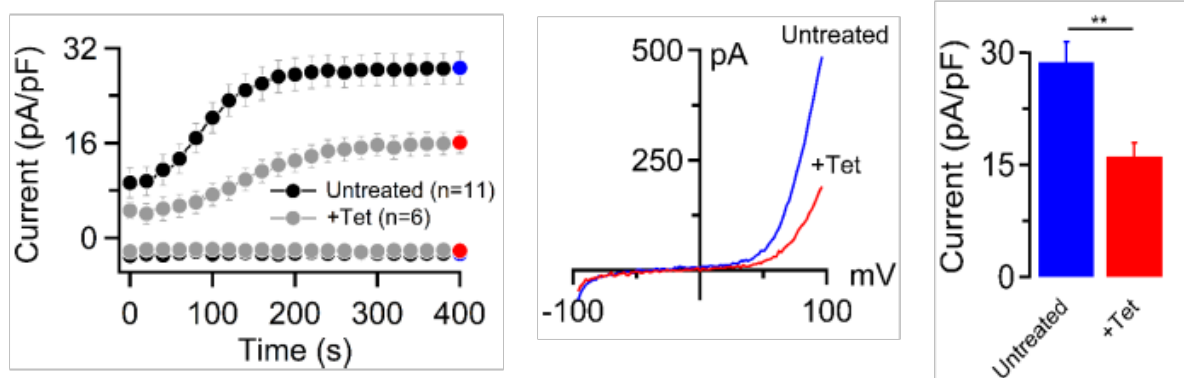


Supplementary Figure S9. Effects of ifenprodil, iloperidone and VER155008 on TRPM8 channels.

(A-D) Time course of exemplary microfluorometric single-cell $[Ca^{2+}]_i$ assays using fura-2-loaded HEK293_{TRPM8-YFP} cells stimulated with 1 mM menthol alone (Control)

(A) or subsequent addition of 1 mM menthol with 10 μ M ifenprodil (B), 10 μ M iloperidone (C) and 10 μ M VER155008 (D), as indicated by the horizontal bars. (E) Statistical analysis of 4-6 independent experiments, as in (A-D). $[Ca^{2+}]_i$ (mean + SEM) was determined at 60 s (open bar), 240 s (black bar), and 360 s (gray bar). ** $P < 0.01$ (one-way ANOVA with Bonferroni post hoc test, homogeneity of variance was confirmed with Levene's test). (F-H) Concentration-response analysis of ifenprodil (F; $IC_{50} = 8.2 \pm 1.9 \mu M$, $h = 2.5 \pm 0.3$), iloperidone (G; $IC_{50} = 6.1 \pm 2.3 \mu M$, $h = 2.9 \pm 0.8$), and VER155008 (H) inhibition of TRPM8. Cell suspensions were loaded with fluo-4 and assayed in a fluorescence image plate reader. Menthol (400 μM) was added after the application of serially diluted compounds. Data represent the mean \pm SD of 3 independent experiments, each carried out in quadruplicates. Concentration-response curves were generated by fitting the data to a four-parameter Hill equation to obtain IC_{50} and the Hill coefficient h .

Suppl. Figure S10



Supplementary Figure S10. Endogenous currents measured in human SHEP-21N cells.

Whole-cell currents were measured in untreated (A) and tetracycline-treated (100 ng/ml for 7 days) (B) SHEP-21N cells. (A) *Left panel:* Current amplitudes (mean \pm SEM) were measured at -80 and +80 mV and plotted over time. *Middle panel:* Representative current-voltage relationships obtained from individual ramps at 400 s

as indicated in the *Left panel*. *Right panel*: Bar graphs of outward currents (+80 mV, mean \pm SEM) obtained at 400 s as indicated in the *Left and Middle* panels. n, number of cells measured; ** $P < 0.01$ (two-tailed t test).

7. Publication II

Title: Structural mechanism of TRPM7 channel regulation by intracellular magnesium

<https://link.springer.com/article/10.1007/s00018-022-04192-7>

<https://doi.org/10.1007/s00018-022-04192-7>



Structural mechanism of TRPM7 channel regulation by intracellular magnesium

Eva Schmidt¹ · Chamali Narangoda² · Wolfgang Nörenberg³ · Miyuki Egawa¹ · Anna Rössig¹ · Marion Leonhardt³ · Michael Schaefer³ · Susanna Zierler^{1,4} · Maria G. Kurnikova² · Thomas Gudermann^{1,5} · Vladimir Chubakov¹

Received: 22 October 2021 / Revised: 26 January 2022 / Accepted: 2 February 2022 / Published online: 7 April 2022
© The Author(s) 2022

Abstract

Zn^{2+} , Mg^{2+} and Ca^{2+} are essential divalent cations implicated in many metabolic processes and signalling pathways. An emerging new paradigm is that the organismal balance of these cations predominantly depends on a common gatekeeper, the channel-kinase TRPM7. Despite extensive electrophysiological studies and recent cryo-EM analysis, an open question is how the channel activity of TRPM7 is activated. Here, we performed site-directed mutagenesis of mouse TRPM7 in conjunction with patch-clamp assessment of whole-cell and single-channel activity and molecular dynamics (MD) simulations to show that the side chains of conserved N1097 form an inter-subunit Mg^{2+} regulatory site located in the lower channel gate of TRPM7. Our results suggest that intracellular Mg^{2+} binds to this site and stabilizes the TRPM7 channel in the closed state, whereas the removal of Mg^{2+} favours the opening of TRPM7. Hence, our study identifies the structural underpinnings through which the TRPM7 channel is controlled by cytosolic Mg^{2+} , representing a new structure–function relationship not yet explored among TRPM channels.

Keywords TRPM7 · TRP channels · Magnesium · PIP_2 · ATP · Molecular dynamics simulations

Introduction

The transient receptor potential cation channel, subfamily M, member 7 (TRPM7) encodes a bi-functional protein comprising a transmembrane channel segment fused to a serine/

threonine-protein kinase domain [1–3]. The TRPM7 channel is highly permeable to divalent cations, including Zn^{2+} , Ca^{2+} , and Mg^{2+} , and there is mounting evidence to suggest that the influx of all three cations underlies the indispensable physiological role of TRPM7 [4–8]. Thus, TRPM7 controls a wide range of biological processes such as organismal Zn^{2+} , Ca^{2+} and Mg^{2+} homeostasis, embryonic development, immune responses, cell motility, proliferation and differentiation [1–3].

TRPM7 currents were discovered in patch-clamp experiments with immune cells after removing Mg^{2+} from pipette solutions [9–11]. In contrast, the addition of free Mg^{2+} and $\text{Mg}\cdot\text{ATP}$ prevented the opening of the TRPM7 channel through different mechanisms [11–13]. Moreover, free Mg^{2+} and $\text{Mg}\cdot\text{ATP}$ inhibit TRPM7 synergistically, since elevation of free Mg^{2+} concentrations increases the potency of $\text{Mg}\cdot\text{ATP}$ [13]. TRPM7 currents were thus termed magnesium-nucleotide-regulated metal ion currents (MagNum) and magnesium-inhibited cation currents (MIC) [11, 12]. In the past two decades, this experimental paradigm was commonly used to identify TRPM7 currents in a wide variety of primary isolated cells and stable cell lines [1–3]. The current consensus is that both Mg^{2+} and $\text{Mg}\cdot\text{ATP}$ act as negative

Maria G. Kurnikova: corresponding author for theoretical analysis.

✉ Thomas Gudermann
thomas.gudermann@lrz.uni-muenchen.de

✉ Vladimir Chubakov
vladimir.chubakov@lrz.uni-muenchen.de

¹ Walther-Straub Institute of Pharmacology and Toxicology, LMU Munich, Munich, Germany

² Chemistry Department, Carnegie Mellon University, Pittsburgh, PA, USA

³ Rudolf-Boehm Institute of Pharmacology and Toxicology, Leipzig University, Leipzig, Germany

⁴ Institute of Pharmacology, Johannes Kepler University Linz, Linz, Austria

⁵ Comprehensive Pneumology Center, a member of the German Center for Lung Research (DZL), Munich, Germany

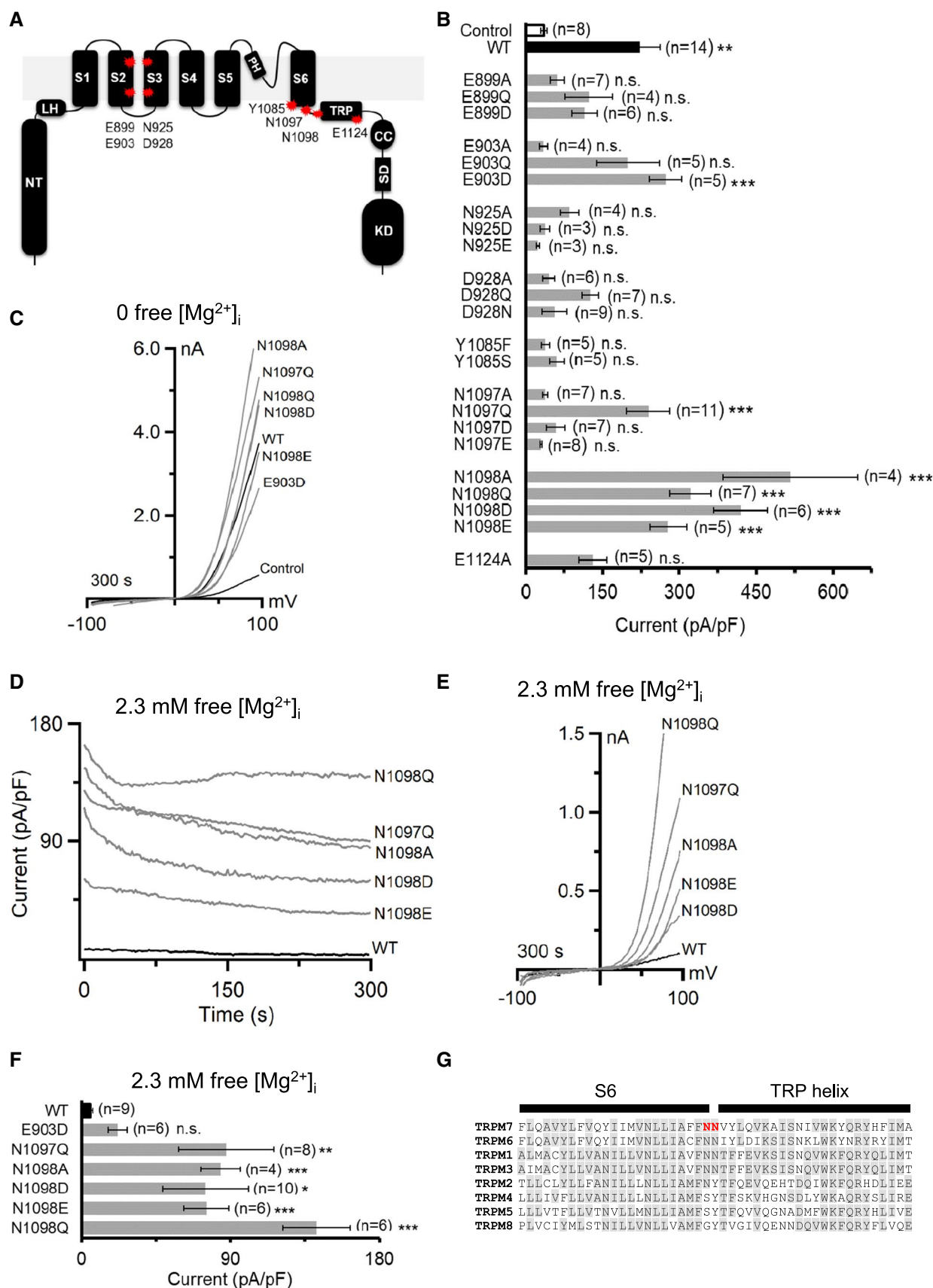


Fig. 1 Assessment of the mouse TRPM7 variants expressed in HEK293T cells. **A** Domain topology of TRPM7. A large N-terminus (NT) of TRPM7 is linked to a pre-S1 helix also known as a linker-helical domain (LH) preceding a channel segment comprising six transmembrane helices (S1–S6) with a short pore loop and a pore helix (PH) located between S5 and S6. The C-terminus of TRPM7 contains a receptor potential domain (TRP) followed by a coiled-coil (CC), kinase substrate (SD) and kinase (KD) domains. Red stars indicate the position of residues in the mouse TRPM7 protein subjected to site-directed mutagenesis in the present study. **B** Whole-cell currents measured in untransfected HEK293T cells (Control, white) and the cells transfected by wild type (WT, black) or indicated mutant variants (grey) of TRPM7-YFP cDNAs. Currents were induced using the standard $[Mg^{2+}]_i$ -free intracellular solution and the standard external solution. Current amplitudes (mean \pm SEM) were acquired at +80 mV (at 300 s). *n*, number of cells measured; n.s., not significant; * $P < 0.05$ ** $P < 0.01$; *** $P < 0.001$ (ANOVA, compared to Control). **C** Representative I–V relationships of currents shown in **B**. **D–F** A subset of TRPM7-YFP variants shown in **B** were examined using an intracellular solution containing 2.3 mM $[Mg^{2+}]_i$ (Suppl. Table S1). **D** Whole-cell currents measured in WT and indicated mutant variants of TRPM7-YFP. Current amplitudes (mean \pm SEM) were acquired at –80 and +80 mV and plotted over time. **E** Representative I–V relationships of currents (at 300 s) illustrated in **D**. **F** Bar graphs of outward currents (mean \pm SEM; +80 mV) shown in **D** at 300 s. *n*, number of cells measured; n.s., not significant; * $P < 0.05$ ** $P < 0.01$; *** $P < 0.001$ (ANOVA, compared to WT). **G** Multiple sequence alignment (ClustalW) of amino acid sequences encoding the S6 and TRP segments in the mouse TRPM1–8 proteins. Grey background indicates the sequence consensus. N1097 and N1098 of TRPM7 are indicated in red

regulators of the ubiquitously expressed TRPM7 channel to correlate the uptake of essential metals with the metabolic state of the cell [1–3].

The molecular mechanism determining TRPM7 sensitivity to intracellular Mg^{2+} remains unclear. Previously, several research groups examined the role of the C-terminal kinase domain with regard to TRPM7 channel sensitivity to Mg^{2+} and obtained controversial results. Thus, deletion of the kinase domain resulted in either non-functional versions of the channel [14], channel variants with unchanged [15] or even increased sensitivity to free Mg^{2+} [5, 15, 16]. In other studies, the introduction of ‘kinase-dead’ point mutations (D1775A and K1648R) in the catalytic site of the kinase moiety or deletion of phosphorylation residues (S1511 and S1567) did not affect the responses of the channel to free Mg^{2+} [14, 17, 18]. However, other researchers observed that TRPM7 with ‘kinase-dead’ mutations (K1648R and G1799D) exhibited reduced responses to free Mg^{2+} [5, 13], whereas the T1482L mutation affecting a putative phosphorylation site in TRPM7 increased Mg^{2+} sensitivity of the channel [19]. While the reason for such inconsistencies remains unclear, the overall consensus is that functional TRPM7 channel variants with impaired kinase moiety retain the sensitivity to intracellular free Mg^{2+} , arguing that an additional Mg^{2+} regulatory domain must exist.

Other studies suggested that Mg^{2+} affects the TRPM7 channel indirectly, for instance, by interfering with the interaction of phosphatidylinositol 4,5-bisphosphate (PIP_2) and TRPM7, but the structural basis of such interference remains unknown [20–22]. More recently, high-resolution structures of a closed TRPM7 channel were resolved by cryo-electron microscopy (cryo-EM) [23]. However, structural rearrangements associated with the Mg^{2+} - and PIP_2 -dependent opening of the TRPM7 channel were not identified in the structures available [23].

Here, we embark on extensive functional analysis, structural modelling and molecular dynamics simulations and propose that a pivotal Mg^{2+} regulatory site of TRPM7 is located within the lower channel gate. Our findings suggest that Mg^{2+} interacts directly with this protein segment and stabilizes TRPM7 in the closed state. In line with this model, we found that a point mutation introduced in the Mg^{2+} regulatory site abolishes the sensitivity of TRPM7 to physiological concentrations of intracellular Mg^{2+} .

Results

Search for amino acid residues involved in the Mg^{2+} -induced inhibition of TRPM7

Recently, several structures of TRPM channels were determined using cryo-EM [24–33]. The investigators noted that TRPM2, TRPM4, TRPM5 and TRPM8 harbour intra-subunit Ca^{2+} -binding sites formed by five negatively charged and polar residues in the S2 and S3 helices and the TRP segment (Suppl. Fig. S1) [24–33]. Interestingly, some of these residues are substituted in TRPM1, TRPM3, TRPM6 and TRPM7 (Suppl. Fig. S1), suggesting that the latter group of channels may contain a binding pocket for another ligand, for instance, Mg^{2+} . To test this hypothesis functionally, we exchanged E899, E903, N925, D928 and E1124 of TRPM7 to an uncharged alanine residue (A) or two structurally related acidic (D or E) and two polar residues (Q or N) (Fig. 1A).

In the pore domain formed by the S5 and S6 helices, the polar side chains of N1097 and N1098 appear to arrange the narrowest constriction in the lower gate of TRPM7 [23]. Since asparagine side chains frequently contribute to Mg^{2+} -binding sites in other channels [34, 35], we hypothesized that N1097 and N1098 could function as an Mg^{2+} recognition site in TRPM7. Accordingly, we produced versions of TRPM7 with modified amino acids at positions N1097 and N1098 (Fig. 1A). Finally, we introduced changes in Y1085 (Fig. 1A) since its side chain hydroxyl group is located in the upper channel gate and may potentially interact with Mg^{2+} [23]. Because of the exceptionally low efficiency of in vitro site-directed mutagenesis of untagged

mouse TRPM7 cDNA in the bicistronic pIRES2-EGFP vector, the functional impact of the introduced mutations was investigated using mouse TRPM7 with a C-terminal YFP tag in the pcDNA3.1 vector (see further details in “[Materials and methods](#)”).

First, we studied whether the TRPM7 mutants can be activated in the absence of cytosolic Mg^{2+} , assuming that mutations with a specific impact on Mg^{2+} -dependent inhibition of the channel should not significantly affect current amplitudes and current–voltage (I–V) relationships of TRPM7 in such an experimental setting. To this end, we transiently transfected HEK293T cells with cDNAs encoding wild-type (WT) and mutant versions of TRPM7-YFP and conducted patch-clamp experiments with YFP-positive cells. Whole-cell currents were elicited by a voltage ramp protocol ranging from -100 to $+100$ mV and a standard Mg^{2+} -free internal solution (Fig. 1B, C). I–V relationships of WT currents exhibited characteristic features, such as tiny inward and large outward currents with a pronounced rectification and a reversal potential of about 0 mV (Fig. 1C). Accordingly, outward currents of TRPM7 variants were used to reliably quantify the effects of the mutations (Fig. 1B). Only six mutant variants (E903D, N1097Q, N1098A, N1098Q, N1098D and N1098E) displayed currents significantly different from endogenous currents in untransfected cells (Fig. 1B). In addition, I–V relationships of these mutant channels resembled those of WT currents (Fig. 1C). Consequently, only the latter six TRPM7 variants were selected for further analysis.

Next, we examined the channel activity of WT and mutant TRPM7 variants in the presence of relatively high levels of intracellular Mg^{2+} . As expected, the addition of free 2.3 mM $[Mg^{2+}]_i$ to the internal solution completely prevented the development of WT currents (Fig. 1D, F). Five channel variants (N1097Q, N1098A, N1098Q, N1098D and N1098E) displayed currents already after break-in, which were modestly reduced over time and exhibited typical I–V characteristics (Fig. 1F, D). In contrast, the E903D variant showed low activity under these experimental conditions (Fig. 1F). Hence, unlike other mutations, exchanges of asparagine residues located in the S6 segment and the TRP helix (Fig. 1G) resulted in active TRPM7 channels in the presence of $[Mg^{2+}]_i$. Consequently, we selected the N1097Q and N1098Q variants for a more detailed assessment.

Impact of N1097Q and N1098Q mutations on TRPM7 channel inhibition by Mg^{2+} and Ba^{2+}

To rule out a potential influence of the YFP tag on the functional analysis of TRPM7, we re-introduced the N1097Q and N1098Q amino acid exchanges into mouse TRPM7 cDNA

inserted into the bicistronic pIRES2-EGFP vector [36, 37]. Immunofluorescent staining of HEK293T cells expressing WT and mutant versions of TRPM7 did not reveal differences in the subcellular distribution of the proteins (Suppl. Fig. S2).

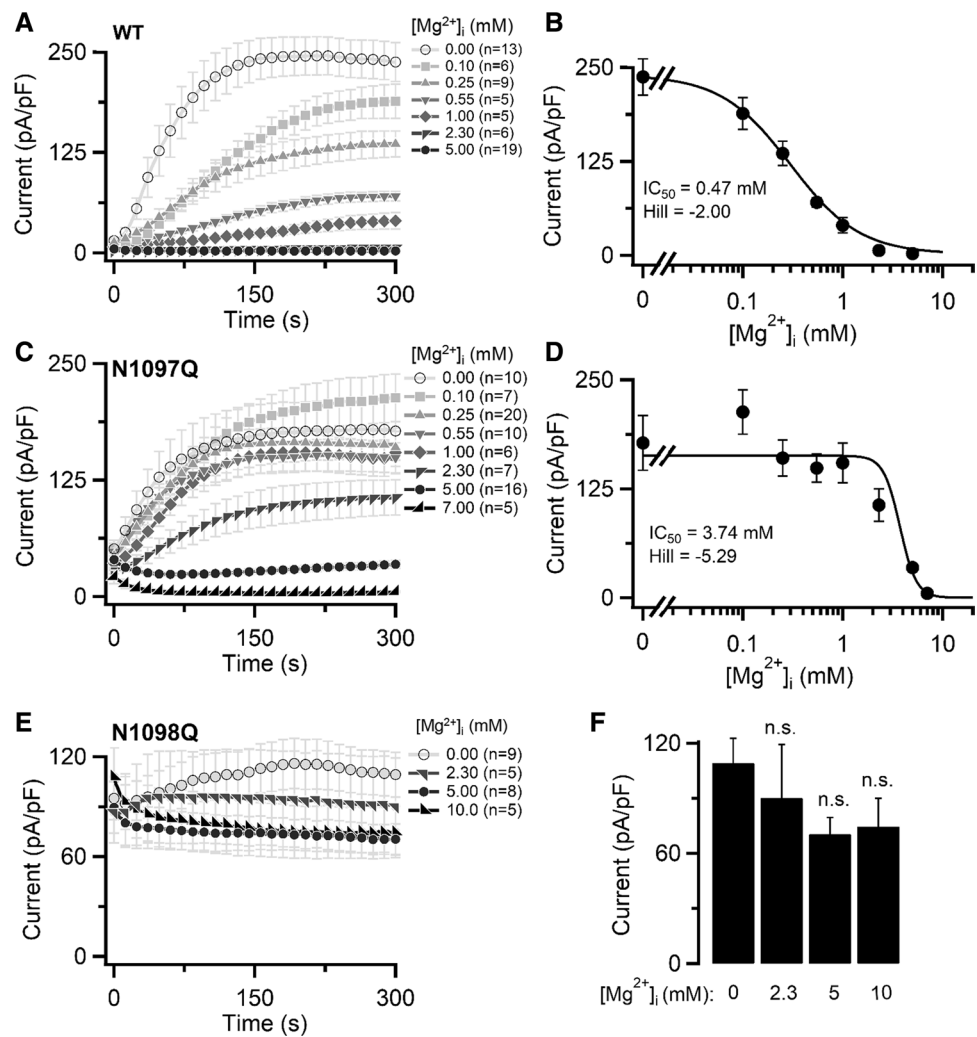
Next, we performed patch-clamp experiments to examine the impact of N1097Q and N1098Q on the concentration-dependent suppression of the channel by free $[Mg^{2+}]_i$ (Fig. 2). The calculated IC_{50} value for WT currents was 0.47 mM (Fig. 2A, B). Currents in cells expressing TRPM7 carrying the N1097Q mutation were inhibited by $[Mg^{2+}]_i$ with an IC_{50} value of 3.74 mM (Fig. 2C, D). As $[Mg^{2+}]_i$ varies between 0.5 and 1.0 mM in most mammalian cells [41], these results suggest that, unlike the WT channel, the N1097Q variant remains active in the presence of physiological concentrations of Mg^{2+} . Remarkably, TRPM7 containing N1098Q was highly active after break-in and remained active over time in the presence of the whole range of $[Mg^{2+}]_i$ examined, thus precluding a reliable calculation of an IC_{50} value (Fig. 2E, F). These results indicate that the N1098Q mutation results in a constitutively active channel insensitive to physiological concentrations of intracellular Mg^{2+} .

Apart from Mg^{2+} , other divalent cations (Ba^{2+} , Ca^{2+} and Zn^{2+}) can suppress TRPM7 currents presumably through a common regulatory site [38]. Hence, we examined whether the N1097Q and N1098Q mutants interfered with the effects of free $[Ba^{2+}]_i$ (0.55 and 1 mM) on the TRPM7 channel variants (Figure S3). We observed that the WT TRPM7 channel was inactive in the presence of both concentrations of free $[Ba^{2+}]_i$ (Suppl. Fig. S3A). The N1097Q variant showed significantly reduced currents only after administration of 1 mM free $[Ba^{2+}]_i$ (Suppl. Fig. S3B), whereas the N1098Q channel remained unaffected under both experimental conditions (Suppl. Fig. S3C).

Effects of N1097Q and N1098Q mutations on TRPM7 channel suppression by Mg-ATP and Mg-GTP

Previously, extensive electrophysiological analyses revealed that free Mg^{2+} and Mg-ATP inhibit TRPM7, most likely through different ligand binding sites [12, 13]. Interestingly, the elevation of free Mg^{2+} levels increased the potency of Mg-ATP, suggesting that Mg^{2+} and Mg-ATP act synergistically on the TRPM7 channel [12, 13]. Therefore, to further verify the role of N1097Q and N1098Q, we compared the concentration-dependent inhibition of the TRPM7 channel variants by intracellular concentrations of Mg-ATP $[Mg-ATP]_i$, in the presence of only 250 μ M free $[Mg^{2+}]_i$. The physiological intracellular concentrations of ATP vary between 2 and 9 mM in most mammalian cells [39]. In a physiological saline solution, the apparent K_d of Mg-ATP

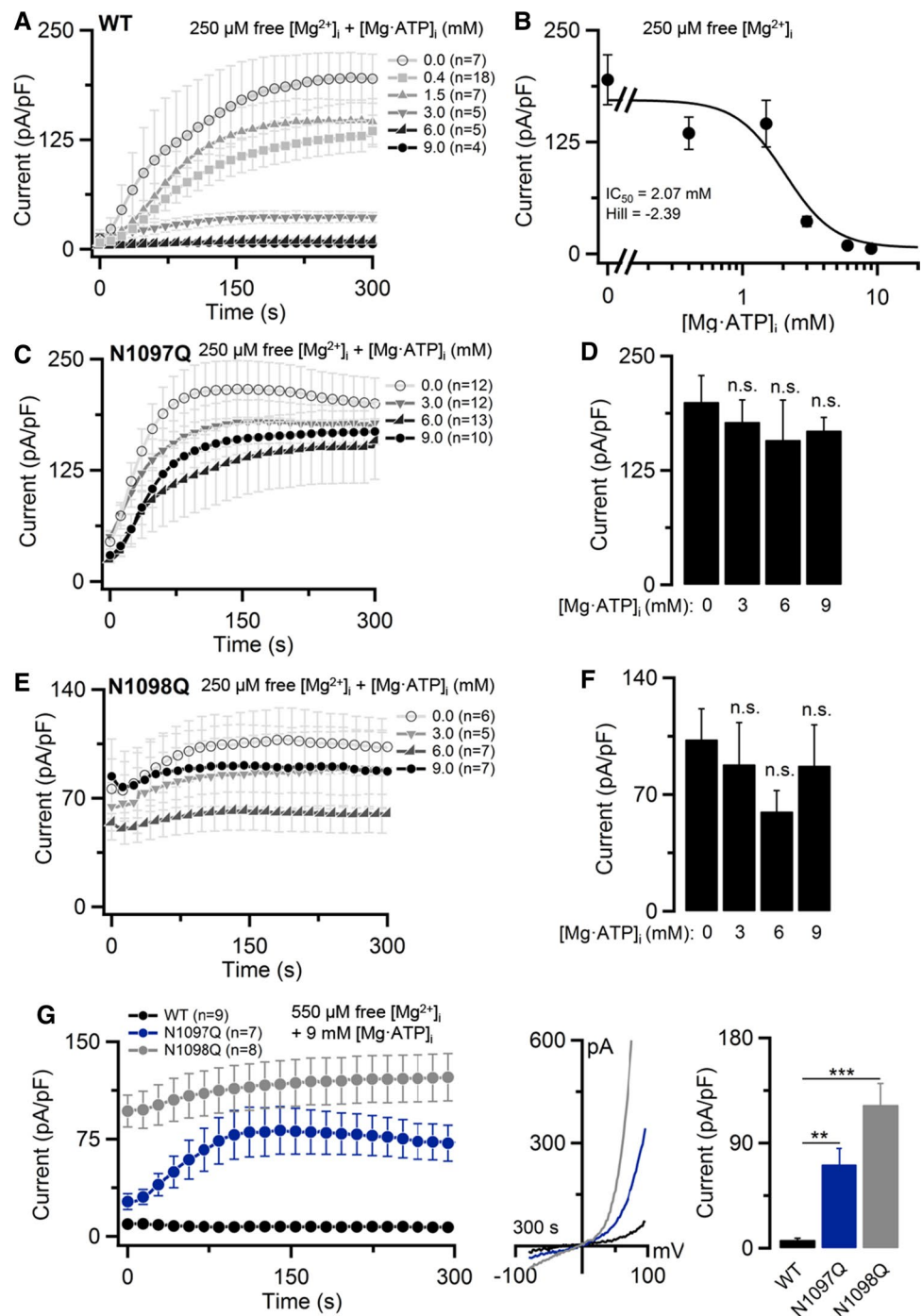
Fig. 2 Inhibition of TRPM7 currents by cytosolic Mg^{2+} . Whole-cell currents measured in HEK293T cells transfected by WT (A, B), N1097Q (C, D) and N1098Q (E, F) variants of TRPM7 cDNAs in pIRES2-EGFP expression vectors. A, C, E Current amplitudes (mean \pm SEM) were measured at +80 mV using internal solutions containing the indicated free $[Mg^{2+}]_i$ (Suppl. Table S1) and plotted over time. B, D Concentration-dependent suppression of currents (+80 mV, 300 s) shown in (A, B). The Hill equation was fitted to determine IC_{50} and the Hill factor. F Bar graphs of outward currents (mean \pm SEM; +80 mV) shown in (E) at 300 s. *n*, number of cells measured



is $\sim 50 \mu M$ [40] and it was estimated that $>90\%$ of cytosolic ATP is present as $Mg\cdot ATP$ [41]. Using internal solutions covering this range of $[Mg\cdot ATP]_i$, we found that WT currents were suppressed with an IC_{50} value of 2.07 mM (Fig. 3A, B). By contrast, TRPM7 mutants N1097Q and N1098Q were characterized by a remarkably low sensitivity to $[Mg\cdot ATP]_i$ at all concentrations examined (Fig. 3C–F). Due to experimental limitations, $[Mg\cdot ATP]_i$ above 10 mM could not be reliably examined. Since other Mg -nucleotides (like $Mg\cdot GTP$) were also capable of suppressing the TRPM7 channel, presumably through a mechanism shared with $Mg\cdot ATP$ [12, 13], we asked whether co-administration of 6 mM $[Mg\cdot GTP]_i$ and 250 μM free $[Mg^{2+}]_i$ will recapitulate the effects of 6 mM $[Mg\cdot ATP]_i$ co-applied with 250 μM free $[Mg^{2+}]_i$ (Suppl. Fig. S4). We observed that the impact of the N1097Q and N1098Q mutations on the channel's response to both Mg -nucleotides were not different in such experimental settings (Suppl. Fig. S4).

Next, we examined the effects of 9 mM $[Mg\cdot ATP]_i$ in the presence of the physiological range of $[Mg^{2+}]_i$ concentrations using an internal solution containing 550 μM and 1 mM free $[Mg^{2+}]_i$. We found that WT currents were entirely suppressed under these conditions (Fig. 3G, Suppl. Fig. S5). In contrast, N1097Q mutant TRPM7 channel currents developed in the presence of 550 μM free $[Mg^{2+}]_i$ (Fig. 3G), but were undetectable after application of 1 mM free $[Mg^{2+}]_i$ (Suppl. Fig. S5). These results suggest that the N1097Q channel variant remained sensitive to $Mg\cdot ATP$, but only in the presence of high concentrations of free Mg^{2+} , in accord with the idea that Mg^{2+} and $Mg\cdot ATP$ independently interact with different TRPM7 channel sites [12, 13], and that the N1097Q mutation primarily affected the Mg^{2+} regulatory mechanism. The N1098Q variant was not suppressed in all experimental settings (Fig. 3E, Suppl. Fig. S5), indicating that the N1098Q mutation engendered a constitutively active channel variant.

Fig. 3 Inhibition of TRPM7 currents by cytosolic Mg·ATP. Whole-cell currents measured in HEK293T cells transfected by WT, N1097Q and N1098Q variants of TRPM7 cDNAs (in pIRES2-EGFP). **A, B** Concentration-dependent suppression of WT TRPM7 by $[Mg\cdot ATP]_i$ in the presence of 250 μM free $[Mg^{2+}]_i$ (Suppl. Table S3). **A** Current amplitudes of the WT channel (mean \pm SEM) measured at +80 mV were plotted over time. **B** Concentration–response curve for currents shown in **A** (+80 mV, 300 s). The Hill equation was used to determine IC_{50} and the Hill factor. **C–F** Effects of $[Mg\cdot ATP]_i$ on the N1097Q (**C, D**) and N1098Q (**E, F**) variants of TRPM7. Measurements were performed as in **A**. However, bar graphs of outward currents (mean \pm SEM; +80 mV) at 300 s were used to analyse the effects of $[Mg\cdot ATP]_i$. **G** Whole-cell currents were measured in the presence of 9 mM $[Mg\cdot ATP]_i$ and 550 μM free $[Mg^{2+}]_i$ (Suppl. Table S4). *Left panel* current amplitudes (mean \pm SEM) acquired at +80 mV were plotted over time. *Middle panel* representative current–voltage (I–V) relationships of currents (at 300 s) illustrated in the *left panel*. *Right panel* bar graphs of outward currents (mean \pm SEM; +80 mV) shown in the *left panel* at 300 s. n, number of cells measured; ns, not significant; ** $P < 0.01$, *** $P < 0.001$ (ANOVA)



Finally, we aimed to assess the activity of TRPM7 variants without manipulations of the cytosolic contents of Mg^{2+} and $Mg\cdot ATP$ using perforated patch recordings (Suppl. Fig. S6). Consistent with earlier studies [21],

WT currents did not develop in this experimental setting, presumably because resting concentrations of Mg^{2+} and $Mg\cdot ATP$ are sufficient to inhibit TRPM7. On the contrary, channel activity of the N1097Q or N1098Q variants was well detectable (Suppl. Fig. S6), supporting the notion that the N1097Q or N1098Q mutations diminish the inhibitory

effects of both Mg^{2+} and $Mg\cdot ATP$ in resting HEK293T cells.

Effects of N1097Q and N1098Q on the sensitivity of TRPM7 to pharmacological agents and PIP_2 depletion

To determine whether the N1097Q or N1098Q amino acid exchanges altered the sensitivity of TRPM7 exclusively to $[Mg^{2+}]_i$ and $[Mg\cdot ATP]_i$ or caused more general changes of regulatory characteristics of the channel, we studied the effects of small synthetic molecules acting as activators or inhibitors of the TRPM7 channel. First, we assessed the action of naltriben, a potent agonist of the TRPM7 channel [42]. In these experiments, we used intracellular solutions containing 9 mM $[Mg\cdot ATP]_i$ and 550 μM free $[Mg^{2+}]_i$. The external application of naltriben led to a fast stimulation of WT and N1097Q currents (Fig. 4A, B). The N1098Q variant did not respond to naltriben (Fig. 4C).

Next, we examined the effect of NS8593, a potent TRPM7 inhibitor [43]. In these experiments, we induced currents

using the standard $[Mg^{2+}]_i$ -free intracellular pipette solution and externally applied NS8593 when currents were fully developed (Fig. 5). We noted that NS8593 caused a rapid inhibition of WT and N1097Q currents (Fig. 5A, B). In analogy to the effects of naltriben (Fig. 4A), the N1098Q mutation abolished the channel's sensitivity to NS8593 (Fig. 5C), indicating that the N1098Q mutant is functionally different from the N1097Q variant with regard to its sensitivity to natural or synthetic ligands.

It is well documented that depletion of plasma membrane PIP_2 results in the inactivation of the TRPM7 channel [20–22]. Therefore, we investigated the response of the TRPM7 variants to such a treatment using a voltage-sensitive phosphatase from *Ciona intestinalis* (Ci-VSP) [44]. Ci-VSP reduces PIP_2 levels in the plasma membranes at positive membrane potentials (Fig. 6A). A catalytically silent mutant of Ci-VSP (Ci-VSP-C363S) cannot hydrolyse PIP_2 and was used as a control (Fig. 6A). Cells co-expressing Ci-VSP or Ci-VSP-C363S together with TRPM7 variants were held at -60 mV to allow induction of TRPM7 currents without activation of Ci-VSP. Then the regular voltage ramp ranging

Fig. 4 Activation of TRPM7 currents by naltriben. Whole-cell currents were measured in HEK293T cells transfected by WT (A), N1097Q (B) and N1098Q (C) variants of TRPM7 cDNAs (in pIRES2-EGFP). *Left panels* current amplitudes (mean \pm SEM) were measured at -80 and $+80$ mV and plotted over time. Currents were measured using an intracellular solution containing 9 mM $[Mg\cdot ATP]_i$ and 550 μM $[Mg^{2+}]_i$ and the standard external solution with or without 100 μM naltriben as indicated by the black bars. *Middle panels* representative I–V relationships obtained from individual ramps before (brown) and after (red) naltriben application as indicated in the *left panels* by coloured data points. *Right panels* bar graphs of outward currents ($+80$ mV, mean \pm SEM) obtained before (brown) and after (red) naltriben application as indicated in the *left panels* by coloured data points. *n*, number of cells measured; *ns*, not significant; ***** $P < 0.001$ (two-tailed *t* test)

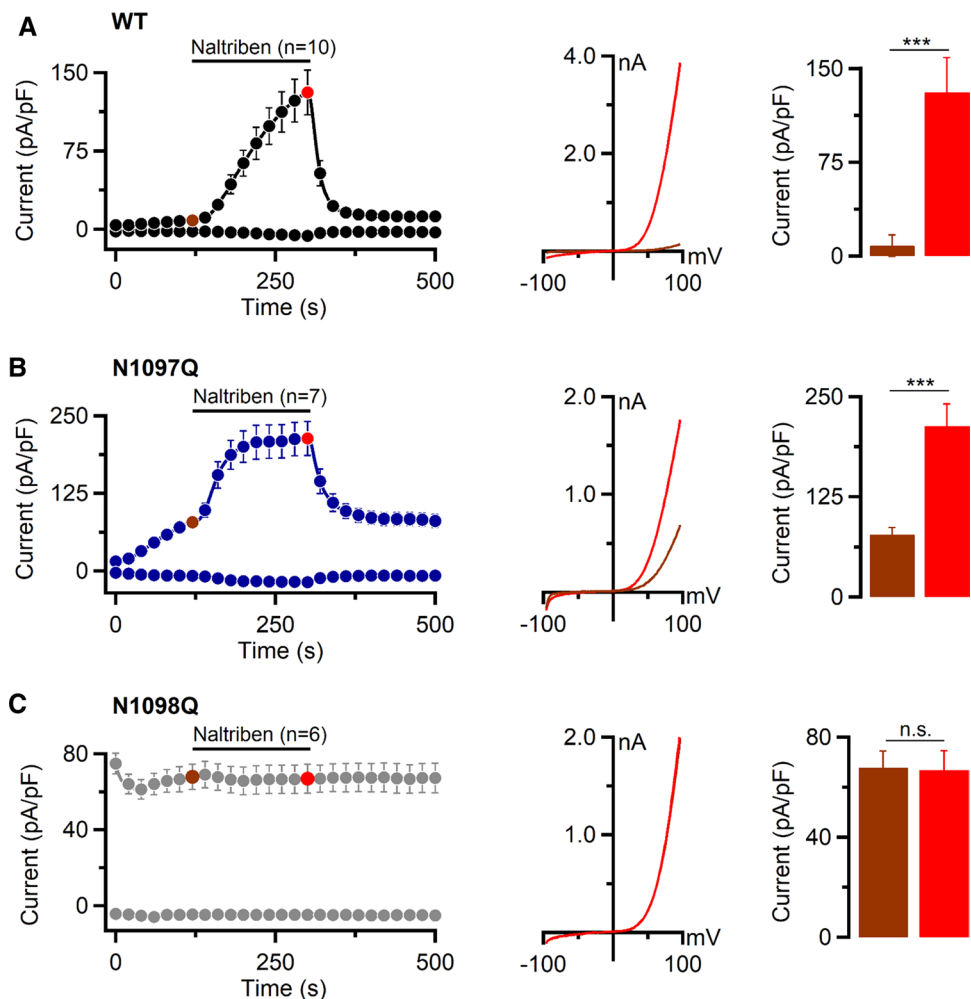
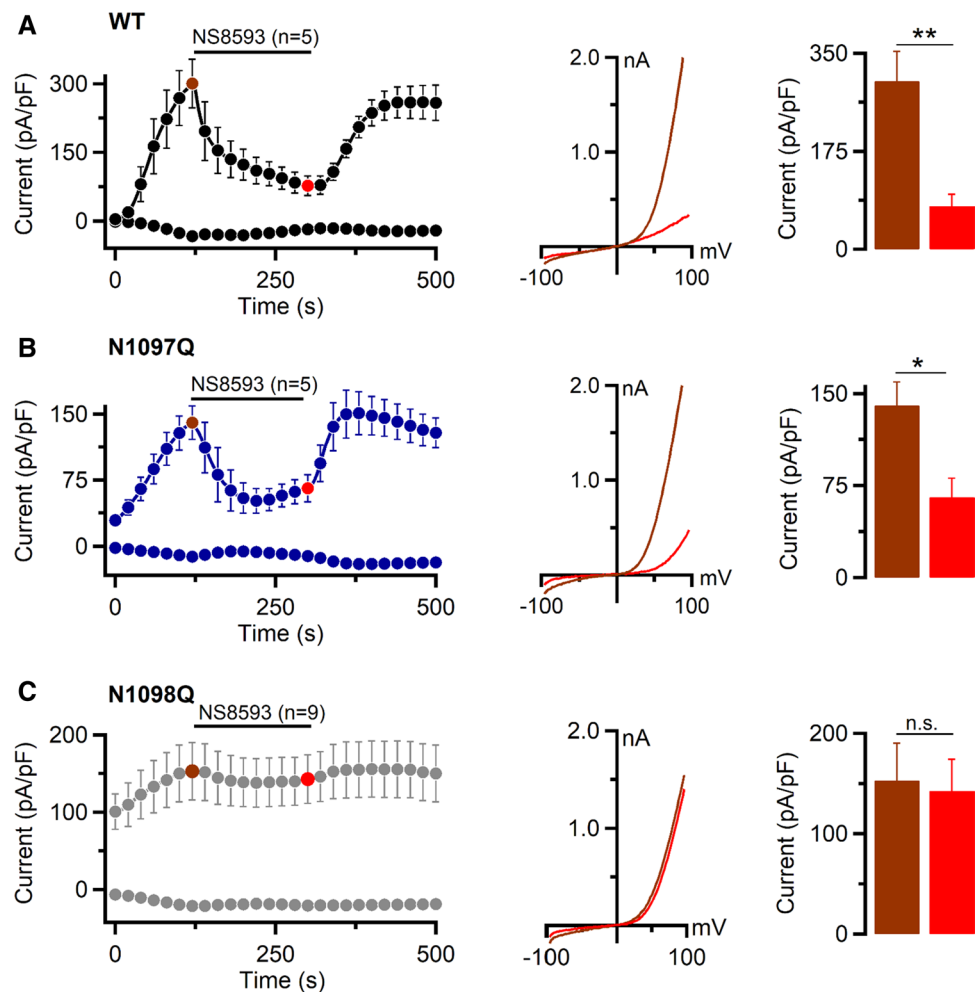


Fig. 5 Effects of NS8593 on TRPM7 currents. Whole-cell currents were measured in HEK293T cells transfected by WT (A), N1097Q (B), and N1098Q (C) variants of TRPM7 cDNAs (in pIRES2-EGFP) expressed in HEK293T cells. *Left panels* current amplitudes (mean \pm SEM) were acquired at -80 and $+80$ mV and plotted over time. Currents were induced using the standard $[Mg^{2+}]_i$ -free intracellular solution and the standard external solution. When currents were activated, the cells were exposed to the standard external solution with $10 \mu M$ NS8593 as indicated by the black bars. *Middle panels* representative I–V relationships obtained from individual ramps before (brown) and after (red) NS8593 application as indicated in the *left panels* by coloured data points. *Right panels* bar graphs of outward currents ($+80$ mV, mean \pm SEM) obtained before (brown) and after (red) NS8593 application as indicated in the *left panels* by coloured data points. *n*, number of cells measured; ns, not significant; * $P < 0.05$; ** $P < 0.01$ (two-tailed *t* test)



from -100 to $+100$ mV was applied to activate Ci-VSP and record TRPM7 currents (Fig. 6B). We found that Ci-VSP, but not Ci-VSP-C363S, suppressed WT and N1097Q currents similarly (Fig. 6C, D). In contrast, N1098Q currents were not affected by Ci-VSP and Ci-VSP-C363S (Fig. 6E). Hence, the N1097Q channel resembles the WT channel in the sensitivity to naltrexone, NS8593 and PIP_2 depletion by Ci-VSP, whereas the N1098Q variant represents a constitutively active channel insensitive to these agents.

Assessment of TRPM7 channel variants in a divalent cation-free (DVF) extracellular solution

A well-known characteristic feature of TRPM7 is the permeation block of the channel pore by extracellular divalent cations [12], causing the characteristic shape of the I–V relationship of TRPM7 currents in the presence of divalent cations in external solutions (Fig. 1C). However, exposure of TRPM7-expressing cells to a DVF solution abolish such a permeation block and entails large monovalent cation currents with a distinguishing semi-linearized I–V relationship

[12]. We examined whether N1097Q or N1098Q would affect this channel feature. As illustrated in Suppl. Fig. S7, application of DVF solution to the WT channel caused rapid increases of outward and inward currents accompanied with expected alterations in the I–V relationships. After the removal of the DVF solution, this characteristic I–V relationship of TRPM7 was reversed. We also noted that the N1097Q or N1098Q variants recapitulated the response of WT TRPM7 (Suppl. Fig. S7), indicating that N1097Q or N1098Q did not impinge on the function of the ion selectivity filter of TRPM7.

Impact of N1097Q on TRPM7 characteristics in excised outside-out patches

For a more thorough examination of the hypothesis that the N1097Q mutation affected the sensitivity of TRPM7 to intracellular Mg^{2+} , we thought to analyse TRPM7 on the single-channel level. However, our extensive attempts to measure TRPM7 currents in inside-out patches were unsuccessful. Therefore, we used previously established experimental

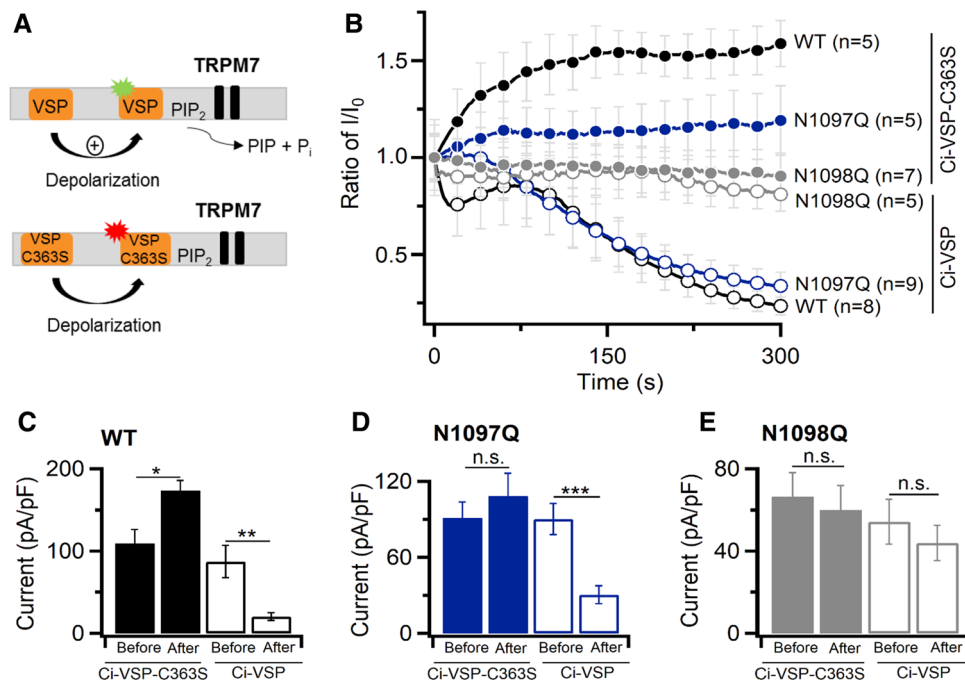


Fig. 6 Assessment of TRPM7 currents after PIP₂ depletion. **A** A diagram showing how wild-type voltage-sensitive phosphatase from *Ciona intestinalis* (Ci-VSP) reduces PIP₂ levels in the plasma membranes. A catalytically silent mutant of Ci-VSP (Ci-VSP-C363S) is unable to affect PIP₂ contents. **B** Time-dependent changes of normalized whole-cell outward currents in HEK293T cells transfected with WT, N1097Q and N1098Q variants of TRPM7 cDNA and Ci-VSP or Ci-VSP-C363S. Cells were held at -60 mV for 2 min to allow induction of TRPM7 without activation of Ci-VSP. Then the voltage ramp

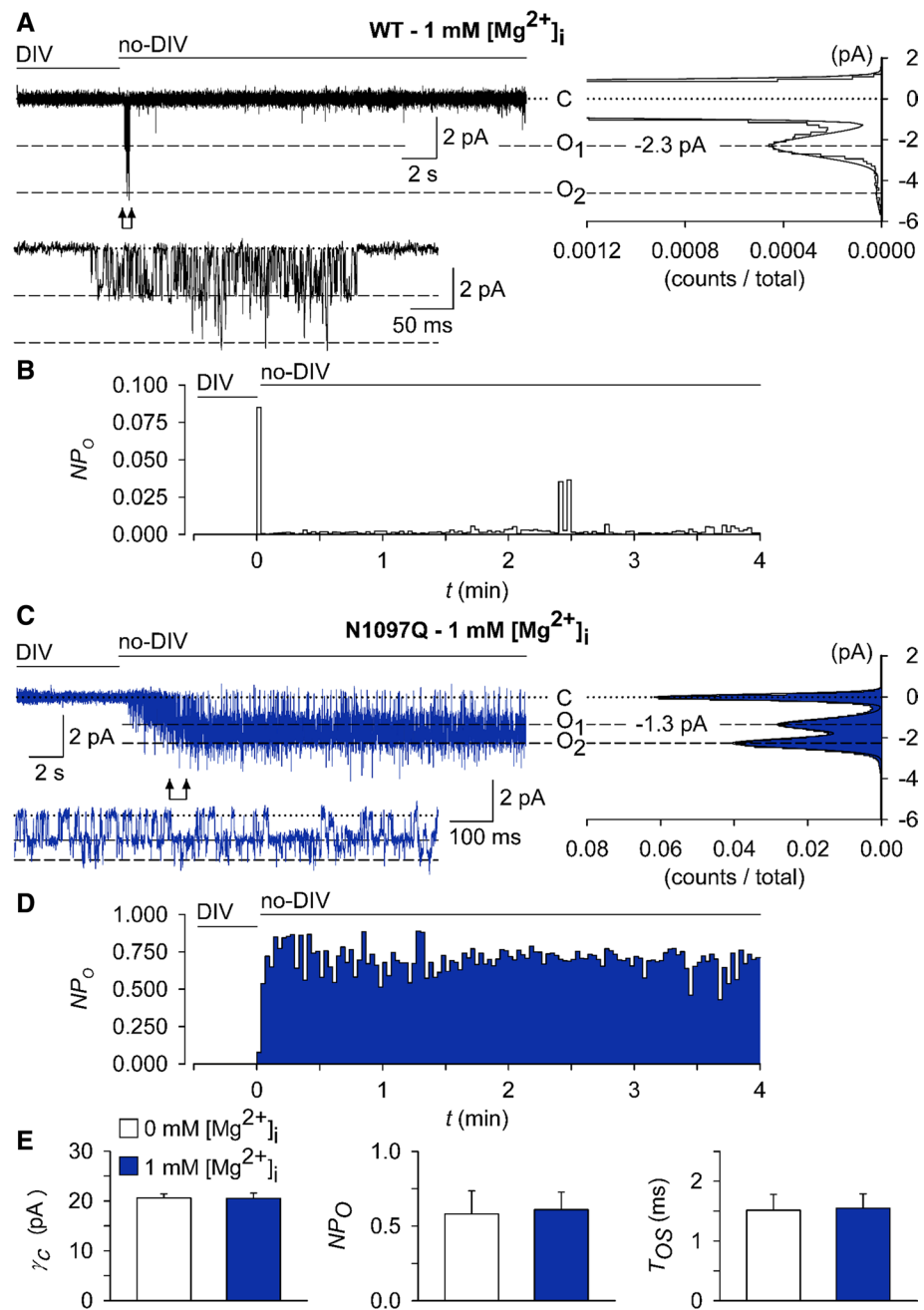
ranging from -100 to $+100$ mV was applied to activate Ci-VSP and record TRPM7 currents. Current amplitudes ($+80$ mV) were normalized to the initial currents (mean \pm SEM) and plotted over time. Data points are shown for every 10 s ramp. *n*, number of cells measured. **C–E** Bar graphs of outward currents ($+80$ mV, mean \pm SEM) shown in **B** immediately and after 300 s of application of voltage ramps from -100 to $+100$ mV. ns, not significant; * $P < 0.05$; ** $P < 0.01$; *** $P < 0.001$ (two-tailed *t* test)

settings to analyse TRPM7 activity in excised outside-out patches [45]. To this end, outside-out patches were excised from transfected HEK293 cells and voltage clamped to -60 mV. TRPM7 activity was evoked by exchanging the standard bath solution with a divalent cations-free (no-DIV) solution. This manoeuvre elicited only multichannel responses, irrespective of whether patches were from WT- or N1097Q-expressing cells, precluding an analysis of single-channel kinetics in these experimental settings (Suppl. Figure 8A, B). Nevertheless, differences between the WT and N1097Q channels were well evident. Single-channel amplitudes and the sojourns in the open state were about twice as large in the WT channels (Suppl. Fig. S8A, B). Estimated from a subset of experiments in which current–voltage relationships could be obtained, the calculated single-channel slope conductances (γ_s) were 41.4 ± 2.5 pS and 23.8 ± 2.4 pS for the WT and N1097Q, respectively [$n = 7$; see Suppl. Fig. S8C for examples; Suppl. Table S5 provides auxiliary chord conductance values (γ_c) from a larger sample]. The corresponding surrogate mean open times (T_{OS}), an admittedly rough estimate for the duration of the open state, were 4.7 ± 0.6 ms and 1.5 ± 0.3 ms for the WT and N1097Q

channel variants, respectively. Despite shortening of T_{OS} , N1097Q did not affect the open probability (NP_O) (Suppl. Fig. S8C and Table S5), suggesting that the N1097Q mutation facilitated gating motions in the TRPM7 protein. Interestingly, besides a 40 pS main level, at least one additional subconductance state for TRPM7 has been described [46]. However, the all-points histograms derived from our data (Fig. 5A, C) showed evenly spaced peaks and lack of overt humps and, therefore, do not point to a significant contribution of such a subconductance state to the overall conductance under our experimental conditions.

To assess the effects of intracellular Mg^{2+} on channel characteristics, we used a pipette solution containing 1 mM free Mg^{2+} . All outside-out patches from cells overexpressing the WT channel exposed to no-DIV solution showed only an initial burst of channel openings followed by lasting quiescence (Fig. 7A, B). Single-channel current amplitudes assessed during the initial outbreaks of activity (-2.3 ± 0.18 pA, Fig. 7A) were similar to those obtained in the absence of intracellular Mg^{2+} (-2.2 ± 0.21 pA; Suppl. Fig. S8, Table S5). N1097Q behaved differently from the WT channel. Exposure to no-DIV solution induced sustained channel

Fig. 7 Impact of intracellular Mg^{2+} on single-channel currents from TRPM7 variants. Currents were recorded at a holding potential of -60 mV in outside-out membrane patches excised from HEK293 cells expressing WT (A, B) and N1097Q (C–E) variants of TRPM7. The WT (A) or N1097Q (C) channels were unblocked by removing the extracellular divalent cations (DIV bath) using a no-DIV solution, as indicated above the current traces. The intracellular solution was no-DIV augmented by 1 mM Mg^{2+} . Insets: currents on an expanded time scale from the segments indicated by arrows. The graphs on the right show all-point histograms from the two 30 s current traces. The dotted line indicates the closed level (C). The broken lines indicate the current level for one channel (O1) or two channels (O2) being open. Single-channel amplitudes (i) taken from O1 were -2.3 pA and -1.3 pA for WT channels (A) and N1097Q (C), respectively. **B, D** The open probabilities (NP_O) assessed for bins of 2 s over the whole 4.5 min duration of the experiments shown in (A, C). Note the different ordinate scaling in **B** and **D**. **E** Statistical evaluation of outside-out recordings with the N1097Q channel. Note that intracellular Mg^{2+} did not affect single-channel chord conductance (γ_C), NP_O and open time (T_{OS} ; $n = 7$ each)



activity of the N1097Q variant, with the NP_O being stable over the whole time of current recordings (Fig. 7C, D). All measured channel characteristics, including chord conductance, NP_O , and T_{OS} were not affected by adding 1 mM intracellular Mg^{2+} (Fig. 7E, Table S5). Finally, using the same experimental settings, we analysed the effects of 2.9 mM $[Mg\cdot ATP]_i$ and 250 μ M free $[Mg^{2+}]_i$ and observed that the WT channel exhibited only an initial burst of channel openings, whereas the N1097Q variant was active and displayed functional characteristics similar to those obtained in the presence of 1 mM free Mg^{2+} (Suppl. Fig. S9). These results corroborate with our analysis of whole-cell currents

reinforcing the idea that the N1097Q substitution abrogated the inhibition of the TRPM7 channel by physiological intracellular Mg^{2+} concentrations.

Modelling and molecular dynamics (MD) simulations of the wild-type and mutant variants of the TRPM7 channel in closed and open conformations

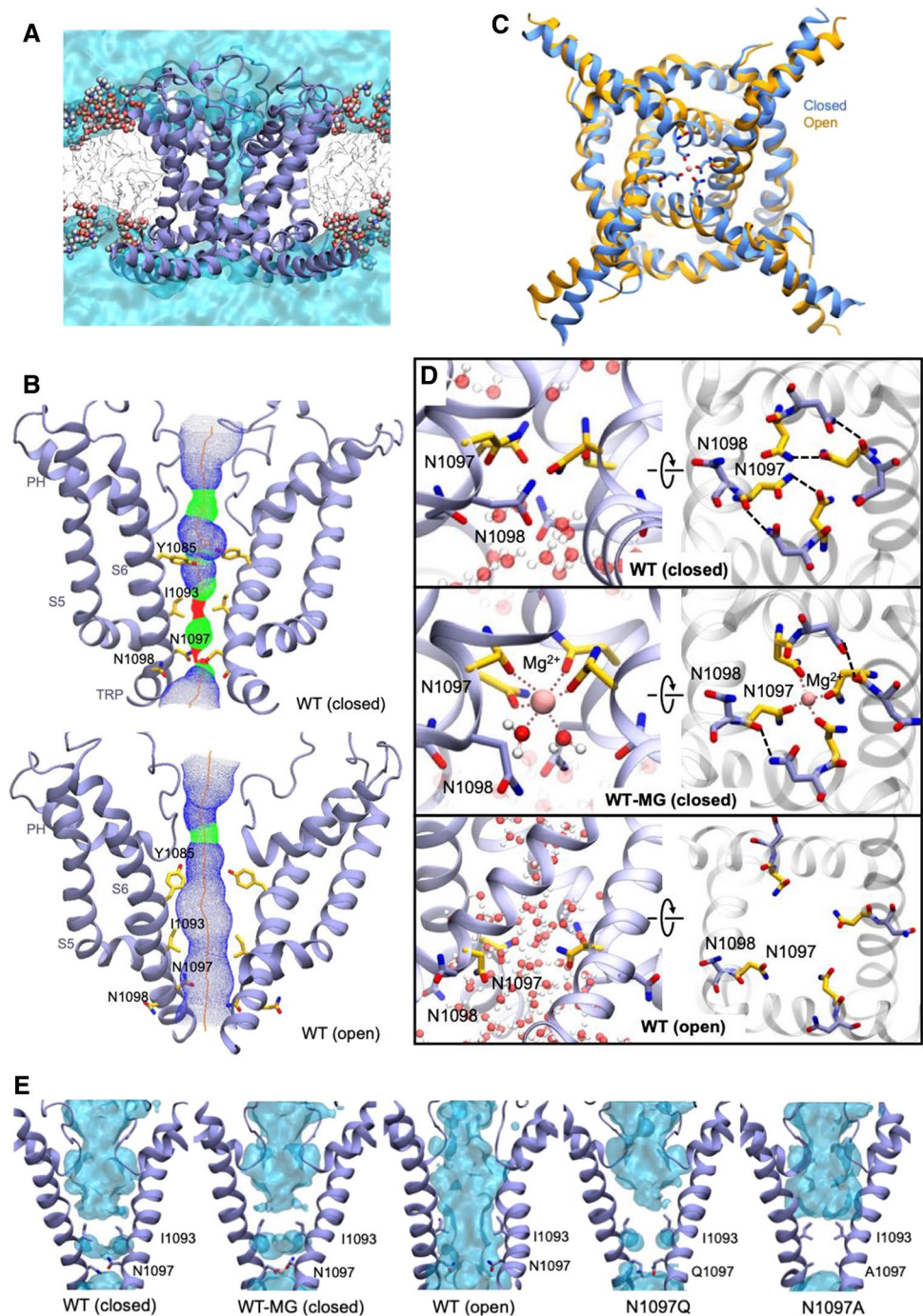
To elucidate a mechanism by which N1097 and N1098 contribute to TRPM7 channel regulation, we opted for protein modelling and MD simulations of the TRPM7 ion

channel domain. The TRPM7 structure in Mg^{2+} -free conditions (PDB 5ZX5) showed the highest resolution of the S5–S6 segment in TRPM7, and, therefore, it was selected for analysis. To perform MD simulations, we constructed a 3D model of the closed channel pore-forming segment of TRPM7 (S4–S5 linker, S5–S6 helices and TRP domain) embedded in a lipid membrane and surrounded by water and ions (Fig. 8A). To develop a TRPM7 open channel structure, we used the homology modelling method. Initially, we attempted to use the open structure of the zebrafish TRPM2

channel as a template [32]. However, the open TRPM2 channel displayed significant conformational changes in the S5 helix driven by the interaction of charged residues in the S4–S5 linker and the TRP box, which are not conserved in TRPM7. Therefore, our analysis relied on the open structure of the human TRPV6 channel (PDB: 6BO8 [47]) (Suppl. Fig. S10).

The homology-modelled open channel structure then was used in targeted MD simulations to open the channel in lipid and water (Fig. 8). We observed that in the

Fig. 8 Models of the channel pore-forming segment of mouse TRPM7 in lipid and water environments in closed and open conformations. **A** A representative structure of the mouse WT TRPM7 simulated channel unit (residues 982 to 1123) in the lipid bilayer and water. **B** A side view of a channel structure in the closed (top panel) and open (bottom panel) conformations. The channel pore-lining residues are shown. **C** Overlap of the closed structure and open structure shown (bottom view). **D** Structure of the channel gate in the closed channel with or without Mg^{2+} and open channel. Persistent water molecules are shown in red. Dashed lines indicate hydrogen bonds formed between N1097 and N1098 residues and Mg^{2+} . Note that the hydrogen bonds are transient, and the specific interactions shown are not present in all frames of the trajectory. **E** Channel's hydration in the simulations is shown for the WT, N1097A and N1097Q variants. Water is shown as a semi-transparent light blue continuum



closed state of the channel, the side chains of I1093 formed a hydrophobic seal excluding water from the channel (Fig. 8E), whereas polar side chains of N1097 build the narrowest segment of the cation permeation path in the pore (Fig. 8B). We found that transient inter-subunit hydrogen bonds were formed between N1097 residues of different subunits and between N1097 and N1098 residues. The most prominent hydrogen bonds were formed between the side chain amino and carbonyl groups of N1097 residues of adjacent subunits and between the side chain amino group of N1098 and the backbone carbonyl group of N1097 of adjacent subunits (Fig. 8D). On average, 3.6 inter-subunit hydrogen bonds involving N1097 and N1098 were present in the tetramer during the simulation (Suppl. Table S6). Our analysis suggests that these hydrogen bonds serve to stabilize the closed state of the channel gate (Fig. 8B, D).

MD simulation of TRPM7 in the open channel state revealed several remarkable structural rearrangements compared to the closed pore state (Fig. 8B, D). Specifically, we observed a loss of the hydrophobic seal formed by I1093 and significantly increased distance between the side chains of N1097. Inter-subunit hydrogen bonds formed by N1097 and N1098 were nearly absent with an average of 0.36 (Suppl. Table S6). Next, we performed MD simulations with Mg^{2+} placed in the pocket formed by the four N1097 in the closed channel (Fig. 8D). We found that Mg^{2+} steadily interacted with the side chain carbonyl groups of N1097 and two water molecules (Fig. 8C, D), stabilizing the closed state of TRPM7.

Finally, we performed MD simulations of the N1097A, N1097Q, N1098Q mutants. The N1097A channel formed a tightly closed gate due to the hydrophobicity of A1097 downstream to the hydrophobic seal formed by I1093 (Fig. 8E), thus explaining the silencing of the channel variant in patch-clamp experiments (Fig. 1). In the absence of Mg^{2+} , the N1097Q variant behaved similarly to the WT channel (Fig. 8E). However, MD simulations in the presence of Mg^{2+} revealed that Mg^{2+} lost coordination with three out of the four side chains of Q1097 (Suppl. Figure 11A), thus explaining the shift in concentration–response Mg^{2+} inhibition of the N1097Q channel (Fig. 2). The N1098Q presented a more complicated picture. In the absence of Mg^{2+} , the N1098Q mutation reduced the average number of inter-subunit hydrogen bonds formed by N1097 and Q1098 to only 0.6 as opposed to 3.6 in the WT structure (Suppl. Table S6, Suppl. Figure 11B). These results suggest that the closed state of the N1098Q channel is significantly less stable than the WT channel. In the presence of Mg^{2+} , the N1098Q channel retained coordination with Mg^{2+} , but the glutamine residue at position 1098 interacted weaker with N1097 than the WT channel (Suppl. Table S6). Hence,

consistent with electrophysiological data, N1097 and N1098 have distinct structural roles in the lower channel gate of TRPM7.

Discussion

There is growing evidence to show that TRPM7 is a central gatekeeper of the cellular uptake of essential divalent cations and that cytosolic Mg^{2+} acts as the principal regulator of this fundamental process. In the present paper, we used a combination of site-directed mutagenesis, electrophysiological techniques and MD simulations to show that side chains of N1097 in mouse TRPM7 form an inter-subunit Mg^{2+} -regulatory site, determining the responses of the channel to changes of cytosolic Mg^{2+} levels. Hence, our study offers a molecular explanation of the key regulatory characteristic of the TRPM7 channel. The primary role of the lower channel gate in sensing the intracellular milieu has not been described yet in TRPM channels. Whether such a mechanism epitomizes a general principle among other TRP channels remains to be answered in the future.

The current view is that intracellular Mg^{2+} and Mg -ATP represent physiologically relevant negative regulators of the channel. Because TRPM7 contains a kinase unit, initial studies attempted to address the regulatory role of this domain [13–15, 21]. However, a kinase-dead point mutation (K1646R in mouse TRPM7) or channel variants lacking the C-terminal segments of the channel, including the kinase moiety, resulted in channels with only modestly changed sensitivity to Mg^{2+} [13–15, 21]. In contrast, the effects of Mg -ATP were dependent on the kinase moiety and upstream coiled-coil segments of TRPM7 in a species-specific fashion [13–15, 21]. These findings can be interpreted to mean that Mg^{2+} and Mg -ATP operate through different regulatory sites in TRPM7 and that Mg^{2+} blocks TRPM7 independently from the kinase domain.

In the present study, we uncovered the structural basis of the inhibitory action of free Mg^{2+} on the TRPM7 channel. Our hypothesis-driven assessment of TRPM7 variants with point mutations spanning different segments of TRPM7 suggests that the lower channel gate determines the Mg^{2+} sensitivity of TRPM7. Thus, a slight modification of the side chain of N1097 (N1097Q mutation) was sufficient to shift the IC_{50} value beyond physiological levels of free Mg^{2+} . Consequently, the N1097Q mutant was active in perforated patch-clamp recordings when the patch pipette solutions did not manipulate the intracellular Mg^{2+} levels. Interestingly, the N1097Q channel showed reduced sensitivity to free Ba^{2+} , implying that other divalent cations can potentially occupy the proposed Mg^{2+} binding site, thus, providing a mechanistic explanation for the inhibition of TRPM7 currents by Ba^{2+} , Ca^{2+} and Zn^{2+}

when applied in the mM range [38]. Significantly, N1097Q did not affect the current amplitudes of the channel in the absence of intracellular or extracellular Mg^{2+} and displayed unchanged I–V characteristics in all experimental settings used. The N1097Q mutant retained the sensitivity to pharmacological agents acting as negative and positive gating modulators of TRPM7, such as NS8593 and naltriben. Moreover, assessing the biophysical properties of the N1097Q mutant on the single-channel level corroborated our conclusion derived from whole-cell data, in that the mutant channel remains active in the presence of physiological concentrations of internal Mg^{2+} . Collectively, these results indicate that the N1097Q mutation selectively affects the inhibitory action of intracellular Mg^{2+} rather than perturbing TRPM7 function unspecifically.

Although the present study primarily aimed to reveal regulatory mechanisms of Mg^{2+} , our experiments also provide new insight into the action of PIP_2 and Mg -ATP on TRPM7. Thus, the N1097Q variant responded to PIP_2 depletion similarly to the WT channel. The latter finding is not surprising because the side chain of N1097 is exposed to the channel pore lumen and, consequently, incapable of interacting directly with membrane PIP_2 . However, we observed that the N1097Q channel was sensitive to unphysiologically high Mg^{2+} concentrations suggesting that an additional action of Mg^{2+} was retained, for instance, the predicted electrostatic Mg^{2+} shielding of negatively charged PIP_2 [20–22]. Also, we observed that in the presence of relatively low Mg^{2+} levels (250 and 550 μM), the N1097Q variant exhibited a significantly reduced sensitivity to Mg -ATP (and Mg -GTP). However, the inhibitory effect of Mg -ATP on N1097Q currents was retained in the presence of 1 mM free Mg^{2+} . These results are consistent with a previous study [13], demonstrating that free Mg^{2+} and Mg -ATP can interact with TRPM7 causing the synergistic inhibition of TRPM7 currents. Accordingly, we suggest that the N1097Q mutation primarily affects the channel's response to free Mg^{2+} , while its sensitivity to Mg -ATP is still preserved.

MD simulations allowed us to interrogate the structural role of N1097 in opening of the TRPM7 channel. Our data suggest that the four side chains of N1097 in a TRPM7 tetramer form an inter-subunit cation-binding site and that the presence of Mg^{2+} in this pocket stabilizes the closed channel state. Accordingly, the lack of Mg^{2+} facilitates channel opening. In line with electrophysiological experiments, the N1097Q variant eradicates the coordination of Mg^{2+} in the lower channel gate due to the difference of one methylene group in the length of side chains of asparagine and glutamine, thus destabilizing the closed channel state in the presence of Mg^{2+} . Unlike N1097Q, a similar modification of an adjacent asparagine, N1098Q, resulted in a gain-of-function mutation completely offsetting the effects

of Mg^{2+} , Ba^{2+} , Mg -ATP, Mg -GTP, PIP_2 and pharmacological agents. Such constitutive activity of the N1098Q channel resembles a previously isolated TRPM7 variant containing the point mutation S1107E in the TRP domain [42]. The S1107E channel was insensitive to physiological levels of free Mg^{2+} , PIP_2 and naltriben [42].

The structural role of N1098 is distinguishable from that of N1097. MD simulations suggest that N1098 forms inter-subunit hydrogen bonds stabilizing the closed state of the WT channel. Consequently, the N1098Q mutation most likely destabilizes such hydrogen bonds resulting in a constitutively active channel variant. The striking functional impact of N1098Q and the closely located S1107E further reinforce the notion that this segment of TRPM7 plays a crucial role in opening of the channel.

Previously, our structure–functional analysis of mouse TRPM7 identified the crucial role of E1047 in the cation selectivity filter of the channel [48]. Together with other researchers [23, 48, 49], we showed that the E1047Q variant of TRPM7 was essentially impermeable to divalent cations, supporting the idea that the side chain of E1047 forms an inter-subunit site that directly interacts with divalent cations entering the channel pore. To this end, the structural impact of E1047 in the cation selectivity filter resembles the role of N1097 in the lower channel gate of TRPM7, implying the channel function of TRPM7 primarily operates using two inter-subunit cation-binding sites interacting with extracellular and cytosolic divalent cations. Since N1097 and N1098 of mouse TRPM7 are conserved within the TRPM1/3/6/7 group of mammalian proteins (Fig. 1G), such a structure–function paradigm may be relevant for this subgroup of TRPM channels as a general principle.

Material and methods

Molecular biology and cell culture

Mouse TRPM7 (in pIRES2-EGFP vector) and TRPM7-YFP (in pcDNA3.1/V5-His TA-TOPO vector) were reported previously [36, 37]. Ci-VSP or Ci-VSP-C363S cDNAs (in pIRES2-EGFP) were provided by Joris Vriens, KU Leuven [50].

Point mutations in TRPM7 were introduced using the QuikChange system (Thermo Fisher Scientific) according to the manufacturer's protocol and verified by sequencing (Eurofins, Germany). Initially, we attempted to introduce the mutations outlined in Fig. 1A in the mouse TRPM7 cDNA in the bicistronic pIRES2-EGFP vector [36, 37]. However, we found that side-directed mutagenesis of this expression construct is highly inefficient and prone to errors likely due to cis-acting IRES sequence. Nevertheless, we could successfully conduct mutagenesis using the mouse TRPM7

with C-terminal YFP tag in pcDNA3.1 vector [36, 37] and, consequently, the primary functional assessment of TRPM7 variants (Fig. 1) was performed using the latter expression construct.

HEK293T cells were grown at 37 °C and 5% CO₂ in Dulbecco's modified Eagle's medium (DMEM, Sigma-Aldrich) supplemented with 10% foetal bovine serum (FBS, Thermo Fisher Scientific), 100 U/ml penicillin and 100 µg/ml streptomycin (P/S, Sigma-Aldrich). Cells ~60% confluence, 3 cm dish) were transiently transfected by 2 µg TRPM7 cDNAs using Lipofectamine 2000 reagent (Thermo Fisher Scientific). In some experiments, 2 µg TRPM7 cDNAs (pIRES2-EGFP) were co-transfected with 1 µg Ci-VSP WT or Ci-VSP-C363S cDNAs (pIRES2-EGFP) as indicated in the corresponding figure legend.

Immunofluorescent staining

HEK293T cells cultured on glass-bottom cell culture dishes (World Precision Instruments) were transiently transfected by 2 µg/dish WT or mutant variants of TRPM7 cDNA (in pIRES2-EGFP) and examined 18–24 h after transfection. Cells were washed twice with PBS, fixed with ice-cold methanol for 20 min at – 20 °C, and blocked for 1 h with 5% (v/v) BSA in PBS at room temperature. The mouse monoclonal anti-TRPM7 antibody (clone 2C7; 0.84 µg/ml; [51]) was applied. The secondary antibody (0.5 µg/ml) was goat anti-mouse IgG conjugated to Alexa Fluor 488 (Molecular Probes). Each incubation was performed in PBS containing 5% (v/v) normal goat serum for 1 h at room temperature, followed by triple washing with PBS. After the final washing, glass coverslips were placed on glass-bottom cell culture dishes using a mounting medium (DakoCytomation). Differential interference contrast (DIC) and Airyscan images of Alexa Fluor 488 were obtained with the confocal laser-scanning microscope LSM 880 AxioObserver (Carl Zeiss). We used a C-Apochromat 63x/1.2 W objective, 488 nm excitation wavelength and 493–630 nm filters, multi-line argon laser 458/488/514 nm and an Airyscan detector. The acquired images were analysed using the ZEN 3.0 SR software (Carl Zeiss).

Electrophysiological techniques

Patch-clamp experiments with HEK293T cells were performed 18–22 h after transfection as reported previously [37, 52] with a few modifications. Whole-cell currents were measured using an EPC10 patch-clamp amplifier and PatchMaster software (Harvard Bioscience). Voltages were corrected for a liquid junction potential of 10 mV. Currents were elicited by a ramp protocol from – 100 mV to + 100 mV over 50 ms acquired at 0.5 Hz and a holding potential of

0 mV. Inward and outward current amplitudes were extracted at – 80 mV and + 80 mV and were normalized to cell size as pA/pF. Capacitance was measured using the automated capacitance cancellation function of EPC10. Patch pipettes were made of borosilicate glass (Science Products) and had resistance 2–3.5 MΩ.

Unless stated otherwise, a standard extracellular solution contained (in mM): 140 NaCl, 2.8 KCl, 1 CaCl₂, 2 MgCl₂, 10 HEPES–NaOH and 11 glucose (all from Roth Industries), pH 7.2. Effects of NS8593 (Tocris) and naltriben (Tocris) were examined by adding the compounds to the standard extracellular solution. A divalent cation-free (DVF) extracellular solution contained (in mM) 140 NaCl, 2.8 KCl, 11 glucose, 10 Na-EDTA and 10 HEPES–NaOH, pH 7.2. For the experiment with TRPM7-YFP (Fig. 1), we used an extracellular solution contained (in mM): 140 NaCl, 2.8 KCl, 1 CaCl₂, 10 HEPES–NaOH, and 11 glucose (all from Roth Industries), pH 7.2. The standard Mg²⁺-free intracellular ([Mg²⁺]_i) pipette solution containing (in mM): 120 Cs-glutamate, 8 NaCl, 10 Cs-EGTA, 5 Cs-EDTA, 10 HEPES–CsOH, pH 7.2.

To obtain [Mg²⁺]_i and [Mg-ATP]_i concentration–response data, the intracellular pipette solutions were prepared as outlined in Suppl. Tables S1–S4. Concentrations of [Mg-ATP]_i and free [Mg²⁺]_i were calculated using the Maxchelator software (maxchelator.stanford.edu).

The concentration–response data were fitted (Prism 8.4.0) with the following equation:

$$E(c) = E_{\min} + (E_{\max} - E_{\min}) \times (1 / (1 + (IC_{50}/c)^h)),$$

with E being the effect/current at a given concentration c of inhibitor; E_{\min} , the minimal effect/current; E_{\max} , the maximal effect; IC_{50} , the half-maximal concentration; h , the Hill factor.

For perforated patch recordings, 320 µM amphotericin B (Sigma-Aldrich) was added to the internal solution containing (in mM): 120 monopotassium glutamate (Sigma-Aldrich), 8 NaCl, 1 MgCl₂, 10 HEPES–KOH, pH 7.2. Cells were held at – 60 mV for 2 min to ensure activation of TRPM7 currents, followed by the standard voltage ramp protocol.

Outside-out patch-clamp recordings with EGFP-positive HEK293 cells were performed the day after transfection with either the WT or the N1097Q mutant of TRPM7, using procedures described previously [45]. The standard extracellular solution contained in these experiments (in mM): 147 NaCl, 2 KCl, 1 MgCl₂, 2 CaCl₂, 13 D-glucose and 10 HEPES (~305 mOsm/l; pH 7.3 with NaOH). A divalent cation-free (no-DIV) solution was produced by omitting Ca²⁺ and Mg²⁺ and supplementing EGTA and EDTA (1 mM each). Patch pipettes had a resistance of 15–20 MΩ when filled with intracellular solutions. These were either identical with the

no-DIV saline or based on it but containing about 1 mM of free Mg^{2+} in addition (2.07 mM added MgCl_2). Baselines in the current traces were corrected and raw single-channel data was evaluated with the QuB program. The mean amplitudes (i) of TRPM7 single-channel currents (digitized at 20 kHz and filtered at 2 kHz) were thereby from all-points amplitude histograms fitted to a sum of multiple Gaussian distributions, with the number of components depending on the apparent number of active channels (N) in a given patch. The probability for N channels being open (NP_O) was, in turn, defined as the ratio of the area occupied by all the peaks for open channels to the total amplitude histogram (summation of the open and closed peaks). The unitary conductance (γ) of WT or mutant TRPM7 channels was either calculated from i as chord conductance (γ_c), assuming a reversal potential of zero mV or, for comparison, in some experiments also derived from the slope of respective current–voltage relationships (γ_s , slope conductance). In multichannel patches, like those usually obtained during this study, uncertainties concerning the “true” value of N , as well as the overlap of channel openings, precludes a detailed dwell time analysis.

To still allow for comparisons, such as between WT and N1097Q channels, the relation [53]:

$$T_{os} = \left(\sum_i L_i t_i \right) / \#O,$$

where t_i is the total time the outside-out currents dwelt on level L_i during the recording and $\#O$ is the total of the number of opening events, was used to estimate a surrogate mean open time (T_{OS}). To this end, channel openings were counted over a prolonged time (4 min) in the outside-out current recordings, using the 50% amplitude threshold criterion implemented in QuB. The dead time imposed was 200 μs (~ 1.2 -fold of the filter rise time), thus excluding shorter events than this from the analysis.

Data are presented as means \pm standard error of the mean (means \pm SEM). Statistical comparisons (Prism 8.4.0 or SigmaPlot 14.0) were made using analysis of variance (ordinary one-way ANOVA) or two-tailed t test, as indicated in the figure legends. Significance was accepted at $P \leq 0.05$.

MD simulations

All MD simulations were carried out using the pmemd.cuda program of AMBER16 molecular dynamics package [54]. The Amber FF99SB-ILDN force field [55] for proteins was used for all simulations combined with Lipid14 model [56] for lipids and TIP3P model for water. All covalent bonds involving hydrogen atoms were constrained using SHAKE [57] to allow an integration time step of 2 fs. Langevin thermostat and Berendsen barostat were used to control temperature and pressure, respectively. All NPT simulations

were carried out using anisotropic pressure scaling. Electrostatic interactions were calculated using particle mesh ewald (PME) method [58] as implemented in Amber, with a non-bonded cutoff distance of 8 Å. Periodic boundary conditions were applied in all directions. In order to maintain the integrity of the pore loop of the protein, backbone hydrogen bond distances in the pore helix (residues 1031–1043) were restrained between 2.6 Å and the initial value during all simulations. Post-processing of trajectories was carried out using CPPTRAJ [59] and VMD [60].

MD simulation setup

Residues 982–1123 (S4-S5 linker, S5 helix, pore loop, S6 helix, and TRP helix) of the cryo-EM structure of the closed TRPM7 channel (PDB: 5ZX5) was used as the starting structure for all simulations. The protein was embedded in a POPC lipid membrane and solvated in water using the CHARMM-GUI Membrane Builder [61]. Additional water molecules were added manually to solvate the ion channel pore. The system was prepared for simulations using the charmm lipid2amber.py script and the tleap program in AmberTools16 (www.ambermd.org). The protein N and C termini were capped with the neutral acetyl and amide groups, and the conserved disulfide bond between residues C1056 and C1066 was introduced. The system was neutralized with Na^+ and Cl^- ions. The final system contained 568 protein residues, 159 lipid molecules, 13,585 water molecules and neutralizing ions.

MD simulations of the closed TRPM7 channel

The prepared TRPM7 closed channel system was equilibrated as follows. First, a short minimization (6000 steps) was performed to remove clashes in the system. The system was then heated from 0.1 to 100 K in NVT ensemble and 100 K to 300 K in NPT ensemble, over 250 ps. The protein heavy atoms were restrained at their initial positions with a harmonic force constant (k) of 10 $\text{kcal mol}^{-1} \text{Å}^{-2}$ during the heating steps (residues 1050–1070 in the pore loop were not restrained in order to enforce the disulphide bond between C1056 and C1066). The system was equilibrated at 300 K in NPT ensemble for 35 ns while gradually decreasing restraints on the protein until only the C_α atoms were restrained with $k = 0.5 \text{ kcal mol}^{-1} \text{Å}^{-2}$. The resulting system was used as the starting structure for the simulations with Mg^{2+} and N1097 mutant simulations (described in the following sections). All restraints on protein C_α atoms were removed except those on residues 1116–1123 of the TRP helix, and the closed channel was equilibrated in NPT ensemble for further 100 ns.

TRPM7 open channel conformation model

The S5, S6, and TRP helices and the S4–S5 linker (residues 982–1022 and 1071–1123) of the TRPM7 open channel were modelled in SWISS-MODEL [62] using the open channel structure of human TRPV6 channel (PDB ID: 6BO8) as a template. The target–template alignment for homology modelling was extracted from a multiple sequence alignment of the transmembrane and TRP regions of known TRPM and TRPV structures (TRPM7, TRPM4, TRPM2, TRPV1, TRPV3, TRPV6) performed using Clustal Omega at EMBL-EBI [63]. Residues 471–513 and 553–605 of PDB: 6BO8 was used to model the open structure of TRPM7.

MD simulations of the open channel

The homology model of the open TRPM7 channel was used to open the equilibrated closed channel by targeted MD simulations with simulated annealing. To open the channel, the C_{α} atoms of residues 982–1022 and 1071–1123 (S4–S5 and S5 helix, S6 and TRP helices) in the closed channel were harmonically restrained to the corresponding coordinates of the open homology model. Simulated annealing was performed in six steps as follows. In each step, (a) the system was equilibrated for 5 ns at 300 K, (b) heated to 350 K over 500 ps, (c) equilibrated at 350 K for 5 ns (or until RMSD of the targeted C_{α} atoms with respect to the reference structure was stable), and (d) cooled back to 300 K over 500 ps. Harmonic restraints were maintained throughout the process, increasing the force constant at the end of each step from 0.05, 0.1, 0.2, 1.0, 2.0 to 2.5 kcal mol⁻¹ Å⁻². The restraints were then released gradually over a period of 25 ns and, finally, unrestrained simulations of the open model were carried out for over 200 ns.

MD simulations of the mutant TRPM7 variants

The partially equilibrated closed TRPM7 channel (see “MD simulations of the closed TRPM7 channel” section) was used to construct the mutants N1097Q, N1097A and N1098Q. Additionally, Mg²⁺ was placed between the residues at the 1097 position to obtain complexes of the wild type (WT-MG), and the N1097Q (N1097Q-MG) and N1098Q (N1098Q-MG) mutants with Mg²⁺. The charge on Mg²⁺ was set to + 1.65. Each system was equilibrated using a protocol similar to that described in the previous section (MD simulations of the closed TRPM7 channel), except restraints on the protein C_{α} atoms were changed from $k = 10$ to 0.5 kcal mol⁻¹ Å⁻² in 20 ns. In WT-MG, N1097Q-MG and N1098Q-MG systems, the magnesium ion was restrained with the same force constant used to restrain the protein, and an additional equilibration step of 100 ns was carried out without restraints on the magnesium

ion while maintaining restraints on the protein C_{α} atoms at $k = 0.5$ kcal mol⁻¹ Å⁻². All systems were simulated for 100 ns with all restraints removed except the restraints on C_{α} atoms of residues 1116–1123.

Supplementary Information The online version contains supplementary material available at <https://doi.org/10.1007/s00018-022-04192-7>.

Acknowledgements We thank the Extreme Science and Engineering Discovery Environment (XSEDE) at the Pittsburgh Supercomputing Center for technical support (allocation TG-MCB180173). We thank Joanna Zaisserer, Lisa Pleninger and Anna Erbacher for their technical assistance.

Authors' contributions All authors read and approved the final manuscript. All authors contributed to the study conception and design as follows: conceptualization: VC, TG, MGK; funding acquisition, VC, TG, MGK, MS; experimental investigation, ES, CN, WN, ME, AR, ML; theoretical investigation, CN, MGK; formal analysis, SZ, MS, CN, MGK; writing—original draft preparation VC, TG, MGK; writing—review and editing, MS, SZ, WN, VC, TG.

Funding Open Access funding enabled and organized by Projekt DEAL. VC, MS, SZ and TG were supported by the Deutsche Forschungsgemeinschaft, TRR 152. TG was supported by Research Training Group 2338 (DFG). CN and MK were supported by grants from NSF 1818213, NSF 1563291, and NIH RO1NS083660.

Availability of data and materials All reagents and data generated or analysed during this study and its supplementary information files are available from the corresponding authors on request.

Declarations

Conflict of interests The authors declare that they have no conflict of interests.

Consent for publication Not applicable.

Ethics approval and consent to participate Not applicable.

Open Access This article is licensed under a Creative Commons Attribution 4.0 International License, which permits use, sharing, adaptation, distribution and reproduction in any medium or format, as long as you give appropriate credit to the original author(s) and the source, provide a link to the Creative Commons licence, and indicate if changes were made. The images or other third party material in this article are included in the article's Creative Commons licence, unless indicated otherwise in a credit line to the material. If material is not included in the article's Creative Commons licence and your intended use is not permitted by statutory regulation or exceeds the permitted use, you will need to obtain permission directly from the copyright holder. To view a copy of this licence, visit <http://creativecommons.org/licenses/by/4.0/>.

References

1. Chubanov V, Mittermeier L, Gudermann T (2018) Role of kinase-coupled TRP channels in mineral homeostasis. *Pharmacol Ther* 184:159–176

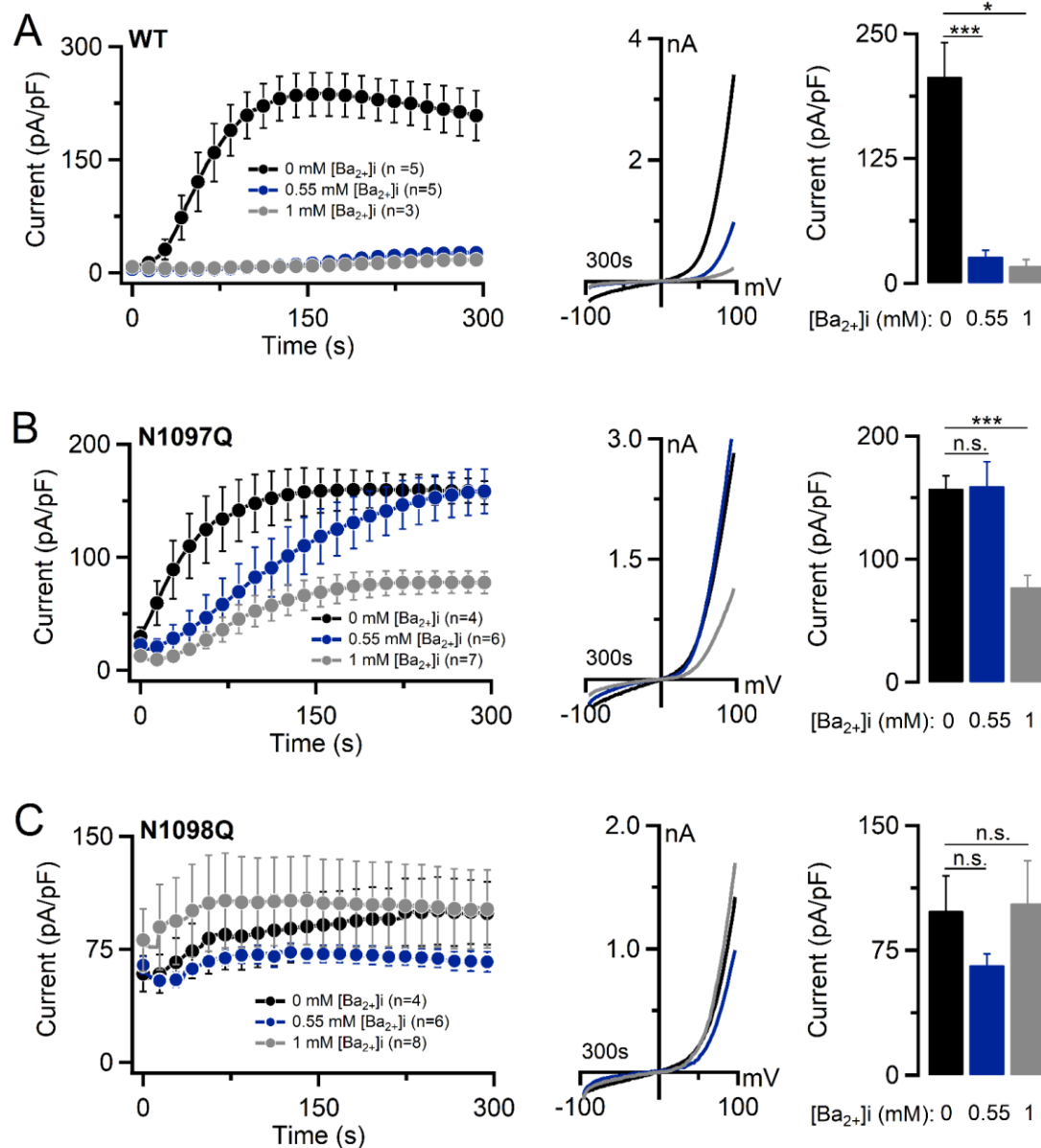
2. Fleig A, Chubanov V (2014) Trpm7. *Handb Exp Pharmacol* 222:521–546
3. Bates-Withers C, Sah R, Clapham DE (2011) TRPM7, the Mg(2+) inhibited channel and kinase. *Adv Exp Med Biol* 704:173–183
4. Mittermeier L et al (2019) TRPM7 is the central gatekeeper of intestinal mineral absorption essential for postnatal survival. *Proc Natl Acad Sci U S A* 116(10):4706–4715
5. Schmitz C et al (2003) Regulation of vertebrate cellular Mg²⁺ homeostasis by TRPM7. *Cell* 114(2):191–200
6. Abiria SA et al (2017) TRPM7 senses oxidative stress to release Zn(2+) from unique intracellular vesicles. *Proc Natl Acad Sci USA* 114(30):E6079–E6088
7. Monteilh-Zoller MK et al (2003) TRPM7 provides an ion channel mechanism for cellular entry of trace metal ions. *J Gen Physiol* 121(1):49–60
8. Faouzi M et al (2017) The TRPM7 channel kinase regulates store-operated calcium entry. *J Physiol* 595(10):3165–3180
9. Kerschbaum HH, Cahalan MD (1999) Single-channel recording of a store-operated Ca²⁺ channel in Jurkat T lymphocytes. *Science* 283(5403):836–839
10. Prakriya M, Lewis RS (2002) Separation and characterization of currents through store-operated CRAC channels and Mg²⁺-inhibited cation (MIC) channels. *J Gen Physiol* 119(5):487–507
11. Kozak JA, Kerschbaum HH, Cahalan MD (2002) Distinct properties of CRAC and MIC channels in RBL cells. *J Gen Physiol* 120(2):221–235
12. Nadler MJ et al (2001) LTRPC7 is a Mg-ATP-regulated divalent cation channel required for cell viability. *Nature* 411(6837):590–595
13. Demeuse P, Penner R, Fleig A (2006) TRPM7 channel is regulated by magnesium nucleotides via its kinase domain. *J Gen Physiol* 127(4):421–434
14. Matsushita M et al (2005) Channel function is dissociated from the intrinsic kinase activity and autophosphorylation of TRPM7/ChaK1. *J Biol Chem* 280(21):20793–20803
15. Jansen C et al (2016) The coiled-coil domain of zebrafish TRPM7 regulates Mg. nucleotide sensitivity. *Sci Rep* 6:33459
16. Ryazanova LV et al (2010) TRPM7 is essential for Mg(2+) homeostasis in mammals. *Nat Commun* 1:109
17. Ryazanova LV et al (2014) Elucidating the role of the TRPM7 alpha-kinase: TRPM7 kinase inactivation leads to magnesium deprivation resistance phenotype in mice. *Sci Rep* 4:7599
18. Kaitsuka T et al (2014) Inactivation of TRPM7 kinase activity does not impair its channel function in mice. *Sci Rep* 4:5718
19. Hermosura MC et al (2005) A TRPM7 variant shows altered sensitivity to magnesium that may contribute to the pathogenesis of two Guamanian neurodegenerative disorders. *Proc Natl Acad Sci U S A* 102(32):11510–11515
20. Runnels LW, Yue L, Clapham DE (2002) The TRPM7 channel is inactivated by PIP(2) hydrolysis. *Nat Cell Biol* 4(5):329–336
21. Kozak JA et al (2005) Charge screening by internal pH and polyvalent cations as a mechanism for activation, inhibition, and rundown of TRPM7/MIC channels. *J Gen Physiol* 126(5):499–514
22. Xie J et al (2011) Phosphatidylinositol 4,5-bisphosphate (PIP(2)) controls magnesium gatekeeper TRPM6 activity. *Sci Rep* 1:146
23. Duan J et al (2018) Structure of the mammalian TRPM7, a magnesium channel required during embryonic development. *Proc Natl Acad Sci U S A* 115(35):E8201–E8210
24. Ruan Z et al (2021) Structures of the TRPM5 channel elucidate mechanisms of activation and inhibition. *Nat Struct Mol Biol* 28(7):604–613
25. Duan J et al (2018) Structure of full-length human TRPM4. *Proc Natl Acad Sci U S A* 115(10):2377–2382
26. Autzen HE et al (2018) Structure of the human TRPM4 ion channel in a lipid nanodisc. *Science* 359(6372):228–232
27. Winkler PA et al (2017) Electron cryo-microscopy structure of a human TRPM4 channel. *Nature* 552(7684):200–204
28. Guo J et al (2017) Structures of the calcium-activated, non-selective cation channel TRPM4. *Nature* 552(7684):205–209
29. Yin Y et al (2019) Structural basis of cooling agent and lipid sensing by the cold-activated TRPM8 channel. *Science* 363(6430):9334
30. Diver MM, Cheng Y, Julius D (2019) Structural insights into TRPM8 inhibition and desensitization. *Science* 365(6460):1434–1440
31. Huang Y et al (2019) Ligand recognition and gating mechanism through three ligand-binding sites of human TRPM2 channel. *Elife* 8:e50175
32. Huang Y et al (2018) Architecture of the TRPM2 channel and its activation mechanism by ADP-ribose and calcium. *Nature* 562(7725):145–149
33. Zhang Z et al (2018) Structure of a TRPM2 channel in complex with Ca(2+) explains unique gating regulation. *Elife* 7:e36409
34. Mesbahi-Vasey S et al (2017) All atom NMDA receptor transmembrane domain model development and simulations in lipid bilayers and water. *PLoS ONE* 12(6):e0177686
35. Payandeh J, Pfoh R, Pai EF (2013) The structure and regulation of magnesium selective ion channels. *Biochim Biophys Acta* 1828(11):2778–2792
36. Chubanov V et al (2004) Disruption of TRPM6/TRPM7 complex formation by a mutation in the TRPM6 gene causes hypomagnesemia with secondary hypocalcemia. *Proc Natl Acad Sci U S A* 101(9):2894–2899
37. Ferioli S et al (2017) TRPM6 and TRPM7 differentially contribute to the relief of heteromeric TRPM6/7 channels from inhibition by cytosolic Mg(2+) and Mg. ATP. *Sci Rep* 7(1):8806
38. Kozak JA, Cahalan MD (2003) MIC channels are inhibited by internal divalent cations but not ATP. *Biophys J* 84(2 Pt 1):922–927
39. Traut TW (1994) Physiological concentrations of purines and pyrimidines. *Mol Cell Biochem* 140(1):1–22
40. Gupta RK et al (1983) Measurement of the dissociation constant of MgATP at physiological nucleotide levels by a combination of 31P NMR and optical absorbance spectroscopy. *Biochem Biophys Res Commun* 117(1):210–216
41. Romani AM (2011) Cellular magnesium homeostasis. *Arch Biochem Biophys* 512(1):1–23
42. Hofmann T et al (2014) Activation of TRPM7 channels by small molecules under physiological conditions. *Pflugers Arch* 466(12):2177–2189
43. Chubanov V et al (2012) Natural and synthetic modulators of SK (K (ca)2) potassium channels inhibit magnesium-dependent activity of the kinase-coupled cation channel TRPM7. *Br J Pharmacol* 166(4):1357–1376
44. Murata Y et al (2005) Phosphoinositide phosphatase activity coupled to an intrinsic voltage sensor. *Nature* 435(7046):1239–1243
45. Norenberg W et al (2016) TRPM7 is a molecular substrate of ATP-evoked P2X7-like currents in tumor cells. *J Gen Physiol* 147(6):467–483
46. Chokshi R, Matsushita M, Kozak JA (2012) Sensitivity of TRPM7 channels to Mg²⁺ characterized in cell-free patches of Jurkat T lymphocytes. *Am J Physiol Cell Physiol* 302(11):C1642–C1651
47. McGoldrick LL et al (2018) Opening of the human epithelial calcium channel TRPV6. *Nature* 553(7687):233–237
48. Mederos y Schnitzler M et al (2008) Evolutionary determinants of divergent calcium selectivity of TRPM channels. *FASEB J* 22(5):1540–1551

49. Li M et al (2007) Molecular determinants of Mg^{2+} and Ca^{2+} permeability and pH sensitivity in TRPM6 and TRPM7. *J Biol Chem* 282(35):25817–25830
50. Toth BI et al (2015) Regulation of the transient receptor potential channel TRPM3 by phosphoinositides. *J Gen Physiol* 146(1):51–63
51. Kollewe A et al (2021) The molecular appearance of native TRPM7 channel complexes identified by high-resolution proteomics. *Elife* 10:e68544
52. Chubanov V et al (2016) Epithelial magnesium transport by TRPM6 is essential for prenatal development and adult survival. *Elife* 5:e20914
53. Nemec J, Wickman K, Clapham DE (1999) Gbetagamma binding increases the open time of IKACH: kinetic evidence for multiple Gbetagamma binding sites. *Biophys J* 76(1 Pt 1):246–252
54. Case DA et al (2005) The Amber biomolecular simulation programs. *J Comput Chem* 26(16):1668–1688
55. Lindorff-Larsen K et al (2010) Improved side-chain torsion potentials for the Amber ff99SB protein force field. *Proteins* 78(8):1950–1958
56. Dickson CJ et al (2014) Lipid14: the amber lipid force field. *J Chem Theory Comput* 10(2):865–879
57. Hauptman HA (1997) Shake-and-bake: an algorithm for automatic solution ab initio of crystal structures. *Methods Enzymol* 277:3–13
58. Darden T et al (1999) New tricks for modelers from the crystallography toolkit: the particle mesh Ewald algorithm and its use in nucleic acid simulations. *Structure* 7(3):R55–60
59. Roe DR, Cheatham TE 3rd (2013) PTRAJ and CPPTRAJ: software for processing and analysis of molecular dynamics trajectory data. *J Chem Theory Comput* 9(7):3084–3095
60. Humphrey W, Dalke A, Schulten K (1996) VMD: visual molecular dynamics. *J Mol Graph* 14(1):33–38
61. Jo S, Kim T, Im W (2007) Automated builder and database of protein/membrane complexes for molecular dynamics simulations. *PLoS ONE* 2(9):e880
62. Waterhouse A et al (2018) SWISS-MODEL: homology modelling of protein structures and complexes. *Nucleic Acids Res* 46(W1):W296–W303
63. Madeira F et al (2019) The EMBL-EBI search and sequence analysis tools APIs in 2019. *Nucleic Acids Res* 47(W1):W636–W641

Publisher's Note Springer Nature remains neutral with regard to jurisdictional claims in published maps and institutional affiliations.

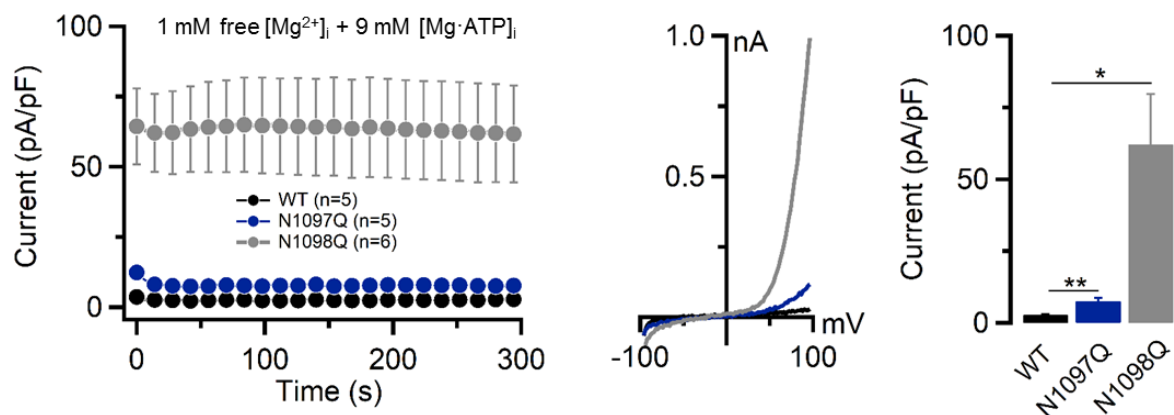
Supplementary figures publication II

In this chapter I only included supplementary figures I produced myself.



Suppl. Figure S3. Inhibition of TRPM7 currents by intracellular Ba^{2+} .

Whole-cell currents were measured in HEK293T cells transfected by WT (**A**), N1097Q (**B**) and N1098Q (**C**) variants of TRPM7 cDNAs (in pIRES2-EGFP). *Left panels*: Current amplitudes (mean \pm SEM) were measured at -80 and +80 mV and plotted over time. Currents were measured using an intracellular solution containing the standard $[Mg^{2+}]_i$ -free intracellular solution and solutions containing 0.55 and 1 mM free $[Ba^{2+}]_i$ (Suppl. Table S2). *Middle panels*: Representative I-V relationships obtained from individual ramps at 300 s in the *Left panels*. *Right panels*: Bar graphs of outward currents (+80 mV, mean \pm SEM) obtained at 300 s as indicated in the *Left panels*. n, number of cells measured; n.s., not significant; ** P < 0.01, *** P < 0.001 (ANOVA).



Suppl. Figure S5. Suppression of TRPM7 currents by 9 mM Mg·ATP in the presence of 1 mM free Mg^{2+} .

Whole-cell currents were measured and analysed analogously to the experiment outlined in Figure 3G, except that 9 mM $[Mg \cdot ATP]_i$ and 1 mM free $[Mg^{2+}]_i$ were included in the intracellular solution (Table S4). n, number of cells measured; n.s., not significant; * $P < 0.05$, ** $P < 0.01$ (ANOVA).

Appendix A: Publication III

Title: The molecular appearance of native TRPM7 channel complexes identified by high-resolution proteomics

<https://elifesciences.org/articles/68544>

<https://doi.org/10.7554/eLife.68544.sa0>

The molecular appearance of native TRPM7 channel complexes identified by high-resolution proteomics

Astrid Kollewe^{1†}, Vladimir Chubnov^{2†}, Fong Tsuen Tseung², Leonor Correia², Eva Schmidt², Anna Rössig², Susanna Zierler^{2,3}, Alexander Haupt¹, Catrin Swantje Müller¹, Wolfgang Bildl¹, Uwe Schulte^{1,4}, Annette Nicke², Bernd Fakler^{1,4*}, Thomas Gudermann^{2,5*}

¹Institute of Physiology II, Faculty of Medicine, University of Freiburg, Freiburg, Germany; ²Walther-Straub Institute of Pharmacology and Toxicology, LMU Munich, Munich, Germany; ³Institute of Pharmacology, Johannes Kepler University Linz, Linz, Austria; ⁴Signalling Research Centres BIOS and CIBSS, Freiburg, Germany; ⁵German Center for Lung Research, Munich, Germany

Abstract The transient receptor potential melastatin-subfamily member 7 (TRPM7) is a ubiquitously expressed membrane protein consisting of ion channel and protein kinase domains. TRPM7 plays a fundamental role in the cellular uptake of divalent cations such as Zn²⁺, Mg²⁺, and Ca²⁺, and thus shapes cellular excitability, plasticity, and metabolic activity. The molecular appearance and operation of TRPM7 channels in native tissues have remained unresolved. Here, we investigated the subunit composition of endogenous TRPM7 channels in rodent brain by multi-epitope affinity purification and high-resolution quantitative mass spectrometry (MS) analysis. We found that native TRPM7 channels are high-molecular-weight multi-protein complexes that contain the putative metal transporter proteins CNNM1-4 and a small G-protein ADP-ribosylation factor-like protein 15 (ARL15). Heterologous reconstitution experiments confirmed the formation of TRPM7/CNNM/ARL15 ternary complexes and indicated that complex formation effectively and specifically impacts TRPM7 activity. These results open up new avenues towards a mechanistic understanding of the cellular regulation and function of TRPM7 channels.

***For correspondence:**

bernd.fakler@physiologie.uni-freiburg.de (BF);

Thomas.Gudermann@lrz.uni-muenchen.de (TG)

[†]These authors contributed equally to this work

Competing interest: The authors declare that no competing interests exist.

Funding: See page 22

Received: 18 March 2021

Preprinted: 09 July 2021

Accepted: 08 November 2021

Published: 12 November 2021

Reviewing Editor: László Csanády, Semmelweis University, Hungary

© Copyright Kollewe et al. This article is distributed under the terms of the [Creative Commons Attribution License](https://creativecommons.org/licenses/by/4.0/), which permits unrestricted use and redistribution provided that the original author and source are credited.

Editor's evaluation

This work will be interesting to people studying TRP family ion channels and more generally, cellular ion homeostasis. It is the first to identify interacting protein partners of the cation channel TRPM7, a key regulator of cellular Mg²⁺ and Zn²⁺ homeostasis, and reveals functional coupling between TRPM7, a putative magnesium transporter, and a small G protein.

Introduction

Transient receptor potential melastatin-subfamily member 7 (TRPM7) encodes a bi-functional protein with a transient receptor potential (TRP) ion channel domain fused to a C-terminal α -type serine/threonine-protein kinase (reviewed in Chubnov et al., 2018; Fleig and Chubnov, 2014; Ryazanov et al., 1997). Among all other known channels and kinases, only its homologue TRPM6 shows a similar design (Ryazanov et al., 1997; Chubnov and Gudermann, 2014).

TRPM7 is involved in various cellular processes such as homeostatic balance, cell motility, proliferation, differentiation, and regulation of immune responses (Chubnov et al., 2018; Fleig and

Chubanov, 2014; Ryazanov et al., 1997). Genetic deletion of *Trpm7* in mice is embryonically lethal, and tissue-specific null mutants have shown defects in cardiac and renal morphogenesis, organismal Zn^{2+} , Mg^{2+} , and Ca^{2+} homeostasis, thrombopoiesis, and mast cell degranulation (*Mittermeier et al., 2019; Chubanov et al., 2004; Jin et al., 2008; Sah et al., 2013b; Sah et al., 2013a; Jin et al., 2012; Stritt et al., 2016; Abiria et al., 2017; Schmitz et al., 2003*). Besides, TRPM7 has emerged as a promising therapeutic target for numerous pathophysiological conditions (*Chubanov et al., 2018; Fleig and Chubanov, 2014; Ryazanov et al., 1997; Hofmann et al., 2014; Aarts et al., 2003; Hermosura et al., 2005*).

The channel-coding segment of TRPM7 comprises six transmembrane helices with a pore-loop sequence between S5 and S6 (*Figure 1A, Duan et al., 2018; Mederos y Schnitzler et al., 2008*). Four subunits assemble to form constitutively active channels highly selective for divalent cations such as Zn^{2+} , Ca^{2+} , and Mg^{2+} (*Nadler et al., 2001; Runnels et al., 2001; Monteilh-Zoller et al., 2003*). Free Mg^{2+} , the Mg-ATP complex, and phosphatidylinositol-4,5-bisphosphate (PIP₂) were described as physiological regulators of the channel activity of TRPM7 (*Nadler et al., 2001; Runnels et al., 2002*). While Mg^{2+} or Mg-ATP act as negative regulators, PIP₂ appears to be a crucial co-factor of the active channel (*Nadler et al., 2001; Runnels et al., 2002*). Mechanistically, however, the effects of Mg^{2+} , Mg-ATP, or PIP₂ on TRPM7 activity are poorly understood, and most likely, there are additional regulators of TRPM7 function with hitherto unknown molecular identity.

The C-terminal α -kinase domain of TRPM7 acts in two ways: First, it autophosphorylates cytoplasmic residues of TRPM7, and second, it may target a variety of proteins with diverse cellular functions such as annexin A1, myosin II, eEF2-k, PLC γ 2, STIM2, SMAD2, and RhoA (*Runnels et al., 2001; Dorovkov and Ryazanov, 2004; Perraud et al., 2011; Clark et al., 2008; Romagnani et al., 2017; Voring et al., 2020; Faouzi et al., 2017*). In immune cells, the TRPM7 kinase domain has been reported to be clipped from the channel domain by caspases in response to Fas-receptor stimulation (*Desai et al., 2012*). In line with this observation, cleaved TRPM7 kinase was detected in several cell lines and shown to translocate to the nucleus, where it promotes histone phosphorylation (*Krapivinsky et al., 2014*).

The majority of the current knowledge about TRPM7 was derived from in vitro experiments with cultured cells, whereas insights into the operation of both channel and α -kinase activity of TRPM7 in native tissues are limited. We, therefore, investigated the molecular architecture of TRPM7 in rodent brain by using blue native polyacrylamide gel electrophoresis (BN-PAGE) and multi-epitope affinity purifications (ME-APs) in combination with high-resolution quantitative mass spectrometry (MS). These approaches showed that native TRPM7 channels are macromolecular complexes with an apparent size of ≥ 1.2 MDa and identified proteins CNNM1-4 and ADP-ribosylation factor-like protein 15 (ARL15) as complex constituents. Subsequent functional studies in *Xenopus laevis* oocytes and HEK293 cells suggested ARL15 and CNNM3 as hitherto unrecognised regulators of the TRPM7 ion channel and kinase activity, respectively.

Results

ME-AP proteomic analyses of native TRPM7 channels

TRPM7 channels assemble from four subunits (*Fleig and Chubanov, 2014*), each of which is about 1860 aa in length and comprises several distinct domains in its extended intracellular N- and C-termini in addition to a transmembrane channel domain (*Figure 1A*). Unexpectedly, analysis by native gel electrophoresis (BN-PAGE) of TRPM7 channels either endogenous to HEK293 cells or exogenously expressed in these cells via transient transfection, elicited a molecular mass of at least 1.2 MDa considerably exceeding the molecular mass of ~850 kDa calculated for TRPM7 tetramers (*Figure 1B, upper panel*). To see whether this large molecular size is a peculiarity of HEK293 cells, we recapitulated the analysis for TRPM7 channels expressed in mouse brain using a recently developed technique that combines BN-PAGE with cryo-slicing and quantitative mass spectrometry (csBN-MS, *Müller et al., 2019*). In this approach, membrane fractions prepared from the entire mouse brain and solubilised with the mild detergent buffer CL-47 (*Schwenk et al., 2016; Schwenk et al., 2012; Müller et al., 2010*) are first separated on a native gel, which is subsequently embedded and cut into 300 μ m gel slices using a cryo-microtome. In a second step, the protein content of each slice is analysed individually by nanoflow liquid chromatography tandem mass spectrometry (nanoLC-MS/MS), providing

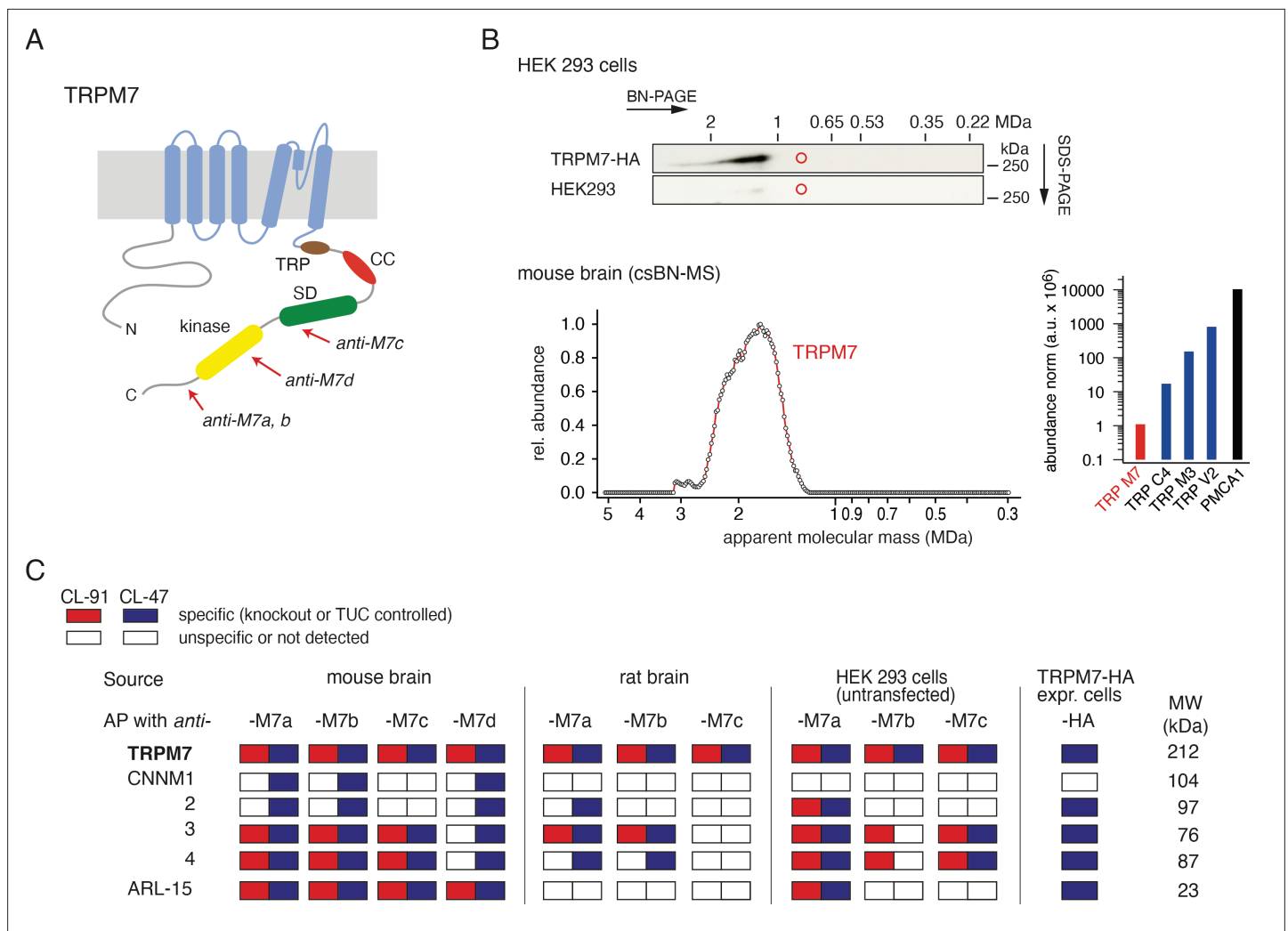


Figure 1. Protein constituents of native transient receptor potential melastatin-subfamily member 7 (TRPM7) channels identified by multi-epitope antibody-based affinity purification (ME-AP) proteomics. **(A)** Topology and localisation of the *anti*-TRPM7 antibodies used for ME-APs. Established hallmark domains of TRPM7 are colour-coded, TRP (transient receptor potential domain, brown), CC (coiled-coil domain, red), kinase (kinase domain, yellow), SD (serine/threonine-rich substrate domain of kinase(s), green). **(B)** *Upper panel*: Two-dimensional gel separation of TRPM7 channels in CL-47 solubilised membrane fractions of HEK293 cells with (*upper panel*) or without (*lower panel*) transfection of HA-tagged *Trpm7*, Western-probed with an *anti*-TRPM7 antibody (Materials and methods). Size (blue native polyacrylamide gel electrophoresis [BN-PAGE]) and molecular weight (SDS-PAGE) are as indicated. *Lower panel*: Abundance-mass profile of TRPM7 obtained by cryo-slicing blue native mass spectrometry (csBN-MS) in a CL-47 solubilised membrane fraction from adult mouse brain (a total of 192 gel slices). Inset: Abundance of the indicated proteins in the mouse brain. Note the large apparent molecular mass of the native TRPM7 channel in both culture cells and mouse brain, markedly exceeding the mass calculated for tetrameric channel assemblies (about 850 kDa, red circles). **(C)** Table summarising the results of all *anti*-TRPM7 APs performed with the indicated antibodies on membrane fractions prepared from rodent brain and cultured HEK293 cells. Solubilisation conditions and specificity of purification of the listed proteins determined by comparison with stringent negative controls are colour-coded as given in the upper left; MW is indicated on the right. TUC refers to series of APs with target-unrelated control antibodies. Note that TRPM7 channels co-assemble with all CNNM family members and ADP-ribosylation factor-like protein 15 (ARL15) in the brain and HEK293 cells.

The online version of this article includes the following figure supplement(s) for figure 1:

Figure supplement 1. The specificity of an *anti*-transient receptor potential melastatin-subfamily member 7 (TRPM7) mouse monoclonal antibody in Western blot assessment of the recombinant TRPM6 and TRPM7 proteins.

information on both the identity and amount of the proteins in each slice; noteworthy, protein amounts are determined with a dynamic range of up to four orders of magnitude (Müller et al., 2010; Schwenk et al., 2010; Bildl et al., 2012). As illustrated in Figure 1B, lower panel, csBN-MS analysis of mouse brain membranes detected the TRPM7 protein with an apparent molecular mass between 1.2 and 2.6 MDa, comparable to the results obtained from HEK293 cells (Figure 1B, upper panel). Moreover, the

determination of the total protein amount by signal integration over all slices showed that TRPM7 levels in the brain are rather low compared to other members of the TRP family of proteins. Thus, the abundance of TRPM7 is about one to three orders of magnitude below that obtained for TRPC4, TRPM3, or TRPV2 (**Figure 1B**, lower right).

Together, these results indicated that native TRPM7 complexes exceed the predicted molecular size of bare tetrameric assemblies in different cellular environments suggesting that the rather simplistic view on the molecular make-up of native TRPM7 channel complexes has to be revised.

To identify proteins that may co-assemble with TRPM7, we used affinity purifications with multiple antibodies targeting distinct epitopes of the TRPM7 protein (**Figure 1A**, **Figure 1—figure supplement 1**) and evaluated the respective eluates of HEK293 cells and rodent brains by high-resolution quantitative MS analysis (ME-APs, **Schwenk et al., 2016**; **Schwenk et al., 2012**; **Müller et al., 2010**; **Schwenk et al., 2010**). HEK293 cells were selected because these cells are widely used for the functional assessment of endogenous and overexpressed TRPM7. The brain was chosen since TRPM7 plays a critical role in neurological injuries and synaptic and cognitive functions (**Aarts et al., 2003**; **Sun et al., 2009**; **Liu et al., 2018**). For these ME-APs, membrane fractions prepared either from whole brains of adult mice and rats or from WT HEK293 cells were solubilised with detergent buffers of mild (CL-47) or intermediate (CL-91) stringency (**Schwenk et al., 2012**; **Müller et al., 2010**; **Schwenk et al., 2010**) prior to TRPM7 purification. TRPM7 was also affinity-isolated from HEK293 cells transiently (over)-expressing C-terminally HA-tagged TRPM7 using an *anti*-HA antibody.

In all APs, TRPM7 could be reliably detected under both solubilisation conditions (**Figure 1C**) with MS-identified peptides covering a large percentage of the primary sequence of TRPM7 in samples from mouse brain as well as from HEK293 cells (77% and 98%, respectively).

All other proteins identified in the ME-APs were evaluated for specificity and consistency of their co-purification with TRPM7 based on protein amounts determined by label-free quantification (see Materials and methods section). The specificity of co-purification was assessed by comparing protein amounts in APs targeting TRPM7 with protein amounts obtained with stringent negative controls. Thus, (i) APs with five different target-unrelated control (TUC) antibodies were used as negative controls for *anti*-TRPM7 APs from rodent brain, (ii) *anti*-TRPM7 APs from a *TRPM7*^{-/-} HEK293 cell line (**Abiria et al., 2017**) served as negative controls for *anti*-TRPM7 APs from WT HEK293 cells, and (iii) HEK293 cells heterologously expressing TRPM7-myc were used as negative

Table 1. Protein constituents of native transient receptor potential melastatin-subfamily member 7 (TRPM7) channels identified by multi-epitope affinity purifications (ME-APs).

Protein ID	Acc. No. UniProtKB	Name	Primary function	Rel. abundance	
				CL-47	CL-91
TRPM7	Q923J1	TRP channel M7	Ion channel	=	=
CNNM1	Q0GA42	Transporter CNNM1, Cyclin-M1	Potential transporter	<<	
CNNM2	Q5U2P1	Transporter CNNM1, Cyclin-M2	Potential transporter	<	<<
CNNM3	Q32NY4	Transporter CNNM1, Cyclin-M3	Potential transporter	<	<<
CNNM4	Q69ZF7	Transporter CNNM1, Cyclin-M4	Potential transporter	<	<<
ARL15	Q8BGR6	ADP-ribosylation factor-like protein 15	Unknown	=	<<
TP4A1 [†]	Q93096	Protein tyrosine phosphatase type IVA 1	Enzyme	<<<	<<
TP4A3 ^{##}	Q9D658	Protein tyrosine phosphatase type IVA 3	Enzyme		<<
TRPM6 ^{###}	Q9BX84	TRP channel M6	Ion channel	<<<	<<

Notes: Relative abundance refers to the amount of TRPM7 as a reference and was classified as follows: = when between 0.33-fold and 3.3-fold of reference, < when between 0.033-fold and 0.33-fold of reference, << when between 0.0033-fold and 0.033-fold of reference, and <<< when less than 0.0033-fold of the reference amount.

■ Transmembrane proteins; ■ cytoplasmic proteins.

[†]Co-purified from HEK293 cells with *anti*-M7a (CL-47) and with *anti*-M7c (CL-91); ^{##}co-purified with *anti*-M7c from rat brain membranes (CL-91); ^{###}co-purified with *anti*-M7a from HEK293 cells (CL-47, CL-91).

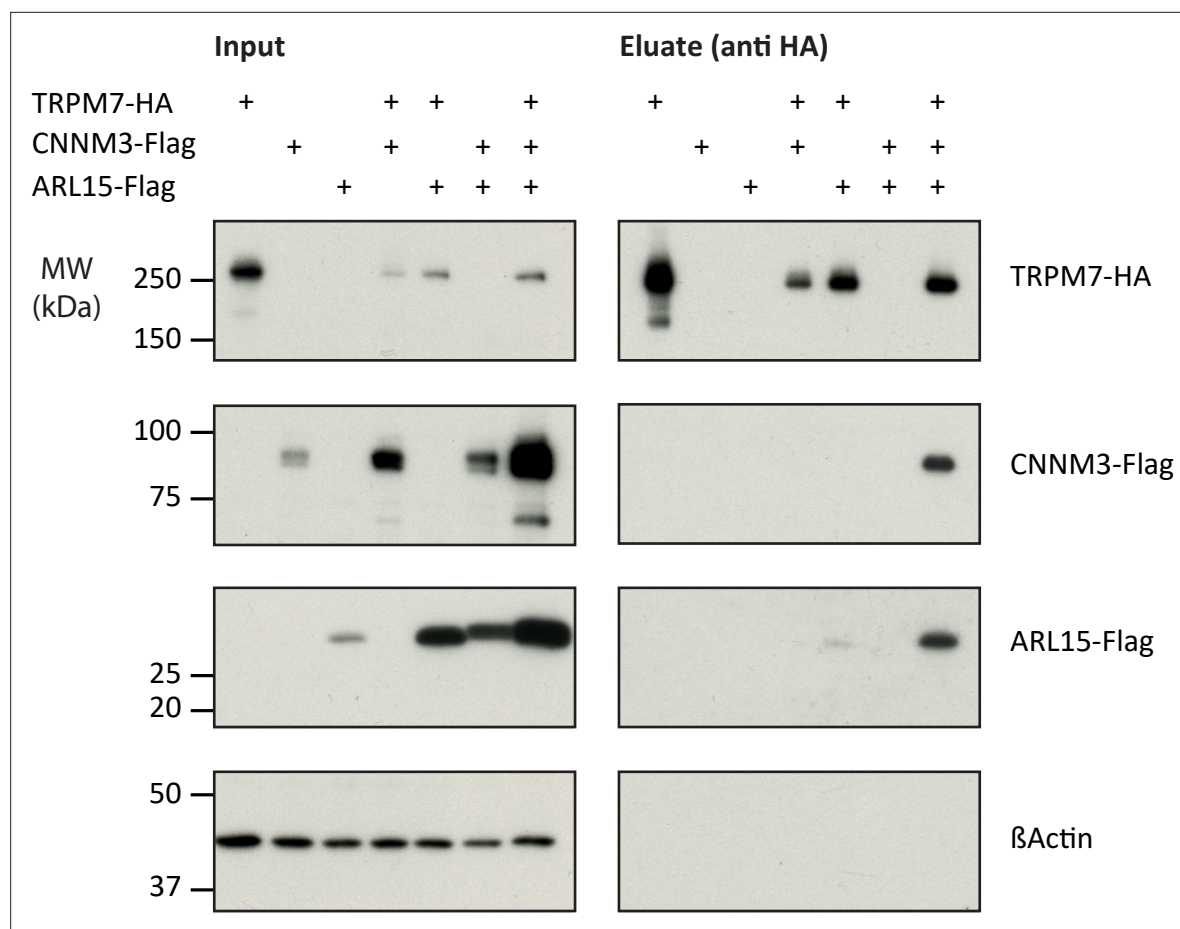


Figure 2. Heterologous reconstitution of transient receptor potential melastatin-subfamily member 7 (TRPM7) complexes in HEK293 cells. Affinity purifications (APs) with *anti*-HA antibody from CL-47 solubilised membrane fractions of *TRPM7*^{-/-} HEK293 cells transiently expressing the proteins indicated above. Input and eluates of the distinct APs were separated by SDS-PAGE and Western-probed with *anti*-Flag, *anti*-HA, and *anti*-β-actin antibodies. Molecular weight (MW) is marked on the left.

The online version of this article includes the following figure supplement(s) for figure 2:

Figure supplement 1. Heterologous reconstitution of transient receptor potential melastatin-subfamily member 7 (TRPM7) complexes in HEK293 cells.

controls for *anti*-HA APs from HEK293 cells overexpressing TRPM7-HA. A protein was considered consistently co-purified if detected in APs with at least two antibodies under the same solubilisation condition. Together, these specificity and consistency criteria identified five proteins as high-confidence interaction partners of TRPM7: ARL15 and the cyclin M family proteins CNM1-4, putative Mg²⁺ transporters (**Figure 1C**, **Table 1**). Neither of these proteins was detected in any of the negative controls. Moreover, they were not only consistently co-purified with several antibodies but with the exception of CNM1 also from both rodent brain and HEK293 cells. Comparison of the degree of association under the two solubilisation conditions revealed that the interaction between TRPM7, ARL15, and CNMs was weakened by the more stringent detergent CL-91 (**Figure 1C**, **Table 1**).

Next, we verified the identified interactions between TRPM7, ARL15, and CNM1-4 in co-expression experiments performed in *TRPM7*^{-/-} HEK293 cells (**Figure 2**). Flag-tagged ARL15 and CNM proteins could be specifically and robustly co-purified with HA-tagged TRPM7 in *anti*-HA APs when all three proteins were present, whereas the association was markedly less efficient when ARL15-Flag or CNM-Flag were co-expressed with TRPM7-HA alone (**Figure 2**, **Figure 2—figure supplement 1**). These results corroborated the ME-AP results from the rodent brain and strongly suggested the formation of ternary complexes containing TRPM7, ARL15, and CNM proteins.

Effects of CNNM3 and ARL15 on TRPM7 channel activity

To investigate if the assembly of TRPM7 with ARL15 and CNNM proteins modified TRPM7 function, we studied their effect(s) on TRPM7 currents by co-expression in *X. laevis* oocytes. This approach allows co-expression of defined protein ratios by cRNA injection and, therefore, is widely used for functional assessment of ion channel complexes, including functional interaction of TRPM7 with TRPM6 (Chubanov et al., 2018; Chubanov et al., 2004). The two-electrode voltage clamp (TEVC) measurement in Figure 3A illustrates a typical current-voltage (I-V) relationship of constitutively active TRPM7 channels characterised by steep outward rectification and very small inward currents over the whole range of negative membrane potentials (Nadler et al., 2001). Co-expression of TRPM7 and CNNM3, the most efficiently co-purified CNNM protein (Figure 1C), neither changed the shape of the I-V relationship nor current amplitudes. In contrast, ARL15 effectively suppressed constitutive TRPM7 currents in a concentration-dependent manner, as deduced from experiments with increasing amounts of ARL15 (Figure 3B and C). Oocytes co-expressing all three proteins TRPM7, CNNM3, and ARL15 did not exhibit TRPM7 currents, similar to the co-expression of TRPM7 and ARL15 (Figure 3A). The suppressive effect was specific for TRPM7, as co-expressed ARL15 did not inhibit another TRP channel, TRPV1, in an analogous experiment (Figure 3—figure supplement 1). Consistently, co-expression of TRPM7 with another ARL family member, ARL8A (Gillingham and Munro, 2007), did not affect TRPM7 currents (Figure 3—figure supplement 2).

Next, we examined if the interference of ARL15 with the TRPM7 function was due to reduced expression levels or altered membrane localisation. Western blot analysis of oocytes injected with *Trpm7* or *Trpm7* and *Arl15* cRNAs did not reveal any change in the expression level of TRPM7 protein (Figure 3D). Using immunofluorescence staining with the anti-M7d antibody, we detected TRPM7 at the cell surface of oocytes injected with *Trpm7* but not in uninjected oocytes (Figure 3E). Notably, the TRPM7 signal was similarly detectable at the cell surface of oocytes co-expressing TRPM7 and ARL15 (Figure 3E).

TRPM7 inward currents at negative membrane potentials are small, and, consequently, quantification of the comparably large outward currents is commonly used for functional assessment of the TRPM7 channel activity. Nevertheless, we asked whether TRPM7 inward currents could be equally suppressed by ARL15 (Figure 3—figure supplement 3A, B). This analysis revealed that ARL15 acted similarly on inward and outward TRPM7 currents, suggesting that ARL15 elicited a general block of the TRPM7 channel.

To obtain further insight into the functional interaction of ARL15 with TRPM7, we investigated whether the kinase activity of TRPM7 is necessary for the inhibitory effect of ARL15. To this end, we examined oocytes expressing a kinase-dead TRPM7 mutant (K1646R, Nadler et al., 2001; Runnels et al., 2002) and observed that the K1646R mutation did not change the sensitivity of TRPM7 for the inhibitory effect of ARL15 (Figure 3—figure supplement 3C).

Finally, we investigated whether ARL15 could also regulate TRPM7 channels in mammalian cells. Using the patch-clamp technique, we measured endogenous TRPM7 currents in HEK293 cells. Similar to previous reports (Chubanov et al., 2004; Ferioli et al., 2017), removing intracellular Mg^{2+} by using a pipette solution free of divalent cations induced endogenous TRPM7 currents (Figure 3—figure supplement 4). Transient expression of ARL15 however caused a significant reduction of these TRPM7 currents (Figure 3—figure supplement 4).

Collectively, these results suggest that the inhibitory effect of ARL15 on TRPM7 currents is specific and concentration-dependent.

Impact of CNNM3 on TRPM7 Mg^{2+} currents and kinase activity

Given the crucial role of TRPM7 and CNNM proteins in membrane Mg^{2+} transport (Mittermeier et al., 2019; Schmitz et al., 2003; Funato and Miki, 2019), we asked whether CNNM3 would specifically affect TRPM7 Mg^{2+} currents rather than exerting a general (i.e., ARL15-like) effect. To this end, we conducted TEVC measurements with TRPM7-expressing oocytes using external saline containing 3 mM Mg^{2+} (instead of 3 mM Ba^{2+} in Figure 3A), implying that at negative membrane potentials, the TRPM7 channel should primarily exhibit Mg^{2+} currents under such experimental conditions (Nadler et al., 2001). TRPM7 expressing oocytes displayed characteristic TRPM7 currents with a very small inward Mg^{2+} component, which was suppressed by co-expression of ARL15 (Figure 4A and B) in accord with previous experiments (Figure 3—figure supplement 3A, B). In contrast, co-expression of CNNM3 did not change the properties of the TRPM7 channel (Figure 4C and D).

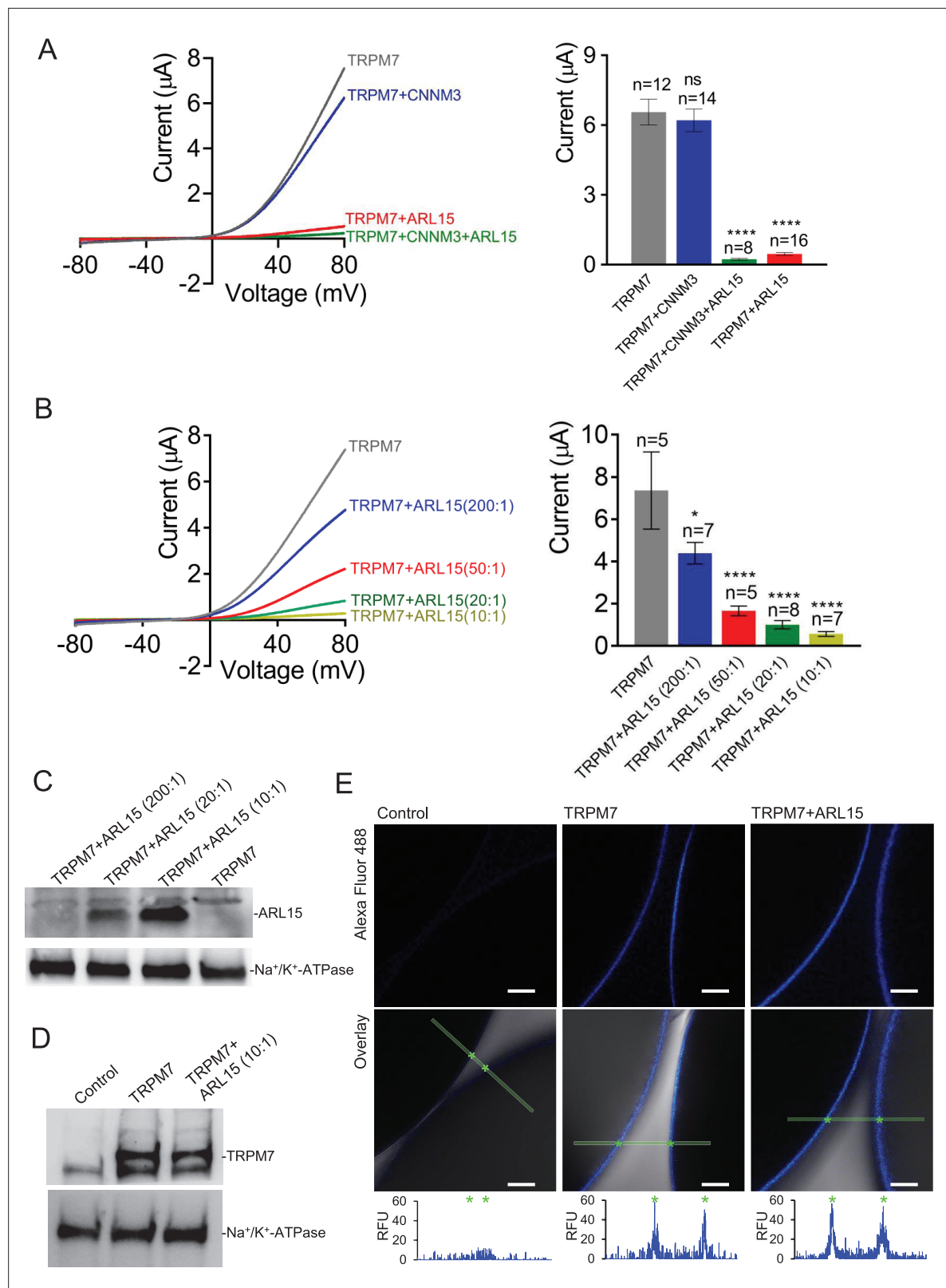


Figure 3. Heterologous expression of transient receptor potential melastatin-subfamily member 7 (TRPM7) in *Xenopus* oocytes. **(A, B)** Two-electrode voltage clamp (TEVC) measurements of TRPM7 currents. **(A) Left panel:** Representative current-voltage (I-V) relationships of TRPM7 currents measured in oocytes expressing TRPM7 alone or TRPM7 with CNNM3 or ADP-ribosylation factor-like protein 15 (ARL15) (cRNAs ratio 2:1), and TRPM7 with CNNM3 and ARL15 (cRNAs ratio 2:1:1). **Right panel:** Current amplitudes (mean \pm standard error of the mean [SEM]) at +80 mV in measurements shown on the Figure 3 continued on next page

Figure 3 continued

left. Two independent batches of injected oocytes ($n = 8\text{--}16$) were examined. $*p < 0.05$; $****p < 0.0001$ (ANOVA). (B) Left panel: Representative I-V relationships of TRPM7 currents measured in oocytes expressing TRPM7 or co-expressing TRPM7 with ARL15 at the indicated ratios of injected cRNAs. Right panel: Current amplitudes (mean \pm SEM) at +80 mV in measurements shown on the left. Two independent batches of injected oocytes ($n = 5\text{--}7$) were examined. $*p < 0.05$; $****p < 0.0001$ (ANOVA). (C) Western blot analysis of ARL15 expression using the anti-Myc antibody in total lysates of oocytes injected with *Trpm7* or *Trpm7* and *Arl15* cRNAs (ratios 200:1, 20:1, and 10:1). Representative results are shown for two independent experiments. Anti- Na^+/K^+ -ATPase antibody was used for loading controls. (D) Western blot analysis of TRPM7 expression using the anti-M7d antibody in total lysates of oocytes injected with *Trpm7* or *Trpm7* and *Arl15* cRNAs (ratio 10:1). Anti- Na^+/K^+ ATPase antibody was used for loading controls. Representative results are shown for two independent experiments. (E) Immunofluorescence staining of un-injected oocytes (control) or oocytes injected with *Trpm7* (TRPM7) or *Trpm7* and *Arl15* cRNAs (TRPM7+ ARL15, ratio 10:1) using anti-M7d antibody and anti-mouse antibody conjugated with Alexa Fluor 488. Confocal images of Alexa Fluor 488 fluorescence (Alexa488) and overlays of Alexa488 with differential interference contrast images (overlay) are depicted for two independent oocytes per image; scale bars, 50 μm . The diagrams depict fluorescence intensity acquired along the green bars shown in overlay images. The stars indicate the cell surface of two oocytes. Typical examples of two independent experiments ($n = 10$ oocytes) are shown.

The online version of this article includes the following figure supplement(s) for figure 3:

Figure supplement 1. Two-electrode voltage clamp (TEVC) measurements of capsaicin-induced TRPV1 currents in *Xenopus* oocytes.

Figure supplement 2. Heterologous expression of transient receptor potential melastatin-subfamily member 7 (TRPM7), ARL8A, and ADP-ribosylation factor-like protein 15 (ARL15) in *Xenopus* oocytes.

Figure supplement 3. Assessment of the importance of the transient receptor potential melastatin-subfamily member 7 (TRPM7) kinase activity for the functional interplay between ADP-ribosylation factor-like protein 15 (ARL15) and TRPM7 by two-electrode voltage clamp (TEVC) measurements.

Figure supplement 4. Impact of ADP-ribosylation factor-like protein 15 (ARL15) on endogenous transient receptor potential melastatin-subfamily member 7 (TRPM7) currents in HEK293 cells.

Next, we studied whether heterologous expression in mammalian cells would allow uncovering any functional effects of CNNM3 on TRPM7. We transiently transfected HEK293 cells with *Trpm7* and *Cnnm3* plasmid cDNAs (ratio 2:1) and performed patch-clamp measurements (**Figure 4—figure supplement 1**). TRPM7 currents were induced using the standard divalent cation-free internal solution and an external buffer containing 1 mM CaCl_2 and 2 mM MgCl_2 . When currents were developed, cells were exposed to mannitol-based saline containing 10 mM Mg^{2+} . In accord with previous publications (**Feroli et al., 2017**), the perfusion of TRPM7-expressing cells with 10 mM Mg^{2+} led to a significant reduction of outward currents accompanied by a relatively modest decrease of inward currents (**Figure 4—figure supplement 1**). Corresponding experiments with cells co-expressing TRPM7 and CNNM3 showed similar results (**Figure 4—figure supplement 1**), compatible with a TRPM7 Mg^{2+} permeability unaltered by co-expression of CNNM3, regardless of the heterologous expression system.

Previously, we found that TRPM7 controls the uptake of Mg^{2+} to maintain the cellular content of this mineral in resting cells (**Mittermeier et al., 2019**). To investigate whether CNNM3 modulates TRPM7-dependent Mg^{2+} uptake, we employed inductively coupled plasma mass spectrometry (ICP-MS) to compare total amounts of magnesium in *TRPM7*^{-/-} HEK293 cells transfected with *Trpm7*, *Cnnm3*, or *Trpm7* plus *Cnnm3* cDNAs (**Figure 4—figure supplement 2**). Next, we normalised the levels of magnesium to cellular sulphur (a biomarker for the total protein content) and observed that transient expression of TRPM7 increased the cellular Mg content, whereas expression of CNNM3 did not change this parameter (**Figure 4—figure supplement 2**). Importantly, we found that co-expression of TRPM7 with CNNM3 did not impact the ability of TRPM7 to regulate the cellular content of Mg^{2+} (**Figure 4—figure supplement 2**). Hence, different experimental approaches did not reveal significant effects of CNNM3 on TRPM7 channel activity.

Since TRPM7 contains a C-terminal kinase domain, we studied whether CNNM3 might modulate the TRPM7 kinase moiety (**Figure 5** and **Figure 5—figure supplement 1**). To assess the activity of the TRPM7 kinase, we relied on the anti-(p)Ser1511 M7 antibody, which specifically recognises the known autophosphorylation site (Ser1511) of mouse TRPM7 (**Romagnani et al., 2017**). To verify that autophosphorylation of Ser1511 is dynamic, and changes of the TRPM7 kinase activity could therefore be visualised by the anti-(p)Ser1511 M7 antibody we treated HEK293 cells transiently overexpressing TRPM7 with TG100-115, a drug-like TRPM7 kinase inhibitor (**Song et al., 2017**). We observed that the exposure of living cells to TG100-115 led to suppression of (p)Ser1511 TRPM7 immunoreactivity in a dose-dependent fashion (**Figure 5—figure supplement 1A**). Moreover, the inhibitory effect of TG100-115 was time-dependent and could be detected 10 min after application of TG100-115

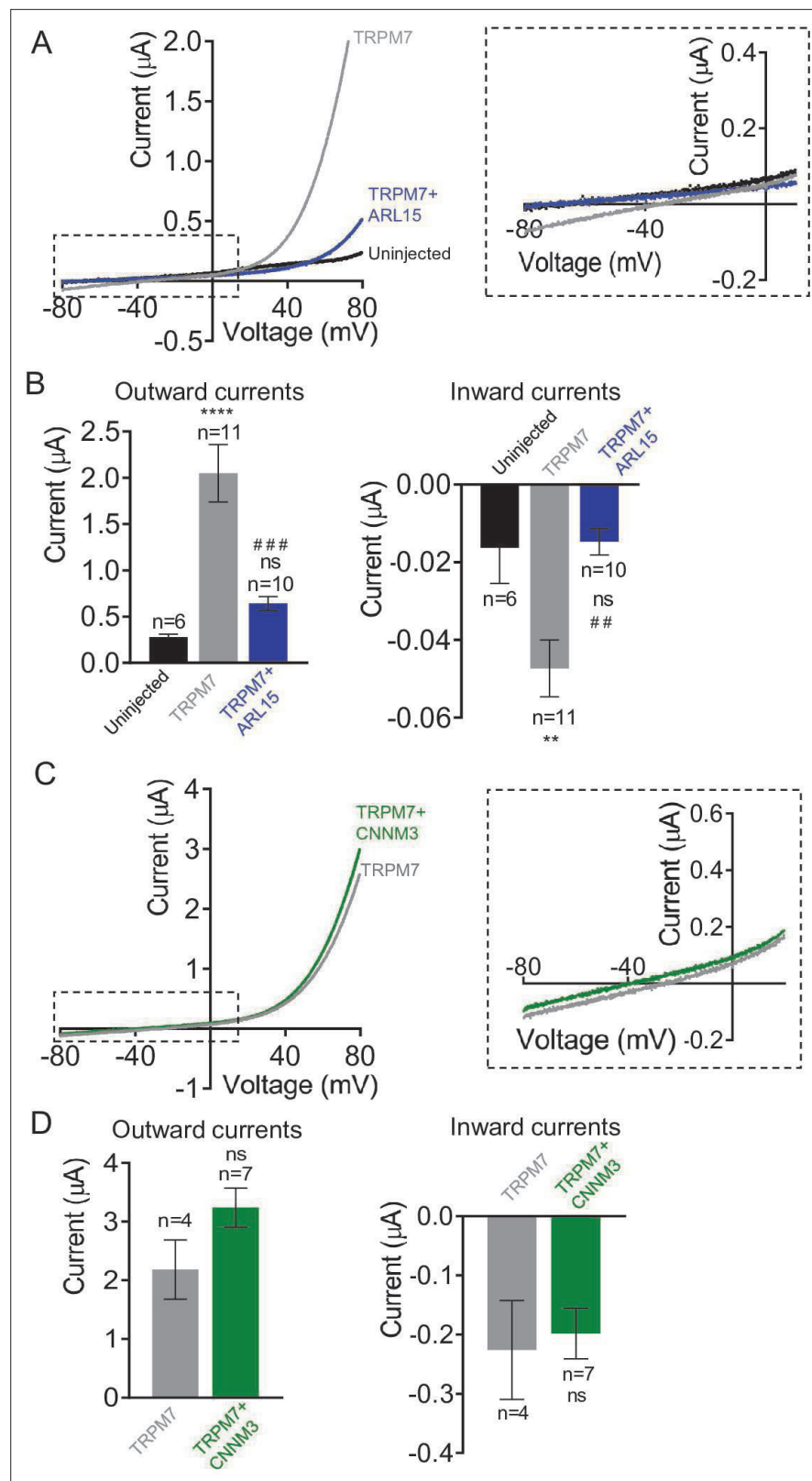


Figure 4. Effects of ADP-ribosylation factor-like protein 15 (ARL15) and CNNM3 on Mg^{2+} currents of the transient receptor potential melastatin-subfamily member 7 (TRPM7) channel expressed in *Xenopus* oocytes.

TEVC measurements were performed using the external ND96 solution containing 3 mM Mg^{2+} and no other divalent cations. (A, B) Assessment of oocytes expressing TRPM7 or co-expressing TRPM7 with ARL15 (cRNA ratio

Figure 4 continued on next page

Figure 4 continued

10:1). (A) Representative I-V relationships of TRPM7 currents. The dashed box in Left panel indicates the area of inward currents enlarged in the Right panel. (B) Current amplitudes (mean \pm SEM) at +80 mV (Outward currents) and at -80 mV (Inward currents) in measurements from (A). Two independent batches of injected oocytes (n=6-11) were examined. ns, not significant; ** P < 0.01, **** P < 0.0001 significant to the Uninjected group (ANOVA). ## P < 0.01, ### P < 0.001 significant to the TRPM7 group (ANOVA). (C, D) Examination of oocytes expressing TRPM7 or co-expressing TRPM7 with CNNM3 (cRNA ratio 2:1). Data were produced and analyzed as explained in (A, B). Two independent batches of injected oocytes (n=4-7) were examined. ns, not significant (two-tailed t-test).

The online version of this article includes the following figure supplement(s) for figure 4:

Figure supplement 1. Heterologous expression of transient receptor potential melastatin-subfamily member 7 (TRPM7) and CNNM3 in HEK293T cells.

Figure supplement 2. Assessment of total magnesium levels in *TRPM7*^{-/-} HEK293T cells transiently transfected with *Trpm7* and *Cnnm3* plasmid cDNAs.

(Figure 5—figure supplement 1B). Furthermore, we found that wash-out of TG100-115 by fresh cell culture medium caused a fast recovery of the (p)Ser1511 TRPM7 signal (Figure 5—figure supplement 1C). Hence, detection of (p)Ser1511 TRPM7 levels seems a reliable means to monitor the TRPM7 kinase activity. Accordingly, we investigated whether co-expression of ARL15 could modulate TRPM7 kinase activity and found no changes in (p)Ser1511 TRPM7 immunoreactivity (Figure 5). Co-expression of CNNM3 however caused a significant reduction of the (p)Ser1511 TRPM7 signal (Figure 5), suggesting that CNNM3 functions as a negative regulator of the TRPM7 kinase.

Identification of new phosphorylation sites in the TRPM7 protein

In addition to subunit assembly, the MS data provided further insight into the post-translational modification(s) of the TRPM7 protein. Thus, TRPM7 purified either from rodent brain or from transfected HEK293 cells showed very similar patterns of serine and threonine phosphorylation, reflected by matching MS/MS spectra of peptides harbouring phosphorylation sites (Figure 6A, Figure 6—figure supplement 1, Supplementary file 2 to Figure 6). Out of the nine shared phospho-sites, four have not been reported for TRPM7 in native tissue before (S1300, S1360, T1466, and S1567; Supplementary file 2 to Figure 6). An additional 26 phosphorylated serine and threonine residues could be assigned to TRPM7 isolated from HEK 293 cells, presumably based on the higher amounts of TRPM7 available for analysis from heterologous (over)-expression material; 22 of these 26 sites match sites previously reported for TRPM7 endogenously or heterologously expressed in cell lines, and four sites were newly detected (S1208, S1480, S1496, S1853; Supplementary file 2 to Figure 6). Most of the identified phosphorylation sites were found to cluster within the C-terminal cytoplasmic domain of TRPM7.

Finally, we asked whether measuring TRPM7 channel activity by TEVC would reveal any functional consequences of TRPM7 phosphorylation. We introduced phosphomimetic mutations in a subset of identified phospho-sites (S1208D, S1360D, S1480D, S1496D, and S1567D) and found that three TRPM7 mutants (S1208D, S1496D, and S1567D) displayed enhanced current amplitudes (Figure 6B and C), whereas their expression levels were similar to WT TRPM7 (Figure 6D). These findings suggest that phosphorylation of TRPM7 may represent a new regulatory mechanism reminiscent of the situation with TRPM8 (Rivera et al., 2021). To substantiate this notion further, it will be interesting to carry out a systematic functional analysis of the surprisingly extensive phosphorylation profile of TRPM7 (Figure 6).

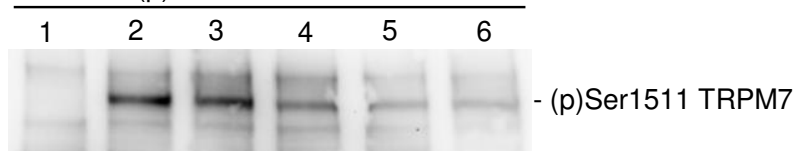
Discussion

In the present study, we investigated the molecular appearance and subunit composition of TRPM7 as present in the cell membrane(s) of the rodent brain. We show that TRPM7 forms macromolecular complexes by assembling with CNNM proteins 1-4 and ARL15. Moreover, functional expression in heterologous expression systems showed that ARL15 strongly affects TRPM7 channel function, while CNNM3 appears to act as a negative regulator of TRPM7 kinase activity.

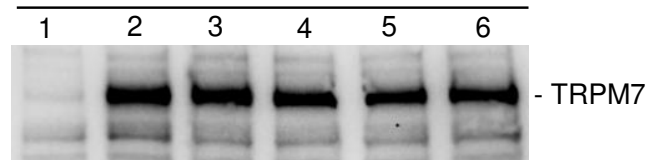
BN-PAGE of membrane fractions isolated from rodent brain and cultured HEK 293 cells identified endogenous TRPM7 in high ~1.2 MDa molecular weight complexes exceeding the calculated

A

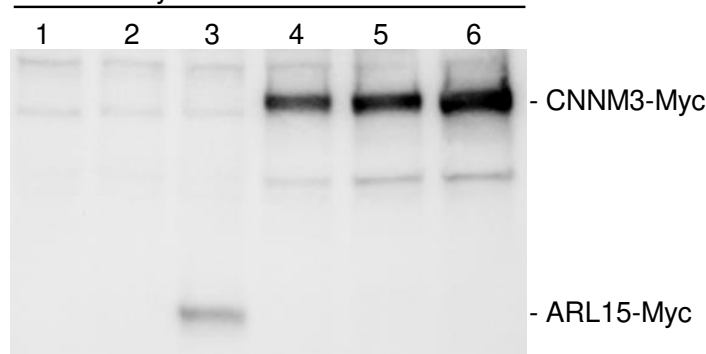
Blot: anti-(p)Ser1511 M7



Blot: anti-M7d



Blot: anti-Myc

**Samples key:**

- 1 - Untransfected cells
- 2 - TRPM7
- 3 - TRPM7 + ARL15 (10:1)
- 4 - TRPM7 + CNNM3 (10:1)
- 5 - TRPM7 + CNNM3 (4:1)
- 6 - TRPM7 + CNNM3 (2:1)

B

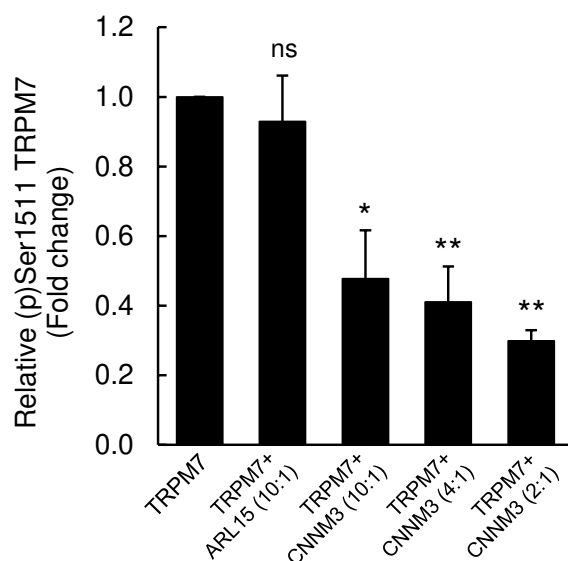


Figure 5. Impact of ADP-ribosylation factor-like protein 15 (ARL15) and CNNM3 on transient receptor potential melastatin-subfamily member 7 (TRPM7) autophosphorylation at Ser1511. **(A)** HEK293 cells were transiently transfected with *Trpm7*, co-transfected with *Trpm7* and *Arl15*, or with *Trpm7* and different amounts of *Cnnm3* plasmid cDNAs. Twenty-four hours after transfection, cell lysates were examined using an anti-(p)Ser1511 M7 antibody (upper panel). After a stripping step, the blot was probed with anti-M7d (middle panel) and anti-Myc antibodies (lower panel) to detect total levels of

Figure 5 continued on next page

Figure 5 continued

TRPM7, ARL15-Myc, and CNNM3-Myc, respectively. Representative results are shown from three independent experiments. (B) Quantification of (p)Ser1511 TRPM7 levels in Western blot experiments ($n = 3$) shown in (A). A relative band density for each sample was obtained by dividing the (p)Ser1511 signal (upper panel) by the corresponding anti-M7d value (middle panel). The relative density of Sample 2 (TRPM7) was set as a 1.0 to calculate changes in (p)Ser1511 TRPM7 (mean \pm standard error of the mean [SEM]) caused by co-transfection of *Arl15* or *Cnnm3* as outlined in the bar graph. ns, not significant; * $p \leq 0.05$, ** $p \leq 0.01$ significant to the control (ANOVA).

The online version of this article includes the following figure supplement(s) for figure 5:

Figure supplement 1. Effects of TG100-115 on transient receptor potential melastatin-subfamily member 7 (TRPM7) autophosphorylation.

molecular mass of TRPM7 tetramers (~850 kDa) and suggesting that the TRPM7 channel kinase is predominantly embedded in a large macromolecular complex. Compared to other native TRP channels, such as TRPC4, TRPM3, and TRPV2, the expression level of TRPM7 was found to be up to three orders of magnitude lower, thus classifying TRPM7 as a very low-abundant protein in the rodent brain and indicating that comprehensive determination of the TRPM7 complexome is technically challenging. The unbiased ME-AP approach paired with stringent negative controls nevertheless allowed for the identification of high-confidence interaction partners based on their specific and consistent co-purification with TRPM7. Consequently, five proteins were found to assemble with native TRPM7, including four members of the *CNNM* gene family encoding putative Mg^{2+} transporters CNNM1-4 and a small G-protein ARL15. The fact that we did not detect all the interactors seen in mouse brain also in APs from rat brain is most likely due to the low abundance of endogenous TRPM7 (~50% less TRPM7 compared to APs from mouse brain). The interaction of TRPM7 with ARL15 and CNNM proteins was successfully confirmed in heterologous expression experiments. We also noted that previous proteome-wide interactome screens in cultured cells suggested an association of ARL15 with TRPM7 (Huttlin et al., 2017; Huttlin et al., 2021), in line with our results.

To obtain first insight into a possible functional impact of ARL15 and CNNM3, the most prominent interaction partners of TRPM7 in our experimental settings, we measured the channel activity of TRPM7 expressed in *Xenopus* oocytes and HEK293 cells. We found that co-expression of TRPM7 with CNNM3 did not lead to significant changes in TRPM7 currents applying a broad range of experimental conditions. Consistently, we observed that the ability of TRPM7 to increase cellular Mg levels was not affected by CNNM3. However, CNNM3 appears to act as a negative regulator of the TRPM7 kinase activity, resembling the action of the drug-like kinase inhibitor TG100-115. Collectively, these results suggest that CNNM3 may represent the first known protein acting as a physiological modulator of the TRPM7 kinase activity.

In contrast to CNNM3, co-expression of TRPM7 with ARL15 in oocytes, but not with the closely related small G-protein ARL8A, caused robust suppression of TRPM7 currents regardless of the experimental conditions applied. Of note, transient expression of ARL15 in HEK 293 cells resulted in inhibition of endogenous TRPM7 currents, reinforcing our conclusion that ARL15 acts as a potent and specific negative regulator of the TRPM7 channel.

The *CNNM* (Cyclin M; CorC) gene family encodes highly conserved metal transporter proteins identified in all branches of living organisms, ranging from prokaryotes to humans (Funato and Miki, 2019; Giménez-Mascarell et al., 2019). There are four family members in mammals, CNNM1-4, widely expressed in the body and abundantly present in the brain (Funato and Miki, 2019; Giménez-Mascarell et al., 2019). The genetic inactivation of *Cnnm4* in mice leads to systemic Mg^{2+} deficiency (Yamazaki et al., 2013). In humans, point mutations in *CNNM2* cause hypomagnesemia (Stuiver et al., 2011), while mutations in *CNNM4* are associated with Jalili syndrome (Parry et al., 2009). Functional expression studies proposed that CNNMs operate as Na^+/Mg^{2+} exchangers responsible for the efflux of cytosolic Mg^{2+} from the cell (Funato and Miki, 2019; Giménez-Mascarell et al., 2019). In contrast to this view, other investigators proposed that CNNM proteins indirectly regulate the influx of Mg^{2+} into the cell (Arjona and de Baaij, 2018). Recently resolved crystal structures of two prokaryotic CNNM-like proteins revealed that CNNMs form dimers and that each monomer contains three transmembrane helices harbouring Mg^{2+} and Na^+ binding sites consistent with the suggested Na^+ -coupled Mg^{2+} transport function of CNNMs (Huang et al., 2021; Chen et al., 2021). While the majority of CNNM proteins in a cell is not bound to TRPM7, the direct association identified in this study suggests a new concept implying that two transporting mechanisms, TRPM7-mediated influx of divalent cations (Zn^{2+} , Mg^{2+} , and Ca^{2+}) and CNNM-dependent Na^+/Mg^{2+} exchange, can be physically coupled under

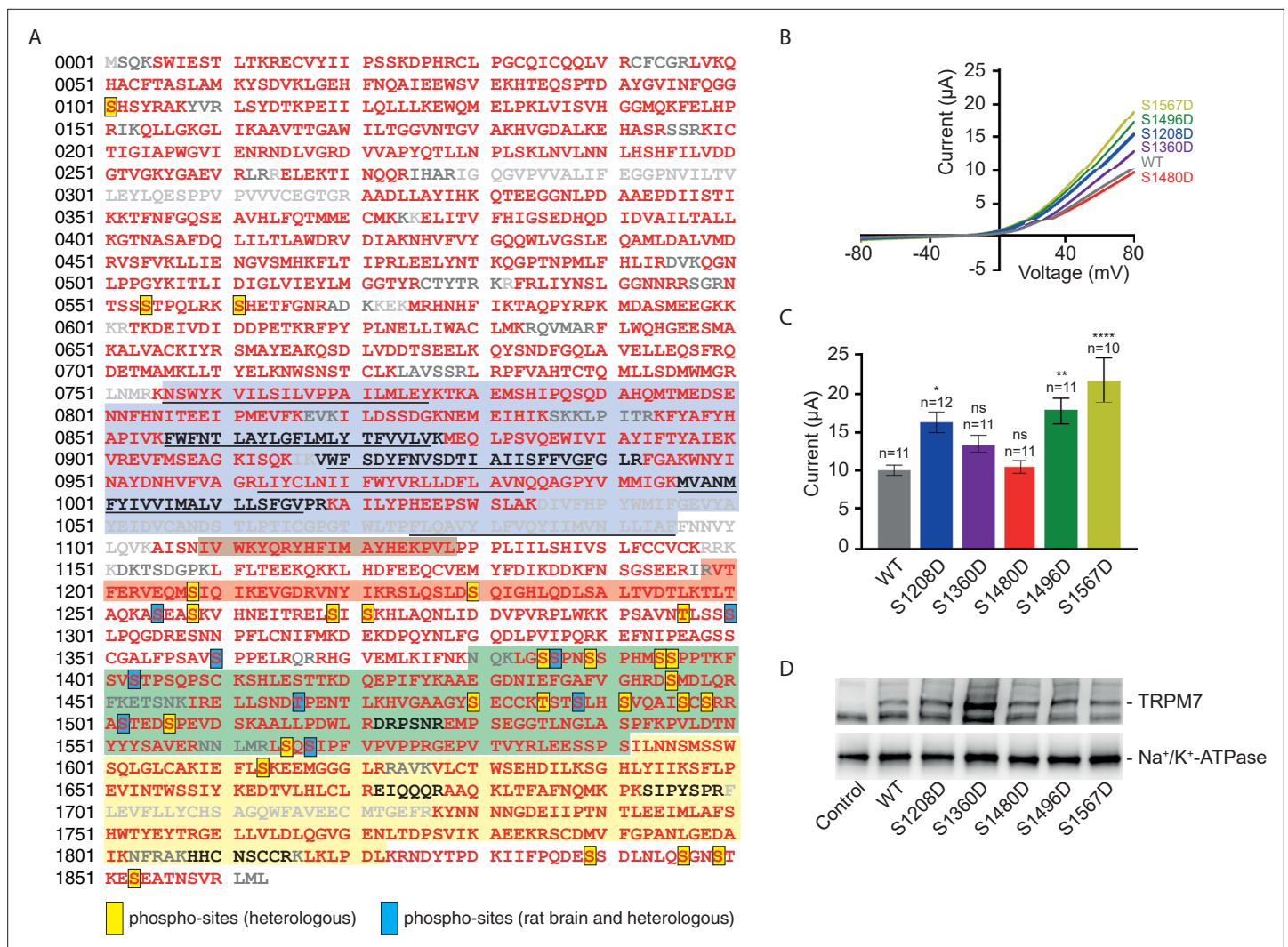


Figure 6. Identification of transient receptor potential melastatin-subfamily member 7 (TRPM7) phospho-sites and functional assessment of phosphomimetic TRPM7 mutants. **(A)** Coverage of the primary sequence of TRPM7 and phosphorylation sites as identified by mass spectrometry (MS) analyses of affinity purifications (APs) from transfected HEK293 cells and rodent brain. Peptides identified by MS are in red; those accessible to but not identified in tandem mass spectrometry (MS/MS) analyses are in black, and peptides not accessible to the MS/MS analyses used are given in grey. Blue boxes indicate phospho-sites identified in the brain and transfected HEK293 cells; those uniquely seen in heterologous expressions are boxed in yellow. Colour coding of hallmark domains is as in **Figure 1A**; S1-S6 helices of TRPM7 are underlined. **(B, C)** Two-electrode voltage clamp (TEVC) measurements of phosphomimetic TRPM7 mutants performed and analysed as explained in **Figure 3A**. **(B)** Representative current-voltage (I-V) relationships of TRPM7 currents measured in oocytes expressing WT and mutant variants of TRPM7, as indicated. **(C)** Current amplitudes (mean \pm standard error of the mean [SEM]) at +80 mV of measurements shown in **(B)**. Two independent batches of injected oocytes ($n = 10$ – 12) were examined. ns, not significant; * $p \leq 0.05$, ** $p \leq 0.01$, **** $p \leq 0.0001$ (ANOVA). **(D)** Western blot analysis of TRPM7 variants with phosphomimetic mutations expressed in *Xenopus* oocytes. Lysates of un-injected oocytes (control) or oocytes injected with WT and indicated mutant variants of *Trpm7* cRNAs were examined using the anti-M7d antibody. The anti- Na^+/K^+ ATPase antibody was used for loading controls. Representative results are shown for three independent experiments.

The online version of this article includes the following figure supplement(s) for figure 6:

Figure supplement 1. Tandem mass spectrometry (MS/MS) spectra illustrating phosphorylation of Ser1567 in transient receptor potential melastatin-subfamily member 7 (TRPM7) from both brain (upper panel) and culture cells (lower panel).

native conditions, thus, warranting future studies to examine the exact functional interplay between the channel-kinase TRPM7 and CNNMs.

ARL15 is a member of the ARF gene family of small G-proteins (Gillingham and Munro, 2007). A common feature of ARFs is their ability to bind and regulate effector proteins in a GTP-dependent manner (Gillingham and Munro, 2007). GDP- and GTP-bound states of ARFs are controlled by GTPase-activating proteins (GAP) in conjunction with GTP exchange factors (GEF) (Gillingham and

Munro, 2007). The best-characterised ARFs are involved in membrane trafficking, phospholipid metabolism and remodelling of the cytoskeleton (**Gillingham and Munro, 2007**). While genome-wide association studies have linked ARL15 to systemic Mg²⁺ homeostasis and energy metabolism in humans (**Corre et al., 2018; Richards et al., 2009**), the particular functional role and corresponding GAP, GEF, and effector proteins of ARL15 remain to be established. To this end, the strong effect of ARL15 in suppressing TRPM7 currents observed in our study may suggest that TRPM7 serves as a specific effector protein of ARL15. The significance of this modulatory effect for native TRPM7 in the rodent brain, however, remains to be shown.

In some TRPM7-APs from HEK293 cells, we detected TRPM6, a genetically related channel, and two proteins representing the gene family of phosphatase of regenerating liver 1 and 3 (also entitled protein tyrosine phosphatases type 4A1 and 3, TP4A1 and 3) (**Table 1**). The Mg²⁺ transporter protein TRPM6 has been described to physically and functionally interact with TRPM7 (**Chubanov et al., 2004; Ferioli et al., 2017; Chubanov et al., 2016**). In the present study, TRPM6, even though detected, could not be consistently co-purified with multiple anti-TRPM7 antibodies, likely because TRPM6 is expressed at very low levels in the brain and HEK293 cells. Nevertheless, a previous study reporting that heterologously expressed ARL15 positively modulates TRPM6 (**Corre et al., 2018**) might suggest an overlap between the TRPM6 and TRPM7 interactomes.

Interestingly, a recent interactome screen based on lentiviral overexpression of tagged proteins in HEK293 and HTC116 cells revealed that TP4A1 and TP4A2 also interact with ARL15 and CNNMs (**Huttlin et al., 2017; Huttlin et al., 2021**). Furthermore, a hypothesis-driven search for interaction partners of CNNMs has shown that TP4A proteins assemble with CNNMs and that such interactions shape Mg²⁺ efflux from cells (**Funato et al., 2014; Hardy et al., 2015; Gulerez et al., 2016; Kostantin et al., 2016; Zhang et al., 2017; Giménez-Mascarell et al., 2017**). These findings are commensurate with our observation that TP4A1 and TP4A3 could be found in TRPM7 APs at low amounts.

Hence, based on the present analysis of native TRPM7 complexes in conjunction with earlier interactome experiments and functional expression studies, it is tempting to speculate that TRPM7/ARL15/CNNMs/TP4As form a protein network orchestrating transport of divalent cations across the cell membrane.

Materials and methods

Key resources table

Reagent type (species) or resource	Designation	Source or reference	Identifiers	Additional information
Strain, strain background (<i>Mus musculus</i>)	C57BL/6	Jackson Labs	JAX stock #000664	Six weeks of age, equal numbers of male and female
Strain, strain background (<i>Ratus norvegicus</i>)	Wistar	Charles River	Strain code:003	Six weeks of age, equal numbers of male and female
Strain, strain background (<i>Xenopus laevis</i>)	<i>Xenopus laevis</i>	NASCO	Cat#:LM00535	
Cell line (human)	HEK293T	Sigma	Cat#:96121229; RRID:CVCL_2737	
Cell line (human)	TRPM7 ^{-/-} HEK293T	DOI:10.1073/pnas.1707380114		
Cell line (human)	HEK293T-Rex cells stably expressing TRPM7	10.1016 /s0092-8674(03)00556-7		
Antibody	Anti-HA (rat monoclonal)	Roche	Cat#:11867423001; RRID:AB_390918	IP (3–15 µg per IP), WB (0.2 µg/ml)
Antibody	Anti-HA (mouse monoclonal)	Invitrogen	Cat#:26183; RRID:AB_2533056	IP (3 µg per IP)
Antibody	Normal rabbit IgG	Millipore	Cat#:12-370; RRID:AB_145841	IP (15 µg per IP)

Continued on next page

Continued

**Reagent type
(species) or
resource**
Designation
Source or reference
Identifiers
Additional information

Antibody	Anti- β Arrestin 2 (mouse monoclonal)	Santy Cruz Biotechnology	Cat#:sc-13140; RRID: AB_626701	WB (1 μ g/ml)
Antibody	Anti-TRPC1 (rabbit polyclonal)	Other	4921	Gift from Veit Flockerzi Immunogen: N-terminus of mouse TRPC1, IP (15 μ g per IP)
Antibody	Anti-TRPC3 (rabbit polyclonal)	Other	1378	Gift from Veit Flockerzi Immunogen: N-terminus of mouse TRPC3, IP (15 μ g per IP)
Antibody	Anti-NMDAR1 (mouse monoclonal)	Millipore	Cat#:MAB1586; RRID: AB_11213180	IP (15 μ g per IP)
Antibody	Anti-LRRTM2 (rabbit polyclonal),	ProteinTech	Cat#:23094-1-AP; RRID: AB_2879209	IP (15 μ g per IP)
Antibody	Anti-DPP10 (mouse monoclonal)	Santa Cruz Biotechnology	sc-398108	IP (15 μ g per IP)
Antibody	Anti-RGS9 (goat polyclonal)	Santa Cruz Biotechnology	sc-8143; RRID: AB_655555	IP (15 μ g per IP)
Antibody	Anti-TRPM7 (mouse monoclonal)	Thermo Fisher Scientific	Cat#:MA5-27620; RRID: AB_2735401	IP (15 μ g per IP)
Antibody	Anti-TRPM7 (mouse monoclonal)	NeuroMab	Cat#:75-114; RRID: AB_2877498	IP (15 μ g per IP)
Antibody	Anti-(p)Ser1511 TRPM7 (mouse monoclonal)	DOI: 10.1038/s41467-017-01960-z		Affinity purified with peptide H2N-DSPEVD(p)SKAALLPC-NH ₂ , WB (2 μ g/ml)
Antibody	Anti-M7c (rabbit polyclonal)	DOI: 10.1038/s41467-017-01960-z		Affinity purified with peptide H2N-DSPEVDSKAALLPC-NH ₂ , IP (15 μ g per IP)
Antibody	Anti-M7d (2C7, mouse monoclonal)	This paper		See 'Materials and methods, Antibodies', IP (15 μ g per IP), WB (0.8 μ g/ml), IF (1.6 μ g/ml)
Antibody	Anti-TRPM7 (4F9, mouse monoclonal)	This paper		See 'Materials and methods, Antibodies', WB (1.4 μ g/ml)
Antibody	Anti-TRPM7 (rabbit polyclonal)	Millipore	Cat#:AB15562; RRID: AB_805460	WB (1 μ g/ml)
Antibody	Anti-Flag (mouse monoclonal)	Sigma	Cat#:F3165; RRID: AB_259529	WB (1 μ g/ml)
Antibody	Anti- β Actin (rabbit polyclonal)	Bioss Inc	Cat#:bs-0061R; RRID: AB_10855480	WB (0.5 μ g/ml)
Antibody	Anti-rabbit IgG (goat polyclonal, HRP conjugate)	abcam	ab7090	WB (1:30000)
Antibody	Anti-mouse IgG (goat polyclonal, HRP conjugate)	abcam	ab7068	WB (1:10000)
Antibody	Anti-mouse IgG (horse polyclonal, HRP conjugate)	Cell Signaling Technology	Cat#:7076	WB (1:1000)
Antibody	Anti-Na ⁺ /K ⁺ ATPase (rabbit monoclonal, HRP conjugate)	Abcam	Cat#:ab185065	WB (1:1000)
Antibody	Anti-Myc (mouse monoclonal, clone 9B11)	Cell Signaling Technology	Cat#:2276	WB (1:1000)

Continued on next page

Continued

**Reagent type
(species) or
resource**
Designation
Source or reference
Identifiers
Additional information

Antibody	Anti-mouse IgG- Alexa Fluor 488 (goat IgG, Alexa Fluor 488 conjugate)	Thermo Fisher Scientific	Cat#:A11029	2 µg/ml
Recombinant DNA reagent	pT7-His ₆ -Trpm7-KD (plasmid)	This paper		See 'Materials and methods, Antibodies'
Peptide, recombinant protein	His ₆ -TRPM7-KD (purified protein)	This paper		See 'Materials and Methods, Antibodies'
Peptide, recombinant protein	TRPM7-KD (purified protein)	This paper		See 'Materials and methods, Antibodies'
Recombinant DNA reagent	Mouse <i>Trpm7</i> cDNA in pIRES2-EGFP vector (plasmid)	DOI: https://doi.org/10.1038/s41598-017-08144-1		Expression in mammalian cells
Recombinant DNA reagent	Mouse <i>Trpm6</i> cDNA in pIRES2-EGFP vector (plasmid)	DOI: https://doi.org/10.1038/s41598-017-08144-1		Expression in mammalian cells
Recombinant DNA reagent	Human <i>TRPM6</i> cDNA in pIRES2-EGFP vector (plasmid)	DOI: https://doi.org/10.1038/s41598-017-08144-1		Expression in mammalian cells
Recombinant DNA reagent	Mouse <i>Trpm7</i> cDNA in pOG1 vector (plasmid)	DOI: 10.1073/pnas.0305252101		cRNA synthesis
Recombinant DNA reagent	Mouse <i>Trpm7</i> -Myc cDNA in pcDNA3.1/V5-His TA-TOPO vector (plasmid)	DOI: 10.1073/pnas.0305252101		Expression in mammalian cells
Recombinant DNA reagent	Mouse <i>Trpm7</i> -HA cDNA in pcDNA3.1/V5-His TA-TOPO vector (plasmid)	DOI: 10.1073/pnas.0305252101		Expression in mammalian cells
Recombinant DNA reagent	Human <i>TRPV1</i> -His cDNA in pNKS2 vector (plasmid)	This paper		See 'Materials and methods, Antibodies, Molecular biology' cRNA synthesis
Recombinant DNA reagent	Mouse <i>Cnnm1</i> -Myc-Flag in pCMV6-Entry (plasmid)	OriGene	Cat#:MR218318	Expression in mammalian cells
Recombinant DNA reagent	Mouse <i>Cnnm2</i> -Myc-Flag in pCMV6-Entry (plasmid)	OriGene	Cat#:MR218370	Expression in mammalian cells
Recombinant DNA reagent	Mouse <i>Cnnm3</i> -Myc-Flag in pCMV6-Entry (plasmid)	OriGene	Cat#:MR224758	Expression in mammalian cells, cRNA synthesis
Recombinant DNA reagent	Mouse <i>Cnnm4</i> -Myc-Flag in pCMV6-Entry (plasmid)	OriGene	Cat#:MR215721	Expression in mammalian cells
Recombinant DNA reagent	Mouse <i>Arl15</i> -Myc-Flag in pCMV6-Entry (plasmid)	OriGene	Cat#:MR218657	Expression in mammalian cells, cRNA synthesis
Recombinant DNA reagent	Mouse <i>Arl8a</i> -Myc-Flag in pCMV6-Entry (plasmid)	OriGene	Cat#:MR201740	Expression in mammalian cells, cRNA synthesis
Commercial assay or kit	Bio-Rad Protein Assay	Bio-Rad	Cat#:5000006	Protein concentration determination
Chemical compound, drug	ComplexioLyte CL-47	Logopharm	Cat#:CL-47-01	Mild detergent buffer
Chemical compound, drug	ComplexioLyte CL-91	Logopharm	Cat#:CL-91-01	Detergent buffer with intermediate stringency
Chemical compound, drug	Trypsin, sequencing grade modified	Promega	Cat#:V5111	
Chemical compound, drug	Leupeptin	Sigma	Cat#:L2884	

Continued on next page

Continued

Reagent type (species) or resource	Designation	Source or reference	Identifiers	Additional information
Chemical compound, drug	Pepstatin A	Sigma	Cat#:P5318	
Chemical compound, drug	Aprotinin	Roth	Cat#:A162.2	
Chemical compound, drug	Phenylmethylsulfonyl fluoride	Roth	Cat#:6367.3	
Chemical compound, drug	Iodoacetamide	Sigma	I6125	
Chemical compound, drug	Aminocaproic acid	Roth	3113.3	
Chemical compound, drug	TG100-115	Selleck Chemicals	Cat#:S1352	
Software, algorithm	msconvert.exe	http://proteowizard.sourceforge.net/		
Software, algorithm	MaxQuant v1.6.3	http://www.maxquant.org		
Software, algorithm	Mascot 2.6	Matrix Science, UK		
Software, algorithm	CellWorks 5.5.1	npi electronic https://www.npielectronic.com		
Software, algorithm	ZEN 2.3	Carl Zeiss https://www.zeiss.de		
Software, algorithm	PatchMaster 2 × 90	Harvard Bioscience https://www.heka.com		
Software, algorithm	Studio Lite 4.0	https://www.licor.com/bio/image-studio-lite		
Other	Dynabeads Protein A	Invitrogen	Cat#:10002D	
Other	Dynabeads Protein G	Invitrogen	Cat#:10004D	
Other	Tissue embedding media	Leica	Cat#:14020108926	Used to support gel slices during cryotomy

Antibodies

Antibodies used for APs were: *anti*-HA (11867423001, Roche) and *anti*-HA (26183, Invitrogen). TUC antibodies were: rabbit IgG (12–370, Millipore), *anti*- β -Arrestin 2 (sc-13140, Santa Cruz), *anti*-TRPC1 (4921, a gift from Veit Flockerzi), *anti*-Sac1 (ABFrontier), *anti*-TRPC3 (1378, a gift from Veit Flockerzi), *anti*-NMDAR1 (MAB1586, Sigma), *anti*-LRRTM2 (23094–1-AP, ProteinTech), *anti*-DPP10 (sc-398108, Santa Cruz), and *anti*-RGS9 (sc-8143, Santa Cruz).

Anti-TRPM7 mouse monoclonal antibody (*anti*-M7a, **Figure 1A**) was purchased from Thermo Fisher Scientific (clone S74-25, [Product # MA5-27620](#)). *Anti*-TRPM7 mouse monoclonal antibody (*anti*-M7b, **Figure 1A**) was obtained from NeuroMab (clone N74/25, [Product # 75–114](#)). Generation of a rabbit polyclonal *anti*-(p)Ser1511 TRPM7 antibody (*anti*-(p)Ser1511 M7, **Figure 5**) was described previously ([Romagnani et al., 2017](#)). Briefly, rabbits were immunised with a phosphorylated peptide H2N-DSPEVD(p)SKAALLPC-NH2 ((p)Ser1511 in mouse TRPM7) coupled via its C-terminal cysteine residue to keyhole limpet hemocyanin (Eurogentec, Belgium). The generated serum was subjected to two rounds of affinity chromatography: a fraction of the antibody was purified using the phosphorylated peptide. Next, an additional round of chromatography was conducted using a non-phosphorylated variant of the peptide (H2N-DSPEVDSKAALLPC-NH2). The latter fraction of antibody was used in AP experiments (*anti*-M7c antibody, **Figure 1A**).

Anti-TRPM7 2C7 mouse monoclonal antibody (*anti*-M7d, **Figure 1A**, **Figure 1—figure supplement 1**) was produced by Eurogentec (Belgium) as follows. The nucleotide sequence coding for His₆-tag followed by a cleavage site sequence for TEV protease and the amino acids 1501–1863 (kinase domain, KD) of mouse TRPM7 protein was synthesised in vitro and cloned into the prokaryotic expression

vector pT7. The resulting expression construct pT7-His₆-Trpm7-KD was verified by sequencing and transformed in *Escherichia coli* (BL21 DE3 pLysS). Next, the transformed *E. coli* strain was amplified in LB medium at 25°C; 1 mM IPTG was used for induction of the His₆-TRPM7-KD protein expression. The harvested cell pellet was disrupted by sonication. His₆-TRPM7-KD was identified in the soluble fraction of the lysate. His₆-TRPM7 was purified on an Ni Sepharose 6 Fast Flow column on an AKTA Avant 25 (GE Healthcare) using an imidazole gradient of 20–500 mM. The fraction containing His₆-TRPM7-KD was dialysed against a Tris buffer (0.5 mM EDTA, 1 mM DTT, and 50 mM Tris HCl pH 7.5). His₆-TRPM7-KD was subjected to TEV protease (New England Biolabs) digestion according to the manufacturer's instructions. Subsequently, non-digested His₆-TRPM7-KD and His₆-tagged fragments were removed using an Ni-Sepharose 6 Fast Flow column. The flow-through containing the cleaved TRPM7-KD was concentrated to 0.5 mg/ml in the Tris buffer and stored at –80°C. SDS-PAGE was used to verify the removal of the His₆-tag.

The standard mouse monoclonal antibody production program of Eurogentec (Belgium) was conducted to immunise four mice using the TRPM7-KD protein and to produce a library of hybridomas. ELISA and Western blot were used to screen the hybridomas and to perform a clonal selection. Two hybridoma clones, 2C7 and 4F9 (isotypes G1;K), were selected based on the antibody quality released in the culture medium. Both clones were propagated, and the corresponding cell culture media were collected for large-scale purification of the IgG fraction using Protein G affinity chromatography. The IgG fractions from 2C7 (0.8 mg/ml) and 4F9 (1.4 mg/ml) were dialysed in PBS and stored at –80°C. The specificity of the 2C7 and 4F9 IgGs (dilution 1:1000) was verified by Western blot analysis of HEK293T cells overexpressing the TRPM6 and TRPM7 proteins (**Figure 1—figure supplement 1**). The 2C7 antibody detected the mouse or human TRPM7, but not the mouse or human TRPM6 (**Figure 1—figure supplement 1**). In contrast, the 4F9 antibody detected only the mouse TRPM7 (**Figure 1—figure supplement 1**). Consequently, the 2C7 antibody (*anti-M7d*) was used in the present study.

Quantification of (p)Ser1511 TRPM7 and *anti-M7d* signals in **Figure 5** was performed using Image Studio Lite 4.0 software (<https://www.licor.com/bio/image-studio-lite>).

Molecular biology

Mouse *Trpm7*, mouse *Trpm6*, and human *TRPM6* cDNA in pIRES2-EGFP vector were reported previously (**Chubanov et al., 2004; Ferioli et al., 2017**). cDNA encoding C-terminally His-tagged human TRPV1 (NG_029716 **Hayes et al., 2000**) was cloned into the pNKS2 vector (**Gloor et al., 1995**) using standard restriction enzyme (BamHI/SmaI) cloning techniques. The mouse *Trpm7* cDNA in the pOG1 and mouse *Trpm7*-Myc and *Trpm7*-HA cDNA variants in pcDNA3.1/V5-His TA-TOPO vector were described earlier (**Chubanov et al., 2004; Ferioli et al., 2017**). Expression constructs encoding Myc-Flag-tagged (C-end) mouse *Cnnm1-4* and *Arl15*, and *Arl8A* cDNAs in the pCMV6-Entry expression vector were acquired from OriGene (MR218318 for *Cnnm1*, MR218370 for *Cnnm2*, MR224758 for *Cnnm3*, MR215721 for *Cnnm4*, MR218657 for *Arl15*, and MR201740 for *Arl8a*) and verified by sequencing. Point mutations in *Trpm7* were introduced using the QuikChange system (Thermo Fisher Scientific) according to the manufacturer's protocol and verified by sequencing (Eurofins, Germany).

Biochemistry

Cell lines, transient transfection: HEK293T cells (Sigma, 96121229, identity confirmed by STR profiling) were cultured at 37°C, 5% CO₂ in Dulbecco's modified Eagle's high glucose GlutaMAX medium (Gibco) supplemented with 10% foetal calf serum (Gibco), 1% penicillin/streptomycin (Gibco) and 10 mM Hepes (Gibco). *TRPM7*^{−/−} HEK293T cells (**Abiria et al., 2017**) were cultured as WT cells with an addition of 10 mM MgCl₂, 3 µg/ml blasticidin S (InvivoGen), and 0.5 µg/ml puromycin (Gibco) to the medium. HEK293T-Rex cells stably expressing the human *TRPM7* were maintained as reported previously (**Schmitz et al., 2003**). The cell lines were tested negative for mycoplasma before use.

WT HEK293T cells were transfected with polyethylenimine (Polysciences) using a DNA to polyethylenimine ratio of 1:2.5. For transfection of *TRPM7*^{−/−} HEK293T cells (**Abiria et al., 2017**), plasmid cDNA was diluted to 30 µg/ml in Hank's balanced salt solution, precipitated by addition of 113 mM CaCl₂ (final concentration) and added to the cells in culture medium lacking blasticidin S, puromycin, and 10 mM MgCl₂. For transfection, *Trpm7*, *Arl15*, and *Cnnm3* plasmid DNAs were mixed at a ratio of 3:1:1.

Preparation of plasma membrane-enriched protein fractions: Freshly excised brains from 25 male and 25 female 6-week-old rats (Wistar, Charles River) or mice (C57BL/6, Jackson Labs) were homogenised in homogenisation buffer (320 mM sucrose, 10 mM Tris/HCl pH 7.4, 1.5 mM MgCl₂, 1 mM EGTA and protease inhibitors leupeptin [Sigma], pepstatin A [Sigma], aprotinin [Roth] [1 µg/ml each], 1 mM phenylmethylsulfonyl fluoride [Roth], 1 mM iodoacetamide [Sigma]), particulates removed by centrifugation at 1080× g and homogenised material collected for 10 min at 200,000× g. After hypotonic lysis in 5 mM Tris/HCl pH 7.4 with protease inhibitors for 35 min on ice, the lysate was layered on top of a 0.5 and 1.3 M sucrose step gradient in 10 mM Tris/HCl pH 7.4, 1 mM EDTA/EGTA, and the plasma membrane-enriched fraction collected after centrifugation (45 min, 123,000× g) at the interface. Membranes were diluted in 20 mM Tris/HCl pH 7.4, collected by centrifugation (20 min, 200,000× g), and resuspended in 20 mM Tris/HCl pH 7.4.

Cultured cells were harvested in phosphate buffer saline with protease inhibitors, collected by centrifugation (10 min, 500× g) and resuspended in homogenisation buffer. After sonication (2 × 5 pulses, duty 50, output 2 [Branson Sonifier 250]), membranes were pelleted for 20 min at 125,000× g and resuspended in 20 mM Tris/HCl pH 7.4. Protein concentration was determined with the Bio-Rad Protein Assay kit according to the manufacturer's instructions.

Immunoprecipitation: Membranes were resuspended in ComplexioLyte CL-47 or CL-91 solubilisation buffer (Logopharm) with added 1 mM EDTA/EGTA and protease inhibitors at a protein to detergent ratio of 1:8 and incubated for 30 min on ice. Solubilised protein was cleared by centrifugation (10 min, 125,000× g, 4°C) and incubated with antibodies cross-linked to Dynabeads (Invitrogen) by overhead rotation for 2 hr on ice. After two short washing steps with ComplexioLyte CL-47 dilution buffer (Logopharm), the captured protein was eluted in Laemmli buffer with dithiothreitol added after elution. Eluted proteins were separated by SDS-PAGE. For MS/MS analysis silver-stained (Heukeshoven and Dernick, 1988) protein lanes were cut-out, split at 50 kDa and pieces individually subjected to standard in-gel tryptic digestion (Pandey and Mann, 2000). For chemiluminescence detection, proteins were Western blotted onto PVDF membranes and probed with the following antibodies: anti-HA (11867423001, Roche), anti-Flag (F3165, Sigma), anti-βActin (bs-0061R, Bioss Inc).

BN-PAGE: Two-dimensional BN-PAGE/SDS-PAGE protein analysis was performed as described previously (Schmidt et al., 2017). Membrane protein fractions were solubilised in ComplexioLyte CL-47 as described above, salts exchanged for aminocaproic acid by centrifugation through a sucrose gradient, and samples loaded on non-denaturing 1–13% linear polyacrylamide gradient gels (anode buffer: 50 mM Bis-Tris, cathode buffer: 50 mM Tricine, 15 mM Bis-Tris, 0.02% Coomassie Blue G-250). For separation in the second dimension, individual gel lanes were isolated, equilibrated in 2× Laemmli buffer (10 min, 37°C), placed on top of SDS-PAGE gels and Western-probed using anti-TRPM7 (AB15562, Millipore).

Complexome profiling

The size distribution of solubilised native TRPM7-associated complexes was investigated using the high-resolution csBN-MS technique detailed in Faouzi et al., 2017. Briefly, membranes isolated from adult mouse brain were solubilised with ComplexioLyte CL-47 (salt replaced by 750 mM aminocaproic acid), concentrated by ultracentrifugation into a 20%/50% sucrose cushion, supplied with 0.125% Coomassie G250 Blue and run overnight on a hyperbolic 1–13% polyacrylamide gel. The region of interest was excised from the lane, proteins fixed in 30% ethanol/15% acetic acid and the gel piece embedded in tissue embedding media (Leica). After careful mounting on a cryo-holder, 0.3 mm slices were harvested, rinsed, and subjected to in-gel tryptic digestion as described (Faouzi et al., 2017).

Mass spectrometry

Tryptic digests (dried peptides) were dissolved in 0.5% (v/v) trifluoroacetic acid and loaded onto a C18 PepMap100 precolumn (300 µm i.d. × 5 mm; particle size 5 µm) with 0.05% (v/v) trifluoroacetic acid (5 min 20 µl/min) using split-free UltiMate 3000 RSLCnano HPLCs (Dionex/Thermo Scientific, Germany). Bound peptides were then eluted with an aqueous-organic gradient (eluent A: 0.5% (v/v) acetic acid; eluent B: 0.5% (v/v) acetic acid in 80% (v/v) acetonitrile; times referring to AP-MS/csBN-MS): 5 min 3% B, 60/120 min from 3% B to 30% B, 15 min from 30% B to 99% B or 20 min from 30% B to 50% B and 10 min from 50% B to 99% B, respectively, 5 min 99% B, 5 min from 99% B to 3% B, 15/10 min 3% B (flow rate 300 nl/min). Eluted peptides were separated in a SilicaTip emitter (i.d.

75 μm ; tip 8 μm ; New Objective, Littleton, MA) manually packed 11 cm (AP-MS) or 23 cm (csBN-MS) with ReproSil-Pur 120 ODS-3 (C18; particle size 3 μm ; Dr Maisch HPLC, Germany) and electrosprayed (2.3 kV; transfer capillary temperature 250/300°C) in positive ion mode into an Orbitrap Elite (AP-MS) or a Q Exactive HF-X (csBN-MS) mass spectrometer (both Thermo Scientific, Germany). Instrument settings: maximum MS/MS injection time = 200/400 ms; dynamic exclusion duration = 30/60 s; minimum signal/intensity threshold = 2000/40,000 (counts), top 10/15 precursors fragmented; isolation width = 1.0/1.4 m/z.

Peak lists were extracted from fragment ion spectra using the 'msconvert.exe' tool (part of ProteoWizard [Chambers et al., 2012]; <http://proteowizard.sourceforge.net/>; v3.0.6906 for Orbitrap Elite and v3.0.11098 for Q Exactive HF-X; Mascot generic format with filter options 'peakPicking true 1-' and 'threshold count 500 most-intense'). Precursor m/z values were preliminarily searched with 50 ppm peptide mass tolerance, their mass offset corrected by the median m/z offset of all peptides assigned, and afterwards searched with 5 ppm mass tolerance against all mouse, rat, and human (mouse/rat brain samples) or only human (HEK293T cell samples) entries of the UniProtKB/Swiss-Prot database. Acetyl (protein N-term), carbamidomethyl (C), Gln-> pyro Glu (N-term Q), Glu-> pyro Glu (N-term E), oxidation (M), phospho (S, T, Y), and propionamide (C) were chosen as variable modifications, and fragment mass tolerance was set to ± 0.8 Da (Orbitrap Elite data) or ± 20 mmu (Q Exactive HF-X data). One missed tryptic cleavage was allowed. The expect value cut-off for peptide assignment was set to 0.5. Related identified proteins (subset or species homologs) were grouped using the name of the predominant member. Proteins either representing exogenous contaminations (e.g., keratins, trypsin, IgG chains) or identified by only one specific peptide were not considered.

Label-free quantification of proteins was carried out as described in Bildl et al., 2012; Müller et al., 2016. Peptide signal intensities (peak volumes, PVs) from FT full scans were determined, and offline mass calibrated using MaxQuant v1.6.3 (<http://www.maxquant.org>). Then, peptide PV elution times were pairwise aligned using LOESS regression (reference times dynamically calculated from the median peptide elution times overall aligned datasets). Finally, PVs were assigned to peptides based on their m/z and elution time (± 1 min/2–3 ppm, as obtained directly or indirectly from MS/MS-based identification) using in-house developed software. PV tables were then used to calculate protein abundance ratios in AP versus control (Figure 1C), the abundance norm value (Figure 1B, lower right) as an estimate for molecular abundance (both described in Schwenk et al., 2010), and csBN-MS abundance profiles (Figure 1B, lower left) as detailed in Müller et al., 2016. The latter were smoothed by sliding, averaging over a window of 5. Slice numbers were converted to apparent complex molecular weights by the sigmoidal fitting of ($\log(\text{MW})$) versus slice number of the observed profile peak maximum of mitochondrial marker protein complexes (Schägger and Pfeiffer, 2000).

Heterologous expression of TRPM7, CNNM3, ARL15, and ARL8A in *X. laevis* oocytes

TEVC measurements: *X. laevis* females were obtained from NASCO (Fort Atkinson, WI) and kept at the Core Facility Animal Models (CAM) of the Biomedical Center (BMC) of LMU Munich, Germany (Az:4.3.2–5682/LMU/BMC/CAM) in accordance with the EU Animal Welfare Act. To obtain oocytes, frogs were deeply anaesthetised in MS222 and killed by decapitation. Surgically extracted ovary lobes were dissociated by 2.5 hr incubation (RT) with gentle shaking in ND96 solution (96 mM NaCl, 2 mM KCl, 1 mM CaCl_2 , 1 mM MgCl_2 , 5 mM HEPES, pH 7.4) containing 2 mg/ml collagenase (Nordmark) and subsequently defolliculated by washing (15 min) with Ca^{2+} -free ND96. Stage V-VI oocytes were then selected and kept in ND96 containing 5 $\mu\text{g}/\text{ml}$ gentamicin until further use.

TEVC measurements were performed as described previously (Chubanov et al., 2004) with a few modifications. Linearised cDNAs of *Trpm7* (in pOGI), *TRPV1* (in pNKS2), *Cnnm3*, *Arl8a*, and *Arl15* (all in pCMV6-Entry) were used for in vitro synthesis of cRNA (T7 or SP6 mMESSAGE mMACHINE transcription kits [Thermo Fisher Scientific]). In Figure 3A, oocytes were injected with 5 ng of *Trpm7* cRNA or co-injected with 2.5 ng of *Cnnm3* (2:1 ratio), 2.5 ng *Arl15* (2:1 ratio), and 2.5 ng of *Cnnm3* with 2.5 ng of *Arl15* cRNAs (2:1:1 ratio). In Figure 3B, oocytes were co-injected with 5 ng of *Trpm7* and 0.025–0.5 ng of *Arl15* cRNAs (200:1–10:1 ratio).

The injected oocytes were kept in ND96 solution, supplemented with 5 $\mu\text{g}/\text{ml}$ gentamicin at 16°C. TEVC measurements were performed 3 days after injection at room temperature (RT) in $\text{Ca}^{2+}/\text{Mg}^{2+}$ -free ND96 containing 3.0 mM BaCl_2 instead of CaCl_2 and MgCl_2 using a TURBO TEC-05X amplifier (npi

electronic) and CellWorks software (npi electronic). In some experiments, ND96 solution contained 3.0 mM MgCl₂ instead of 3.0 mM BaCl₂, as indicated in the corresponding figure legends. Oocytes were clamped at a holding potential of −60 mV, and 0.5 s ramps from −80 to +80 mV were applied at 6 s intervals. For statistical analysis, current amplitudes were extracted at −80 or +80 mV for individual oocytes, as indicated in the corresponding figure legends. Statistical significance (ANOVA) was calculated using GraphPad Prism 7.03.

Western blot: Oocytes ($n = 6$ per group) were treated with a lysis buffer (Pierce IP Lysis Buffer, Pierce) containing protease inhibitor and phosphatase inhibitor cocktails (Biotool), mixed (1:1) with 2× Laemmli buffer, heated at 70°C for 10 min, and cooled on ice. Samples were separated by SDS-PAGE (4–15% gradient Mini-PROTEAN, Bio-Rad) and electroblotted on nitrocellulose membranes (GE Healthcare Life Science). After blocking with 5% (w/v) non-fat dry milk in Tris-buffered saline with 0.1% Tween 20 (TBST). To probe for TRPM7 expression (**Figure 3D**), the upper part of the membrane was incubated with anti-M7d antibody (0.8 µg/ml) diluted in TBST with 5% (w/v) BSA, followed by washing in TBST, incubation with a horseradish peroxidase-coupled polyclonal horse anti-mouse IgG (#7076, Cell Signaling Technology; 1:1,000 in TBST with 5% (w/v) non-fat dry milk), and washing again in TBST. Blots were visualised using a luminescence imager (ChemiDoc Imaging System, Bio-Rad). The lower part of the membrane was developed using a horseradish peroxidase-coupled rabbit monoclonal anti-Na⁺/K⁺ ATPase antibody (ab185065, Abcam; 1:1000). To detect ARL15 (**Figure 3C**), the lower part of the membrane was incubated with a mouse anti-Myc antibody (clone 9B11, #2276, Cell Signaling Technology; 1:1000), and the upper part of the membrane was assessed by anti-Na⁺/K⁺ ATPase antibody.

Immunofluorescent staining: Oocytes were fixed in 4% (w/v) PFA (Electron Microscopy Sciences) in ND96 solution for 15 min at RT, followed by incubation in ice-cold methanol for 60 min at −18°C. After washing in ND96 (3×, RT), oocytes were incubated in ND96 containing 5% (w/v) BSA for 30 min at RT. Anti-M7d antibody (1.6 µg/ml in ND96 with 5% BSA) was applied overnight at 4°C. Afterwards, oocytes were washed in ND96 (3×, RT), and a goat anti-mouse IgG conjugated with Alexa Fluor 488 (Thermo Fisher Scientific; 2 µg/ml in ND96 with 5% BSA) was applied for 1 hr at RT. After washing in ND96 (3×, RT), differential interference contrast (DIC) and confocal images were obtained with a confocal laser scanning microscope LSM 880 AxioObserver (Carl Zeiss). We used a Plan-Apochromat 10×/0.45 objective, 488 nm excitation wavelengths and 493–630 nm filters. Acquired DIC and confocal images were analysed using the ZEN2.3 software (Carl Zeiss).

Patch-clamp experiments with HEK293T cells

WT HEK293T cells were cultured using 3 cm dishes and Dulbecco's modified Eagle's medium (DMEM, high glucose; Merck) supplemented with 10% FBS, 100 µg/ml streptomycin, 100 U/ml penicillin (all from Thermo Fisher Scientific). Cells were maintained in a humidified cell culture incubator (Heraeus, Thermo Fisher Scientific) at 37°C and 5% CO₂. To investigate the effect of CNNM3 on the TRPM7 channel, cells were transiently transfected by 2 µg *Trpm7* (in pIRES2-EGFP) or 2 µg *Trpm7* plus 0.5 µg *Cnnm3* (in pCMV6-Entry) expression constructs using Lipofectamine 2000 reagent (Thermo Fisher Scientific). To examine the effects of ARL15 on endogenous TRPM7 currents, HEK293T cells were transfected by 1 µg WT *Arl15* (in pCMV6-Entry) and 0.1 µg *EGFP* cDNAs (in pcDNA3.1/V5-His TA-TOPO).

Patch-clamp measurements were conducted with EGFP-positive cells 18–22 hr after transfection, as reported previously (Chubanov et al., 2004; Ferioli et al., 2017), with minor modifications. Whole-cell currents were measured using an EPC10 patch-clamp amplifier and PatchMaster software (Harvard Bioscience). Voltages were corrected for a liquid junction potential of 10 mV. Currents were elicited by a ramp protocol from −100 to +100 mV over 50 ms acquired at 0.5 Hz and a holding potential of 0 mV. Inward and outward current amplitudes were extracted at −80 and +80 mV and were normalised to the cell size as pA/pF. Capacitance was measured using the automated capacitance cancellation function of EPC10. Patch pipettes were made of borosilicate glass (Science Products) and had resistance 2–3.5 MΩ. Unless stated otherwise, a standard extracellular solution contained (in mM): 140 NaCl, 2.8 KCl, 1 CaCl₂, 2 MgCl₂, 10 HEPES-NaOH, and 11 glucose (all from Sigma-Aldrich), pH 7.2. For assessing Mg²⁺ currents, the extracellular solutions contained (in mM): 10 HEPES-NaOH, 260 mannitol, and 10 MgCl₂, pH 7.2. Solutions were adjusted to 290 mOsm using a Vapro 5520 osmometer (Wescor Inc). The standard divalent cation-free intracellular pipette solution contained (in mM): 120 Cs-glutamate, 8 NaCl, 10 Cs-EGTA, 5 Cs-EDTA, 10 HEPES-CsOH (all from Sigma-Aldrich), pH

7.2. Data are presented as means \pm standard error of the mean (means \pm SEM). Statistical comparisons (Prism 8.4.0) were made using one-way ANOVA or a two-tailed t-test, as indicated in the figure legends. Significance was accepted at $p \leq 0.05$.

Determination of cellular Mg contents

The total content of Mg in *TRPM7*^{-/-} HEK293T cells (Abiria et al., 2017) was determined by ICP-MS in ALS Scandinavia (Sweden) as reported previously (Mittermeier et al., 2019) with several modifications. The cells were cultured in DMEM (Merck) supplemented with 10% FBS, 100 μ g/ml streptomycin, 100 U/ml penicillin, and 10 mM MgCl₂ (all from Thermo Fisher Scientific) in a humidified cell culture incubator (Heraeus, Thermo Fisher Scientific) at 37°C and 5% CO₂. To conduct ICP-MS experiments, *TRPM7*^{-/-} HEK293T cells were plated in 10 cm² dishes at ~50% confluence in standard DMEM (without additional 10 mM Mg²⁺) and transiently transfected with 20 μ g *Trpm7*, 10 μ g *Cnnm3*, or 20 μ g *Trpm7* plus 10 μ g *Cnnm3* plasmid cDNAs using Lipofectamine 2000 reagent (Thermo Fisher Scientific). After 24 hr, the cells were washed with serum-free DMEM, mechanically detached, and cell suspensions collected in 10 ml plastic tubes. After centrifugation (3 min, 1000 rpm), the medium was removed, and the cell pellet was resuspended in 5 ml PBS and passed to a fresh 10 ml tube. The cell suspension was centrifuged (3 min, 3500 rpm), the supernatant removed, and the cell pellet frozen at -20°C. Cell pellets were analysed by ICP-MS in ALS Scandinavia (Sweden). The experiment was repeated five times. Elementary Mg levels were normalised to elementary contents of sulphur (S) and represented as mean \pm SEM. Data were compared by one-way ANOVA (Prism 8.4.0). Significance was accepted at $p \leq 0.05$.

Acknowledgements

VC, TG, SZ, US, and BF were supported by the Deutsche Forschungsgemeinschaft (German Research Foundation, DFG), TRR 152 (P02, P14 and P15). BF and US were supported by the DFG under Germany's Excellence Strategy (CIBSS-EXC2189 project ID: 390939984) and Project-ID 403222702 – SFB 1381. AN was supported by the DFG Project-ID 335447717 – SFB 1328 (P15). TG and AN were supported by Research Training Group 2338 (DFG). We thank Veit Flockerzi for *anti-TRPC1/3* antibodies, David Clapham for *TRPM7*^{-/-} HEK293T cells, Carsten Schmitz for HEK293T-REx cells stably expressing *TRPM7*, and Ilia Rodushkin for the support in ICP-MS. We thank Joanna Zaisserer, Lisa Pleninger, Yves Haufe, Monika Haberland, and Anna Erbacher for their technical assistance.

Additional information

Funding

Funder	Grant reference number	Author
Deutsche Forschungsgemeinschaft	TRR 152 P15	Vladimir Chubarov Thomas Gudermann
Deutsche Forschungsgemeinschaft	TRR 152 P02	Bernd Fakler Uwe Schulte
Deutsche Forschungsgemeinschaft	SFB 1328 P15	Annette Nicke
Deutsche Forschungsgemeinschaft	SFB 1381	Bernd Fakler
Deutsche Forschungsgemeinschaft	Research Training Group 2338	Thomas Gudermann Annette Nicke
Deutsche Forschungsgemeinschaft	TRR 152 P14	Susanna Zierler

The funders had no role in study design, data collection and interpretation, or the decision to submit the work for publication.

Author contributions

Astrid Kollwe, Data curation, Formal analysis, Investigation, Visualization, Writing – original draft, Writing – review and editing; Vladimir Chubanov, Conceptualization, Data curation, Funding acquisition, Investigation, Resources, Supervision, Writing – original draft, Writing – review and editing; Fong Tsuen Tseung, Leonor Correia, Eva Schmidt, Anna Rössig, Catrin Swantje Müller, Wolfgang Bildl, Investigation; Susanna Zierler, Data curation, Formal analysis, Methodology, Visualization; Alexander Haupt, Formal analysis, Investigation, Writing – review and editing; Uwe Schulte, Data curation, Formal analysis, Funding acquisition, Writing – review and editing; Annette Nicke, Data curation, Formal analysis, Methodology, Resources, Writing – review and editing; Bernd Fakler, Conceptualization, Data curation, Funding acquisition, Project administration, Resources, Writing – original draft, Writing – review and editing; Thomas Gudermann, Conceptualization, Data curation, Funding acquisition, Project administration, Writing – original draft, Writing – review and editing

Author ORCIDs

Vladimir Chubanov  <http://orcid.org/0000-0002-6042-4193>
 Alexander Haupt  <http://orcid.org/0000-0001-5647-5724>
 Annette Nicke  <http://orcid.org/0000-0001-6798-505X>
 Bernd Fakler  <http://orcid.org/0000-0001-7264-6423>
 Thomas Gudermann  <http://orcid.org/0000-0002-0323-7965>

Decision letter and Author response

Decision letter <https://doi.org/10.7554/eLife.68544.sa1>

Author response <https://doi.org/10.7554/eLife.68544.sa2>

Additional files**Supplementary files**

- Supplementary file 1. Numerical data for peak volumes, abundance norm values, relative abundance, and ratio distance values obtained through analysis of the mass spectrometry (MS) data.
- Supplementary file 2. Mass spectrometry (MS) spectra of phosphorylated transient receptor potential melastatin-subfamily member 7 (TRPM7), CNNM3, and CNNM4 peptides identified in affinity purifications (APs) from HEK293 and rodent brain.
- Supplementary file 3. Phosphorylation sites in transient receptor potential melastatin-subfamily member 7 (TRPM7), CNNM3, and CNNM4 identified in affinity purifications (APs) from transfected HEK293 cells and rodent brain. Excel file contains one worksheet: The phosphorylated residues of TRPM7, CNNM3, and CNNM4 identified by mass spectrometry (MS) in the present study are outlined in conjunction with previously published data (*Nguyen et al., 2019; Zhou et al., 2013; Cai et al., 2017; Huttlin et al., 2010*).
- Transparent reporting form

Data availability

The mass spectrometry proteomics data have been deposited to the ProteomeXchange Consortium via the PRIDE partner repository with the dataset identifier PXD025279 and <https://www.ebi.ac.uk/pride/archive/projects/PXD025279>.

The following dataset was generated:

Author(s)	Year	Dataset title	Dataset URL	Database and Identifier
Haupt A, Fakler B	2021	The molecular appearance of native TRPM7 channel complexes identified by high-resolution proteomics	https://www.ebi.ac.uk/pride/archive/projects/PXD025279	PRIDE, PXD025279

References

Aarts M, Iihara K, Wei W-L, Xiong Z-G, Arundine M, Cerwinski W, MacDonald JF, Tymianski M. 2003. A key role for TRPM7 channels in anoxic neuronal death. *Cell* 115: 863–877. DOI: [https://doi.org/10.1016/s0092-8674\(03\)01017-1](https://doi.org/10.1016/s0092-8674(03)01017-1), PMID: 14697204

- Abiria SA**, Krapivinsky G, Sah R, Santa-Cruz AG, Chaudhuri D, Zhang J, Adstamongkonkul P, DeCaen PG, Clapham DE. 2017. TRPM7 senses oxidative stress to release Zn²⁺ from unique intracellular vesicles. *PNAS* **114**: E6079–E6088. DOI: <https://doi.org/10.1073/pnas.1707380114>
- Arjona FJ**, de Baaij JHF. 2018. CrossTalk opposing view: CNNM proteins are not Na⁺/Mg²⁺ exchangers but Mg²⁺ transport regulators playing a central role in transepithelial Mg²⁺ (re)absorption. *The Journal of Physiology* **596**: 747–750. DOI: <https://doi.org/10.1113/JP275249>, PMID: 29383729
- Bildl W**, Haupt A, Müller CS, Biniossek ML, Thumfart JO, Hüber B, Fakler B, Schulte U. 2012. Extending the dynamic range of label-free mass spectrometric quantification of affinity purifications. *Molecular & Cellular Proteomics* **11**: M111.007955. DOI: <https://doi.org/10.1074/mcp.M111.007955>, PMID: 22067099
- Cai N**, Bai Z, Nanda V, Runnels LW. 2017. Mass Spectrometric Analysis of TRPM6 and TRPM7 Phosphorylation Reveals Regulatory Mechanisms of the Channel-Kinases. *Scientific Reports* **7**: 42739. DOI: <https://doi.org/10.1038/srep42739>, PMID: 28220887
- Chambers MC**, Maclean B, Burke R, Amodei D, Ruderman DL, Neumann S, Gatto L, Fischer B, Pratt B, Egertson J, Hoff K, Kessner D, Tasman N, Shulman N, Frewen B, Baker TA, Brusniak MY, Paulse C, Creasy D, Flashner L, et al. 2012. A cross-platform toolkit for mass spectrometry and proteomics. *Nature Biotechnology* **30**: 918–920. DOI: <https://doi.org/10.1038/nbt.2377>, PMID: 23051804
- Chen YS**, Kozlov G, Moeller BE, Rohaim A, Fakih R, Roux B, Burke JE, Gehring K. 2021. Crystal structure of an archaeal CorB magnesium transporter. *Nature Communications* **12**: 4028. DOI: <https://doi.org/10.1038/s41467-021-24282-7>, PMID: 34188059
- Chubanov V**, Waldegger S, Mederos y Schnitzler M, Vitzthum H, Sassen MC, Seyberth HW, Konrad M, Gudermann T. 2004. Disruption of TRPM6/TRPM7 complex formation by a mutation in the TRPM6 gene causes hypomagnesemia with secondary hypocalcemia. *PNAS* **101**: 2894–2899. DOI: <https://doi.org/10.1073/pnas.0305252101>, PMID: 14976260
- Chubanov V**, Gudermann T. 2014. Handbook of Experimental Pharmacology. Springer. DOI: https://doi.org/10.1007/978-3-642-54215-2_20, PMID: 24756719
- Chubanov V**, Ferioli S, Wisnowsky A, Simmons DG, Leitzinger C, Einer C, Jonas W, Shymkiv Y, Bartsch H, Braun A, Akdogan B, Mittermeier L, Sytik L, Torben F, Jurinovic V, van der Vorst EP, Weber C, Yildirim ÖA, Sotlar K, Schürmann A, et al. 2016. Epithelial magnesium transport by TRPM6 is essential for prenatal development and adult survival. *eLife* **5**: e20914. DOI: <https://doi.org/10.7554/eLife.20914>, PMID: 27991852
- Chubanov V**, Mittermeier L, Gudermann T. 2018. Role of kinase-coupled TRP channels in mineral homeostasis. *Pharmacology & Therapeutics* **184**: 159–176. DOI: <https://doi.org/10.1016/j.pharmthera.2017.11.003>, PMID: 29129644
- Clark K**, Middelbeek J, Dorovkov MV, Figdor CG, Ryazanov AG, Lasonder E, van Leeuwen FN. 2008. The alpha-kinases TRPM6 and TRPM7, but not eEF-2 kinase, phosphorylate the assembly domain of myosin IIA, IIB and IIC. *FEBS Letters* **582**: 2993–2997. DOI: <https://doi.org/10.1016/j.febslet.2008.07.043>, PMID: 18675813
- Corre T**, Arjona FJ, Hayward C, Youhanna S, de Baaij JHF, Belge H, Nägele N, Debaix H, Blanchard MG, Traglia M, Harris SE, Ulivi S, Rueedi R, Lamparter D, Macé A, Sala C, Lenarduzzi S, Ponte B, Pruijm M, Ackermann D, et al. 2018. Genome-Wide Meta-Analysis Unravels Interactions between Magnesium Homeostasis and Metabolic Phenotypes. *Journal of the American Society of Nephrology* **29**: 335–348. DOI: <https://doi.org/10.1681/ASN.2017030267>, PMID: 29093028
- Desai BN**, Krapivinsky G, Navarro B, Krapivinsky L, Carter BC, Febvay S, Delling M, Penumaka A, Ramsey IS, Manasian Y, Clapham DE. 2012. Cleavage of TRPM7 releases the kinase domain from the ion channel and regulates its participation in Fas-induced apoptosis. *Developmental Cell* **22**: 1149–1162. DOI: <https://doi.org/10.1016/j.devcel.2012.04.006>, PMID: 22698280
- Dorovkov MV**, Ryazanov AG. 2004. Phosphorylation of annexin I by TRPM7 channel-kinase. *The Journal of Biological Chemistry* **279**: 50643–50646. DOI: <https://doi.org/10.1074/jbc.C400441200>, PMID: 15485879
- Duan J**, Li Z, Li J, Hulse RE, Santa-Cruz A, Valinsky WC, Abiria SA, Krapivinsky G, Zhang J, Clapham DE. 2018. Structure of the mammalian TRPM7, a magnesium channel required during embryonic development. *PNAS* **115**: E8201–E8210. DOI: <https://doi.org/10.1073/pnas.1810719115>
- Faouzi M**, Kilch T, Horgen FD, Fleig A, Penner R. 2017. The TRPM7 channel kinase regulates store-operated calcium entry. *The Journal of Physiology* **595**: 3165–3180. DOI: <https://doi.org/10.1113/JP274006>, PMID: 28130783
- Ferioli S**, Zierler S, Zaißerer J, Schredelseker J, Gudermann T, Chubanov V. 2017. TRPM6 and TRPM7 differentially contribute to the relief of heteromeric TRPM6/7 channels from inhibition by cytosolic Mg²⁺ and Mg-ATP. *Scientific Reports* **7**: 8806. DOI: <https://doi.org/10.1038/s41598-017-08144-1>, PMID: 28821869
- Fleig A**, Chubanov V. 2014. Handbook of Experimental Pharmacology. Springer. DOI: https://doi.org/10.1007/978-3-642-54215-2_21, PMID: 24756720
- Funato Y**, Yamazaki D, Mizukami S, Du L, Kikuchi K, Miki H. 2014. Membrane protein CNNM4-dependent Mg²⁺ efflux suppresses tumor progression. *The Journal of Clinical Investigation* **124**: 5398–5410. DOI: <https://doi.org/10.1172/JCI76614>, PMID: 25347473
- Funato Y**, Miki H. 2019. Molecular function and biological importance of CNNM family Mg²⁺ transporters. *Journal of Biochemistry* **165**: 219–225. DOI: <https://doi.org/10.1093/jb/mvy095>, PMID: 30476181
- Gillingham AK**, Munro S. 2007. The small G proteins of the Arf family and their regulators. *Annual Review of Cell and Developmental Biology* **23**: 579–611. DOI: <https://doi.org/10.1146/annurev.cellbio.23.090506.123209>, PMID: 17506703
- Giménez-Mascarell P**, Oyenarte I, Hardy S, Breiderhoff T, Stuiver M, Kostantin E, Diercks T, Pey AL, Ereño-Orbea J, Martínez-Chantar ML, Khalaf-Nazzal R, Claverie-Martin F, Müller D, Tremblay ML,

- Martínez-Cruz LA. 2017. Structural Basis of the Oncogenic Interaction of Phosphatase PRL-1 with the Magnesium Transporter CNNM2. *The Journal of Biological Chemistry* **292**: 786–801. DOI: <https://doi.org/10.1074/jbc.M116.759944>, PMID: 27899452
- Giménez-Mascarell P, González-Recio I, Fernández-Rodríguez C, Oyenarte I, Müller D, Martínez-Chantar ML, Martínez-Cruz LA. 2019. Current Structural Knowledge on the CNNM Family of Magnesium Transport Mediators. *International Journal of Molecular Sciences* **20**: E1135. DOI: <https://doi.org/10.3390/ijms20051135>, PMID: 30845649
- Gloor S, Pongs O, Schmalzing G. 1995. A vector for the synthesis of cRNAs encoding Myc epitope-tagged proteins in *Xenopus laevis* oocytes. *Gene* **160**: 213–217. DOI: [https://doi.org/10.1016/0378-1119\(95\)00226-v](https://doi.org/10.1016/0378-1119(95)00226-v), PMID: 7543868
- Gulerez I, Funato Y, Wu H, Yang M, Kozlov G, Miki H, Gehring K. 2016. Phosphocysteine in the PRL-CNNM pathway mediates magnesium homeostasis. *EMBO Reports* **17**: 1890–1900. DOI: <https://doi.org/10.15252/embr.201643393>, PMID: 27856537
- Hardy S, Uetani N, Wong N, Kostantin E, Labbé DP, Bégin LR, Mes-Masson A, Miranda-Saavedra D, Tremblay ML. 2015. The protein tyrosine phosphatase PRL-2 interacts with the magnesium transporter CNNM3 to promote oncogenesis. *Oncogene* **34**: 986–995. DOI: <https://doi.org/10.1038/onc.2014.33>, PMID: 24632616
- Hayes P, Meadows HJ, Gunthorpe MJ, Harries MH, Duckworth MD, Cairns W, Harrison DC, Clarke CE, Ellington K, Prinjha RK, Barton AJL, Medhurst AD, Smith GD, Topp S, Murdock P, Sanger GJ, Terrett J, Jenkins O, Benham CD, Randall AD, et al. 2000. Cloning and functional expression of a human orthologue of rat vanilloid receptor-1. *Pain* **88**: 205–215. DOI: [https://doi.org/10.1016/S0304-3959\(00\)00353-5](https://doi.org/10.1016/S0304-3959(00)00353-5), PMID: 11050376
- Hermosura MC, Nayakanti H, Dorovkov MV, Calderon FR, Ryazanov AG, Haymer DS, Garruto RM. 2005. A TRPM7 variant shows altered sensitivity to magnesium that may contribute to the pathogenesis of two Guamanian neurodegenerative disorders. *PNAS* **102**: 11510–11515. DOI: <https://doi.org/10.1073/pnas.0505149102>, PMID: 16051700
- Heukeshoven J, Dernick R. 1988. Improved silver staining procedure for fast staining in PhastSystem Development Unit. I. Staining of sodium dodecyl sulfate gels. *Electrophoresis* **9**: 28–32. DOI: <https://doi.org/10.1002/elps.1150090106>, PMID: 2466645
- Hofmann T, Schäfer S, Linseisen M, Sytik L, Gudermann T, Chubanov V. 2014. Activation of TRPM7 channels by small molecules under physiological conditions. *Pflügers Archiv* **466**: 2177–2189. DOI: <https://doi.org/10.1007/s00424-014-1488-0>, PMID: 24633576
- Huang Y, Jin F, Funato Y, Xu Z, Zhu W, Wang J, Sun M, Zhao Y, Yu Y, Miki H, Hattori M. 2021. Structural basis for the Mg²⁺ recognition and regulation of the CorC Mg²⁺ transporter. *Science Advances* **7**: abe6140. DOI: <https://doi.org/10.1126/sciadv.abe6140>
- Huttlin EL, Jedrychowski MP, Elias JE, Goswami T, Rad R, Beausoleil SA, Villén J, Haas W, Sowa ME, Gygi SP. 2010. A tissue-specific atlas of mouse protein phosphorylation and expression. *Cell* **143**: 1174–1189. DOI: <https://doi.org/10.1016/j.cell.2010.12.001>, PMID: 21183079
- Huttlin EL, Bruckner RJ, Paulo JA, Cannon JR, Ting L, Baltier K, Colby G, Gebreab F, Gygi MP, Parzen H, Szpyt J, Tam S, Zarraga G, Pontano-Vaites L, Swarup S, White AE, Schweppe DK, Rad R, Erickson BK, Obar RA, et al. 2017. Architecture of the human interactome defines protein communities and disease networks. *Nature* **545**: 505–509. DOI: <https://doi.org/10.1038/nature22366>, PMID: 28514442
- Huttlin EL, Bruckner RJ, Navarrete-Perea J, Cannon JR, Baltier K, Gebreab F, Gygi MP, Thornock A, Zarraga G, Tam S, Szpyt J, Gassaway BM, Panov A, Parzen H, Fu S, Golbazi A, Maenpää E, Stricker K, Guha Thakurta S, Zhang T, et al. 2021. Dual proteome-scale networks reveal cell-specific remodeling of the human interactome. *Cell* **184**: 3022–3040. DOI: <https://doi.org/10.1016/j.cell.2021.04.011>, PMID: 33961781
- Jin J, Desai BN, Navarro B, Donovan A, Andrews NC, Clapham DE. 2008. Deletion of Trpm7 disrupts embryonic development and thymopoiesis without altering Mg²⁺ homeostasis. *Science* **322**: 756–760. DOI: <https://doi.org/10.1126/science.1163493>, PMID: 18974357
- Jin Jie, Wu L-J, Jun J, Cheng X, Xu H, Andrews NC, Clapham DE. 2012. The channel kinase, TRPM7, is required for early embryonic development. *PNAS* **109**: E225–E233. DOI: <https://doi.org/10.1073/pnas.1120033109>, PMID: 22203997
- Kostantin E, Hardy S, Valinsky WC, Kompatscher A, de Baaij JHF, Zolotarov Y, Landry M, Uetani N, Martínez-Cruz LA, Hoenderop JGJ, Shrier A, Tremblay ML. 2016. Inhibition of PRL-2-CNNM3 Protein Complex Formation Decreases Breast Cancer Proliferation and Tumor Growth. *The Journal of Biological Chemistry* **291**: 10716–10725. DOI: <https://doi.org/10.1074/jbc.M115.705863>, PMID: 26969161
- Krapivinsky G, Krapivinsky L, Manasian Y, Clapham DE. 2014. The TRPM7 chanzyme is cleaved to release a chromatin-modifying kinase. *Cell* **157**: 1061–1072. DOI: <https://doi.org/10.1016/j.cell.2014.03.046>, PMID: 24855944
- Liu Y, Chen C, Liu Y, Li W, Wang Z, Sun Q, Zhou H, Chen X, Yu Y, Wang Y, Abumaria N. 2018. TRPM7 Is Required for Normal Synapse Density, Learning, and Memory at Different Developmental Stages. *Cell Reports* **23**: 3480–3491. DOI: <https://doi.org/10.1016/j.celrep.2018.05.069>, PMID: 29924992
- Mederos y Schnitzler M, Wäring J, Gudermann T, Chubanov V. 2008. Evolutionary determinants of divergent calcium selectivity of TRPM channels. *FASEB Journal* **22**: 1540–1551. DOI: <https://doi.org/10.1096/fj.07-9694com>, PMID: 18073331
- Mittermeier L, Demirkhanyan L, Stadlbauer B, Breit A, Recordati C, Hilgendorff A, Matsushita M, Braun A, Simmons DG, Zakharian E, Gudermann T, Chubanov V. 2019. TRPM7 is the central gatekeeper of intestinal

- p>mineral absorption essential for postnatal survival.
- PNAS*
- 116**
- : 4706–4715. DOI:
- <https://doi.org/10.1073/pnas.1810633116>
- , PMID: 30770447
- Monteilh-Zoller MK**, Hermosura MC, Nadler MJS, Scharenberg AM, Penner R, Fleig A. 2003. TRPM7 provides an ion channel mechanism for cellular entry of trace metal ions. *The Journal of General Physiology* **121**: 49–60. DOI: <https://doi.org/10.1085/jgp.20028740>, PMID: 12508053
- Müller CS**, Haupt A, Bildl W, Schindler J, Knaus H-G, Meissner M, Rammner B, Striessnig J, Flockerzi V, Fakler B, Schulte U. 2010. Quantitative proteomics of the Cav2 channel nano-environments in the mammalian brain. *PNAS* **107**: 14950–14957. DOI: <https://doi.org/10.1073/pnas.1005940107>, PMID: 20668236
- Müller CS**, Bildl W, Haupt A, Ellenrieder L, Becker T, Hunte C, Fakler B, Schulte U. 2016. Cryo-slicing Blue Native-Mass Spectrometry (csBN-MS), a Novel Technology for High Resolution Complexome Profiling. *Molecular & Cellular Proteomics* **15**:669–681. DOI: <https://doi.org/10.1074/mcp.M115.054080>, PMID: 26598645
- Müller CS**, Bildl W, Klugbauer N, Haupt A, Fakler B, Schulte U. 2019. High-Resolution Complexome Profiling by Cryoslicing BN-MS Analysis. *Journal of Visualized Experiments* **10**: 152. DOI: <https://doi.org/10.3791/60096>
- Nadler MJ**, Hermosura MC, Inabe K, Perraud AL, Zhu Q, Stokes AJ, Kurosaki T, Kinet JP, Penner R, Scharenberg AM, Fleig A. 2001. LTRPC7 is a Mg²⁺-ATP-regulated divalent cation channel required for cell viability. *Nature* **411**: 590–595. DOI: <https://doi.org/10.1038/35079092>, PMID: 11385574
- Nguyen TTA**, Li W, Park TJ, Gong LW, Cologna SM. 2019. Investigating Phosphorylation Patterns of the Ion Channel TRPM7 Using Multiple Extraction and Enrichment Techniques Reveals New Phosphosites. *Journal of the American Society for Mass Spectrometry* **30**: 1359–1367. DOI: <https://doi.org/10.1007/s13361-019-02223-5>, PMID: 31140077
- Pandey A**, Mann M. 2000. Proteomics to study genes and genomes. *Nature* **405**: 837–846. DOI: <https://doi.org/10.1038/35015709>, PMID: 10866210
- Parry DA**, Mighell AJ, El-Sayed W, Shore RC, Jalili IK, Dollfus H, Bloch-Zupan A, Carlos R, Carr IM, Downey LM, Blain KM, Mansfield DC, Shahrabi M, Heidari M, Aref P, Abbasi M, Michaelides M, Moore AT, Kirkham J, Inglehearn CF. 2009. Mutations in CNNM4 cause Jalili syndrome, consisting of autosomal-recessive cone-rod dystrophy and amelogenesis imperfecta. *American Journal of Human Genetics* **84**: 266–273. DOI: <https://doi.org/10.1016/j.ajhg.2009.01.009>, PMID: 19200525
- Perraud AL**, Zhao X, Ryazanov AG, Schmitz C. 2011. The channel-kinase TRPM7 regulates phosphorylation of the translational factor eEF2 via eEF2-k. *Cellular Signalling* **23**: 586–593. DOI: <https://doi.org/10.1016/j.cellsig.2010.11.011>, PMID: 21112387
- Richards JB**, Waterworth D, O’Rahilly S, Hivert M-F, Loos RJF, Perry JRB, Tanaka T, Timpson NJ, Semple RK, Soranzo N, Song K, Rocha N, Grundberg E, Dupuis J, Florez JC, Langenberg C, Prokopenko I, Saxena R, Sladek R, Aulchenko Y, et al. 2009. A genome-wide association study reveals variants in ARL15 that influence adiponectin levels. *PLoS Genetics* **5**: 12. DOI: <https://doi.org/10.1371/journal.pgen.1000768>, PMID: 20011104
- Rivera B**, Moreno C, Lavanderos B, Hwang JY, Fernández-Trillo J, Park K-S, Orio P, Viana F, Madrid R, Pertusa M. 2021. Constitutive Phosphorylation as a Key Regulator of TRPM8 Channel Function. *The Journal of Neuroscience* **41**: 8475–8493. DOI: <https://doi.org/10.1523/JNEUROSCI.0345-21.2021>, PMID: 34446569
- Romagnani A**, Vettore V, Rezzonico-Jost T, Hampe S, Rottoli E, Nadolni W, Perotti M, Meier MA, Hermanns C, Geiger S, Wennemuth G, Recordati C, Matsushita M, Muehlich S, Proietti M, Chubanov V, Gudermann T, Grassi F, Zierler S. 2017. TRPM7 kinase activity is essential for T cell colonization and alloreactivity in the gut. *Nature Communications* **8**: 1917. DOI: <https://doi.org/10.1038/s41467-017-01960-z>, PMID: 29203869
- Runnels LW**, Yue L, Clapham DE. 2001. TRP-PLIK, a bifunctional protein with kinase and ion channel activities. *Science* **291**: 1043–1047. DOI: <https://doi.org/10.1126/science.1058519>, PMID: 11161216
- Runnels LW**, Yue L, Clapham DE. 2002. The TRPM7 channel is inactivated by PIP(2) hydrolysis. *Nature Cell Biology* **4**: 329–336. DOI: <https://doi.org/10.1038/ncb781>, PMID: 11941371
- Ryazanov AG**, Ward MD, Mendola CE, Pavur KS, Dorovkov MV, Wiedmann M, Erdjument-Bromage H, Tempst P, Parmer TG, Prostko CR, Germino FJ, Hait WN. 1997. Identification of a new class of protein kinases represented by eukaryotic elongation factor-2 kinase. *PNAS* **94**: 4884–4889. DOI: <https://doi.org/10.1073/pnas.94.10.4884>, PMID: 9144159
- Sah R**, Mesirca P, Mason X, Gibson W, Bates-Withers C, Van den Boogert M, Chaudhuri D, Pu WT, Mangoni ME, Clapham DE. 2013a. Timing of myocardial trpm7 deletion during cardiogenesis variably disrupts adult ventricular function, conduction, and repolarization. *Circulation* **128**: 101–114. DOI: <https://doi.org/10.1161/CIRCULATIONAHA.112.000768>, PMID: 23734001
- Sah R**, Mesirca P, Van den Boogert M, Rosen J, Mably J, Mangoni ME, Clapham DE. 2013b. Ion channel-kinase TRPM7 is required for maintaining cardiac automaticity. *PNAS* **110**: E3037–E3046. DOI: <https://doi.org/10.1073/pnas.1311865110>, PMID: 23878236
- Schägger H**, Pfeiffer K. 2000. Supercomplexes in the respiratory chains of yeast and mammalian mitochondria. *The EMBO Journal* **19**: 1777–1783. DOI: <https://doi.org/10.1093/emboj/19.8.1777>, PMID: 10775262
- Schmidt N**, Kollewe A, Constantin CE, Henrich S, Ritzau-Jost A, Bildl W, Saalbach A, Hallermann S, Kulik A, Fakler B, Schulte U. 2017. Neuroplastin and Basigin Are Essential Auxiliary Subunits of Plasma Membrane Ca²⁺-ATPases and Key Regulators of Ca²⁺ Clearance. *Neuron* **96**: 827–838. DOI: <https://doi.org/10.1016/j.neuron.2017.09.038>, PMID: 29056295
- Schmitz C**, Perraud A-L, Johnson CO, Inabe K, Smith MK, Penner R, Kurosaki T, Fleig A, Scharenberg AM. 2003. Regulation of vertebrate cellular Mg²⁺ homeostasis by TRPM7. *Cell* **114**: 191–200. DOI: [https://doi.org/10.1016/s0092-8674\(03\)00556-7](https://doi.org/10.1016/s0092-8674(03)00556-7), PMID: 12887921
- Schwenk J**, Metz M, Zolles G, Turecek R, Fritzius T, Bildl W, Tarusawa E, Kulik A, Unger A, Ivankova K, Seddik R, Tiao JY, Rajalu M, Trojanova J, Rohde V, Gassmann M, Schulte U, Fakler B, Bettler B. 2010. Native GABA(B)

- p>receptors are heteromultimers with a family of auxiliary subunits.
- Nature*
- 465**
- : 231–235. DOI:
- <https://doi.org/10.1038/nature08964>
- , PMID: 20400944
- Schwenk J**, Harmel N, Brechet A, Zolles G, Berkefeld H, Müller CS, Bildl W, Baehrens D, Hüber B, Kulik A, Klöcker N, Schulte U, Fakler B. 2012. High-resolution proteomics unravel architecture and molecular diversity of native AMPA receptor complexes. *Neuron* **74**: 621–633. DOI: <https://doi.org/10.1016/j.neuron.2012.03.034>, PMID: 22632720
- Schwenk J**, Pérez-Garci E, Schneider A, Kollwe A, Gauthier-Kemper A, Fritzius T, Raveh A, Dinamarca MC, Hanuschkin A, Bildl W, Klingauf J, Gassmann M, Schulte U, Bettler B, Fakler B. 2016. Modular composition and dynamics of native GABAB receptors identified by high-resolution proteomics. *Nature Neuroscience* **19**: 233–242. DOI: <https://doi.org/10.1038/nn.4198>, PMID: 26691831
- Song C**, Bae Y, Jun J, Lee H, Kim ND, Lee K-B, Hur W, Park J-Y, Sim T. 2017. Identification of TG100-115 as a new and potent TRPM7 kinase inhibitor, which suppresses breast cancer cell migration and invasion. *Biochimica et Biophysica Acta. General Subjects* **1861**: 947–957. DOI: <https://doi.org/10.1016/j.bbagen.2017.01.034>, PMID: 28161478
- Stritt S**, Nurden P, Favier R, Favier M, Ferioli S, Gotru SK, van Eeuwijk JMM, Schulze H, Nurden AT, Lambert MP, Turro E, Burger-Stritt S, Matsushita M, Mittermeier L, Ballerini P, Zierler S, Laffan MA, Chubanov V, Gudermann T, Nieswandt B, et al. 2016. Defects in TRPM7 channel function deregulate thrombopoiesis through altered cellular Mg(2+) homeostasis and cytoskeletal architecture. *Nature Communications* **7**: 11097. DOI: <https://doi.org/10.1038/ncomms11097>, PMID: 27020697
- Stuiver M**, Lainez S, Will C, Terryn S, Günzel D, Debaix H, Sommer K, Kopplin K, Thumfart J, Kampik NB, Querfeld U, Willnow TE, Némec V, Wagner CA, Hoenderop JG, Devuyst O, Knoers NVAM, Bindels RJ, Meij IC, Müller D. 2011. CNNM2, encoding a basolateral protein required for renal Mg2+ handling, is mutated in dominant hypomagnesemia. *American Journal of Human Genetics* **88**: 333–343. DOI: <https://doi.org/10.1016/j.ajhg.2011.02.005>, PMID: 21397062
- Sun H-S**, Jackson MF, Martin LJ, Jansen K, Teves L, Cui H, Kiyonaka S, Mori Y, Jones M, Forder JP, Golde TE, Orser BA, Macdonald JF, Tymianski M. 2009. Suppression of hippocampal TRPM7 protein prevents delayed neuronal death in brain ischemia. *Nature Neuroscience* **12**: 1300–1307. DOI: <https://doi.org/10.1038/nn.2395>, PMID: 19734892
- Voringer S**, Schreyer L, Nadolni W, Meier MA, Woerther K, Mittermeier C, Ferioli S, Singer S, Holzer K, Zierler S, Chubanov V, Liebl B, Gudermann T, Muehlich S. 2020. Inhibition of TRPM7 blocks MRTF/SRF-dependent transcriptional and tumorigenic activity. *Oncogene* **39**: 2328–2344. DOI: <https://doi.org/10.1038/s41388-019-1140-8>, PMID: 31844251
- Yamazaki D**, Funato Y, Miura J, Sato S, Toyosawa S, Furutani K, Kurachi Y, Omori Y, Furukawa T, Tsuda T, Kuwabata S, Mizukami S, Kikuchi K, Miki H. 2013. Basolateral Mg2+ extrusion via CNNM4 mediates transcellular Mg2+ transport across epithelia: a mouse model. *PLOS Genetics* **9**: 12. DOI: <https://doi.org/10.1371/journal.pgen.1003983>, PMID: 24339795
- Zhang H**, Kozlov G, Li X, Wu H, Gulerez I, Gehring K. 2017. PRL3 phosphatase active site is required for binding the putative magnesium transporter CNNM3. *Scientific Reports* **7**: 48. DOI: <https://doi.org/10.1038/s41598-017-00147-2>
- Zhou H**, Di Palma S, Preisinger C, Peng M, Polat AN, Heck AJR, Mohammed S. 2013. Toward a comprehensive characterization of a human cancer cell phosphoproteome. *Journal of Proteome Research* **12**: 260–271. DOI: <https://doi.org/10.1021/pr300630k>, PMID: 23186163

Supplementary figures publication III

In this chapter I only included supplementary figures I produced myself.

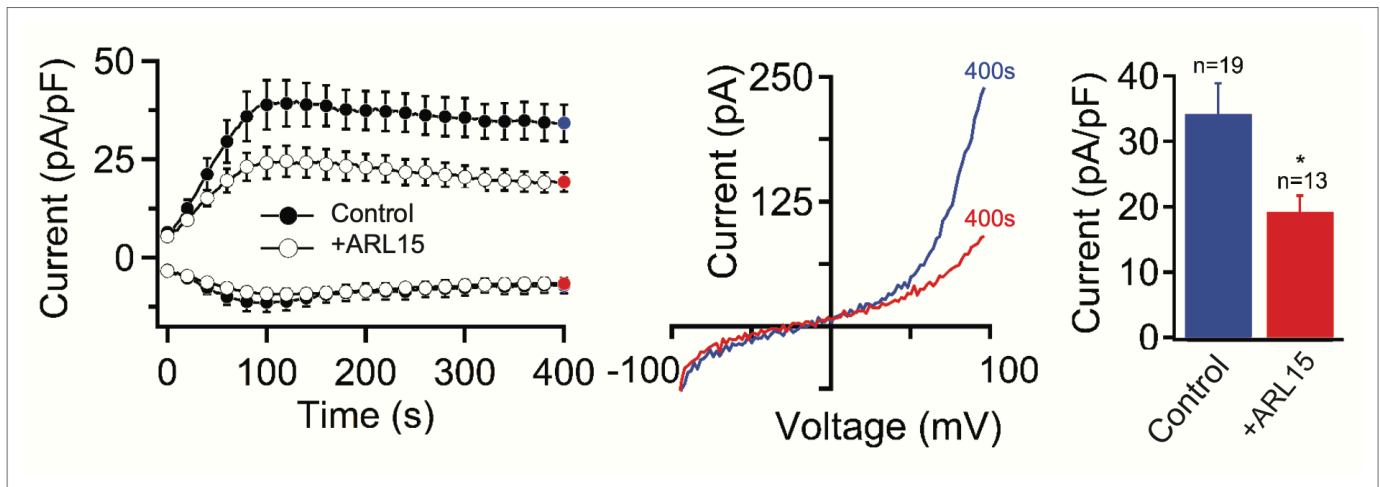


Figure 3—figure supplement 4. Impact of ADP-ribosylation factor-like protein 15 (ARL15) on endogenous transient receptor potential melastatin-subfamily member 7 (TRPM7) currents in HEK293 cells. Whole-cell endogenous TRPM7 currents were recorded in untransfected cells (control) and cells transfected with *Arl15* plasmid DNAs. Currents were induced using the Mg^{2+} -free internal solution and the standard external solution containing 3 mM Ca^{2+} (no Mg^{2+}). *Left panel:* Current amplitudes (mean \pm standard error of the mean [SEM]) were acquired at -80 and $+80$ mV and plotted over time. *Middle panel:* Representative current-voltage (I-V) relationships of currents (at 400 s) shown in *left panel*. *Right panel:* Bar graphs of outward currents (mean \pm SEM) in (A) at 400 s shown in *left panel*. n, number of cells measured. ns, not significant; * $p \leq 0.05$ (two-tailed t-test).

References

1. Rössig, A., et al., *Pharmacological agents selectively acting on the channel moieties of TRPM6 and TRPM7*. Cell Calcium, 2022. **106**: p. 102640.
2. Chubanov, V., et al., *Natural and synthetic modulators of SK (K_{Ca})₂ potassium channels inhibit magnesium-dependent activity of the kinase-coupled cation channel TRPM7*. Br J Pharmacol, 2012. **166**(4): p. 1357-76.
3. Chubanov, V., et al., *Epithelial magnesium transport by TRPM6 is essential for prenatal development and adult survival*. Elife, 2016. **5**.
4. Chubanov, V., et al., *Disruption of TRPM6/TRPM7 complex formation by a mutation in the TRPM6 gene causes hypomagnesemia with secondary hypocalcemia*. Proc Natl Acad Sci U S A, 2004. **101**(9): p. 2894-9.
5. Zhang, Z., et al., *N-Myc-induced up-regulation of TRPM6/TRPM7 channels promotes neuroblastoma cell proliferation*. Oncotarget, 2014. **5**(17): p. 7625-34.
6. Massey, A.J., et al., *A novel, small molecule inhibitor of Hsc70/Hsp70 potentiates Hsp90 inhibitor induced apoptosis in HCT116 colon carcinoma cells*. Cancer Chemother Pharmacol, 2010. **66**(3): p. 535-45.
7. Romagnani, A., et al., *TRPM7 kinase activity is essential for T cell colonization and alloreactivity in the gut*. Nat Commun, 2017. **8**(1): p. 1917.
8. Schmitz, C., et al., *Regulation of vertebrate cellular Mg²⁺ homeostasis by TRPM7*. Cell, 2003. **114**(2): p. 191-200.
9. Lutz, W., et al., *Conditional expression of N-myc in human neuroblastoma cells increases expression of alpha-prothymosin and ornithine decarboxylase and accelerates progression into S-phase early after mitogenic stimulation of quiescent cells*. Oncogene, 1996. **13**(4): p. 803-12.
10. Schmidt, E., et al., *Structural mechanism of TRPM7 channel regulation by intracellular magnesium*. Cell Mol Life Sci, 2022. **79**(5): p. 225.
11. Nadler, M.J., et al., *LTRPC7 is a Mg.ATP-regulated divalent cation channel required for cell viability*. Nature, 2001. **411**(6837): p. 590-5.
12. Kollwe, A., et al., *The molecular appearance of native TRPM7 channel complexes identified by high-resolution proteomics*. Elife, 2021. **10**.
13. Chubanov, V. and T. Gudermann, *Trpm6*. Handb Exp Pharmacol, 2014. **222**: p. 503-20.
14. Fleig, A. and V. Chubanov, *Trpm7*. Handb Exp Pharmacol, 2014. **222**: p. 521-46.
15. Chubanov, V., et al., *TRPM channels in health and disease*. Nat Rev Nephrol, 2023.
16. Montell, C., *The TRP superfamily of cation channels*. Sci STKE, 2005. **2005**(272): p. re3.

17. Voets, T., et al., *TRPM6 forms the Mg²⁺ influx channel involved in intestinal and renal Mg²⁺ absorption*. J Biol Chem, 2004. **279**(1): p. 19-25.
18. Fujiwara, Y. and D.L. Minor, Jr., *X-ray crystal structure of a TRPM assembly domain reveals an antiparallel four-stranded coiled-coil*. J Mol Biol, 2008. **383**(4): p. 854-70.
19. Owsianik, G., et al., *Permeation and selectivity of TRP channels*. Annu Rev Physiol, 2006. **68**: p. 685-717.
20. Ferioli, S., et al., *TRPM6 and TRPM7 differentially contribute to the relief of heteromeric TRPM6/7 channels from inhibition by cytosolic Mg(2+) and Mg.ATP*. Sci Rep, 2017. **7**(1): p. 8806.
21. Venkatachalam, K. and C. Montell, *TRP channels*. Annu Rev Biochem, 2007. **76**: p. 387-417.
22. Vriens, J., et al., *Invertebrate TRP proteins as functional models for mammalian channels*. Pflugers Arch, 2004. **449**(3): p. 213-26.
23. Dorovkov, M.V. and A.G. Ryazanov, *Phosphorylation of annexin I by TRPM7 channel-kinase*. J Biol Chem, 2004. **279**(49): p. 50643-6.
24. Clark, K., et al., *TRPM7, a novel regulator of actomyosin contractility and cell adhesion*. EMBO J, 2006. **25**(2): p. 290-301.
25. Deason-Towne, F., A.L. Perraud, and C. Schmitz, *Identification of Ser/Thr phosphorylation sites in the C2-domain of phospholipase C gamma2 (PLCgamma2) using TRPM7-kinase*. Cell Signal, 2012. **24**(11): p. 2070-5.
26. Perraud, A.L., et al., *The channel-kinase TRPM7 regulates phosphorylation of the translational factor eEF2 via eEF2-k*. Cell Signal, 2011. **23**(3): p. 586-93.
27. Brandao, K., et al., *TRPM6 kinase activity regulates TRPM7 trafficking and inhibits cellular growth under hypomagnesian conditions*. Cell Mol Life Sci, 2014. **71**(24): p. 4853-67.
28. Demeuse, P., R. Penner, and A. Fleig, *TRPM7 channel is regulated by magnesium nucleotides via its kinase domain*. J Gen Physiol, 2006. **127**(4): p. 421-34.
29. Matsushita, M., et al., *Channel function is dissociated from the intrinsic kinase activity and autophosphorylation of TRPM7/ChaK1*. J Biol Chem, 2005. **280**(21): p. 20793-803.
30. Duan, J., et al., *Structure of the mammalian TRPM7, a magnesium channel required during embryonic development*. Proc Natl Acad Sci U S A, 2018. **115**(35): p. E8201-E8210.
31. Nadezhdin, K.D., et al., *Structural mechanisms of TRPM7 activation and inhibition*. Nat Commun, 2023. **14**(1): p. 2639.
32. Monteilh-Zoller, M.K., et al., *TRPM7 provides an ion channel mechanism for cellular entry of trace metal ions*. J Gen Physiol, 2003. **121**(1): p. 49-60.

33. Runnels, L.W., L. Yue, and D.E. Clapham, *TRP-PLIK, a bifunctional protein with kinase and ion channel activities*. Science, 2001. **291**(5506): p. 1043-7.
34. Kerschbaum, H.H. and M.D. Cahalan, *Single-channel recording of a store-operated Ca²⁺ channel in Jurkat T lymphocytes*. Science, 1999. **283**(5403): p. 836-9.
35. Kerschbaum, H.H., J.A. Kozak, and M.D. Cahalan, *Polyvalent cations as permeant probes of MIC and TRPM7 pores*. Biophys J, 2003. **84**(4): p. 2293-305.
36. Chubanov, V., et al., *Hypomagnesemia with secondary hypocalcemia due to a missense mutation in the putative pore-forming region of TRPM6*. J Biol Chem, 2007. **282**(10): p. 7656-67.
37. Schmitz, C., et al., *The channel kinases TRPM6 and TRPM7 are functionally nonredundant*. J Biol Chem, 2005. **280**(45): p. 37763-71.
38. Li, M., J. Jiang, and L. Yue, *Functional characterization of homo- and heteromeric channel kinases TRPM6 and TRPM7*. J Gen Physiol, 2006. **127**(5): p. 525-37.
39. Thebault, S., et al., *Role of the alpha-kinase domain in transient receptor potential melastatin 6 channel and regulation by intracellular ATP*. J Biol Chem, 2008. **283**(29): p. 19999-20007.
40. Zhang, Z., et al., *The TRPM6 kinase domain determines the Mg.ATP sensitivity of TRPM7/M6 heteromeric ion channels*. J Biol Chem, 2014. **289**(8): p. 5217-27.
41. Xie, J., et al., *Phosphatidylinositol 4,5-bisphosphate (PIP(2)) controls magnesium gatekeeper TRPM6 activity*. Sci Rep, 2011. **1**: p. 146.
42. Kozak, J.A., H.H. Kerschbaum, and M.D. Cahalan, *Distinct properties of CRAC and MIC channels in RBL cells*. J Gen Physiol, 2002. **120**(2): p. 221-35.
43. Prakriya, M. and R.S. Lewis, *Separation and characterization of currents through store-operated CRAC channels and Mg²⁺-inhibited cation (MIC) channels*. J Gen Physiol, 2002. **119**(5): p. 487-507.
44. Romani, A.M., *Cellular magnesium homeostasis*. Arch Biochem Biophys, 2011. **512**(1): p. 1-23.
45. Romani, A.M. and A. Scarpa, *Regulation of cellular magnesium*. Front Biosci, 2000. **5**: p. D720-34.
46. Huttlin, E.L., et al., *Dual proteome-scale networks reveal cell-specific remodeling of the human interactome*. Cell, 2021. **184**(11): p. 3022-3040 e28.
47. Qin, Y., et al., *A multi-scale map of cell structure fusing protein images and interactions*. Nature, 2021. **600**(7889): p. 536-542.
48. Bai, Z., et al., *CNNM proteins selectively bind to the TRPM7 channel to stimulate divalent cation entry into cells*. PLoS Biol, 2021. **19**(12): p. e3001496.
49. Funato, Y. and H. Miki, *Molecular function and biological importance of CNNM family Mg²⁺ transporters*. J Biochem, 2019. **165**(3): p. 219-225.

50. Gimenez-Mascarell, P., et al., *Current Structural Knowledge on the CNNM Family of Magnesium Transport Mediators*. Int J Mol Sci, 2019. **20**(5).
51. Gimenez-Mascarell, P., et al., *Structural Insights into the Intracellular Region of the Human Magnesium Transport Mediator CNNM4*. Int J Mol Sci, 2019. **20**(24).
52. Arjona, F.J. and J.H.F. de Baaij, *CrossTalk opposing view: CNNM proteins are not Na(+) /Mg(2+) exchangers but Mg(2+) transport regulators playing a central role in transepithelial Mg(2+) (re)absorption*. J Physiol, 2018. **596**(5): p. 747-750.
53. Gillingham, A.K. and S. Munro, *The small G proteins of the Arf family and their regulators*. Annu Rev Cell Dev Biol, 2007. **23**: p. 579-611.
54. Richards, J.B., et al., *A genome-wide association study reveals variants in ARL15 that influence adiponectin levels*. PLoS Genet, 2009. **5**(12): p. e1000768.
55. Hardy, S., et al., *PRL-1/2 phosphatases control TRPM7 magnesium-dependent function to regulate cellular bioenergetics*. Proc Natl Acad Sci U S A, 2023. **120**(14): p. e2221083120.
56. Schlingmann, K.P., et al., *Hypomagnesemia with secondary hypocalcemia is caused by mutations in TRPM6, a new member of the TRPM gene family*. Nat Genet, 2002. **31**(2): p. 166-70.
57. Fonfria, E., et al., *Tissue distribution profiles of the human TRPM cation channel family*. J Recept Signal Transduct Res, 2006. **26**(3): p. 159-78.
58. Walder, R.Y., et al., *Mutation of TRPM6 causes familial hypomagnesemia with secondary hypocalcemia*. Nat Genet, 2002. **31**(2): p. 171-4.
59. Shalev, H., et al., *Clinical presentation and outcome in primary familial hypomagnesaemia*. Arch Dis Child, 1998. **78**(2): p. 127-30.
60. Walder, R.Y., et al., *Mice defective in Trpm6 show embryonic mortality and neural tube defects*. Hum Mol Genet, 2009. **18**(22): p. 4367-75.
61. Woudenberg-Vrenken, T.E., et al., *Transient receptor potential melastatin 6 knockout mice are lethal whereas heterozygous deletion results in mild hypomagnesemia*. Nephron Physiol, 2011. **117**(2): p. p11-9.
62. Aarts, M., et al., *A key role for TRPM7 channels in anoxic neuronal death*. Cell, 2003. **115**(7): p. 863-77.
63. Gwanyanya, A., et al., *Magnesium-inhibited, TRPM6/7-like channel in cardiac myocytes: permeation of divalent cations and pH-mediated regulation*. J Physiol, 2004. **559**(Pt 3): p. 761-76.
64. Kim, B.J., et al., *Regulation of transient receptor potential melastatin 7 (TRPM7) currents by mitochondria*. Mol Cells, 2007. **23**(3): p. 363-9.
65. Mishra, R., et al., *Mg2+- and MgATP-inhibited and Ca2+/calmodulin-sensitive TRPM7-like current in hepatoma and hepatocytes*. Am J Physiol Gastrointest Liver Physiol, 2009. **297**(4): p. G687-94.

66. Numata, T., T. Shimizu, and Y. Okada, *TRPM7 is a stretch- and swelling-activated cation channel involved in volume regulation in human epithelial cells*. *Am J Physiol Cell Physiol*, 2007. **292**(1): p. C460-7.
67. Ryazanova, L.V., et al., *TRPM7 is essential for Mg(2+) homeostasis in mammals*. *Nat Commun*, 2010. **1**: p. 109.
68. Faouzi, M., et al., *The TRPM7 channel kinase regulates store-operated calcium entry*. *J Physiol*, 2017. **595**(10): p. 3165-3180.
69. Visser, D., et al., *TRPM7 triggers Ca²⁺ sparks and invadosome formation in neuroblastoma cells*. *Cell Calcium*, 2013. **54**(6): p. 404-15.
70. Brauchi, S., et al., *TRPM7 facilitates cholinergic vesicle fusion with the plasma membrane*. *Proc Natl Acad Sci U S A*, 2008. **105**(24): p. 8304-8.
71. Clark, K., et al., *TRPM7 regulates myosin IIA filament stability and protein localization by heavy chain phosphorylation*. *J Mol Biol*, 2008. **378**(4): p. 790-803.
72. Sahni, J., et al., *TRPM7 regulates quiescent/proliferative metabolic transitions in lymphocytes*. *Cell Cycle*, 2010. **9**(17): p. 3565-74.
73. Tani, D., et al., *Cell cycle-dependent regulation of store-operated I(CRAC) and Mg²⁺-nucleotide-regulated MagNuM (TRPM7) currents*. *Cell Calcium*, 2007. **41**(3): p. 249-60.
74. Wei, C., et al., *Calcium flickers steer cell migration*. *Nature*, 2009. **457**(7231): p. 901-5.
75. Jin, J., et al., *Deletion of Trpm7 disrupts embryonic development and thymopoiesis without altering Mg²⁺ homeostasis*. *Science*, 2008. **322**(5902): p. 756-60.
76. Jin, J., et al., *The channel kinase, TRPM7, is required for early embryonic development*. *Proc Natl Acad Sci U S A*, 2012. **109**(5): p. E225-33.
77. McNeill, M.S., et al., *Cell death of melanophores in zebrafish trpm7 mutant embryos depends on melanin synthesis*. *J Invest Dermatol*, 2007. **127**(8): p. 2020-30.
78. Sun, H.S., et al., *Suppression of hippocampal TRPM7 protein prevents delayed neuronal death in brain ischemia*. *Nat Neurosci*, 2009. **12**(10): p. 1300-7.
79. Zhang, J., et al., *Hypoxia induces an increase in intracellular magnesium via transient receptor potential melastatin 7 (TRPM7) channels in rat hippocampal neurons in vitro*. *J Biol Chem*, 2011. **286**(23): p. 20194-207.
80. Tseveleki, V., et al., *Comparative gene expression analysis in mouse models for multiple sclerosis, Alzheimer's disease and stroke for identifying commonly regulated and disease-specific gene changes*. *Genomics*, 2010. **96**(2): p. 82-91.
81. Du, J., et al., *TRPM7-mediated Ca²⁺ signals confer fibrogenesis in human atrial fibrillation*. *Circ Res*, 2010. **106**(5): p. 992-1003.
82. Touyz, R.M., et al., *Differential regulation of transient receptor potential melastatin 6 and 7 cation channels by ANG II in vascular smooth muscle*

- cells from spontaneously hypertensive rats. *Am J Physiol Regul Integr Comp Physiol*, 2006. **290**(1): p. R73-8.
83. Zhang, Y.H., et al., *Evidence for functional expression of TRPM7 channels in human atrial myocytes*. *Basic Res Cardiol*, 2012. **107**(5): p. 282.
84. Yue, Z., et al., *Transient receptor potential (TRP) channels and cardiac fibrosis*. *Curr Top Med Chem*, 2013. **13**(3): p. 270-82.
85. Rios, F.J., et al., *Chanzyme TRPM7 protects against cardiovascular inflammation and fibrosis*. *Cardiovasc Res*, 2020. **116**(3): p. 721-735.
86. Hu, F., et al., *Role of TRPM7 in cardiac fibrosis: A potential therapeutic target (Review)*. *Exp Ther Med*, 2021. **21**(2): p. 173.
87. Chen, J.P., et al., *TRPM7 regulates the migration of human nasopharyngeal carcinoma cell by mediating Ca(2+) influx*. *Cell Calcium*, 2010. **47**(5): p. 425-32.
88. Jiang, J., et al., *Transient receptor potential melastatin 7-like current in human head and neck carcinoma cells: role in cell proliferation*. *Cancer Res*, 2007. **67**(22): p. 10929-38.
89. Kim, B.J., et al., *Suppression of transient receptor potential melastatin 7 channel induces cell death in gastric cancer*. *Cancer Sci*, 2008. **99**(12): p. 2502-9.
90. Meng, X., et al., *TRPM7 mediates breast cancer cell migration and invasion through the MAPK pathway*. *Cancer Lett*, 2013. **333**(1): p. 96-102.
91. Stritt, S., et al., *Defects in TRPM7 channel function deregulate thrombopoiesis through altered cellular Mg(2+) homeostasis and cytoskeletal architecture*. *Nat Commun*, 2016. **7**: p. 11097.
92. Gualdani, R., et al., *A TRPM7 mutation linked to familial trigeminal neuralgia: Omega current and hyperexcitability of trigeminal ganglion neurons*. *Proc Natl Acad Sci U S A*, 2022. **119**(38): p. e2119630119.
93. Mittermeier, L., et al., *TRPM7 is the central gatekeeper of intestinal mineral absorption essential for postnatal survival*. *Proc Natl Acad Sci U S A*, 2019. **116**(10): p. 4706-4715.
94. Zierler, S., et al., *Waixenicin A inhibits cell proliferation through magnesium-dependent block of transient receptor potential melastatin 7 (TRPM7) channels*. *J Biol Chem*, 2011. **286**(45): p. 39328-35.
95. Chubarov, V., et al., *Natural and Synthetic Modulators of the TRPM7 Channel*. *Cells*, 2014. **3**(4): p. 1089-101.
96. Chubarov, V. and T. Gudermann, *Mapping TRPM7 Function by NS8593*. *Int J Mol Sci*, 2020. **21**(19).
97. Qin, X., et al., *Sphingosine and FTY720 are potent inhibitors of the transient receptor potential melastatin 7 (TRPM7) channels*. *Br J Pharmacol*, 2013. **168**(6): p. 1294-312.
98. Guan, Z., et al., *CCT128930 is a novel and potent antagonist of TRPM7 channel*. *Biochem Biophys Res Commun*, 2021. **560**: p. 132-138.

99. Hofmann, T., et al., *Activation of TRPM7 channels by small molecules under physiological conditions*. Pflugers Arch, 2014. **466**(12): p. 2177-89.
100. Schafer, S., et al., *Mibefradil represents a new class of benzimidazole TRPM7 channel agonists*. Pflugers Arch, 2016. **468**(4): p. 623-34.
101. Song, C., et al., *Identification of TG100-115 as a new and potent TRPM7 kinase inhibitor, which suppresses breast cancer cell migration and invasion*. Biochim Biophys Acta Gen Subj, 2017. **1861**(4): p. 947-957.

Acknowledgements

Being part of the research group of Prof. Dr. Thomas Gudermann and Dr. Vladimir Chubanov at the Walther-Straub-Institute of Pharmacology and Toxicology of the Ludwig-Maximilians-University Munich was a great opportunity for me. It was an excellent way of being introduced into the scientific world and for that I am deeply grateful.

First of all, I would like to sincerely thank **Prof. Dr. Thomas Gudermann** for giving me the possibility to be part of his institute and the research training group GRK 2338. I am very thankful for his kind support, especially by making the pivotal, collaborative stay in Leipzig possible.

I am most grateful to **Dr. Vladimir Chubanov** for his time, his reliability and his outstanding effort, that he put into our research project. I could profit immensely from his scientific knowledge, his analytic abilities and his realism so that he became a role model for me.

Also, I would like to express my profound gratitude to **Prof. Dr. Michael Schaefer** from the Rudolf-Boehm-Institute for Pharmacology and Toxicology in Leipzig without whom the high-throughput screening would not have been successful. Special thanks go out to **PD Dr. Kerstin Hill** for her support and to **Nicole Urban** for her great technical assistance. I thank them and the whole team in Leipzig for their comprehensive hospitality.

For introducing me into electrophysiological technique and her valuable advice I would like to thank **Prof. Dr. Susanna Zierler** sincerely.

I thank all my former and present colleagues in our research group: **Anna Erbacher, Joanna Zaisserer, Miyuki Egawa, Eva Schmidt, Sebastian Weidenbach and Leonor Correia** for the particularly encouraging, helpful and collegial atmosphere in the lab. I am immensely thankful to **Joanna Zaisserer** for her precise and patient introduction into the manual work of the laboratory and her experimental support throughout the project. For her extremely professional and thorough proofreading of my thesis I would like to thank **Anna Erbacher**. A special thanks also goes to **Miyuki Egawa** and **Eva Schmidt** for their technical and emotional support during the patch-clamp experiments. Last but not least I would like to thank **Marius Näher** for being a good friend inside the laboratory.

A big thank you also to my old flatmates, **Vera Britz** and **Patrick Hoffmann**, for their nightly support and encouragement in Fürstenried.

Personally, I want to thank **Felix Stieglmeier** for his particular involvement during the whole time of my thesis, thereby not missing any up or down. You are a constant source of happiness, stability and great joy in my life.

Finally, I am forever grateful to my parents, **Gudrun Rössig** und **Jürgen Rössig**, and my brother **Paul Rössig** for their continuous financial, emotional and loving support.